Experimental Investigations and Modeling of Standard PVB at Finite Strains subjected to Quasistatic Loads

Alexander Pauli

Vollständiger Abdruck der von der Fakultät für Bauingenieurwesen und Umweltwissenschaften der Universität der Bundeswehr München zur Erlangung des akademischen Grades eines

Doktor-Ingenieurs (Dr.-Ing.)

angenommenen Dissertation.

Gutachter:

1. Univ.-Prof. Dr.-Ing. Geralt Siebert
2. Univ.-Prof. Dr.-Ing. Jens Schneider
3. Univ.-Prof. Dr.-Ing. habil. Alexander Lion

Die Dissertation wurde am 06.06.2024 bei der Universität der Bundeswehr München eingereicht und durch die Fakultät für Bauingenieurwesen und Umweltwissenschaften am 14.11.2024 angenommen. Die mündliche Prüfung fand am 14.11.2024 statt.

Danksagung

Die vorliegende Arbeit entstand im Rahmen meiner Tätigkeit als wissenschaftlicher Mitarbeiter in den Jahren 2018 bis 2024 am Institut für Konstruktiven Ingenieurbau der Universität der Bundeswehr München.

Mein außerordentlicher Dank gilt Univ.-Prof. Dr.-Ing. Geralt Siebert für die Möglichkeit, bei ihm promovieren zu dürfen. Insbesondere bedanke ich mich für die stete Förderung, die große Freiheit in meiner Forschungsarbeit und das mir entgegengebrachte Vertrauen.

Bei Herrn Univ.-Prof. Dr.-Ing. Jens Schneider bedanke ich mich für die Übernahme des Zweitgutachtens sowie die anregenden Gespräche und Diskussionen, die das Gelingen meiner Arbeit entscheidend beeinflussten. Außerdem gilt mein besonderer Dank Herrn Univ.-Prof. Dr.-Ing. habil. Alexander Lion für das Interesse an meiner Arbeit und die Übernahme des Drittgutachtens. Schließlich bedanke ich mich herzlich bei Herrn Univ.-Prof. Dr.-Ing. Thomas Braml für die Übernahme des Prüfungsvorsitzes.

Bei meinen Kollegen am Institut und Labor für konstruktiven Ingenieurbau bedanke ich mich für das hervorragende Arbeitsklima, welches nicht nur durch viele anregende, fachliche Diskussionen entstand, sondern auch durch einen freundschaftlichen Umgang, der über die dienstliche Zeit hinausging. Insbesondere bedanke ich mich bei Prof. Dr.-Ing. Michael Kraus, der mich stets unterstützte und förderte, für die fruchtbare Zusammenarbeit. Darüber hinaus bedanke ich mich bei Dr.-Ing. Martin Botz, M.Sc. Dominik Offereins, und M.Sc. Tom Reisewitz für die tolle Zusammenarbeit, die Unterstützung bei Projekten und in der Forschung sowie das freundschaftliche Verhältnis.

Für die Unterstützung durch Bereitstellung unzähliger Probekörper sowie den regen fachlichen Austausch und freundschaftlichen Umgang, bedanke ich mich bei Herrn Ingo Stelzer von der Firma Kuraray Europe GmbH.

Meiner Familie danke ich für das umfassende Verständis in allen Lebenslagen sowie den familiären Rückhalt und den engen Zusammenhalt.

Mein größter Dank gilt meiner Verlobten, Dr. med. Deborah Erhart, für ihre stete Unterstützung in allen Lebenslagen und ihr hohes Maß an Verständnis.

München, im November 2024,

Alexander Pauli

Abstract

Due to the increasing use of load-bearing glazing in structural engineering, the residual load-bearing capacity of laminated glass is increasingly coming into focus. This is currently assessed exclusively on the basis of large-scale component tests. However, this approach is associated with high costs, a great deal of time and the use of materials. One way to save these resources is to theoretically characterize the residual load-bearing capacity. However, a the moment there is no reliable calculation model. In order to develop such a model, it first makes sense to divide the residual load-bearing behavior into three mechanisms: the behavior of the polymer interlayer, the bond between the film and the glass, and the interaction of the glass fragments or the fracture edges. The subject of this work is the characterization of the interlayer material polyvinyl butyral (PVB), which can be classified as an amorphous thermoplastic. To this end, the material is investigated experimentally and described mechanically. The work can therefore be roughly divided into an experimental part and a modeling part. The modeling part is supplemented by some engineering approaches.

In the experimental part of the work, uniaxial tensile tests up to failure, relaxation tests and cyclic tests are carried out, in each case at room temperature. Strain rates, load levels and load reversal points are varied. As part of the subsequent modeling, a thermodynamically consistent material model of finite, non-linear viscoelasticity is constructed. The structure of the model is represented by a discrete spectrum of three networks, each with several Maxwell elements described by different potential and viscosity functions. The individual viscosity functions are constructed in such a way that they can represent the time-dependent mechanisms of the material. This generally formulated model is then reduced to the uniaxial stress state under the assumption of incompressible material behavior and implemented numerically. Following on from this, the various material parameters of the potential and viscosity functions are calibrated using the test data from the experimental part of the work. The results show a very good agreement between simulation and experiment, i.e. the model is very well suited to reproduce the time-dependent behavior of PVB at room temperature up to large deformations.

The modeling section is supplemented by three engineering approaches. Firstly, a method is presented for using relatively short tests to infer the long-term behavior of a polymer under large deformations and to model it without taking the time dependency into account. In addition, a simplified analytical approach for modeling the residual load-bearing capacity of laminated safety glass made of coarse breaking glass with an intermediate layer of PVB is presented. This approach is based on a simplified version of the previously constructed material model. Finally, a resistance value for PVB under uniaxial loading is calibrated based on the failure tests.

Overall, the construction of this material model for PVB and the engineering approaches derived from it represent an important milestone on the way to a numerical residual load-bearing capacity model. With the help of this material model, it is not only possible to accurately describe the behavior of PVB at room temperature, but also to better characterize other necessary material parameters such as the bond between glass and interlayer.

Zusammenfassung

Durch den zunehmenden Einsatz von lastabtragenden Verglasungen im konstruktiven Ingenieurbau rückt die Resttragfähigkeit von Verbundglas zunehmend in den Fokus. Diese wird aktuell ausschließlich auf Grundlage von Großbauteilversuchen beurteilt. Diese Herangehensweise ist jedoch mit hohen Kosten, großem Zeitaufwand und Materialeinsatz verbunden. Einen Weg zum Einsparen dieser Ressourcen stellt die theoretische Charakterisierung der Resttragfähigkeit dar. Aktuell fehlt dafür jedoch ein zuverlässiger Berechnungsmodell. Um ein solches Modell zu entwickeln ist es zunächst sinnvoll, das Resttragverhalten in drei Mechanismen zu unterteilen: das Verhalten der polymeren Zwischenschicht, den Verbund von Folie und Glas sowie die Interaktion der Glasbruchstücke bzw. der Bruchkanten. Gegenstand dieser Arbeit ist die Charakterisierung des Zwischenschichtmaterials Polyvinylbutyral (PVB), das den amorphen Thermoplasten zugeordnet werden kann. Dafür wird das Material experimentell untersucht und mechanisch beschrieben. Die Arbeit lässt sich daher grob in einen experimentellen Teil, und einen Modellierungsteil untergliedern. Der Modellierungsteil wird dabei noch um einige ingenieurmäßige Ansätz ergänzt.

Im experimentellen Teil der Arbeit werden einachsige Zugversuche bis zum Bruch, Relaxationsversuche sowie zyklische Versuche, jeweils bei Raumtemperatur, durchgeführt. Dehnraten, Belastungsniveaus sowie Lastumkehrpunkte werden dabei variiert. Im Rahmen der anschließenden Modellierung wird ein thermodynamisch konsistentes Materialmodell endlicher, nichtlinearer Viskoelastizität konstruiert. Die Struktur des Modells wird durch ein diskretes Spektrum, bestehend aus drei Netzwerken mit jeweils mehreren Maxwell-Elementen und unterschiedlichen Potential- sowie Viskositätsfunktionen dargestellt. Die einzelnen Viskositätsfuntionen sind dabei so konstruiert, dass sie die zeitabhängigen Mechanismen des Materials abbilden können. Dieses allgemein formulierte Modell wird anschließend unter der Annahme inkompressiblen Materialverhaltens auf den uniaxialen Spannungszustand reduziert und numerisch implementiert. Daran anknüpfend werden die verschiedenen Materialparameter der Potential- und Viskositätsfunktionen an den Versuchsdaten des experimentellen Teils der Arbeit kalibriert. Es zeigt sich dabei eine sehr gute Übereinstimmung zwischen Simulation und Versuch, d.h. das Modell eignet sich sehr gut, um das zeitabhängige Verhalten von PVB bei Raumtemperatur bis hin zu großen Verformungen abzubilden.

Der Modellierungsteil wird um drei ingenieurmäßige Ansätze ergänzt. Zum einen wird ein Verfahren vorgestellt, um mit relativ kurzen Versuchen auf das Langzeitverhalten eines Polymers bei großen Verformungen zu schließen, und dieses, ohne Berücksichtigung der Zeitabhängigkeit, zu modellieren. Drüber hinaus wird ein vereinfachter analytischer Ansatz zur Modellierung der Resttragfähigkeit von VSG aus grobbrechenden Gläsern mit Zwischenschicht aus PVB vorgestellt. Dieser Ansatz basiert auf einer vereinfachten Version des zuvor konstruierten Materialmodells. Schließlich wird auf Grundlage der Bruchversuche ein Widerstandswert für PVB unter uniaxialer kalibriert.

Insgesamt stellen die Konstruktion dieses Materialmodells für PVB sowie die daraus abgeleiteten ingenieurmäßigen Ansätze einen wichtigen Meilenstein auf dem Weg zu einem numerischen Resttragfähigkeitsmodell dar. Mit Hilfe dieses Materialmodells ist es nämlich nicht nur möglich, das Verhalten von PVB bei Raumtemperatur genau zu beschreiben, sondern auch andere notwendige Materialparameter wie den Verbund von Glas und Folie besser zu charakterisieren.

Contents

List of Figures

List of Tables

List of Symbols

Stress and Deformation Measures

$\mathbf{F}$	Deformation gradient
J	Determinant of the deformation gradient
$\mathbf{H}$	Displacement gradient
$\mathbf{R}$	Rotation tensor
$\mathbf{U}$	Right stretch tensor
$\mathbf{V}$	Left stretch tensor
$\mathbf{C}$	Right Cauchy Green tensor
$\mathbf{b}$	Left Cauchy Green tensor
$\mathbf{L}$	Spatial velocity gradient
$\mathbf{D}$	Deformation rate tensor (symmetric part of the spatial velocity gradient)
$\mathbf{W}$	Spin tensor (skew-symmetric part of the spatial velocity gradient)
$\mathbf{E}$	Green Lagrange strain tensor
$\mathbf{a}$	Euler Almansi strain tensor
$\mathbf{B}$	Biot strain tensor
$\boldsymbol{\varepsilon}$	Hencky strain tensor
$\mathbf{e}$	Linearized strain tensor
$\hat{\mathbf{\Gamma}}$	Strain tensor on the intermediate configuration
ε	Strain quantity
$\mathbf{T}$	Second Piola Kirchhoff stress tensor
$\mathbf{P}$	First Piola Kirchhoff stress tensor
$\boldsymbol{\sigma}$	Cauchy stress tensor
$\boldsymbol{\tau}$	Kirchhoff stress tensor
σ	Stress quantity
σ_{hyp}	Hyperelastic stress function

Others

$\mathbf{x}$	Position vector of the current configuration
$\mathbf{X}$	Position vector of the reference configuration
$\mathbf{g}$	Basis vector with respect to the current configuration
$\mathbf{G}$	Basis vector with respect to the reference configuration
$\mathbf{u}$	Displacement vector
$\mathbf{n}$	Normal vector
${}_0C$	Reference configuration
${}_iC$	Current configuration
$\mathbf{Q}$	Arbitrary second order tensor
$\mathrm{I}_{\mathbf{Q}}$	First invariant of second order tensor
$\mathrm{II}_{\mathbf{Q}}$	Second invariant of second order tensor
$\mathrm{III}_{\mathbf{Q}}$	Third invariant of second order tensor
$\mathbf{1}$	Unity tensor (2^{nd}order)
λ_i	Eigenvalues of a second order tensor
$\mathbb{1}$	Unity tensor (4^{th}order)
$\boldsymbol{\nu}$	Vector of state variables
q	Internal variable (scalar-valued)
$\mathbf{q}$	Internal variable (tensor-valued)
ϕ	stationary point

Material Properties

E	Time-independent part of the Young's modulus
E_{el}	Time-dependent part of the Young's modulus
E_0	Instantaneous Young's modulus
μ	Shear modulus
C_{30}	Shear modulus
τ	Relaxation time
η	Viscosity
$\mathbb{C}$	Material stiffness tensor (4^{th}order)

Physical Quantities

t	Time	$[s]$
s	Past time	$[s]$
ρ	Density with respect to the current configuration	$[kg/m^3]$
ρ	Density with respect to the reference configuration	$[kg/m^3]$
Π	Total potential energy	$[J]$
e	Internal energy (thermal + distortion energy)	$[J]$
Ψ	Distortion energy	$[J]$
Υ	Configurational free energy	$[J]$
m	Mass	$[kg]$
θ	Temperature	$[K]$
$\tilde{\mathbf{q}}$	Heat flux vector	$[W]$
r	Heat source	$[J]$
s	Entropy	$[J/K]$
$\tilde{\mathbf{t}}$	Surface force	$[N]$
$\tilde{\boldsymbol{b}}$	Volume force	$[N]$
$\mathbf{t}$	Traction vector	$[N]$
$\Delta\mathbf{f}_s$	Sum of forces on a cut surface with respect to the current configuration	$[N]$
$\Delta\mathbf{F}_s$	Sum of forces on a cut surface with respect to the reference configuration	$[N]$
$d\mathbf{f}_s$	Cutting force with respect to the current configuration	$[N]$
$d\mathbf{F}_s$	Cutting force with respect to the reference configuration	$[N]$
$\mathbf{v}$	Velocity vector	$[m/s]$
Δa	Cut surface with respect to the current configuration	$[m^2]$
ΔA	Cut surface with respect to the reference configuration	$[m^2]$
da	Surface element with respect to the current configuration	$[m^2]$
dA	Surface element with respect to the reference configuration	$[m^2]$
v	Volume with respect to the current configuration	$[m^3]$
V	Volume with respect to the reference configuration	$[m^3]$

Statistical Quantities

m_x	Mean, based on a normal distribution
s_x	Estimated value for the standard deviation, based on a normal distribution
m_y	Mean, based on a lognormal distribution
s_y	Estimated value for the standard deviation, based on a lognormal distribution
X_k	Characteristic value of a building material or product property
X_d	Design value of a building material or product property
η_d	Conversion coefficient between sample properties and decisive properties in the component
γ_m	Partial safety factor for a component property
k_n	fractile factor for characteristic values
γ_m	Partial safety factor for a component property
γ_M	Partial safety factor for a component property taking into account model uncertainties and size deviations
γ_{Rd}	Partial safety factor to take into account the model uncertainties of the resistance model
α_R	Resistance weighting factor
β	Reliability index
σ_E	Standard deviation of the effect of the impact
σ_R	Standard deviation of the resistance

Operator

∇	Nabla operator
$\cdot$	Scalar product
:	Frobenius scalar product
$\dot{(\,)}$	Ordinary derivative with respect to time
$\frac{\partial(\,)}{\partial x}$	Partial derivative with respect to x
$\frac{d(\,)}{dx}$	Total derivative with respect to x
$\overset{\triangle}{(\,)}$	Oldroyd derivative of strain tensor with respect to the current configuration
$\overset{\nabla}{(\,)}$	Oldroyd derivative of stress tensor with respect to current configuration
$\times$	Cross product
$(\,)^T$	Transposed
$(\,)_{el}$	Elastic part
$(\,)_{in}$	Inelastic part
$(\,)_{vol}$	Volumetric part, spherical part
$(\,)_{iso}$	Isochoric part
$\bar{(\,)}$	Isochoric part
$(\,)_{dev}$	Deviatoric part
$\hat{(\,)}$	Defined on intermediate configuration
$(\,)^{ov}$	Over stress
$(\,)^{\infty}$	Equilibrium response
$\mathbf{f}(\,)$	Function of ( )
$\mathcal{L}_{\Phi}(\,)$	Lie derivative
$\mathcal{L}(\,)$	Langevin function
$\Phi^*(\,)$	Pull back operation on ( )
$\Phi_*(\,)$	Push forward operation on ( )
$ln(\,)$	Natural logarithm
$sign(\,)$	Signum function
$(\,)_R$	( ) with respect to the reference configuration
$D(\,)$	Directional derivative
$\delta(\,)$	Virtual quantity
$(\,)_h$	Homogeneous part
$(\,)_p$	Particulate part

Abbreviations

FEM	Finite Element Method
$XFEM$	Extended Finite Element Method
DEM	Discrete Element Method
BEM	Boundary Element Method
FDM	Finite Difference Method
TTG	Thermally Toughened Glass
ANG	Annealed Glass
HSG	Heat Strengthened Glass
PVB	Polyvinylbutyral
SG	Sentry Glass
EVA	Ethylenvinylacetat
LG	Laminated Glass
LSG	Laminated Safety Glass
$PFLS$	Post Fracture Limit State
FLS	Fracture Limit State
TCB	Through Crack Bending
TCT	Through Crack Tension
CSS	Compressive Shear Strength
$DMTA$	Dynamic-Mechanical-Thermal Analysis
WLF	Williams Landel Ferry
Var	Coefficient of variation
QQ	Quantile-Quantile
PDF	Probability Density Function
CDF	Cumulative Distribution Function
KS	Kolmogorow-Smirnow

1. Introduction

With today's demands for ever-slimmer and more transparent buildings, structural glass design has become increasingly essential and continues to grow in significance. Initially, glazing was used mainly as an infill element. However, it is used today, and will continue to be used in the future, as a structural element in façades, in fall-protecting balustrades, and for roofing, sometimes even walkable or drivable. Therefore, laminated glass (LG) is used for increased safety requirements (e.g., overhead or fall-protection glazing). According to DIN EN ISO 12543-1:2022-03 [85], laminated glass must consist of one glass-ply attached to a polymer interlayer or several glass-plies joined by one or more interlayers. If the laminated glass meets increased safety requirements in the event of breakage, such as reducing the opening in the pane, retaining glass splinters, reducing the risk of cuts, and ensuring a specific residual load-bearing capacity, it is declared laminated safety glass [85, 86]. According to DIN EN ISO 12543-2:2022-03 [86], the pendulum impact test (cf. [76]) is used to differentiate between LG and LSG. Glass laminates with PVB interlayer are generally considered laminated safety glass.

According to CEN/TS 19100-1:2024-01 [44], there are different *Limit State Scenarios* (LSS) which demand different verifications of the safety requirements. DIN 18008-1:2020-05 [68], DIN 18008-5:2013-07 [69], DIN 18008-6:2018-02 [70] regulates the examination of the broken state in the case of overhead (part 1), accessible (part 6), and walk-on glazings (part 5). The various breakage patterns of differently toughened glasses and the complex material behavior of the polymeric interlayers play a crucial role in assessing the residual load-bearing behavior of laminated safety glass and give reason to examine this condition more closely. CEN/TS 19100-1:2024-01 [44] distinguishes between the *Fracture Limit State* (FLS) and the *Post Fracture Limit State* (PFLS). The FLS describes the state during breakage and is thus defined as a state where the risk of injury caused by broken glass shards, and the risk of falling through the glazing is no longer prevented, and the ability of limiting the failure to that glass component is no longer ensured. The PFLS describes the state after the breakage and thus the condition of an entirely broken glazing, where redundant load transfer and alternative load paths are no longer possible.

CEN/TS 19100-1:2024-01 [44], CEN/TS 19100-2:2024-01 [45], CEN/TS 19100-3:2024-06 [46] requires that sufficient safety is ensured for a certain duration (Time to secure the environment, to replace the broken pane, to remove load, etc.) in the PFLS. Verifying the safety requirements within the PFLS can be done theoretically or experimentally. In the case of experimental verification, it is crucial to ensure a sufficiently accurate representation of reality and a representative number of test repetitions. Theoretical approaches that are only allowed for loads perpendicular to the pane according to CEN/TS 19100-2:2024-01 [45] must consider all possible actions and be equivalent to the experimental approaches. According to CEN/TS 19100-2:2024-01 [45], "the mechanical behavior of glass in the PFLS is governed by the size and shape of the shards (glass type), type and thickness of the interlayer, the bond between interlayer and glass," and "the delamination depth of the interlayer in contact of the single shards." Accordingly, different load transfer mechanisms are required to verify the PFLS theoretically. From a scientific point of view, this approach goes along with the definitions of Kott [157], who, besides the intact state *State I*, defined a partially broken state, *State II*, where at least one glass pane is intact, and a completely broken state, *State III*, where all glass plies are broken.

Delincé [67] followed Kott [157] but emphasized the interlayer's role that changes significantly from *State I* (intact state [157]) to *State III*. It provides a shear bond between the individual glass panes in the intact state and shows a bridging behavior in the broken state.

Several approaches have to be taken into account to approach the topic of the theoretical description of the residual load-bearing capacity of laminated glass. Besides the investigations on the overall behavior of fully fractured LG, the individual load-bearing mechanisms, interlayer, bond between glass and interlayer, and contact of single glass shards, listed by CEN/TS 19100-2:2024-01 [45] must be examined in detail. The following sections present an overview of several approaches achieved by various research groups over the last decades, categorized into experimental investigations, and numerical and analytical modeling approaches.

As experimentally proving residual load-bearing capacity is common practice in structural glass design, research on experimentally characterizing laminated glass in the broken state is presented in the first of the following sections. The first part describes various experiments on glass laminates to represent the overall behavior in the fractured state, and the second part presents experiments to isolate the broken laminate's load-bearing mechanisms such as interlayer, bond between glass and interlayer, and friction between glass shards. All presented experimental approaches are concerned with quasistatic loads.

Subsequently, numerical modeling approaches for the whole fractured laminate, and the single load-bearing mechanisms are described, considering both quasistatic and dynamic approaches. Overall modeling approaches, however, mainly exist for dynamic loadings, whereas approaches describing the individual load-bearing mechanisms exist for quasistatic loads. In addition to the main applications in civil engineering (load-bearing capacity of LSG under static loads according to CEN/TS 19100-1:2024-01 [44], DIN 18008-1:2020-05 [68]), examples for modeling broken LSG from mechanical engineering and structural protection are presented. The choice of the application is crucial, as the type of loading decides the material and interface models.

The third section describes the analytical modeling approaches, considering quasistatic loads only. There are two general approaches: the equivalent stiffness models and the explicitly defined models. The decision between the two methods depends on the degree of prestress in combination with the thickness or, rather, the type of the breakage pattern. Coarse breakage patterns accompany an explicit description, and fine breakage patterns accompany equivalent stiffness approaches.

The first chapter concludes with a discussion of the presented methods and findings. Based on this discussion, the motivation and the resulting questions aimed at being solved in this thesis are derived and presented.

1.1. Residual Load-Bearing-Capacity - Experimental Approaches

The first section of this chapter presents several experimental investigations on laminated glass or its components considering quasistatic loading that various research groups have carried out in recent years. These investigations are categorized into four groups:

- The overall behavior of broken laminated glass
- The adhesion between glass and interlayer
- The interaction of the glass fragments
- The mechanical behavior of the interlayer

1.1.1. LSG

Several tests, such as 3- or 4-point bending with in-plane and out-of-plane loading or uniaxial and biaxial tension or compression tests, are possibly carried out on broken glass laminates.

Bennison et al. [21] carried out tests on circular laminated glass panes consisting of annealed glass with PVB interlayer (ANG/PVB/ANG) subjected to equi-biaxial loading utilizing an articulated loading punch and a rigid three-ball support. They investigated the failure of the laminates under different loading rates in combination with high ($50°C$) and low temperatures (-$60°C$) and the location of the first crack initiation. By analyzing the test results, they observed that laminates with full shear coupling (high rate, low temperature) promote first cracking at the bottom side of the lower ply, while laminates without shear coupling (low rate, high temperature) promote first cracking at the bottom side of the upper glass ply (facing the load).

Kott and Vogel [158] conducted out-of-plane tests on laminated glass panes. They considered 4-sided line supports and 4-point bending conditions under various loading situations. The laminates, composed of annealed, heat-strengthened (HSG), or thermally toughened glasses (TTG) with a PVB interlayer, were pre-damaged to produce different fracture patterns, leading to distinct residual support mechanisms. The pre-damaged specimens were then subjected to a displacement-controlled load with constant velocity at room temperature. After the breakage of both plies, three scenarios emerged: immediate collapse, continued loading to failure, and dead load loading, with the time to failure measured. Only laminated glass with a coarse breakage pattern (ANG, HSG) could provide a residual load-bearing capacity.

Feirabend and Sobek [105] investigated the pre- and post-breakage behavior of laminates made from two plies of thermally toughened glass with both PVB and SG interlayers reinforced by stainless steel meshes. They carried out 4-point bending tests under different temperatures and constant, displacement-controlled testing velocities on pre-damaged laminates until failure, measuring load, time, and displacement. The laminates with reinforced interlayer showed a considerably better residual post-breakage behavior, especially at high temperatures, however, at the price of poorer transparency compared to the non-inforced configuration.

Castori and Speranzini [42] performed four-point bending tests (out-of-plane) with constant displacement-controlled velocity on LSG with two layers of annealed glass joined by different types of interlayers (PVB, SGP, EVA, trilayer with a layer of PET between two layers of EVA (XLAB)) with various thicknesses (single, double, triple) until the breakage of all glass plies. Subsequently, they conducted the same test at a higher velocity on the fully broken samples until failure, constantly measuring displacement, strain, and force throughout the test procedure. Concerning the SG, EVA, and PVB, the highest initial and residual loads were observed for the SG interlayer laminates, followed by EVA and PVB. However, the evaluation of the test results of the XLAB laminates resulted in an even higher initial load but with a significantly reduced load in the fractured state. Overall, the laminates with the EVA interlayer achieved the lowest, and those with the SG interlayers achieved the highest mean deflections but, on the other hand, also the highest residual loads.

Wellershoff et al. [266] carried out the *Bulge Test* on fully broken laminates made of two plies of TTG bonded with PVB interlayers. The bulge test requires a circular-shaped specimen clamped along the edge, loaded with a constantly increasing air pressure. At the same time, an optical measurement system monitors the corresponding deformation of the specimen. For this study, they conducted the tests at a constant pressure rate considering different temperatures. Subsequently, they evaluated the micro-delamination between the glass fragments and the interlayer and derived the biaxial stresses depending on deformation.

Biolzi and Simoncelli [26] investigated the residual strength of thermally toughened glass with different interlayers (PVB, DG41, and SG). To this end, they conducted tests on rectangular plates supported on two sides with simple bearings subjected to an incremental line load in an

out-of-plane direction. After breaking the lower ply, they established two series, both loaded until failure with the force and displacement continuously monitored for all tests: one with the crack in the top ply (series 1) and one with the crack in the bottom ply (series 2). Load and displacement at total collapse revealed that the specimens of series 2 reached higher deflections and lower forces than those of series 1. However, the deflections and forces of the different laminates were in the same range for series 2. They varied for series 1, with the PVB laminates showing the lowest force and the highest deflection at failure.

1.1.2. Interface

Some methods for the experimental investigation of the bond between interlayer and glass are presented below. A good overview of the methods available for investigating the adhesion behavior of laminated glass can be found in Schuster et al. [232]. In the industry, pummel, compressive shear, and peel tests are standard methods for quality assurance and quantifying adhesion between glass and interlayer in laminated glass. However, this establishment is mainly caused by the easy handling of these tests, which have limitations. For example, the force measured in the peel test includes the inelastic work generated by the deformation of the interlayer and the cohesive energy. Therefore, it is difficult to distinguish which part is how large [115, 14], which is particularly problematic when determining energy release rates and interfacial fracture toughness. Furthermore, the highly subjective nature of the Pummel test is an obstacle to objective quantification of adhesion [232]. Although several approaches, such as [232, 54], who used a mechanized Pummel apparatus, and Kraus and Drass [160], who proposed an evaluation method based on artificial intelligence, have increased the objectivity of the Pummel test in recent years, it still provides too little information about mechanical adhesion behavior. Therefore, the Pummel test is not considered further. Due to these limitations within the industrial tests, various academic ways of experimentally investigating the bond between interlayer and glass have evolved over the years.

Through Crack Tension Sha et al. [238] developed a tensile adhesion test to investigate the bond between glass and interlayer. The test is based on a three-point bending test of a glass laminate with coincident cracks, called the *flexural adhesion test*. A rectangular sample of laminated glass, consisting of two layers of glass joined by an interlayer, is cracked on both sides and subjected to an in-plane tensile load. They carried out this test on standard PVB with three different levels of adhesion, constantly tracking load over displacement. They concluded that this test approach gives more realistic and promising results than the widely used peel and pummel tests. Muralidhar et al. [185] further developed this test to represent the polymer ligaments in cracked laminates and proposed the *Through Crack Tension* (TCT) test, which other researchers have since used. Iwasaki and Sato [140] used the TCT test to conduct experimental investigations on the interfacial fracture toughness of LSG made from PVB and found that the fracture toughness is strongly related to the applied strain rate. Delincé [67] presented a large experimental study of TCT testing with different configurations and a wide range of temperatures in two series. The first series included creep tests, and the second included tests at different constant displacement rates. Franz [107] provided TCT tests on different interlayer materials, performed at different strain rates at standard climate. Del Linz et al. [65] conducted TCT tests displacement controlled at velocities from 0.01 to 10 [m/s] for different interlayer thicknesses. Chen et al. [52] built on the tests of Franz [107] and conducted further TCT tests at different strain rates, interlayer thicknesses, and adhesion levels. They constantly tracked the deformation using digital image correlation and measured the delamination length and angle. They found that the strain rate significantly affects the

interfacial fracture energy of laminated glass with a PVB interlayer. Furthermore, the adhesion level dominates the delamination ability. However, the influence of PVB thickness on the energy release rate was insignificant.

Through Crack Bending Franz [107] adopted the *flexure adhesion test* described by Sha et al. [238] and changed the mode from three to four-point bending on broken glass laminates with a coincident crack at a small scale (l_{max}=200 mm), referring to the test as *Through Crack Bending Test* (TCB). Franz [107] subjected the specimens at a constant speed to a specified deflection and held them in this position for one hour (relaxation) at room temperature, constantly measuring the load. After the tests, he evaluated the area of delamination and the stress within the interlayer. Subsequently, he transferred the test to a larger scale (1100 mm x 3600 mm) to gain further insight into the residual load-bearing behavior of laminated glass. Botz [30] built on these larger-scale tests but conducted the tests at a constant force level (creep) for 24 hours, investigating different temperatures and, in addition to coincident fractures, fractures with a crack offset, and fractures caused by ball drop. Both examined different interlayers. Angelides et al. [6] performed three-point flexure tests (see *flexure adhesion test*) at a low strain rate and a low temperature (-100°C) on laminates randomly cracked at several locations to evaluate the response of laminates subjected to blast at average temperatures. Angelides et al. [7] extended the series of tests performing three and four-point bending tests at the same low temperatures for different randomly distributed randomly cracked laminates. They were able to significantly increase the ultimate load capacity compared to that at low strain rates at room temperature.

Compressive Shear Another approach is the *Compressive Shear Strength* (CSS) test, commonly used in the polymer industry. A 2-ply laminate is subjected to combined compression and shear at a specified angle to the loading direction to investigate the adhesion between a polymer and a rigid substrate. Force, deflection, and crack length are measured during the test, serving as the basis for calculating a specific energy release rate that can be derived. Jagota et al. [141] used this test to investigate the interfacial adhesion between glass and standard PVB at different shear strain rates. Furthermore, interlayer manufacturers use this test for quality control.

Peel The *Peel Test*, based on DIN EN 1895:2002-02 [80], is conducted on a (glass/foil/aluminum-foil) laminate with a crack in the glass, separating it into two parts only connected by the interlayer-aluminum-composite. The first part is fixed by horizontal roller supports preventing vertical movement, and the second part is clamped at an angle of 90 degrees to be moved by a testing machine. By moving the cylinder, the interlayer is separated from the glass, while the aluminum acts as a stiff backing foil to prevent large deformations in the interlayer. The Evaluation of forces, displacement, and detached area gains information about the fracture toughness of the interface of glass and interlayer. Pelfrene et al. [202] used this test to investigate the delamination of PVB-glass-laminates at a constant test velocity for different adhesion levels.

1.1.3. Glass

When investigating the fracture behavior of glass, it is essential to distinguish between different types of glass. For rough-breaking glasses (ANG, HSG), predicting the breakage pattern caused by a defined fracture event is almost impossible due to its stochastic nature. There is, however, an approach to determine a conservative fracture pattern based on Johann's Yield Line Theory [237, 157, 5]. This approach is no longer practical for finely refracted glass (TTG). However, other approaches are possible due to the almost homogeneous crack distribution. For example,

Nielsen et al. [189] investigated the general fracture behavior of thermally toughened soda lime glass using specimens of 300 x 300 mm with different thicknesses and levels of thermal toughening. Using optical measuring instruments such as high-speed cameras and a scanning electron microscope (SEM), they discovered a specific adhesion between the fragments after fracture, known as microscale crack bridging, which is an exciting aspect, especially regarding the residual load-bearing capacity. Furthermore, Nielsen and Bjarrum [188] determined the remaining strain energy after breakage within thermally toughened soda lime glass by measuring and calculating the remaining stress within a single fragment. They used a Scattered Light Polariscope (SCALP) to measure and the numerical model established by Nielsen [187] to calculate the stress. Additionally, they recorded the geometry and texture of the surface using 3D scans.

Pourmoghaddam and Schneider [207] presented a different approach to determining the fracture pattern of thermally toughened soda lime glass by evaluating the relation between thickness and residual stress before and fragment size after fracture. They measured the prestress of intact monolithic glasses of different thicknesses and levels of prestress using a SCALP, broke the glass panes, and recorded scans of the fracture patterns. Based on the recorded fracture patterns, they derived the correlation between residual stress and fragment density. With these investigations, Pourmoghaddam et al. [208] formulated an algorithm based on linear fracture mechanics, spatial point processes, and Voronoi tesselations to predict the macroscale breakage pattern of TTG. Using this method in combination with the approaches of Nielsen [187], Nielsen and Bjarrum [188], Nielsen et al. [190] derived the in-plane expansion of the thermally toughened glass in case of fracture.

Utilizing fragments extracted from broken monolithic glasses of different thicknesses and prestress, left from the study presented by Pourmoghaddam and Schneider [207], Pauli et al. [201] investigated the friction between single glass fragments using shear frame tests in accordance with DIN EN ISO 17892-10:2019-04 [88].

1.1.4. Interlayer

There are several methods and procedures to investigate the bulk interlayer material experimentally. Bergström [24] gives a good overview of possible strategies for investigating polymer materials. It is crucial to distinguish between investigating the intact behavior or failure and damage mechanisms. Different methods and procedures are feasible, depending on the case. There is a general distinction between different stress states (uniaxial, biaxial, planar, pure shear, simple shear) in tension and compression and various times (velocity, relaxation, creep), all procedures possibly combined with different temperatures and levels of humidity. The following is an overview of the recent investigations carried out on PVB.

Quasistatic Tensile Tests A dogbone sample, cut from a plane sheet of bulk material, is clamped on both sides within a testing machine. The machine's cylinder moves within a respective time scheme, subjecting the specimen to a tensile load, while the respective course of load and time follows a user-defined specification. Constantly tracking force and displacement, the test velocity is controlled via the measured displacement or force over time. Displacement control is typically preferred. However, force control is recommended for creep tests. In addition to the measuring devices incorporated in the machine, a mechanical or optical measurement should measure deformation without possible slippage.

Elzière [103] carried out uniaxial tension tests with different strain rates and temperatures with loading and unloading.

Bennison et al. [22], Iwasaki and Sato [140], Liu et al. [172], Hooper et al. [134], Kuntsche [165], Del Linz et al. [64] conducted uniaxial tension tests with different strain rates until failure. Xu et al. [270] conducted uniaxial tension tests on PVB at different strain rates and temperatures until failure.

Centelles et al. [43], Knight et al. [152] carried out uniaxial tests at low and high strain rates under a constant temperature on PVB, EVA, and SGP interlayers subjected to environmental aging (under high temperature, high humidities, and humidity and temperature cycles).

Botz et al. [31] conducted creep tests on PVB specimens under different temperatures and humidities. Schuster [231] carried out relaxation tests at different load levels and temperatures.

Dynamic-Mechanical-Thermal Analysis Dynamic-mechanical-thermal analysis (DMTA) is a method to investigate a material's time- and temperature-dependent behavior. The specimens are subjected to a harmonic oscillating, sinusoidal excitation while the corresponding response is measured constantly. From the amplitude of excitation and response, the so-called complex modulus is calculated. Considering a complex plane, this modulus is expressed as a complex pointer with an inclination corresponding to the phase shift between excitation and response. The triangle, spanned by the complex pointer and the real axis, represents the storage (along the real axis) and the loss modulus (along the imaginary axis). The storage modulus (conservation of energy) represents the elastic behavior of the material, and the loss modulus (dissipation of energy) represents the viscous behavior of the material. Repeating this procedure for a particular spectrum of frequencies leads to curves representing complex, storage, and loss modulus. Repeating this procedure for different temperatures yields several curves of different stiffness aligned to the respective temperature for each modulus. By assigning a reference temperature and shifting all stiffness curves with lower stiffness (at higher temperatures) to the left (lower frequency equivalent to longer duration) and the curves with higher stiffness to the right (higher frequency equivalent to shorter duration), the other curves extend the reference curve, resulting in a master curve for each modulus. These master curves represent the moduli for a respective temperature over a broad span of frequencies. The shift of the curves follows the time-temperature superposition principle that considers the analogy of time and temperature based on temperature-dependent molecular movements. Commonly used principles are the WLF and the Arrhenius equation.

Hooper et al. [134], Kuntsche [165], Elzière [103], Schuster et al. [233], Kraus and Niederwald [161] carried out DMTA tests on PVB. Kraus and Niederwald [161] developed a straightforward method to derive Prony parameters from a DMTA measurement, employing an equation system solved by a linear regression analysis. This method is much less time-consuming than, for example, the method proposed by Kuntsche [165], and provides results with the same accuracy as Kuntsche [165].

1.2. Residual Load-Bearing-Capacity - Numerical Modeling Approaches

Besides the different experimental approaches, which primarily aim to characterize the behavior of fractured laminated glass and its single load-bearing mechanisms, there are several approaches to numerically describe or even predict the behavior observed during the experiments. The subsequent presentation of the approaches of various research groups on the numerical modeling of the residual load-bearing capacity of laminated glass or numerically describing the single load-bearing mechanisms is organized utilizing the following categories:

- The overall behavior of broken laminated glass

- The adhesion between glass and interlayer
- The interaction of the glass fragments
- The mechanical behavior of the interlayer

1.2.1. Methods

The governing, physical problems in civil and mechanical engineering can be described as a structure subjected to a particular load. Idealizing such a physical problem into a mathematical model leads to a description by differential equations. There are several methods to evolve the solution to such problems. In the following, the Finite Element Method (FEM), the Extended Finite Element Method (XFEM), and the Discrete Element Method (DEM), which are the most common approaches in modeling the residual load-bearing capacity of laminated glass, are presented along with respective examples from the literature.

FEM The Finite Element Method (FEM), introduced by Zienkiewicz and Cheung [280], as one of the first, is the most widely used method for accounting for this. The method involves dividing a complex area into a finite number of elements connected via nodes. The single elements are solved locally and merged into a global system. [17].

The finite element method is the approach that is mainly used in modeling glass laminates, especially under dynamic loads. However, there are different configurations to describe the glass laminates. Du Bois et al. [100] simulated two-layer laminated glass under impact loading, using one shell element representing both glass plies and a membrane element representing the interlayer connected by fixed coincident nodes. Timmel et al. [247] resumed this model for the same application but added a second shell element for the glass, also connected with shared nodes. They considered a brittle failure for the glass ply exposed to tension. In the case of failure, one ply is completely erased. The different Young's moduli are calculated such that both shell elements together ($E^{II} + E^{*}$) represent the intact state, and the resisting one (E^{II}) represents the broken state. Larcher et al. [166], Hooper et al. [135] simulated two-layer laminated glass windows exposed to blast loads using a model with three layers of shell elements. Larcher et al. [166] used an element deletion method to consider the failure of the laminate, Hooper et al. [135] separated the analysis into a pre- and a postcrack model. They assumed a linear elastic material law for the glass and the interlayer in the cracked model, zero stiffness for the glass (mass is contained), and a rate-dependent Johnson-Cook plasticity law [148] for the interlayer in the post-crack model. Pelfrene et al. [203], Alter et al. [2] modeled two-layer laminated glass with shell elements for the glass and solid elements for the interlayer, Pelfrene et al. [203] in the context of blast loads, and Alter et al. [2] in the context of slow velocity impact, both enabling glass fracture using the element deletion method. Hidallana-Gamage et al. [128], Chen et al. [49], Osnes et al. [197], Hála et al. [121] used solid elements for glass and interlayer. However, Hidallana-Gamage et al. [128] used the element deletion method, Chen et al. [49] cohesive elements, Osnes et al. [197] a specific node separation technique and Hála et al. [121] utilized a smeared crack model to describe the breakage of the laminate.

XFEM When modeling cracks within a finite element model, a detailed representation requires a very fine mesh in the vicinity of the crack, which causes a large amount of computation time. XFEM can be used to make such problems numerically efficient and save computation time without losing accuracy. Originally developed by Moës et al. [182] to model cracks independently of an FE mesh, XFEM extends a conventional FE model in the areas of cracks using special ansatz functions to allow modeling cracks without refining the FE mesh [47].

The method is used by Xu et al. [268, 271] for the analysis of the slow velocity impact on coarse-breaking laminated glass.

DEM In addition to classical FEM and XFEM, it is also possible to solve physical problems in engineering using the Discrete Element Method (DEM). The idea behind DEM, initially developed by [60] for granular assemblies, is to divide a domain into discrete elements (particles) connected by contact. Their motion is modeled explicitly, particle by particle, governed by Newton's second law. The method is mainly used to solve non-continuous problems such as discontinuous materials (granular, powder) [144].

This method has been used extensively and is still used to model the low-velocity impact on laminated glass, mainly in the context of automobile glass. Zang et al. [275] developed a three-dimensional DEM model to simulate impacts on laminated safety glass in automotive engineering. They found that DEM can represent the interactions between cracks well but has problems representing large deformations. Lei and Zang [168], therefore, formulated a model combining FEM and DEM in which the FEM domain is connected to the DEM domain via a penalty function. DEM represents the glass, and FEM represents the intermediate layer. Xu et al. [269] also used a combination of FEM and DEM to be numerically efficient. Therefore, in the initial state, the model is completely described in terms of finite elements. After reaching a yield criterion based on the tensile strength of glass, the model is divided into two subdomains: the finite element model and the discrete element subdomains. Wang et al. [264] uses the same approach. However, the case for laminated glass is more precise as it considers delamination and more accurate material formulations.

Baraldi et al. [15] used the Discrete-Element-Method to simulate the residual load-bearing capacity of balustrades made of laminated glass with TTG. However, only a respective two-dimensional cross-section of a balustrade (cantilever and two-sided supports) with finite thickness in the direction perpendicular to the plane is modeled. The two layers of broken LG are composed of rigid elements of the same width and length (glass fragments), longitudinally connected by a continuous interface layer (interlayer), and transversely connected by discrete interfaces for each contact (glass-glass). Vertical interfaces do not support any tensile forces but are considered to possess infinite compressive strength. Horizontal interfaces possess tensile and compressive strength related to the stiffness of the interlayer and independent shear strength, representing the limit of delamination. Rotational stiffness and frictional effects are not considered. The general behavior of the interface, describing the interlayer, is governed by an elastoplastic material law with a yield criterion similar to the Mohr-Coulomb criterion. The initial elastic stiffness of glass is considered 10^3 higher than the initial stiffness of the interlayer.

Wang et al. [265] introduced a similar model based on a combined Voronoi and FEM/DEM approach, considering only the already broken state of laminated glass made of TTG. They used cohesive zone elements with bilinear separation-traction to represent the interaction between the single glass fragments, ensuring a smooth transition from cohesive-dominant to friction-dominant behavior. Furthermore, the respective glass fracture morphology is considered to evaluate the particle sizes, and 50 finite elements discretize each glass fragment. They used a plastic material law for the interlayer and described the bond between the interlayer and the glass based on fracture energy. However, they did not consider partial debonding.

1.2.2. Interface

Besides the overall modeling of laminated glass in the fractured state, one crucial aspect is the description of the bond between glass and interlayer. The level of adhesion influences the deformability of the interlayer and, therefore, the amount of energy dissipated during fracture. At

an adhesion level that is too high, the interlayer reaches its fracture strain almost immediately. However, at too low adhesion, the overall deflection of the laminate might be too high in the broken state. Regarding numerical modeling, this problem is perceived as separating a bonded contact. Three approaches are commonly used to model this behavior [51, 178]. The simplest techniques are the "shared node method," where the elements of glass and interlayer share the same nodes on the interfaces, and the constraint-based method, which is a similar approach. A more advanced method is using penalty springs to connect glass and interlayer. However, the cohesive zone modeling approach is the method that allows for the most realistic presentation of adhesion.

Shared-node and constraint based method The shared-node method, where the elements at the interaction surfaces share their nodes, is the simplest way of modeling the permanently effective, complete bond between separate elements. Liu et al. [173], Zhao et al. [278] used this method to simulate the fracture behavior of windscreens under dynamic impact. This method is numerically very efficient, requiring no additional interface treatment. However, it is impossible to model delamination or any other realistic adhesion behavior with this approach, as relative displacements between interlayer and glass are impossible. The constraint-based method is similar. However, the connected elements do not share the nodes; the individual nodes are fixed to each other, utilizing explicit constraints applied to the nodes on the interface. Pyttel et al. [209], Peng et al. [205] used this formulation to model low-velocity impacts on windshields. After glass failure, the contact between the glass and interlayer is erased, and all connected glass elements fail. Deleting the contact after the failure of the aligned elements is an advantage over the shared node approach. However, modeling realistic delamination is not possible with that approach either.

Penalty-based approach The penalty formulation involves the introduction of additional terms containing virtual springs into the equations of motion. These springs enforce contact constraints by generating forces to prevent penetration or sliding between contacting surfaces. They are calculated from the relative displacement between connected nodes and a penalty parameter governing the stiffness of the virtual springs. One approach to model delamination is deleting contact elements when the penalty forces reach a particular failure criterion. Zhang et al. [277] used this approach and defined a failure criterion depending on normal and shear stresses on the interface. After reaching this criterion, the contact between the glass and the interlayer is erased. Pelfrene et al. [203] used a similar method but added a cohesive zone at the interface to account for a particular traction separation relation. Besides these applications in the context of FEM, there also exist approaches within DEM or FEM/DEM. For example, Lei and Zang [168] used penalty springs to connect glass represented by discrete elements and interlayer represented by finite elements in the context of the FE/DE method.

Cohesive Zone Elements The most realistic approach to modeling delamination is the interelement crack method using cohesive zone models [243]. This method, originally proposed by Dugdale [101], Barenblatt [16], requires additional nodes at the interfaces. Fracture is modeled through the separation of elements along their edges. A traction separation law governs crack propagation and starts when the force at the cohesive zone overcomes a particular cohesive strength [246]. There are two different basic approaches [164]: the intrinsic approach (initially elastic) and the extrinsic approach (initially rigid). The intrinsic method was first introduced within the context of FEM by Needleman [186]. There is no traction at the beginning, followed by an increased traction resistance for increasing separation. After reaching a specific failure strength, the traction resistance decreases with further separation. The extrinsic

method, based on the original approach [101, 16], further developed by Camacho and Ortiz [40], considers the traction strength to be maximal initially, decreasing with increasing separation. However, in both approaches, the area under the traction separation curve corresponds to the fracture toughness of the interface.

Many researchers used intrinsic cohesive elements to describe the delamination behavior of laminated glass based on experimental investigations and derive respective material parameters such as the fracture toughness and the energy release rate. Rahul-Kumar et al. [211], Pelfrene et al. [202] used peel tests, Jagota et al. [141], Rahul-Kumar et al. [212] compressive shear tests and Muralidhar et al. [185], Franz [107], Del Linz et al. [65], Chen et al. [53] TCT tests. D'Ambrosio et al. [61] numerically investigated the shapes of the detached areas on idealized elementary cells representing LSG for different parameters (interlayer thickness, size, shape of glass fragments, and debonded area). Based on the TCT tests performed by Franz and Schneider [108], Chen et al. [53] carried out a numerical study on the delamination behavior of LSG and observed that, under the assumption of stable delamination, the cohesive strength mainly influences the peak force, and the fracture energy dominates the plateau force. Other researchers also used intrinsic cohesive elements to describe the delamination within the modeling of laminated glass in case of fracture. Chen et al. [50], Wang et al. [264] simulated the impact damage of laminated glass in the context of FEM and FEM/DEM using a mixed mode failure criterion based on the model of van den Bosch et al. [260] and Wang et al. [265] simulated glass laminates under quasistatic loading in the context of FEM/DEM.

On the other hand, several approaches use extrinsic cohesive models. Pelfrene et al. [203], Osnes et al. [197] carried out finite element simulations in the context of laminated glass windows subjected to blast loads, Gao and Zang [113] simulated glass beams exposed to dynamic impact in the context of FEM/DEM.

However, according to Chen et al. [51], Martín et al. [178], the intrinsic approach should be preferred in modeling the adhesion between glass and interlayer.

1.2.3. Glass

In numerically modeling the bulk glass material in modeling LSG in the fractured state, distinguishing between quasistatic and dynamic cases is crucial. When considering the post-fracture behavior of laminated glass under quasistatic loading, further described in the following, the glass is already considered broken, emphasizing the importance of describing the contact and friction between glass shards. A respective fracture pattern can be derived from yield line theories [146] for coarse breaking glass and from statistical methods and fracture mechanics [208, 190] for fine breaking glass. Using finite element analysis and experiments, Nielsen [187], Nielsen and Bjarrum [188] determined the changes in a fragment's surface shape and the remaining stresses and deformations. Pauli et al. [201] investigated the friction between single glass fragments utilizing shear frame tests on the same glass fragments of different thicknesses and initial prestress, [207] presented in their study. A FEM simulation of the shear frame tests, based on a Mohr-Coulomb yield criterion, led to promising results.

However, concerning dynamic impacts or blasts, the fracture process of the glass is modeled in particular. Song et al. [243] provided a list of possible approaches. The element deletion method, in which the stiffness of elements is set to zero once they have reached a particular failure criterion, was used by Larcher et al. [166], Hidallana-Gamage et al. [128] to simulate the blast resistance of laminated glass windows, and Peng et al. [205], Liu et al. [173] to model the low-velocity impact on laminated glass windshields. The continuum damage mechanics approach, in which the damage is taken into account directly in the constitutive law (compare Kachanov [150]), was used by Zhao et al. [278] to model the fracture of laminated glass windshields under

head impact. The smeared crack model, introduced by Hillerborg et al. [129], was used by Pelfrene et al. [204], Hála et al. [121] to simulate the low-velocity impact on laminated glass. Xu et al. [272] proposed an intrinsic solid-shell cohesive zone model for the impact fracture of laminated glass windshields. [269, 264] implemented an extrinsic cohesive fracture model into a DEM model to describe the gradual glass-ply cracking process. Chen et al. [49] modeled the breakage of LSG caused by a low-velocity impact as a gradual separation of the area immediately before the crack front, considering frictional sliding effects between the cohesive elements.

1.2.4. Interlayer

The PVB intermediate layer is a polymer, more precisely an amorphous thermoplastic. Boyce et al. [33] describe amorphous thermoplastics as a combination of physical entanglement of polymer chains, multiple rigid links between the entanglements, and intermolecular interactions. Their mechanical behavior is governed by an initial strain rate-dependent pressure, temperature-dependent yielding followed by true strain softening and rate-, and temperature-dependent hardening at larger strains. Depending on the application, the spectrum of modeling approaches in the literature ranges from linear elastic to nonlinear viscoplastic. Haupt [123] suggested the following separation between the single material modeling approaches of solids concerning their strain and stress relation:

- Elasticity, rate-independent without static hysteresis
- Plasticity, rate-independent with static hysteresis
- Viscoelasticity, rate-dependent without static hysteresis
- viscoplasticity, rate-dependent with static hysteresis

Structural glass engineering requires various considerations for modeling the pure intermediate layer. Apart from the differentiation on the time scale, a distinction must be made between the intact and broken state. In the intact state, the shear modulus of the interlayer decides a corresponding shear bond between the individual plies, depending on the load duration and the temperature. It can be described by the theory of linear viscoelasticity using a Prony series in combination with a time-temperature shift principle when considering different temperatures. This approach is sufficiently accurate, and no further considerations regarding the intact state are necessary. However, in the broken state, large deformations prevail, resulting in the need for other modeling approaches. Dividing the state of large deformations into quasistatic and dynamic loading leads to some simplifications. In the dynamic case (impact, blast), the loading rate is so high that temporal effects have a much smaller influence than in the quasistatic case. Models of elasticity, hyperelasticity, or plasticity, therefore, seem acceptable. However, for quasistatic considerations, temporal effects must be considered strictly, which requires models containing time dependency. Models of finite deformation viscoelasticity or -plasticity account for that.

Elasticity Linear Elastic material behavior, also referred to as *Cauchy Elasticity*, can be rheologically described in terms of a Hooke's spring. Many structural glass design and mechanical engineering approaches follow the assumption of linear elastic material behavior for the PVB interlayer for modeling laminated glass in the fractured state. Examples of structural glass design considering quasistatic loads are the works of Seshadri et al. [237], Bennison and Stelzer [20], Galuppi and Royer-Carfagni [110, 111, 112]. Furthermore, Xu et al. [269] used this approach to model laminated glass under low-velocity impacts and Hooper et al. [135] for blast

loads.

Hyperelastic, referred to as *Green Elasticity*, incorporates the *Cauchy Elasticity* but is subject to the stricter requirement that it must be derived from an energy potential. There are several approaches for such potentials: incompressible approaches, based on statistical mechanics [261, 251, 11], based on a description of invariants [216, 183, 274, 151] and models based on principal stretches [194]. Furthermore, there are compressible approaches [195, 4, 27].

Du Bois et al. [100], Wang et al. [264], for instance, used hyperelastic materials to describe laminated glass exposed to blast and low-velocity impact.

Plasticity Elastoplastic material behavior is the expansion of elasticity concerning inelastic deformations without considering time dependencies. A standard description is the formulation of a set of equations, known as Prandtl Reuß equations, differentiating between different cases, e.g., the elastic and the plastic case. If a particular yield and a loading condition are satisfied simultaneously, the initially elastic material behavior becomes plastic, following a respective flow rule. However, this flow is formulated independently of the velocity of a deformation process, and therefore, neither deformation rates nor relaxation properties are represented by that theory. [125]

Kott [157], Belis et al. [19] assumed elastoplastic material formulations for the PVB interlayer for the analytical modeling, and Baraldi et al. [15], Wang et al. [265] for the numerical modeling of the residual load-bearing capacity of laminated glass subjected to quasistatic loading. Furthermore, Timmel et al. [247], Larcher et al. [166], Hidallana-Gamage et al. [128] used elastoplastic material behavior for the numerical simulation of laminated glass subjected to dynamic loads.

Viscoelasticity The formulation of viscoelasticity is similar to that of elastoplasticity, as it follows the same principle. However, compared to elastoplastic material behavior, governed by a "strong memory" and therefore showing a rate-independent hysteresis, viscoelastic material is governed by the "principle of fading memory" and therefore shows a rate-dependent hysteresis [125]. One crucial aspect in modeling the behavior of laminated glass interlayers subjected to quasistatic loads is the time dependency of the interlayer, an aspect that elastic or elastoplastic approaches can not cover, making the viscoelastic material description an auspicious approach. The classification of viscoelasticity proposed by Reese and Govindjee [214] is a significant framework that divides the field into linear, finite linear, and finite approaches and is a decisive starting point for the following considerations.

The theory of Linear Viscoelasticity is based on small deformations and the assumption of a linear relationship between stresses and strains, yielding the coincidence of all stress and strain measures Tschoegl [257]. Furthermore, the theory of linear viscoelasticity is the foundation of describing a time-dependent modulus, described by the commonly known Prony series, a widespread approach in structural glass design. Kuntsche [165], Kraus [159], Schuster [231] provided Prony parameters based on DMTA tests, Rahul-Kumar et al. [211], Pelfrene et al. [202] used linear viscoelasticity to describe the interlayer in the context of delamination. However, the theory is limited to small deformations and, therefore, is not valid for describing glass laminates in a broken state.

The theory of Finite Linear Viscoelasticity describes linear time-dependent material behavior considering large deformations. It was originally proposed by Lubliner [176], and further de-

veloped and implemented numerically by Simo [240], Holzapfel and Simo [132], Holzapfel [130]. From a rheological point of view, it is described by combining a single hyperelastic spring, representing the initial stiffness, and a Prony series, representing the stiffness decay over time. This approach is used extensively in modeling laminated glass subjected to blast [203, 64] and slow velocity impact [222, 2]. Furthermore, Del Linz et al. [65] used this approach to model the delamination in laminated glass. Sticking to the general theory but applying a different framework, Kolling et al. [154] proposed a tabulated hyperelastic material model accounting for rate-dependent material behavior.

The theory of Finite Viscoelasticity can be seen as the physically consistent extension of linear viscoelasticity to finite deformations based on the dissipation inequality and a multiplicative split of the deformation gradient. Haupt and Tsakmakis [126] gave an overview of physically consistent relations of stress and strain measures within this theory. From a rheological point of view, these models consist of one or more Maxwell elements in parallel with a single spring in parallel. The Maxwell element represents the "non-equilibrium behavior," the time-dependent response of the material, and the single spring represents the time-independent "equilibrium behavior." Arbitrary hyperelastic potentials govern the springs, and the dampers depend on the evolution equation derived from the dissipation inequality, which incorporates particular viscosity functions. These functions are mathematical formulations of material-specific time scales and possibly depend on process variables such as strain rate or stress. One crucial aspect is the treatment of the volumetric material behavior, which can be assumed incompressible or compressible. Incompressibility utilizes Lagrange multipliers that represent the hydrostatic pressure; compressibility requires a split of the deformations into isochoric and volumetric parts. Along with the split of the deformations goes the split of the corresponding hyperelastic potentials and the evolution equations.

Reese and Govindjee [214] proposed a well-known framework for modeling rubbers based on the structure of the three-parameter Maxwell model, considering compressible material behavior.

Sedlan and Haupt [236] adopted a modeling approach of finite viscoelasticity for carbon black-filled rubber material based on the general framework presented by Lion [170], under the assumption of incompressible material behavior. In their model, the viscosity function is intricately linked to an internal variable that captures the influence of thixotropy and two additional process variables that account for the rate and magnitude of deformation. For the equilibrium component of their model, they extended the Mooney-Rivlin model [183, 216], for the non-equilibrium parts, they used the Neo-Hookean model [250].

Hoo Fatt and Ouyang [133] proposed a hyper-viscoelastic constitutive equation to describe the material behavior of Styrene Butadiene Rubber at high strain rates. They proposed new hyperelastic potentials for the equilibrium and the instantaneous response of the material, assuming incompressible material behavior.

Koprowski-Theiß et al. [156] proposed a model designed to capture the complex behavior of non-linear finite viscoelasticity in rubber containing porous carbon black, taking into account the compressible material behavior. This model establishes the equilibrium component based on the potential formulation introduced by Yeoh [274], and the non-equilibrium behavior by a set of modified Neo-Hookean elements. The viscosity function is influenced by process-dependent relaxation times, depending on the amount and the rate of deformation experienced by the material.

Scheffer [225] extended the basic framework established by Koprowski-Theiß et al. [156] under the assumption of incompressible material behavior. They supplemented the Neo-Hookean elements originally proposed by Koprowski-Theiß et al. [156] with a modified Yeoh potential.

Furthermore, they chose a different formulation of the viscosity functions.

Justine [149] proposed an approach for describing mineral nonwovens for a wide temperature range under the assumption of compressible material behavior and thermal effects. She used the compressible formulation of Blatz and Ko [28] and applied a flow rule incorporating a temperature-dependent viscosity and a structure variable to account for thixotropic effects. However, this model is only capable of isothermal considerations.

Schröder et al. [228] developed a more general model based on the relevant quantities of the second law of thermodynamics. They used a compressible formulation for the equilibrium response and assumed incompressibility for the non-equilibrium components, both formulations following the Neo-Hookean potential. Furthermore, they expanded the structure of the generalized Maxwell element by a thermocouple. They applied the Williams-Landel-Ferry (WLF) formulation [267] for the description of the relation between time and temperature.

Del Linz et al. [64] used the model proposed by Hoo Fatt and Ouyang [133] to model the behavior of laminated glass under bast loads.

Viscoplasticity The theory of viscoplasticity is the enrichment of the theory of plasticity by a rate dependency within the flow rule. The proportionality factor relating the inelastic deformation rate with the stress within the theory of plasticity is replaced by a material function accounting for rate dependency. This material function contains a physical quantity that represents the viscosity [125]. The kinematics and the modeling of compressibility or incompressibility follow the same rules as within the theory of finite viscoelasticity.

To describe the behavior of glassy polymers such as polymethylmethacrylate (PMMA), Boyce et al. [33] proposed a material model consisting of two networks that follow the rheological structure of a three-parameter Maxwell element. The intermolecular resistance (network A) is covered by an elastic spring derived from the elastic modulus tensor acting on the natural logarithmic strain [3] and a viscoplastic damper in parallel following a plastic flow based on the double kink model [10]. The temperature-dependent entropic hardening (network B) is represented by a Langevin spring based on non-Gaussian statistics Wang and Guth [263] model. Boyce et al. [34] built upon this approach, modifying the description of network B using the hyperelastic model presented by [11] and a viscoplastic damper to express the molecular network resistances. Dupaix and Boyce [102] built up on that model [34] describing the experimental investigations on the finite strain behavior of poly(ethylene terephthalate) (PET) and poly(ethylene terephthalate)-glycol (PETG). However, they used a strongly temperature-dependent shear modulus for the initial stiffness of the elastic spring of network A. Mulliken and Boyce [184] modeled polycarbonate (PC) and poly(methyl methacrylate) at high strain rates or low temperatures. They used the model structure proposed by Boyce et al. [33], but decomposed the intermolecular network resistance (network A) into two rate-activated processes represented by two Maxwell elements in parallel, each utilizing a viscoplastic damper. The first part considers rotations of the polymer chain segments, and the second considers intermolecular resistance. A model for polyetheretherketone (PEEK) and (PC), following the same principle structure, was proposed by Zhu et al. [279].

Like these models, Polanco-Loria et al. [206] proposed a model consisting of two networks, A and B, representing the intermolecular and the network resistance. Network A comprises a spring, representing the initial stiffness, modeled by the Neo-Hookean model, in series with a Bingham element to ensure that viscous effects only occur over a particular resistance threshold. The friction element is represented by a yield stress and an equivalent stress criterion [210], the damper follows a non-associative flow rule incorporating a plastic strain-rate tensor derived from a plastic potential. Network B is characterized by a hyperelastic spring based on the formulation of Anand [4]. Garcia-Gonzalez et al. [114] extended this model by a thermoelement,

accounting for entropy and temperature changes. Johnsen et al. [147] used a similar approach to Mulliken and Boyce [184]. However, they considered only one elastic Hencky spring in series with two dampers [213] in parallel, representing the intermolecular network of low-density cross-linked polyethylene (XLPE) for main and secondary relaxation processes. They considered the entropic strain hardening using the 8-chain model [11]. Their model accounts for strain rate, temperature dependency, and self-heating at elevated strain rates.

The well-known Bergström-Boyce model [25] was developed to describe the mechanical behavior of carbon-filled black rubber. It has the same structure as the model proposed by Boyce et al. [33]. However, for the description of the intermolecular resistance, they created a different plastic flow rule, including reptational motion and contour length variations, considering Brownian motion within a constrained tube. The elastic part of the intermolecular resistance and the network resistance are modeled using the 8-chain model [11]. A similar approach, also for carbon-filled black rubber, was proposed by Lion [169]. However, he separated viscoelastic and plastic behavior and extended the three-parameter Maxwell model by a Prandtl element in parallel. Additionally, considering thermal effects, a similar model is presented by Lion [171].

Osnes et al. [197] used the model proposed by Bergström and Boyce [25] to model the resistance of laminated glass windows subjected to blast.

1.3. Residual Load-Bearing-Capacity - Analytical Modeling Approaches

Concerning the modeling of laminated safety glass, it is essential to differentiate between fine and coarse-breaking glass, especially when considering analytical approaches. Different approaches are utilized, depending on the fracture. Laminates consisting of fine-breaking glass are modeled by assuming an equivalent stiffness, and laminates consisting of coarse-breaking glass are modeled explicitly, considering all load-bearing mechanisms individually.

1.3.1. Equivalent Stiffness Approaches

Bennison and Stelzer [20] proposed a homogenized approach to analytically model the residual load-bearing mechanism of laminated safety glass utilizing an effective modulus for LSG made of TTG.

Galuppi and Royer-Carfagni [110] introduced an analytical approach to model the behavior of broken laminated, heat-treated glass (TTG), assuming a symmetric crack pattern (cracks are parallel, and glass fragments are quadratic) under plane strain and plane stress conditions. The approach is an extension of the simple approach of an effective stiffness for broken laminated glass proposed by Bennison and Stelzer [20]. In contradiction to Bennison and Stelzer [20], they took the length of detachment between the glass and interlayer and the size of the glass fragment into account. Therefore, they added a correction term to the formulation of the effective stiffness depending on the detachment length and fragment size. That term considers the tension stiffening of the glass shards due to the bond between glass and interlayer. It is treated as diffusion of the axial stresses and modeled as a perturbed stress field (corrective, fictitious out-of-plane stress) [122], which is described by non-dimensional shape functions. The complementary energy function is minimized, and the lower bound for the effective stiffness is derived and fed into the correction term (stiffening coefficient) to find the optimal set of shape functions for the respective loading situation. However, for simplification, the adhesion between glass and interlayer was considered perfect in the bonded zones and zero in the debonded zones, and linear elasticity was assumed for all materials.

Galuppi and Royer-Carfagni [111] extended the model proposed by Galuppi and Royer-Carfagni [110] to equi-biaxial stress states. Based on numerical investigations of the delamination considering a traction-separation law, the shape of the detachment zone is assumed to be circular. In this approach, the complementary energy function depends on the radius of the bonded area, the interlayer's thickness, and the glass fragments' length. It can be observed that, depending on the ratio of the radius of the bonded region and the fragment size, the model's response is either governed by the elastic properties of the interlayer or the stiffening effect of the glass fragments.

Galuppi and Royer-Carfagni [112] provided a different extension to Galuppi and Royer-Carfagni [110], presenting a smeared view of the crack pattern. They modeled the highly non-linear behavior of the interlayer, using a secant modulus for a linear elastic approach. Based on these considerations, they calculated effective bending stiffnesses for in and out-of-plane loading. The bending moment due to in-plane-loading is presented by a compressive force, modeled by the sound glass, and tensile force, modeled by effective modulus [110]. The bending moment for out-of-plane-loading is based on an internal equilibrium, in which compressive stresses arise from direct contact with glass shards and tensile stresses arise from the interlayer, stiffened due to tension-stiffening effects.

D'Ambrosio et al. [61] provided a simple, analytical approach similar to those introduced by Bennison and Stelzer [20], Galuppi and Royer-Carfagni [110, 111, 112], to estimate the residual load-bearing capacity of laminated heat-treated glass (TTG) for engineering practice. The approach is based on the ratio of the total area to the area of detachment derived from a numerical case study [62]. This ratio is contained in a specific factor that yields a lower bound of the effective stiffness of the broken LSG by multiplying it with the stiffness of the interlayer.

1.3.2. Explicit Modeling Approaches

Seshadri et al. [237] proposed an analytical approach to describe the post-breakage behavior of rectangular-shaped glass/PVB/glass laminates with hinged support along the edges, exposed to a centric single out-of-plane load. The shape of the broken glass shards is considered triangular, and only rigid body motions are possible for the glass shards—the interlayer acts in a membrane state. As frictional effects are not considered in the model, the overall energy is split into strain energy, resulting from large strains within the interlayer and adhesion energy, that must be applied to overcome the fracture resistance. The rate dependency arising from the viscoelastic effects of the interlayer and the fracture energy is gathered in one factor. The governing kinematic mechanisms are the in-plane opening between the glass shards and the out-of-plane deformation of the laminate.

Kott [157] proposed an analytical approach to calculate the residual load-bearing capacity based on the yield line theory, originally introduced by Johansen [146]. Several plastic hinges within the broken laminate must be formed depending on the boundary conditions (bearing, loading) to allow the respective kinematic mechanisms. He defined several conditions, named: *fans mechanism*, *pyramid mechanism*, *edge mechanism* for 4-side supported bearings, and several *line mechanisms* for 2-side supported bearings, amongst others. Based on these considerations, he derived different ultimate load-bearing capacities. Moreover, he discovered that the residual load capacity can be significantly enhanced by increasing the thickness of the interlayer and adopting an asymmetric construction of the laminate. This finding opens up exciting possibilities for improving the design and performance of laminated glass. However, it's crucial to note that these enhancements in residual strength can only be achieved if appropriate flow joints are formed and fracture mechanisms are adjusted. Therefore, understanding the influence of different loads and glass types on fracture patterns is crucial to maximizing the

residual strength of laminated glass.

Belis et al. [19] further developed the concept proposed by Kott [157], making use of the one introduced by Seshadri et al. [237] to consider local delamination. However, in contrast to Kott [157], they only considered the *line mechanism* achieved by the 4-point bending test and its respective boundary conditions.

1.4. Motivation

As presented in the last sections, extensive studies investigating the residual load-bearing capacity of laminated glass have been conducted in the past decades and are still carried out today. However, although theoretical approaches are allowed by [44], in practice, it is still state of the art to evaluate the residual load-bearing capacity of laminated safety glass under quasi-static loads experimentally because none of the existing modeling approaches is capable of a sufficient description of the complex behavior. The experimental investigation, however, is very time- and cost-intensive and consumes a lot of resources, a fact unacceptable regarding sustainability. This thesis aims to enable a theoretical evaluation.

Several experiments on glass laminates, considering residual load-bearing behavior, such as equal-biaxial flexure [21], 4-point bending tests untils failure [42], bulge tests [266] revealed the decisive importance of the interlayer. Acting as a bridging ligament between the broken glass shards [67], the knowledge of the behavior of the bulk material and of the bond between interlayer and glass, which, if too soft, causes failure due to large deflections of the overall system and, if too strong, causes failure due to exceeding the elongation at the break of the interlayer, is of crucial importance. Another extensive study on breakage of 2-ply-glass laminates with PVB interlayer under various loading and bearing configurations, conducted by Kott and Vogel [158], revealed that only coarse-breaking glass (ANG, HSG) could provide residual load-bearing capacity. The observations made during the experiments emphasized that the interlayer, the bond between glass and interlayer, and the nature of the glass shards are the key elements to the residual load-bearing capacity of laminated safety glass, which goes in line with the definition of [45].

PVB has been extensively investigated in recent years, considering its effect within the intact and fully fractured state of laminated glass. The investigations of the impact on the intact state are primarily limited to DMTA [103, 161] tests to derive time- and temperature-dependent values for the shear modulus and model the shear transfer between intact glass plies for numerous loading conditions. These tests revealed an intensely time- and temperature-dependent material behavior [165, 231]. Tensile tests carried out until failure generally serve to investigate its behavior within the post-fracture state, where finite deformations must be taken into account. PVB showed a strong rate dependence and a highly non-linear stress-strain relationship [134, 64, 270] with almost no changes in volume [165]. In addition to the rate dependence, the hysteresis formation and, thus, the ability of the material to dissipate energy was investigated utilizing cyclic tests consisting of a single loading and unloading [103]. PVB formed large hystereses, characterized by a crucial difference between the loading and unloading paths. However, the most critical behavior regarding residual load-bearing capacity is the material's reaction to constant loading over time, such as creep [31] or relaxation [231]. PVB showed a striking drop in stress in the relaxation test and an increase in elongation in the creep test immediately after reaching the desired load level, followed by an almost asymptotic behavior with a low gradient. Besides the reaction to creeping loads, Botz et al. [31] also revealed a strong dependence on moisture. Generally, its behavior is considered isotropic and viscoelastic [231].

There are several modeling approaches to describe the bond between glass and interlayer, like

the shared node [209, 205] and the penalty-based approach [168, 277], both used for modeling low-velocity impacts on windshields and the cohesive zone elements, following intrinsic [50, 264] or extrinsic approaches [197, 203], for modeling slow velocity impacts on glass windshields [50, 264], glazings subjected to quasistatic loads [265] and blast loads [197, 203]. Chen et al. [51], Martín et al. [178] recommended using cohesive zone elements with intrinsic approaches. However, these models must be calibrated using experiments. The most promising experimental approaches are the peel [202] and the TCT test [65, 52], both utilized to evaluate the laminate's interfacial fracture energy. Besides modeling the interface, modeling the interlayer is necessary to identify parameters for the fracture energy. [107, 53] calibrated intrinsic cohesive zone element on TCT tests using hyperelastic material laws for the interlayer, [65] used a finite linear viscoelastic model.

Furthermore, there are investigations into the glass shards. When considering the nature of these glass shards, it is crucial to differentiate between fine- and coarse-breaking glasses. Due to the stochastic fracture pattern occurring in coarse-breaking glass, most approaches reduce the fracture to yield lines [237, 157, 5]. On the other hand, fine breaking glass has been studied in more detail [207, 188]. [208] even proposed an approach to anticipate the breakage pattern of TTG based on its thickness and level of prestress. Furthermore, there exist several numerical modeling approaches for describing the actual breakage of glass under dynamic impacts, such as the element deletion method [166, 128, 205, 173], continuum damage approaches [278] or even cohesive zone models [269, 264].

Likewise, several modeling approaches for PVB interlayers exist to describe low-velocity impacts on windshields, explosion impacts on windows, and residual load-bearing capacity under quasi-static loads. These range from elastic approaches for analytical equivalent stiffness models considering quasi-static loads [20, 110, 111, 112] or numerical models for blast [135] through plastic approaches for analytically explicitly formulated models considering quasi-static loads [19, 157] and numerical models considering blast [247, 166, 128] to viscoelastic approaches for numerical models considering low-velocity impact [222, 2] or blast [203, 64] and even viscoplastic approaches for numerical models considering explosion [197]. Furthermore, a first investigation and modeling approach of the nonlinear viscoelasticity exists [231]. Most material models describing the interlayer are calibrated on uniaxial tension tests at different strain rates [2, 66, 197].

As the previous considerations revealed, it is essential to differentiate between dynamic and quasi-static loading conditions when modeling broken laminated glass. Besides the dependency of the glass breakage on the load, this is mainly because of the interlayer, which shows a strongly nonlinear, time-dependent behavior at finite deformations. For dynamic loading, the material dependency on high strain rates plays a predominant role; for quasi-static loading, rate dependency on low strain rates in combination with creep and relaxation behavior is decisive. Within both considerations, finite deformations of the interlayer must be considered. However, this thesis aims to provide a contribution to the modeling of residual load-bearing capacity within structural glass design concerning quasi-static loads. As the bridging element between the glass shards in the case of breakage [67], the behavior of the interlayer is governed by its bulk material and adhesion, and is considered an essential part of modeling the residual load-bearing behavior. However, as investigations on the interface between glass and interlayer revealed [107, 103, 53], a crucial part of calibrating respective material parameters is the modeling of the bulk interlayer material; a description of the interlayer is considered the most critical part of modeling the residual load-bearing capacity. The approaches in structural glass design used to model the interlayer so far cannot describe the complex behavior of PVB at finite strains concerning time. However, several models and modeling frameworks are qualitatively capable of providing the required description of polymers. Approaches for elastomers [169, 25, 236, 226,

149] and models for thermoplastics [33, 34, 184, 279] exist. These models follow very complex formulations designed for specific materials under defined circumstances, making a transfer to PVB a tedious task. However, besides the models accurately tailored to a particular material, there are also general frameworks for describing viscoelastic materials at finite strains [214, 180].

This thesis aims to contribute to the theoretical description of the residual load-bearing capacity by the characterization and modeling of PVB concerning the most critical influences. It creates a test database to describe the time-dependent behavior of PVB at large deformations considering time and rate dependency for the quasistatic loading. It proposes a corresponding model formulation to describe this behavior. Furthermore, it presents an engineering approach that connects the description of complicated material behavior with a simple model. This research presents a novel approach to the theoretical evaluation of the residual load-bearing capacity of laminated safety glass, explicitly focusing on the time-dependent behavior of the PVB interlayer at large deformations.

For a clear understanding there is a tabularized structure of the thesis on the next page.

1	**Introduction**			
	1.1	1.2	1.3	1.4
	Experimental Investigations	Numerical Modeling	Analytical Modeling	Motivation

2	**Methodology**			
	2.1, 2.2	2.3, 2.4	2.5	2.6
	Mechanical Foundation	Numerical Basics	Material Properties	Experimental Methods

3	**Experiments**		
	3.1	3.2	3.3
	Preparation and Conditioning	Test Procedure	Test Results

4	**Modeling**			
	4.1	4.2, 4.3, 4.4	4.5	4.6
	Construction	Implementation	Calibration	Simulation

5	**Engineering Approaches**		
	5.1	5.2	5.3
	Hyperelastic Approach	RLBC Model	Failure

6	**Discussion**		
	6.1	6.2	6.3
	Experiments	Modeling	Engineering Approaches

7	**Conclusion and Outlook**

2. Methodology

There are several vital elements to consider when creating a model tailored to a specific material. Besides the experimental investigations, serving to calibrate the material parameters and validate the model, the general kinematics and constitutive equations play a crucial role. Furthermore, several numerical tools are needed to implement the model and identify the material parameters. Therefore, this chapter lays the groundwork of mechanical and numerical fundamentals necessary to construct and implement a material model for large deformations, considering time-dependent effects. Furthermore, laminated glass and its components, focusing on PVB, are briefly described, as well as the experimental apparatus and measuring equipment used to characterize the material presented.

2.1. Continuum Mechanics

Continuum mechanics considers the physical quantities at a material point, consistently represented by continuously differentiable tensor functions of the place. The material point inside a body and its environment represents a complete model of the material behavior at this point. Furthermore, in the mathematical model, it is the carrier of all physical state variables, such as stresses, distortions, and temperature. The property of continuity requires continuous function curves of the state variables and their continuous and sufficient differentiability to calculate derivatives at the material point. In this way, any intrinsic structure of the material is abstracted and homogenized. Consequently, a simple transfer of the methods and concepts of continuum mechanics (e.g., elasticity theory) to investigations in which the micro- or mesomechanical structure of the material is essential is not possible. The most important equations and relations will be explainedHowever, a certain level of prior knowledge in continuum mechanics is required. For a more detailed description, the reader is referred to the fundamental works in that field [256, 255, 109, 120, 125, 198, 244, 48, 1], to name just some examples. The following relations mainly follow the considerations of Haupt [125] and Parisch [198].

2.1.1. Kinematics

The fundamental principle of continuum mechanics is the assumption of matter being continuously distribued in space, represented by individual material points, the places of physical processes. Describing their change in place with respect to time is the task of kinematics.

2.1.1.1. Description of Deformation

The following considerations are based on observations within Euclidean space, although this assumption is by no means obligatory and in the context of intermediate configurations, for example, not applicable [125]. Two reference systems are required to describe the movement of a body, each of which has a position vector. Below, the two reference systems are assumed to be two superimposed cartesian systems to simplify matters, i.e., both position vectors start in the same reference system ($\mathbf{E}_K$). The position vector $\mathbf{X}(t = 0)$ describes the configuration of the undeformed body ($_0C$) and assigns a vector to each material point. Its coordinates are referred

to as material coordinates, and the associated configuration is called reference configuration. The position vector $\mathbf{x}(t > 0)$ describes the movement of the material points in space as a function of the time. Its coordinates are referred to as spatial coordinates, and the associated configuration is called current configuration ($_iC$). Although the choice of material and spatial coordinates, is arbitrary in general, in the following convective coordinates are assumed. They have the property that the coordinate lines in the current configuration are material lines. In simple terms, this means that the coordinate lines are attached to a material body and deform together with it.

The movement in space is defined by the two reversible, unique, non-linear mappings $\mathbf{x} = \mathbf{x}(\mathbf{X}, t)$ and $\mathbf{X} = \mathbf{X}(\mathbf{x}, t)$, respectively. The mapping $\mathbf{x} = \mathbf{x}(\mathbf{X}, t)$ tracks a fixed material point over time and is called the Lagrangian approach (observer sits in a boat and observes the water), the mapping $\mathbf{X} = \mathbf{X}(\mathbf{x}, t)$ tracks all material points over time that pass a specific location and is called the Eulerian approach (observer stands on a bridge and observes the water).

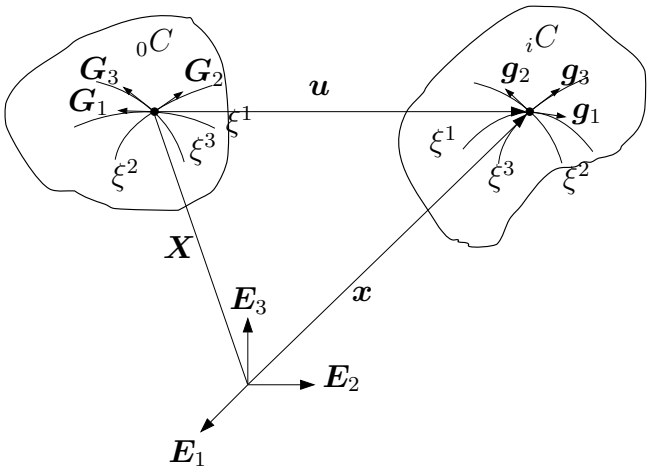

Figure 2.1.: Transformation between Reference and Current Configuration

Under the request that the reference configuration coincides with the material body at time $t = t_0$, motion can be expressed in terms of the reference configuration $\mathbf{X}$ and the displacement field $\mathbf{u}$:

$$\mathbf{x}(\mathbf{X}, t) = \mathbf{X} + \mathbf{u}(\mathbf{x}, t) \tag{2.1}$$

The transformation between the configurations takes place using the *Jacobian matrix* $\mathbf{J}$, whereby its determinant J must be unequal zero to create a unique solution. It describes the transformation of the description of a body in the reference system to the description in the current system. To represent the *Jacobian* concerning the description of deformations, the deformation gradient $\mathbf{F}$, an invertible, second-order tensor is defined. It can be expressed as the derivative of the current with respect to the reference configuration:

$$\mathbf{F} = \frac{d\mathbf{x}}{d\mathbf{X}} = \frac{d\mathbf{u}(\mathbf{X}, t)}{d\mathbf{X}} + \frac{d\mathbf{X}}{d\mathbf{X}} = \mathbf{H} + \mathbf{1} \tag{2.2}$$

where $\mathbf{H}$ equals the displacement gradient and $\mathbf{I}$ equals the unity matrix ($\mathbf{F} = F^k{}_L \mathbf{g}_k \otimes \mathbf{G}^L = \frac{\partial x^k}{\partial X^L} \mathbf{g}_k \otimes \mathbf{G}^L$). Using the relations of Eq. 2.2 two operations are defined:

- *push forward* $\Phi_*(\cdot)$: $\quad \Phi_*(d\mathbf{X}) = \mathbf{F} d\mathbf{X} = d\mathbf{x}$
- *pull back* $\Phi^*(\cdot)$: $\quad \Phi^*(d\mathbf{x}) = \mathbf{F}^{-1} d\mathbf{x} = d\mathbf{X}$

In structural mechanics, the deformation of a body can thus be described unambiguously by comparing the reference and current configurations. Two local, mutually dual basis systems derived from the parameter lines of the convective coordinates ξ^K are defined for expressing these configurations. This results in a covariant basis system, spanned by the vectors that form tangents to the parameter lines ($\mathbf{G}_K$, $\mathbf{g}_K$), and a contravariant basis system, spanned by the vectors that are formed from the gradients of the parameter lines ($\mathbf{G}^L$, $\mathbf{g}^L$). The covariant vectors, tangential to the parameter lines, are assigned contravariant coordinates; the contravariant vectors, normal to the coordinate surfaces, are assigned covariant coordinates. This crosswise pairing ensures that the vectors are invariant under coordinate transformations ($\mathbf{G}_K \cdot \mathbf{G}^L = \mathbf{g}_K \cdot \mathbf{g}^L = \delta_K^L$). A metric tensor formed from the scalar products of the individual basis vectors can be formulated for each basis system (g_{KL}, g^{KL}, G_{KL}, G^{KL}) and contains the dimensions of the basis vectors and angles to each other. The deformation of a body can thus be formed by comparing the metric of the reference configuration and the metric of the instantaneous configuration.

Considering the position vectors $\mathbf{X} = \mathbf{X}(\xi^K)$ with respect to the reference configuration and $\mathbf{x} = \mathbf{x}(\xi^K)$ with respect to the current configuration, the differentials of the position vectors result in:

$$\frac{\partial \mathbf{x}}{\partial \xi^K} = \mathbf{g}_K \qquad \frac{\partial \xi^K}{\partial \mathbf{X}} = \mathbf{G}^K \qquad \frac{\partial \mathbf{X}}{\partial \xi^K} = \mathbf{G}_K \qquad \frac{\partial \xi^K}{\partial \mathbf{x}} = \mathbf{g}^K$$

$\mathbf{G}_K$ and $\mathbf{g}_K$ are the tangent vectors on the parameterlines ξ^K with respect to the reference and the current configuration, $\mathbf{G}^K$ and $\mathbf{g}^\mathbf{K}$ are the gradient vectors on the parameterlines ξ^K with respect to the reference and the current configuration. Employing the deformation gradient that represents the transformation between reference and current configuration yields:

$$\mathbf{F} = \frac{\partial \mathbf{x}}{\partial \xi^K} \otimes \frac{\partial \xi^K}{\partial \mathbf{X}} = \mathbf{g}_K \otimes \mathbf{G}^K \qquad \mathbf{F}^{-1} = \frac{\partial \mathbf{X}}{\partial \xi^K} \otimes \frac{\partial \xi^K}{\partial \mathbf{x}} = \mathbf{G}_K \otimes \mathbf{g}^K \tag{2.3}$$

With the introduction of the dual basis systems, some further considerations regarding the *pull back* $\Phi^*(\cdot)$ and *push forward* $\Phi_*(\cdot)$ operations are necessary, as they differ for co- and contravariant coordinate representations. $\mathbf{Q}$, representing an arbitrary second-order tensor, follows a covariant representation for $()^\flat$ and a contravariant representation for $()^\sharp$. The push forward and pull backward operation utilizing the deformation gradient yields:

$$\Phi_*(\mathbf{Q}^\sharp) = \mathbf{F}\mathbf{Q}^\sharp\mathbf{F}^T \qquad \Phi_*(\mathbf{Q}^\flat) = \mathbf{F}^{-T}\mathbf{Q}^\flat\mathbf{F}^{-1} \tag{2.4}$$

$$\Phi^*(\mathbf{Q}^\sharp) = \mathbf{F}^{-1}\mathbf{Q}^\sharp\mathbf{F}^{-T} \qquad \Phi^*(\mathbf{Q}^\flat) = \mathbf{F}^T\mathbf{Q}^\flat\mathbf{F} \tag{2.5}$$

After describing the kinematics in general terms, Cartesian reference systems are assumed to increase clarity for the following sections. However, the general deformation and stress measures formulated in index notation are given for information.

2.1.1.2. Polar Decomposition

Invertible second-order tensors can be decomposed multiplicatively into symmetric and orthogonal parts. Applying a multiplicative decomposition to the deformation gradient $\mathbf{F}$, leads the symmetric parts $\mathbf{U}$ and $\mathbf{V}$ and the orthogonal part $\mathbf{R}$.

$$\mathbf{F} = \mathbf{R}\mathbf{U} = \mathbf{V}\mathbf{R} \tag{2.6}$$

$\mathbf{R}$ is the orthogonal rotation tensor, representing rigid body motions, $\mathbf{U} = +\sqrt{\mathbf{C}}$ is the right, and $\mathbf{V} = +\sqrt{\mathbf{b}}$ is the left stretch tensor. A reasonable strain measure should not contain rigid

body motions, so the right and left Cauchy Green tensors are introduced based on the right and left stretch tensors. Considering the relation of a normalized, orthogonal (orthonormal) rotation tensor $\mathbf{R}\mathbf{R}^T = \mathbf{1}$, it is fairly obvious that all rigid body motions are canceled out, in the representation of the right $\mathbf{C}$ and left $\mathbf{b}$ Cauchy Green tensor

$$\mathbf{C} = \mathbf{F}^T\mathbf{F} = \mathbf{U}^T\mathbf{R}^T\mathbf{R}\mathbf{U} = \mathbf{U}^T\mathbf{U}; \qquad \mathbf{b} = \mathbf{F}\mathbf{F}^T = \mathbf{V}\mathbf{R}\mathbf{R}^T\mathbf{V}^T = \mathbf{V}\mathbf{V}^T, \tag{2.7}$$

where $\mathbf{C} = (\mathbf{G}^K \otimes \mathbf{g}_K)(\mathbf{g}_L \otimes \mathbf{G}^L) = g_{KL}\mathbf{G}^K \otimes \mathbf{G}^L$ and $\mathbf{b} = G^{KL}\mathbf{g}_K \otimes \mathbf{g}_L$.

2.1.2. Strain Measures

There are several deformation measures to describe the strain within a body. These measures can be defined concerning different configurations. The Green Lagrange strain tensor $\mathbf{E}$, operating on the reference configuration, and the Euler Almansi strain tensor $\mathbf{a}$, operating on the current configuration, are derived as follows:

$$\mathbf{E} = \frac{1}{2}(\mathbf{C} - \mathbf{1}) \qquad \mathbf{a} = \frac{1}{2}(\mathbf{1} - \mathbf{b}^{-1}) \tag{2.8}$$

Both of these measures are defined with respect to a contravariant basis system ($\mathbf{E} = \frac{1}{2}(g_{KL} - G_{KL})\mathbf{G}^K \otimes \mathbf{G}^L$ and $\mathbf{a} = \frac{1}{2}(g_{KL} - G_{KL})\mathbf{g}^K \otimes \mathbf{g}^L$). Furthermore, deformation measures exist that are not clearly defined by the reference or the current configuration. They are referred to as Engineering or Biot strain $\mathbf{B}$ and as True or Hencky strain $\boldsymbol{\varepsilon}$:

$$\mathbf{B} = \mathbf{C}^{\frac{1}{2}} - \mathbf{1} \qquad \boldsymbol{\varepsilon} = \frac{1}{2}ln(\mathbf{1} + 2\mathbf{E}) = \frac{1}{2}ln(\mathbf{C}) \tag{2.9}$$

A qualitative overview of these stress measures is given within Fig. 2.2. However, differentiating between these measures only plays a role for large strains. In the case of small deformations all strain measures coincide. This phenomenon is explained below using the example of the linearization of the Green Lagrange strain tensor:

$$\mathbf{E} = \frac{1}{2}(\mathbf{C} - \mathbf{1}) = \frac{1}{2}(\mathbf{F}^T\mathbf{F} - \mathbf{1}) = \frac{1}{2}[(\mathbf{H} + \mathbf{1})^T(\mathbf{H} + \mathbf{1}) - \mathbf{1}] = \frac{1}{2}[\mathbf{H} + \mathbf{H}^T + \mathbf{H}\mathbf{H}^T] \tag{2.10}$$

For small deformations, the term $\mathbf{H}\mathbf{H}^T$ is small of higher order and can be omitted. Thus, the linearized stretch tensor holds:

$$\mathbf{e} = \frac{1}{2}(\mathbf{H} + \mathbf{H}^T) \tag{2.11}$$

2.1.3. Stress Measures

If a body in equilibrium with an external force is cut through, corresponding forces act on the cut surface Δa, summarized in a force vector $\Delta\mathbf{f}_s$. According to Cauchy, the following limit value exists, which leads to the traction vector $\mathbf{t}$:

$$\lim_{\Delta a \to 0} \frac{\Delta \mathbf{f}_s}{\Delta a} = \frac{d\mathbf{f}_s}{da} = \mathbf{t}(\mathbf{x}, \mathbf{n}) \tag{2.12}$$

The intersection surface through the body is defined by an outwardly directed normal vector $\mathbf{n}$. The traction vector acts in the direction of the acting force and can be calculated from the cutting force $d\mathbf{f}_s$ and the surface element da. Three such perpendicular intersections are

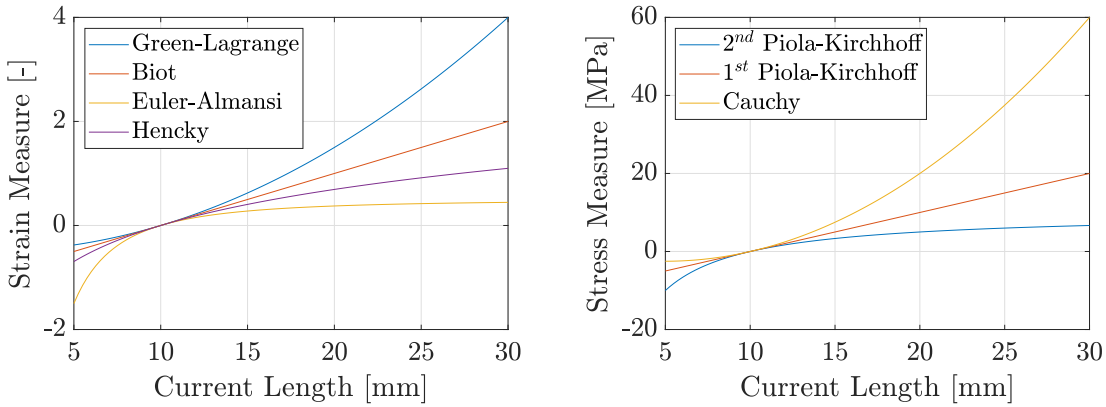

Figure 2.2.: Qualitative Overview of different strain and stress measures of 1D truss; initial length 10 [mm], initial crosssection 10 [mm^2], force [-50:200] [N]

sufficient to fully describe the stress state of a body. The nine coordinates of the traction vector correspond to the entries of the stress tensor at the material point.

$$\mathbf{t} = \boldsymbol{\sigma} \cdot \mathbf{n} \tag{2.13}$$

The associated Cauchy stress tensor operates on the current configuration, measuring with the deformed surface and acting on the deformed solid element. Considering the polar decomposition, the internal force $d\mathbf{f}_s$ undergoes a change in length in addition to the rotation, and the surface element undergoes a distortion in addition to the rotation. The normal vector is rotated with the rotation matrix $\mathbf{R}$, and the surface element is distorted with $J\mathbf{V}^{-T}$. The corresponding transformation rules result in:

$$d\mathbf{F}_s = \mathbf{F}^{-1} \cdot d\mathbf{f}_s = \mathbf{R}^T\mathbf{V}^{-1} \cdot d\mathbf{f}_s \tag{2.14}$$

$$\mathbf{n}da = J\mathbf{F}^{-T} \cdot \mathbf{N}dA = J\mathbf{V}^{-T}\mathbf{R} \cdot \mathbf{N}dA \tag{2.15}$$

These rules can be used to determine other measures of stress. The Cauchy stress tensor $\boldsymbol{\sigma}$ is the thermodynamically conjugated counterpart to the Euler-Almansi strain tensor $\mathbf{a}$, operating on the current configuration. In contrast, the thermodynamically conjugated counterpart to the Green-Lagrange strain tensor, operating on the reference configuration, is the 2^{nd} Piola Kirchhoff (2^{nd}PK) stress tensor $\mathbf{T}$. They can be connected by the 1^{st} Piola Kirchhoff (1^{st}PK) stress tensor $\mathbf{P}$, which relates the force at the current configuration to the undeformed area of the reference configuration and is referred to as "Engineering stress":

$$\mathbf{T} = \mathbf{F}^{-1}\mathbf{P} \qquad \boldsymbol{\sigma} = J^{-1}\mathbf{P}\mathbf{F}^T \tag{2.16}$$

where $\mathbf{T} = J\sigma^{IJ}\mathbf{G}_I \otimes \mathbf{G}_J$, $\boldsymbol{\sigma} = \sigma^{IJ}\mathbf{g}_I \otimes \mathbf{g}_J$, and $\mathbf{P} = J\sigma^{IJ}\mathbf{g}_I \otimes \mathbf{G}_J$. Furthermore, the weighted Cauchy stress tensor $J\boldsymbol{\sigma}$ is commonly summarized to the Kirchhoff stress tensor $\boldsymbol{\tau} = J\boldsymbol{\sigma}$. A qualitative overview of these stress measures is given within Fig. 2.2.

2.1.3.1. Related Measures

For many materials, it is reasonable to split the deformation into shape-changing and volume-changing parts. Metals, for example, are considered resistant to hydrostatic pressure but sensitive to deviatoric stresses. Furthermore, treating incompressible material behavior, which many polymers show, requires a split into deviatoric and volumetric parts. Considering the

deformation gradient $\mathbf{F}$ and the Cauchy stress tensor $\boldsymbol{\sigma}$ and using $J = det(\mathbf{F})$ leads to the following relations of conjugated parts of stress and deformation:

$$\mathbf{F} = \mathbf{F}_{iso}\mathbf{F}_{vol} \qquad \mathbf{F}_{iso} = J^{-\frac{1}{3}}\mathbf{F} \qquad \mathbf{F}_{vol} = J^{\frac{1}{3}}\mathbf{1} \tag{2.17}$$

$$\boldsymbol{\sigma} = \boldsymbol{\sigma}_{dev} + \boldsymbol{\sigma}_{vol} \qquad \boldsymbol{\sigma}_{dev} = \boldsymbol{\sigma} - \frac{1}{3}Sp(\boldsymbol{\sigma})\mathbf{1} \qquad \boldsymbol{\sigma}_{vol} = \frac{1}{3}Sp(\boldsymbol{\sigma})\mathbf{1} \tag{2.18}$$

2.1.4. Objective Rates

In many cases, it is not sufficient to only describe the amount of deformation. In addition, the time taken to apply the deformation is of essential interest, especially regarding material modeling. The deformation gradient depends on time and deformation. The time derivative of the deformation gradient $\mathbf{F}$ leads to the spatial velocity gradient $\mathbf{L}$:

$$\dot{\mathbf{F}} = \frac{\partial \dot{\mathbf{x}}}{\partial \mathbf{X}} = \frac{\partial \dot{\mathbf{x}}}{\partial \mathbf{x}}\frac{\partial \mathbf{x}}{\partial \mathbf{X}} = \mathbf{L}\mathbf{F} \qquad \rightarrow \qquad \mathbf{L} = \dot{\mathbf{F}}\mathbf{F}^{-1} \tag{2.19}$$

$$\dot{\mathbf{1}} = \frac{d}{dt}(\mathbf{F}\mathbf{F}^{-1}) = \dot{\mathbf{F}}\mathbf{F}^{-1} + \mathbf{F}(\mathbf{F}^{-1}\dot{}) = \mathbf{0} \qquad \rightarrow \qquad (\mathbf{F}^{-1}\dot{}) = -\mathbf{F}^{-1}\dot{\mathbf{F}}\mathbf{F}^{-1} \tag{2.20}$$

The spatial velocity gradient can be divided into a symmetric part, called deformation rate tensor $\mathbf{D}$, and a skew-symmetric part, called spin tensor $\mathbf{W}$:

$$\mathbf{D} = \frac{1}{2}(\mathbf{L} + \mathbf{L}^T) \qquad \mathbf{W} = \frac{1}{2}(\mathbf{L} - \mathbf{L}^T) \tag{2.21}$$

Under the assumption of irrotational deformations, $\mathbf{W} = 0$ can be assumed. This approach is commonly used in the modeling of viscoplasticity [34, 184].

However, an objective tensor field must have an objective time derivative to represent an objective material formulation. The time derivative of a Lagrangian Tensor field is objective because it is defined on the reference configuration. However, the time derivative of an Eulerian Tensor field is not objective because it is defined on the current configuration. To achieve a time-derivative of a tensor field that is not objective, a *Lie derivative* [273] must be carried out:

$$\mathcal{L}_\Phi(\cdot) = \Phi_*[\frac{d}{dt}\Phi^*(\cdot)] \tag{2.22}$$

This derivative contains three steps:

1. *pull back* operation from a tensor of the current configuration to a tensor on the reference configuration (e.g. $\mathbf{E} = \Phi^*(\mathbf{a})$)
2. objective time derivative on the reference configuration (e.g. $\frac{d}{dt}\mathbf{E} = \dot{\mathbf{E}}$)
3. *push forward* operation to the current configuration (e.g. $\mathbf{D} = \Phi_*(\dot{\mathbf{E}})$)

Applying the Lie derivative to the Euler Almansi strain measure and the Cauchy stress, results in the Oldroyd rate of the deformation and the stress:

$$\mathcal{L}_\Phi(\boldsymbol{\sigma}) = \Phi_*[\frac{d}{dt}\Phi^*(\boldsymbol{\sigma})] = \overset{\nabla}{\boldsymbol{\sigma}} = \mathbf{F}[\frac{d}{dt}(\mathbf{F}^{-1}\boldsymbol{\sigma}\mathbf{F}^{-T})]\mathbf{F}^T = \dot{\boldsymbol{\sigma}} - \mathbf{L}\boldsymbol{\sigma} - \boldsymbol{\sigma}\mathbf{L}^T \tag{2.23}$$

$$\mathcal{L}_\Phi(\mathbf{a}) = \Phi_*[\frac{d}{dt}\Phi^*(\mathbf{a})] = \overset{\triangle}{\mathbf{a}} = \mathbf{F}^{-T}[\frac{d}{dt}(\mathbf{F}^T\mathbf{a}\mathbf{F})]\mathbf{F}^{-1} = \dot{\mathbf{a}} + \mathbf{L}^T\mathbf{a} + \mathbf{a}\mathbf{L} \tag{2.24}$$

This relation also holds for any intermediate configuration concerning the particular transformation tensors and, therefore, is used within the concept of Dual Variables.

2.1.5. Balance Equations

In the following, the balance equations of mechanics and thermodynamics are introduced. They act as boundary conditions for each differential element and must be fulfilled either in weak (integral) or strong (equilibrium) form. Furthermore, they will be the foundation of the material model derived in this thesis.

2.1.5.1. Balance of Mass

The first theorem of balance postulates that the mass, described by the steady scalar density $\rho = \rho(\mathbf{x}, t)$ with respect to the volume, within a continuum is constant over time $dv = JdV$:

$$\frac{dm}{dt} = \frac{d}{dt} \int \rho dv = 0 \tag{2.25}$$

After some manipulations, Eq. 2.25 results in the balance of mass:

$$\dot{\rho} + \rho(\nabla \cdot \mathbf{v}) = 0 \tag{2.26}$$

2.1.5.2. Balance of Momentum

Following Newton, the sum of all forces acting on a continuum must be equal to the change of momentum concerning time. Considering the surface force $\tilde{\mathbf{t}}(\mathbf{x}, t)$, the volume force $\tilde{\mathbf{b}}(\mathbf{x}, t)$, and the velocity $\mathbf{v}$, the balance of momentum results in:

$$\int \tilde{\mathbf{t}} da + \int \tilde{\mathbf{b}} dv = \frac{d}{dt} \int \mathbf{v} \rho dv \tag{2.27}$$

The surface integral is converted into a volume integral using the theorem of Gauß, and the surface forces $\tilde{\mathbf{t}}$ are written as $\boldsymbol{\sigma} \cdot \mathbf{n}$ using the Cauchy theorem, which holds for the current configuration. Considering these relations and assuming continuous tensor fields, Eq. 2.27 results in:

$$\rho \dot{\mathbf{v}} = (\nabla \cdot \boldsymbol{\sigma}) + \tilde{\mathbf{b}} \tag{2.28}$$

2.1.5.3. Balance of Angular Momentum

Following Cauchy, in addition to the equilibrium of forces, the sum of the moments acting on a continuum must equal zero. The balance of angular momentum, based on this requirement, yields:

$$\int (\mathbf{x} \times \tilde{\mathbf{t}}) da + \int (\mathbf{x} \times \tilde{\mathbf{b}}) \rho dv = \int (\mathbf{x} \times \dot{\mathbf{v}}) \rho dv \tag{2.29}$$

Evaluating and rearranging Eq. 2.29 leads to the symmetry of the Cauchy stress tensor:

$$\boldsymbol{\sigma} = \boldsymbol{\sigma}^T \tag{2.30}$$

2.1.5.4. First Law of Thermodynamics

The first law of thermodynamics called the "balance of energy," states that thermal energy can be transformed into mechanical energy and postulates energy conservation for a thermodynamic process. It leads to the assumption that the time rate of the sum of kinetic and internal energy equals the work done on the system and the thermal energy supplied. Therefore, the specific

internal energy per unit mass $e(\boldsymbol{\nu}, \mathbf{x}, s)$ is introduced (s equals the entropy and $\boldsymbol{\nu}$ equals the vector of state variables). Using

$$\boldsymbol{\sigma} : \mathbf{L} = \boldsymbol{\sigma} : \mathbf{D} + \boldsymbol{\sigma} : \mathbf{W} = \boldsymbol{\sigma} : \mathbf{D},$$

as $\boldsymbol{\sigma}$ is symmetric (balance of angular momentum) and $\mathbf{W}$ is skew-symmetric, the first law of thermodynamics states

$$\int \dot{e}\rho dv = \int \boldsymbol{\sigma} : \mathbf{D} dv - \int (\nabla \cdot \tilde{\mathbf{q}}) dv + \int r\rho dv, \tag{2.31}$$

and for continuous tensor fields, Eq. 2.31 results in:

$$\dot{e}\rho = \boldsymbol{\sigma} : \mathbf{D} - \nabla \cdot \tilde{\mathbf{q}} + r\rho, \tag{2.32}$$

where $\tilde{\mathbf{q}}$ equals the heat flux vector, r is the heat source related to the unit of mass.

2.1.5.5. Second Law of Thermodynamics

The second law of thermodynamics postulates that the rate of the increase of entropy of a closed system is equal to or greater than the rate of entropy transferred to the system from outside. That requirement restricts the direction in which a thermodynamic process can occur and can be called the "balance of entropy." From the postulate of positive entropy production, the special form of the Clausius Duhem inequality can be derived [255] in integral form:

$$\frac{d}{dt} \int s\rho dv \geq \int \frac{r}{\theta} \rho dv - \int \frac{1}{\theta} \tilde{\mathbf{q}} \cdot \mathbf{n} da \tag{2.33}$$

For a completely reversible process, the equal sign holds; in any other case, the greater sign must be considered. Using the balance of energy (cf. Eq. 2.32) to introduce mechanical power $\boldsymbol{\sigma} : \mathbf{D}$ and internal energy e, Eq. 2.34 yields the second law of thermodynamics in local form, with the absolute temperature θ and its conjugated quantity, the entropy s:

$$\boldsymbol{\sigma} : \mathbf{D} - \rho(\dot{e} - \theta\dot{s}) - \frac{1}{\theta} \tilde{\mathbf{q}} \cdot \nabla\theta \geq 0 \tag{2.34}$$

For isothermal processes, the second law of thermodynamics is simplified considerably. To this end, the Helmholtz Free Energy per unit mass is defined via

$$\Psi = e - \theta s, \tag{2.35}$$

with $\dot{\Psi} = \dot{e} - \dot{\theta}s - \theta\dot{s} = \dot{e}$. Considering isothermal processes ($\dot{\theta} = 0$) leads to $\dot{\Psi} = \dot{e} - \theta\dot{s}$. The resulting expression presents a simplified formulation of the Clausius Duhem inequality and is an essential formulation for structural mechanics. It contains the potential for elastic deformations Ψ and is used later in this thesis.

$$\boldsymbol{\sigma} : \mathbf{D} - \rho\dot{\Psi} \geq 0 \tag{2.36}$$

A pull-back operation on Eq. 2.36 to the reference configuration leads to

$$\mathbf{T} : \dot{\mathbf{E}} - \rho_R \dot{\Psi} \geq 0, \tag{2.37}$$

where $\mathbf{T}$ equals the second Piola-Kirchhhoff stress tensor, $\dot{\mathbf{E}}$ equals the rate of the Green Lagrange strain tensor, and $\rho_R = \rho(\mathbf{X}, t)$ equals the density with respect to the reference configuration.

2.1.6. Principles of Material Modeling

Mechanical modeling of solid materials is based on the approach of simple materials. A mechanical simple material is defined as a material whose stress at a time is determined only by the strain history [191, 192]. Coleman [56] expanded the "mechanical" theory of simple materials to the more general "thermomechanical" theory of simple materials. Within this theory, a thermomechanical, simple material requires that the entropy, the internal energy, the stress, and the heat flux be determined by the history of the deformation gradient, the history of the temperature, and the present value of the temperature gradient [56]. The more general theory goes along with the Clausius Duhem inequality and is used later in this thesis.

Haupt [125] introduced three levels for modeling material behavior: constitutive equations, material symmetry properties, and conditions of kinematic constraints. Constitutive equations formulate the individual response of any material to a given input process. Considering elastic behavior, they can be described in terms of simple material functions; considering inelastic behavior, they must be formulated in terms of functional relations. These functional relations can be implicitly formulated using differential equations and internal variables [58, 175, 179] or explicitly, using integrals over the process history [174]. Material symmetry considers the material's directionality and holds for stress-strain relations that stay invariant for changes in the reference configuration. In general, simple materials can be divided into fluids and solids each following different properties of material symmetry. Kinematic constraints are restrictions of a body's movement, defined a priori. This concept is independent of any stress-strain relation and material symmetry. An example of such a restraint is material incompressibility, which does not allow changes in volume.

For constructing material models on the three levels introduced by Haupt [125], three general principles arise, according to Truesdell and Toupin [256], Truesdell and Noll [255]: the principle of determinism, the principle of local action, and the principle of frame-indifference (objectivity). Thereby, the principle of determinism, stating that the current stress state in one material point within a body is uniquely defined by the history of the motion of the body, is restricted by the principle of local action, stating that the stress state in one material point is only influenced by the history of motions of its neighboring points. The principle of material frame indifference or material objectivity completes the principles and states that every representation of material properties must be invariant concerning any frame change. In other words, constitutive equations must be independent of the frame of reference. Furthermore, objectivity must be the requirement for derivatives. Well-known examples satisfying the requirement of objectivity are the derivatives proposed by [143], Zaremba [276], and Oldroyd [196]. Regardless of these considerations, every material must satisfy the compatibility with the balance relations of continuum mechanics (compare Sec. 2.1.5) at any time.

2.1.6.1. Multiplicative Split

Splitting the total deformations into elastic and inelastic parts is necessary to consider inelastic deformations in elastoplastic, viscoelastic, and viscoplastic modeling. In the regime of small deformations, linearized strain measures coincide, and this split can be performed additively. However, considering finite deformations, an additive decomposition is no longer physically meaningful, as it leads to two parts that can not be distinguished clearly into elastic or inelastic parts. A multiplicative split of the deformation gradient overcomes that problem, separating the deformation into elastic and inelastic parts.

$$\mathbf{F} = \mathbf{F}_{el}\mathbf{F}_{in} \tag{2.38}$$

This approach was proposed by Lee [167] in the context of elastoplasticity, transferred to finite linear viscoelasticity by Lubliner [176], and later used extensively in modeling finite viscoelasticity and -plasticity [33, 214, 169, 25].

2.1.6.2. Dual Variables

To establish physically consistent material models, especially when using evolution equations for internal variables, the respective tensors and their derivatives must fulfill the principle of objectivity. For establishing physically consistent evolution equations for tensor-valued internal variables, it is, therefore, obligative to use tensors that, as well as their time derivatives, remain unaltered during a change of reference. This requirement is given for tensors formulated concerning the reference configuration. However, a material model exclusively formulated concerning the reference configuration is not reasonable, especially when it comes to the formulation of plastic or viscoelastic material models. These models depend on tensor-valued internal variables that are described by evolution equations, possibly formulated on intermediate configurations.

Haupt and Tsakmakis [126] provided the framework of *Dual Variables*, a guideline for assigning kinematic and static variables. They connected different configurations, utilizing conjugated pairs of stress and strain and stress and strain rates, ensuring thermodynamic consistency. Motivated by the observation that the *Jauman rate*, which is the simplest objective tensor rate, produces physically unrealistic results for particular loading conditions, they added guidelines from the mechanical balance equations to the principle of objectivity within their framework. Their concept is based on the assumption that the physically significant scalar products of stress and strain tensors ($\mathbf{T} : \mathbf{E}$, $\dot{\mathbf{T}} : \mathbf{E}$, $\mathbf{T} : \dot{\mathbf{E}}$, $\dot{\mathbf{T}} : \dot{\mathbf{E}}$) remain invariant, when introducing stress and strain tensors that do not operate on the reference configuration. For the time-derivatives, they use the *Oldroyd rate* [196].

$$\overset{\triangle}{\mathbf{a}} = \dot{\mathbf{a}} + \mathbf{L}^T\mathbf{a} + \mathbf{a}\mathbf{L} \qquad \overset{\triangledown}{\boldsymbol{\sigma}} = \dot{\boldsymbol{\sigma}} - \mathbf{L}\boldsymbol{\sigma} - \boldsymbol{\sigma}\mathbf{L}^T$$

Initially developed for elastoplasticity and viscoplasticity, this concept is extensively used to model polymer materials (compare Lion [169], Sedlan and Haupt [236], Scheffer et al. [226]). It ensures that the constitutive modeling of elastic and inelastic properties can be done separately without losing consistency regarding stress power and incremental stress power. In other words, stress power and incremental stress power are invariant within physically reasonable intermediate configurations. Therefore, they provide a set of configurations and transformations for strains and strain rates as well as stresses and stress rates.

This approach offers the possibility of transferring concepts holding for minor strains to finite deformation without losing thermodynamical consistency, which is a significant benefit, especially for modeling polymers. The transformation concepts are presented in Fig. 2.3 to Fig. 2.5.

2.1.6.3. Internal Variables

As mentioned, functional relations must be considered for modeling inelastic material behavior. These relations can be described either utilizing functionals or evolution equations. In this thesis, the theory of viscoelasticity is described in terms of the concept of *internal variables*, introduced by Green and Tobolsky [119]. They explained relaxation phenomena, assuming that forming new physical bonds and breaking old ones might decrease the stress within chains subjected to constant extension. They described this mechanism as linear differential equations

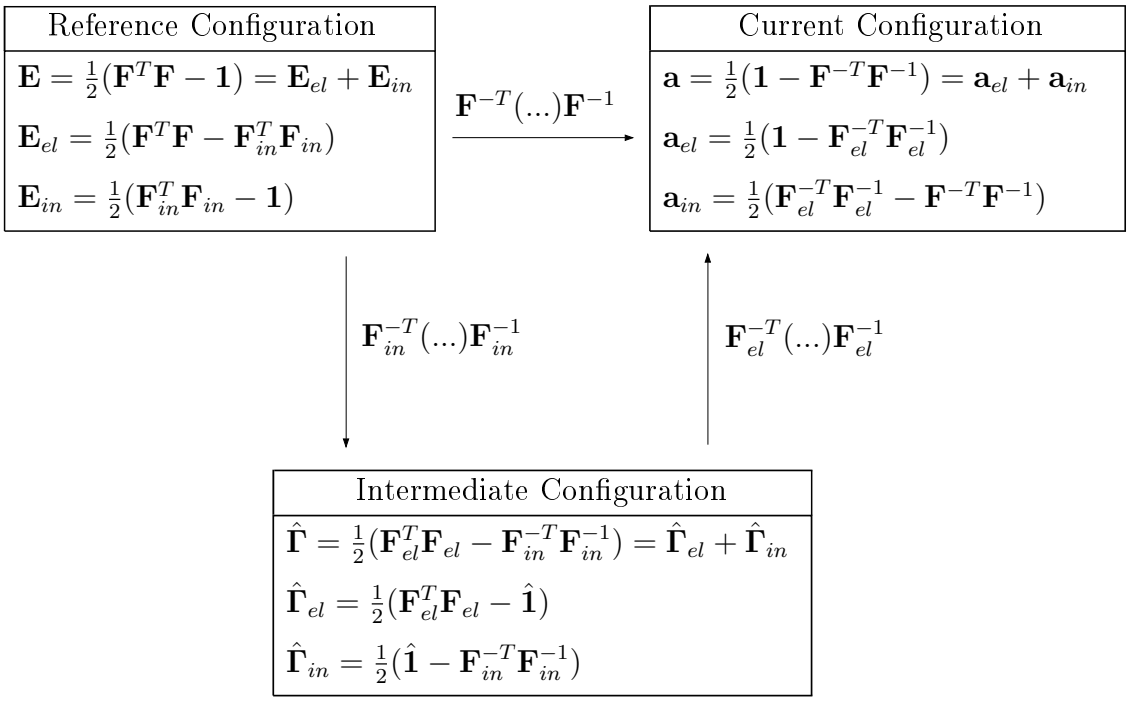

Figure 2.3.: Transformation-Properties for Deformations

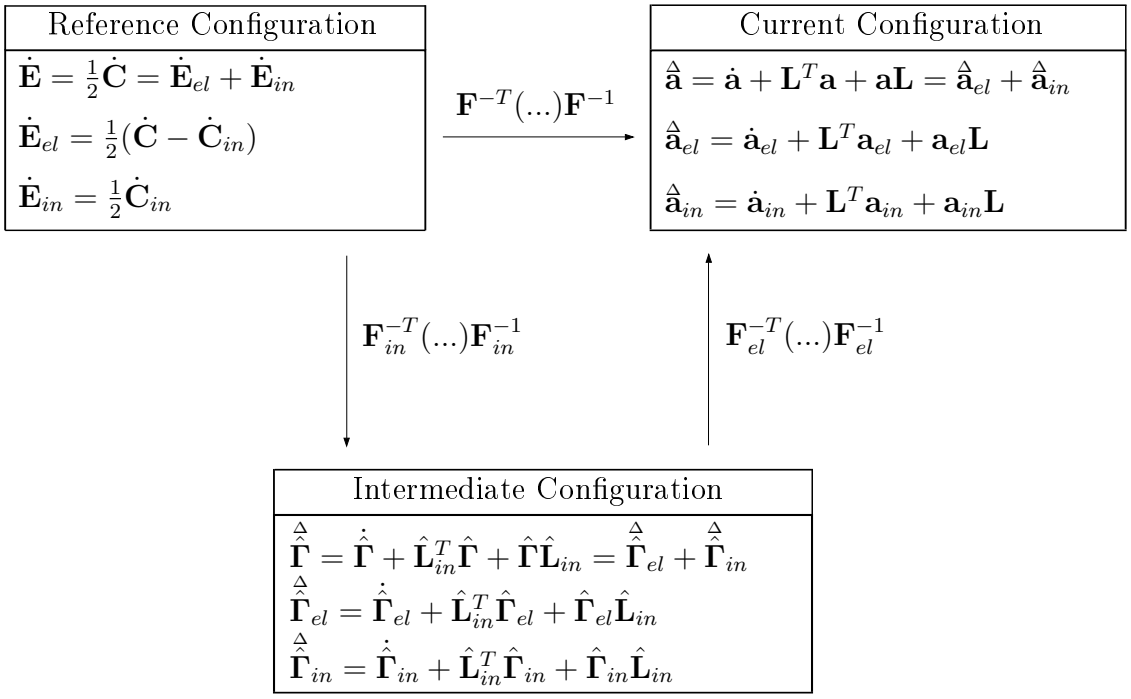

Figure 2.4.: Transformation-Properties for Deformation-Rates

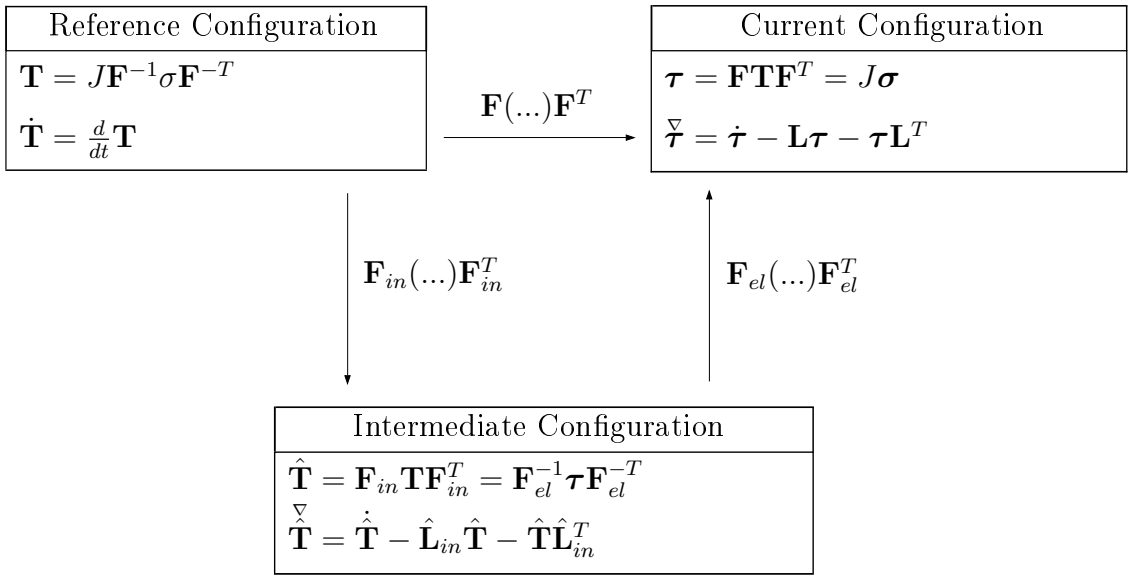

Figure 2.5.: Transformation-Properties for Stresses

utilizing internal variables of the strain type to describe the internal strains of the chains. The basic concept of internal variables is based on the consideration that the stress tensor can be represented as a function of the current strain tensor, which depends on a finite number of internal variables simultaneously [123].

$$\mathbf{T} = \mathbf{f}(\mathbf{E}, q_1, ..., q_n) \tag{2.39}$$

The parameters $q_1, ..., q_n$ represent the process history and are called internal variables. They can be used to describe the memory properties of materials. Ordinary differential equations (evolution equations) must be introduced to determine these internal variables. They depend on their current values and the input history, which can be presented by the strain tensor $\mathbf{E}$, for example.

$$\dot{q}_k(t) = \mathbf{f}_k(\mathbf{E}(t), q_1(t), ..., q_n(t)), \qquad k = 1, ..., N \tag{2.40}$$

They can be interpreted as additional constitutive equations describing dynamical processes within the material's microstructure by making their macroscopic effects visible. One well-known example of an internal variable is the inelastic strain tensor $\mathbf{E}_{in}$ within the theory of viscoelasticity or -plasticity.

2.2. Material Modeling

The material formulations used in this work are now to be described with the help of the Clausius Duhem inequality (Eq. 2.37) and the necessary relationships from continuum mechanics (Sec. 2.1). The behavior of PVB under consideration of large deformations and time dependence will be investigated. The material under large deformations will be described using hyperelastic models, and the time dependence will be determined using viscoelasticity. The viscoelasticity theory will be subdivided into linear, finite linear, and finite viscoelasticity based on the definition by Reese and Govindjee [214]. The rheological models on which the two material formulations are based are shown in Fig. 2.6. The theory of hyperelasticity, which can

be characterized, among other things, by the fact that the loading and unloading paths lie on the same line, can be illustrated using Hooke's spring. The theory of viscoelasticity, which can be characterized by the fact that the loading and unloading paths form a velocity-dependent hysteresis, can be illustrated using a Maxwell element (spring and damper connected in series).

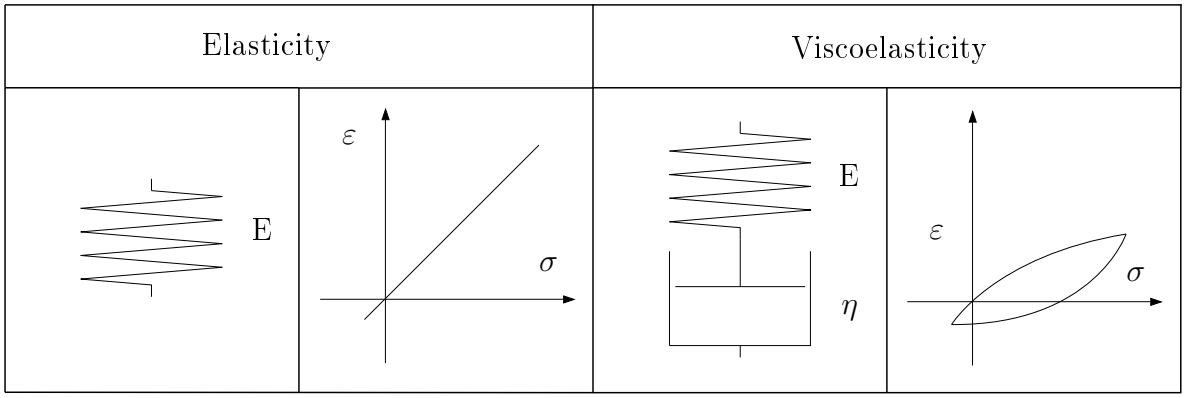

Figure 2.6.: Rheological Models

2.2.1. Hyperelasticity

According to Truesdell [253], elastic materials are referred to as *Cauchy-elastic*, and hyperelastic materials are referred to as *Green-elastic*. Within Green's theory, there must be a strain-energy function, while in Cauchy's theory, there is not necessarily a strain-energy function. So, the more general theory of Cauchy incorporates the theory of Green, but not vice versa. Three work theorems must be satisfied by hyperelastic materials.

Truesdell and Noll [255] stated:

(1) "The work done by the actual surface tractions in every closed homogeneous deformation process is non-negative."

(2) "The work done by the actual surface tractions in a homogeneous deformation process depends only on the initial and final configurations."

Caprioli [41] stated:

(3) "If there is a configuration $\mathbf{x}$ such that the actual work done in every homogeneous deformation process from $\mathbf{x}$ is non-negative, the material is hyperelastic and its strain energy function σ satisfies the inequality $\sigma(\mathbf{F}) \geq \sigma(\mathbf{1})$ where $\mathbf{F}$ is the gradient, with respect to $\mathbf{x}$ as reference configuration, of any deformation. In addition, the configuration $\mathbf{x}$ must be a natural state, i.e. the stress corresponding to $\mathbf{x}$ is zero."

Coleman [55] stated:

(4) "For any homogeneous deformation process, whose initial and final configurations are distinct and differ by only a pure stretch, the work done by the actual contact force is greater than the virtual work done if the contact force had been held at their initial values (dead loading): $W_{12} > W_{12}^{*}$"

(5) "The material is hyperelastic, and its strain energy obeys the inequality: $\sigma(\mathbf{F}_2) - \sigma(\mathbf{F}_1) - tr[\sigma_{\mathbf{F}}(\mathbf{F}_1)^T(\mathbf{F}_2 - \mathbf{F}_1)] > 0$ whenever $\mathbf{F}_1\mathbf{F}_2$ and $\mathbf{G} = \mathbf{F}_1\mathbf{F}_2^{-1}$ holds with positive-definite and symmetric $\mathbf{G}$"

Furthermore, due to the restriction caused by the principle of frame indifference, the strain-energy function must be of the special form that only depends on the deformation gradient [118], whether through the right or left Cauchy Green tensor. For the additional assumption of isotropy, it holds the fundamental theorem of Truesdell [254]: *If the strain-energy function* $\sigma(\mathbf{F})$ *of a hyperelastic material has a strict minimum at* $\mathbf{F} = \mathbf{1}$*, the material is a simple solid, and any minimizing configuration is a natural state.*

Smith and Rivlin [242] stated that the energy function under the assumption of isotropy is invariant if it can be expressed in terms of several invariant scalars, which satisfy certain algebraic relations. They showed that a polynomial series can express the energy function in the invariant scalars. As the energy function can be expressed in terms of the Cauchy Green tensor, this polynomial series can be explicitly described as a symmetric function of the principal stretches or as a function of the principal invariants of the stretch tensors [255]. Green and Adkins [117] suggested corresponding explicit forms of the stress-strain relation. Besides that, Rivlin [216, 217, 218, 219] derived a general polynomial description of the strain energy function in the context of large elastic deformations of isotropic materials, a simplified version of that description is the Neo Hookean model, which is related to the Gaussian model. Further considerations on the network of long-chain molecules were done by Treloar [249, 250, 252]. Treloar [251] also provided a data set of experiments on vulcanized rubber, a validation base for new modeling assumptions since then.

Boyce and Arruda [32] showed a good overview of different models of hyperelasticity, dividing them into models that assume incompressible material behavior and models that assume compressible behavior in general. Furthermore, they showed that the Helmholtz free energy, which in the case of hyperelasticity equals the deformation energy, can be formulated either based on statistical assumptions, as a function of invariants, or as a function of the principal stretches. However, a clear separation is not possible as the statistical models also depend on principal stretches or invariants.

2.2.2. Incompressible Hyperelasticity

Since the compressive modulus of polymers often exceeds their shear modulus by a multiple, they can be assumed incompressible in a simplified way. With this assumption, there is no more volume change, i.e., $J = 1$, and in consequence, the right Cauchy Green tensor equals its isochoric part $\mathbf{C} = \bar{\mathbf{C}}$. In order to nevertheless fulfill the force equilibrium, a Lagrangian multiplier p is introduced. From a physical point of view, this multiplier reflects the hydrostatic pressure. The corresponding system of equations concerning the reference configuration yields:

$$\mathbf{T} = \mathbf{T}_{iso} + \mathbf{T}_{vol} \tag{2.41}$$

$$\mathbf{T}_{iso} = \frac{\partial \Psi}{\partial \mathbf{C}} \tag{2.42}$$

$$\mathbf{T}_{vol} = p\mathbf{C}^{-1} \tag{2.43}$$

The Lagrangian multiplier is then derived utilizing the respective boundary conditions. Concerning the uniaxial case with a load pointing in xx-direction, the stresses in the transversal directions must be equal to zero ($\mathbf{T}^{<yy>} = \mathbf{T}^{<zz>} = 0$).

2.2.2.1. Statistics-Based Models

The statistical mechanics models are based on the assumption of randomly distributed and differently oriented molecular chains. The simplest model based on this methodology is the

Gaussian model [261, 251]. It results in:

$$\Psi = \frac{1}{2} N k \theta (\mathrm{I}_{\mathbf{C}} - 3) \tag{2.44}$$

where N equals the number of polymer chains, k equals the Boltzmann's constant, θ equals the absolute temperature, and $\mathrm{I}_{\mathbf{C}}$ equals the first invariant of the right Cauchy Green tensor. However, this model works only up to moderately significant distortions, and fails to predict the material response at large deformations. To overcome this problem, non-Gaussian approaches, utilizing Langevin chain statistics, are common. The respective Langevin function results in:

$$\mathcal{L}(x) = \coth(x) - \frac{1}{x} \tag{2.45}$$

A famous example, known for a very accurate prediction of the material response of polymers up to large deformations is the 8-chain model, introduced by Arruda and Boyce [11]:

$$\Psi = N k \theta \lambda_{lock} \left[\beta_{chain} \lambda_{chain} + \lambda_{lock} ln\left(\frac{\beta_{chain}}{sinh(\beta_{chain})} \right) \right] \tag{2.46}$$

where $\beta_{chain} = \mathcal{L}^{-1}\left(\frac{\lambda_{chain}}{\lambda_{lock}}\right)$, λ_{lock} is the locking stretch, and $\lambda_{chain} = \sqrt{\frac{1}{3}\left(\lambda_1^2 + \lambda_2^2 + \lambda_3^2\right)}$. For further examples of statistical models and a detailed overview, the reader is referred to Treloar [248]. Fig. 2.7 shows the modeling of Treloar's uniaxial tension data using the 8-chain model with the parameters $Nk\theta = 0.2787$, $\lambda_{lock} = 5.0773$.

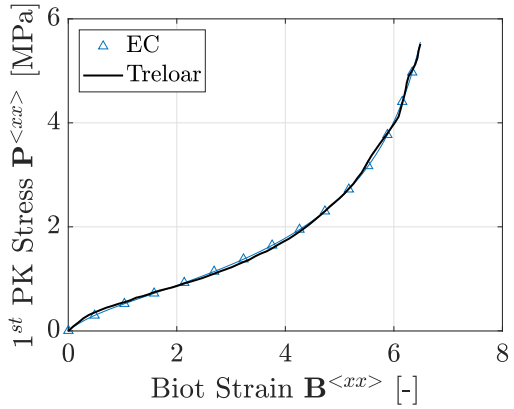

Figure 2.7.: Approaching Treloar's data with the 8-chain model

2.2.2.2. Invariants-Based Models

Symmetrical second-order tensors in three-dimensional space can be transformed from a coordinate matrix by principal axis transformation $\mathbf{Q} = Q^{ij}\mathbf{e}_i \otimes \mathbf{e}_j$ to the diagonal matrix $\mathbf{Q} = \sum_{i=1}^{3} \lambda_i \mathbf{n}^i \otimes \mathbf{n}^i$. This transformation corresponds to a rotation of the basis vectors e_i into the main directions n_i. The coordinates Q^{ij} become the principal values λ_i, with the corresponding values obtained by solving the eigenvalue problem.

$$(\mathbf{Q} - \lambda \mathbf{1}) \cdot \mathbf{n} = \mathbf{0} \tag{2.47}$$

The solution to this eigenvalue problem leads to the characteristic equation of the second-order tensor:

$$\lambda^3 - \mathrm{I}_{\mathbf{Q}} \lambda^2 + \mathrm{II}_{\mathbf{Q}} \lambda - \mathrm{III}_{\mathbf{Q}} = 0 \tag{2.48}$$

Since the eigenvalues λ_i, which represent the solutions of this equation, are base-independent scalars, the coefficients of the characteristic equation, which are referred to as invariants of the second-level tensor, are also base-independent.

$$\mathrm{I}_{\mathbf{Q}} = Sp(\mathbf{Q}) \tag{2.49}$$

$$\mathrm{II}_{\mathbf{Q}} = \frac{1}{2}\Big((Sp(\mathbf{Q}))^2 - Sp(\mathbf{Q}^2)\Big) \tag{2.50}$$

$$\mathrm{III}_{\mathbf{Q}} = det(\mathbf{Q}) \tag{2.51}$$

If $\mathbf{Q}$ is in principal axis representation and the eigenvalues $(\lambda_1, \lambda_2, \lambda_3)$ are known, the formulation of the invariants is simplified as follows:

$$\mathrm{I}_{\mathbf{Q}} = \lambda_1 + \lambda_2 + \lambda_3 \tag{2.52}$$

$$\mathrm{II}_{\mathbf{Q}} = \lambda_1\lambda_2 + \lambda_2\lambda_3 + \lambda_3\lambda_1 \tag{2.53}$$

$$\mathrm{III}_{\mathbf{Q}} = \lambda_1\lambda_2\lambda_3 \tag{2.54}$$

Since these relationships can be transferred to symmetric second-order tensors, they can also be applied to the left or right Cauchy Green tensor. The invariants of the right Cauchy Green tensor $\mathbf{C}$ thus result in $\mathrm{I}_{\mathbf{C}}, \mathrm{II}_{\mathbf{C}}, \mathrm{III}_{\mathbf{C}}$. Three common hyperelastic potentials that are used in structural mechanics are presented below. The most simple approach is the Neo-Hookean model proposed by Treloar [250], Rivlin [216]:

$$\Psi = C_{10}(\mathrm{I}_{\mathbf{C}} - 3) = \frac{\mu}{2}(\mathrm{I}_{\mathbf{C}} - 3) \tag{2.55}$$

where $C_{10} = Nk\theta$ can be assumed. Adding the dependence on the second invariant to the Neo-Hookean model leads to the Mooney-Rivlin model [183, 216]:

$$\Psi = C_{10}(\mathrm{I}_{\mathbf{C}} - 3) + C_{01}(\mathrm{II}_{\mathbf{C}} - 3) \tag{2.56}$$

An example of a higher-order formulation concerning the first invariant is the Yeoh model [274]:

$$\Psi = C_{10}(\mathrm{I}_{\mathbf{C}} - 3) + C_{20}(\mathrm{I}_{\mathbf{C}} - 3)^2 + C_{30}(\mathrm{I}_{\mathbf{C}} - 3)^3 \tag{2.57}$$

Essential requirements for higher-order models are polyconvexity and Drucker stability. The latter enforces the tangential stiffness, represented by the Hessian matrix, to be positive definite. Furthermore, the calibrated material parameters must be physically realistic and yield stable constitutive responses.

This selection does not purport to provide a comprehensive overview of hyperelastic models based on invariant-dependent formulations; instead, it presents a subjective choice of several standard models. Fig. 2.8 illustrates the described models fitted to Treloar's experimental data, compared with the experimental data itself to provide an impression of the model's quality. The fits were generated using Matlab's curve fitting tool with default settings, as the objective here is solely to demonstrate the qualitative capabilities of the individual models. Fig. 2.8 shows the modeling of Treloar's uniaxial tension data using the Neo-Hookean ($\mu = 0.4452$), Yeoh ($C_{10} = 0.1406$, $C_{20} = 2.337e-14$, $C_{30} = 2.333e-05$), and Mooney-Rivlin ($C_{10} = 0.2464$, $C_{01} = 2.22e-14$) models.

2.2.2.3. Stretch-Based Models

A similar approach is the formulation of the potential using principal stretches. Here, the potential is not formulated as a function of the invariants of the characteristic equation, but

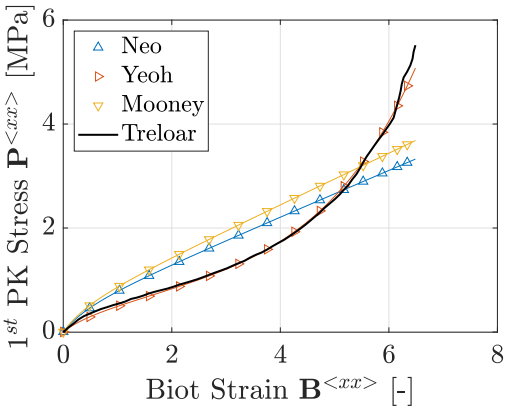

Figure 2.8.: Approaching Treloar's data with several invariant based models

directly with the eigenvalues λ_i, which represent the solution of the characteristic equation and coincide with the principal stretches in the case of the right or left distortion tensor. The model of Ogden [194] represents a very well-known approach to this:

$$\Psi = \sum_{i}^{n} \frac{\mu_n}{\alpha_n} \left(\lambda_1^{\alpha_n} + \lambda_2^{\alpha_n} + \lambda_3^{\alpha_n} - 3 \right) \tag{2.58}$$

Fig. 2.9 shows the modeling of Treloar's uniaxial tension data using the 2-term Ogden model ($\mu_{01} = 0.3479$, $\alpha_{01} = 1.778$, $\mu_{02} = 0.0001154$, $\alpha_{02} = 6.725$).

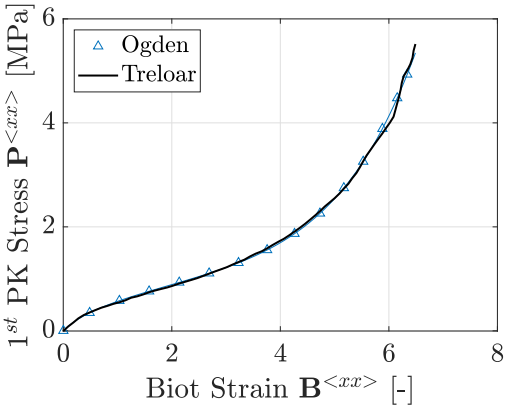

Figure 2.9.: Approaching Treloar's data with the Ogden model

2.2.3. Compressible Hyperelasticity

For compressible plastics, e.g., foams with a transverse strain coefficient far below 0.5, the assumption of incompressible material behavior is insufficient. A common approach is consistently separating the material response into volume-changing and shape-changing components. For compressible material behavior, the isochoric stress in Eq. 2.42 depending on the right Cauchy Green tensor $\mathbf{C}$ is replaced by a formulation depending on the isochoric right Cauchy-Green tensor $\bar{\mathbf{C}}$ and the expression for the hydrostatic pressure in Eq. 2.43 is replaced by a

volumetric potential depending on the determinant J of the deformation gradient $\mathbf{F}$.

$$\mathbf{T} = \mathbf{T}_{iso} + \mathbf{T}_{vol} \tag{2.59}$$

$$\mathbf{T}_{iso} = \frac{\partial \Psi_{iso}}{\partial \bar{\mathbf{C}}} \tag{2.60}$$

$$\mathbf{T}_{vol} = \frac{\partial \Psi_{vol}}{\partial J}\mathbf{C}^{-1} \tag{2.61}$$

Concerning the energy potential, this means defining an isochoric and a volumetric potential. Usually, the isochoric potential depends on the isochoric part of the distortion tensor, and the volumetric part depends on the determinant of the deformation gradient. A commonly used version of the Neo-Hookean model results in:

$$\Psi = \Psi_{iso} + \Psi_{vol} = \frac{\mu}{2}(\mathrm{I}_{\bar{\mathbf{C}}} - 3) + \frac{\kappa}{2}(J-1)^2 \tag{2.62}$$

Further examples were provided, for instance, by Ogden [195], Anand [4], Bischoff et al. [27] amongst others. Fig. 2.10 shows the results of Neo-Hookean models with different compression moduli (in the figure represented by the respective Poissons ratio) in comparison with the incompressible Neo-Hookean model. Fig. 2.10 shows the influence of the Poisson's ratio ν on the stress-strain response compared to the incompressible case ($\nu = 0.5$).

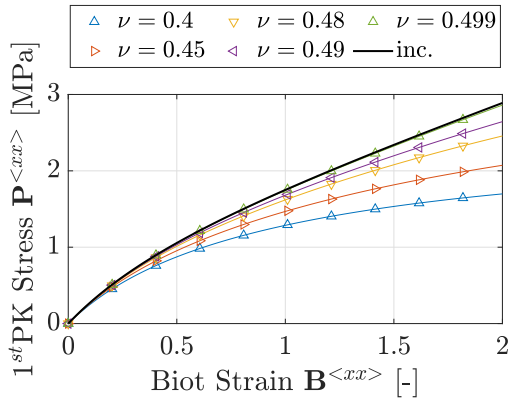

Figure 2.10.: Neo Hookean Model ($\mu = 1$) for different compression moduli

2.2.4. Viscoelasticity

The foundation of viscoelasticity is based on the principle of fading memory [57] and the dissipation inequality [56].

Lubliner [175], Haupt [123] broke the the modeling of the time-dependent part within the theory of viscoelasticity down to three approaches: (1) by means of viscous stresses, depending on the rate of strain as it is done within the theory of Navier Stokes for instance; (2) by means of the principle of fading memory, introduced by Coleman and Noll [59], where the present stress is influenced by the entire history of strain (explicit, functional approach); (3) utilizing evolution equations with internal state variables [58, 259] (implicit approach, based on the description in terms of differential equations).

In contrast to that, Reese and Govindjee [214] suggested a separation of the theory of viscoelasticity based on its applicability, without considering the actual modeling of the time dependence in detail: (1) linear viscoelasticity (2) finite linear viscoelasticity (3) finite viscoelasticity.

The structure of the following sections is based on the suggestion made by Reese and Govindjee [214], utilizing explicit and implicit approaches to explain the three parts of the theory of viscoelasticity based on the three-parameter Maxwell model.

2.2.5. Linear Viscoelasticity

The theory of linear viscoelasticity, which only applies to small deformations and small perturbations outside thermodynamic equilibrium, uses either the overstress or the inelastic strain as the internal variable. For small deformations, the relationship between these two variables is linear, and all stress and strain measures coincide. The structure of the evolution equation is thus apparent [257]. The deformations within the linear viscoelasticity are based on the linearised strain tensor $\mathbf{e}$ (Eq. 2.11), which can be additively divided into an elastic $\mathbf{e}_{el}$ and an inelastic part $\mathbf{e}_{in}$ and thus corresponds to the kinematics of the rheological Maxwell model.

The Clausius Duhem inequality with respect to the reference configuration, considering the linearized strain tensor into Eq. 2.37, and the free energy per unit volume, yields:

$$\mathbf{T} : \dot{\mathbf{e}} - \dot{\Psi} \geq 0 \tag{2.63}$$

For the sake of simplicity, the three dimensional expression is reduced to one dimension in the following, leading:

$$\sigma\dot{\varepsilon} - \dot{\Psi} \geq 0 \tag{2.64}$$

Accordingly, the formulation of the potemtial for elastic deformations reads:

$$\Psi = \frac{1}{2}E\varepsilon^2 + \frac{1}{2}E_{el}(\varepsilon - \varepsilon_{in})^2 \tag{2.65}$$

After some manipulations, the time-derivative of the potential reads:

$$\dot{\Psi} = E\varepsilon\dot{\varepsilon} + E_{el}(\varepsilon - \varepsilon_{in})\dot{\varepsilon} - E_{el}(\varepsilon - \varepsilon_{in})\dot{\varepsilon}_{in} \tag{2.66}$$

Inserting Eq. 2.65 into Eq. 2.63 and summarizing it, results in:

$$\sigma\dot{\varepsilon} - \Big[E\varepsilon\dot{\varepsilon} + E_{el}(\varepsilon - \varepsilon_{in})\dot{\varepsilon} - E_{el}(\varepsilon - \varepsilon_{in})\dot{\varepsilon}_{in}\Big] \geq 0 \tag{2.67}$$

Sorting Eq. 2.67 yields:

$$\Big[\sigma - \Big(E\varepsilon + E_{el}(\varepsilon - \varepsilon_{in})\Big)\Big]\dot{\varepsilon} + \Big[E_{el}(\varepsilon - \varepsilon_{in})\Big]\dot{\varepsilon}_{in} \geq 0 \tag{2.68}$$

From Eq. 2.68 the stress and the residual inequality can be derived. The stress leads to:

$$\sigma = E\varepsilon + E_{el}(\varepsilon - \varepsilon_{in}) \tag{2.69}$$

The residual inequality, represented by the evolution equation of linear viscoelasticity utilizing the inelastic strain as an internal variable, reads:

$$E_{el}(\varepsilon - \varepsilon_{in})\dot{\varepsilon}_{in} \geq 0 \tag{2.70}$$

making Eq. 2.70 a quadratic form leads to thermomechanical consistency, represented by the following evolution equation that contains the inelastic strain as internal variable:

$$\dot{\varepsilon}_{in} = \frac{1}{\eta}E_{el}(\varepsilon - \varepsilon_{in}) \tag{2.71}$$

where the viscosity η must be greater than zero.

Another approach to formulate the constitutive equations of linear viscoelasticity, using the overstress as an internal variable, can be derived as follows. These corresponding relations result in the following:

$$q = E_{el}\varepsilon_{el} = \eta\dot{\varepsilon}_{in} \tag{2.72}$$

$$\dot{q} = E_{el}\dot{\varepsilon}_{el} \tag{2.73}$$

$$\varepsilon = \varepsilon_{el} + \varepsilon_{in} \tag{2.74}$$

$$\dot{\varepsilon} = \dot{\varepsilon}_{el} + \dot{\varepsilon}_{in} \tag{2.75}$$

Here, q corresponds to the overstress, representing the Maxwell element's time-dependent stress. Transforming Eq. 2.72 and Eq. 2.75 and inserting into Eq. 2.73 under the consideration of $\tau = \frac{\eta}{E_{el}}$, results in the evolution equation of linear viscoelasticity utilizing the overstress as an internal variable:

$$\dot{q} + \frac{1}{\tau}q = E_{el}\dot{\varepsilon} \tag{2.76}$$

The analytical solution of Eq. 2.76 results in:

$$q = \int_{s=0}^{s=t} E_R(t-s)\frac{d\varepsilon(s)}{ds}ds \tag{2.77}$$

with E_R equals the time-dependent modulus, represented by the convolution core of the linear functional of viscoelasticity:

$$E_R(t-s) = E_{el}e^{-\frac{t-s}{\tau}} \tag{2.78}$$

The total stress results in:

$$\sigma = E\varepsilon + q \tag{2.79}$$

Two possibilities for deriving the material model of linear viscoelasticity were presented: one approach based on the Clausius-Duhem inequality, which utilizes the inelastic strain as an internal variable, and the other based on rheological considerations, which utilizes the overstress as an internal variable. The approach, based on the Clausiusis-Duhem inequality, is used in the following to derive the equations corresponding to the theory of finite linear and finite viscoelasticity. The theory of finite viscoelasticity also uses the inelastic strain as an internal variable, whereas the finite linear theory uses the overstress.

2.2.6. Finite Linear Viscoelasticity

The modeling of viscoelasticity within the regime of large strains goes back to the model on the viscoelasticity of polymeric rubber, proposed by Green and Tobolsky [119], who extended the kinetic theory of Treloar [249, 250] by relaxation effects. Valanis [259] and Lubliner [176] further developed that model. Lubliner [176] used a first multiplicative split of the deformation gradient into isochoric and volumetric parts as suggested by Flory [106] and further suggested a second multiplicative split of the deformation gradient into elastic and inelastic (viscous) parts, where the inelastic parts refer to the time-dependent effects. Such a procedure was originally suggested by Lee [167] in the context of elastoplasticity. The internal variables were treated as functionals of the histories of the external variables. With this, the functionals form solutions

of rate equations (evolution equations [175]. Within the finite, linear viscoelasticity theory, an extension of the model proposed by Lubliner [176] was given by Simo [240] and further developed and implemented in FE by Holzapfel and Simo [132], Holzapfel [130]. The theory of finite linear viscoelasticity is based on a hyperelastic formulation for the equilibrium part and a convolution integral representing the dissipative part, formulated by inner variables on the stress type. It can be related to the theory of linear viscoelasticity.

The derivation of the theory of finite linear viscoelasticity again starts at the Clausius Duhem inequality concerning the reference configuration:

$$\mathbf{T} : \dot{\mathbf{E}} - \dot{\Psi} \geq 0 \tag{2.80}$$

The strain energy density per unit volume is described by the following potential:

$$\Psi(\mathbf{C}, \mathbf{\Gamma}) = \Psi^{\infty}(J, \bar{\mathbf{C}}) + \Upsilon(\bar{\mathbf{C}}, \mathbf{\Gamma}) = \Psi^{\infty}_{iso}(\bar{\mathbf{C}}) + \Psi^{\infty}_{vol}(J) + \Upsilon(\bar{\mathbf{C}}, \mathbf{\Gamma}) \tag{2.81}$$

Where $\mathbf{\Gamma}$ is a non-measurable internal history variable, and Υ is a configurational free energy ensuring a non-negative dissipation (must vanish for $t \to \infty$) and describing the relaxational state of polymer chains. $\bar{\mathbf{C}}$ is the isochoric part of the right Cauchy Green tensor, and J is the determinant of the deformation gradient $\mathbf{F}$. Stress is received by deriving energy from the stretch tensor. The derivative concerning time reads:

$$\dot{\Psi} = \frac{\partial \Psi^{\infty}_{iso}(\bar{\mathbf{C}})}{\partial \mathbf{C}} : \frac{\partial \mathbf{C}}{\partial t} + \frac{\partial \Psi^{\infty}_{vol}(J)}{\partial \mathbf{C}} : \frac{\partial \mathbf{C}}{\partial t} + \frac{\partial \Upsilon(\bar{\mathbf{C}}, \mathbf{\Gamma})}{\partial \mathbf{C}} : \frac{\partial \mathbf{C}}{\partial t} + \frac{\partial \Upsilon(\bar{\mathbf{C}}, \mathbf{\Gamma})}{\partial \mathbf{\Gamma}} : \frac{\partial \mathbf{\Gamma}}{\partial t} \tag{2.82}$$

Inserting Eq. 2.82 into Eq. 2.80 yields:

$$\frac{1}{2}\mathbf{T} : \dot{\mathbf{C}} - \Big[\frac{\partial \Psi^{\infty}_{iso}}{\partial \mathbf{C}} : \dot{\mathbf{C}} + \frac{\partial \Psi^{\infty}_{vol}}{\partial \mathbf{C}} : \dot{\mathbf{C}} + \frac{\partial \Upsilon}{\partial \mathbf{C}} : \dot{\mathbf{C}} + \frac{\partial \Upsilon}{\partial \mathbf{\Gamma}} : \dot{\mathbf{\Gamma}}\Big] \geq 0 \tag{2.83}$$

Sorting Eq. 2.83 leads to the expression for the stress tensor:

$$\mathbf{T} = 2\Big[\frac{\partial \Psi^{\infty}_{iso}}{\partial \mathbf{C}} + \frac{\partial \Psi^{\infty}_{vol}}{\partial \mathbf{C}} + \frac{\partial \Upsilon}{\partial \mathbf{C}}\Big] \tag{2.84}$$

and with $\mathbf{q} = -2\frac{\partial \Upsilon(\bar{\mathbf{C}}, \mathbf{\Gamma})}{\partial \mathbf{\Gamma}}$, yields the dissipation inequality:

$$\mathbf{q} : \dot{\mathbf{\Gamma}} \geq 0 \tag{2.85}$$

making it a quadratic form to ensure thermodynamical consistency yields:

$$\dot{\mathbf{\Gamma}} = \frac{1}{\eta}\mathbf{q} \tag{2.86}$$

$\mathbf{q}$ is an internal variable governed by the differential equation of linear viscoelasticity, and η is the viscosity. Furthermore, $\mathbf{q}$ and $\mathbf{\Gamma}$ are defined as conjugated variables along with the constitutive equations $\mathbf{q} = -2\frac{\partial \Upsilon(\bar{\mathbf{C}}, \mathbf{\Gamma})}{\partial \mathbf{\Gamma}}$ and $\bar{\mathbf{q}} = 2\frac{\partial \Upsilon(\bar{\mathbf{C}}, \mathbf{\Gamma})}{\partial \bar{\mathbf{C}}}$, which restrict the internal configurational free energy Υ [130]. The relation between these restrictions can be established employing a Legendre Transformation [240]. The evolution equation for the overstress is then obtained by:

$$\dot{\mathbf{q}} + \frac{1}{\tau}\mathbf{q} = \frac{d}{dt}\Big[2\frac{\partial \Psi^{ov}_{iso}(\bar{\mathbf{C}})}{\partial \mathbf{C}}\Big] \tag{2.87}$$

with the restriction for $\Psi^{ov}_{iso}(\bar{\mathbf{C}})$ [132]:

$$\Psi^{ov}_{iso}(\bar{\mathbf{C}}) = \beta \Psi^{\infty}_{iso}(\bar{\mathbf{C}}) \tag{2.88}$$

The equation for the overstress therefore results in the following convolution integral

$$\mathbf{q} = \int_{s=0}^{s=t} e^{-\frac{t-s}{\tau}} \frac{d}{ds}\Big[2\frac{\partial \Psi_{iso}^{ov}(\bar{\mathbf{C}})}{\partial \mathbf{C}}\Big] ds \tag{2.89}$$

leading to the total stress

$$\mathbf{T} = 2\frac{\partial \Psi_{iso}^{\infty}(\bar{\mathbf{C}})}{\partial \mathbf{C}} + 2\frac{\partial \Psi_{vol}^{\infty}(J)}{\partial \mathbf{C}} + \mathbf{q} \tag{2.90}$$

2.2.7. Finite Viscoelasticity

The theory of finite viscoelasticity is already discussed Koh and Eringen [153], Haupt [123, 124], by building upon the general framework of linear viscoelasticity but considering large deformations. However, in contrast to the theory of finite linear viscoelasticity, which is also based on the theory of linear viscoelasticity considering large deformations but is restricted to small perturbations away from the thermodynamical equilibrium, it is not limited by that restriction and , therefore, is more general. It is based on the approach proposed by Lubliner [176] following a multiplicative decomposition of the deformation gradient. The considerations of Haupt [124] were further developed by [169], resulting in a thermomechanical sound model with excellent accuracy in describing actual experimental data.

The approach used in this thesis follows the general concept proposed by Reese and Govindjee [214] and Middendorf [180] using an additive split of the energy into equilibrium and non-equilibrium parts, utilizing the multiplicative decomposition of the deformation gradient Lubliner [176], and the concept of Dual Variables [126]. The evolution equation follows the approach using internal variables [58, 175], considering viscosity formulations similar to that presented by Sedlan and Haupt [236], Lion [171]. Like the approach for the linear viscoelasticity, finite viscoelasticity is derived from the Clausius Duhem inequality, which, for the reference configuration, results in:

$$\mathbf{T} : \dot{\mathbf{E}} - \dot{\Psi} \geq 0 \tag{2.91}$$

Since a description in the Total Lagrangian formulation has some advantages for the later implementation in an FE code, the model is derived below concerning the reference configuration. The free energy per unit volume is first divided into an isochoric and a volumetric component to describe the material as generally as possible:

$$\Psi = \Psi_{iso} + \Psi_{vol} \tag{2.92}$$

Furthermore, the energy is split up into a part that is within the thermodynamical equilibrium $(\,)^{\infty}$ and a part that is not within the thermodynamical equilibrium $(\,)^{ov}$. Finally, the isochoric part of the Helmholtz free Energy reads:

$$\Psi_{iso} = \Psi_{iso}^{\infty}(\mathbf{E}) + \Psi_{iso}^{ov}(\hat{\mathbf{\Gamma}}_{el}) \tag{2.93}$$

$$\Psi_{vol} = \Psi_{vol}^{\infty}(\mathbf{E}) + \Psi_{vol}^{ov}(\hat{\mathbf{\Gamma}}_{el}) \tag{2.94}$$

To follow the kinematics of linear viscoelasticity, which performs an additive splitting of the strain into elastic and inelastic components, a multiplicative splitting of the deformation gradient is required for large deformations. This multiplicative division leads to a fictitious, stress-free

intermediate configuration [25]. In this configuration, an additive split of the distortions into elastic and inelastic components is possible.

$$\hat{\mathbf{\Gamma}} = \frac{1}{2}\Big(\mathbf{F}_{el}^{T}\mathbf{F}_{el} - \mathbf{F}_{in}^{-T}\mathbf{F}_{in}^{-1}\Big) = \hat{\mathbf{\Gamma}}_{el} + \hat{\mathbf{\Gamma}}_{in} \tag{2.95}$$

Therefore, the evolution equation, which follows the dissipation inequality, must be formulated on this intermediate configuration. Nevertheless, the equilibrium parts of the energy (cf. Eq. 2.93) are defined on the reference configuration, which results in an inadmissible description of different configurations. The total formulation must, therefore, first be transformed into the intermediate configuration. The kinematics follows the concept of dual variables [126].

2.2.7.1. Transformation to the Intermediate Configuration

To maintain objectivity, when transforming the formulation of the Clausius Duhem inequality to an intermediate configuration, the strain rate tensor must be expressed in terms of an Oldroyd derivative. The respective equation yields:

$$\hat{\mathbf{T}} : \overset{\vartriangle}{\hat{\mathbf{\Gamma}}} - \dot{\hat{\Psi}} \geq 0 \tag{2.96}$$

Using the derivation rules

$$\frac{d}{dt}\Psi(\mathbf{E}) = \frac{\partial \Psi}{\partial \mathbf{E}} : \frac{d}{dt}\mathbf{E}, \qquad \frac{d}{dt}\Psi(\hat{\mathbf{\Gamma}}_{el}) = \frac{\partial \Psi}{\partial \hat{\mathbf{\Gamma}}_{el}} : \frac{d}{dt}\hat{\mathbf{\Gamma}}_{el},$$

and the relations presented in Fig. 2.3 to 2.5 yields the following expression for the Clausius Duhem inequality on the intermediate configuration:

$$\hat{\mathbf{T}} : \overset{\vartriangle}{\hat{\mathbf{\Gamma}}} - \mathbf{F}_{in}\frac{\partial \Psi_{iso}^{\infty}(\mathbf{E})}{\partial \mathbf{E}}\mathbf{F}_{in}^{T} : \overset{\vartriangle}{\hat{\mathbf{\Gamma}}} - \mathbf{F}_{in}\frac{\partial \Psi_{vol}^{\infty}(\mathbf{E})}{\partial \mathbf{E}}\mathbf{F}_{in}^{T} : \overset{\vartriangle}{\hat{\mathbf{\Gamma}}} - \frac{\partial \hat{\Psi}_{iso}^{ov}(\hat{\mathbf{\Gamma}}_{el})}{\partial \hat{\mathbf{\Gamma}}_{el}} : \dot{\hat{\mathbf{\Gamma}}}_{el} - \frac{\partial \hat{\Psi}_{vol}^{ov}(\hat{\mathbf{\Gamma}}_{el})}{\partial \hat{\mathbf{\Gamma}}_{el}} : \dot{\hat{\mathbf{\Gamma}}}_{el} \geq 0 \tag{2.97}$$

Eq. 2.97 can be skilfully sorted by reformulating the elastic part of the distortion rate defined on the intermediate configuration as follows:

$$\begin{aligned}
\dot{\hat{\mathbf{\Gamma}}}_{el} &= \dot{\hat{\mathbf{\Gamma}}} - \dot{\hat{\mathbf{\Gamma}}}_{in} = \overset{\vartriangle}{\hat{\mathbf{\Gamma}}} - \hat{\mathbf{L}}_{in}^{T}\hat{\mathbf{\Gamma}} - \hat{\mathbf{\Gamma}}\hat{\mathbf{L}}_{in} - \hat{\mathbf{D}}_{in} + \hat{\mathbf{L}}_{in}^{T}\hat{\mathbf{\Gamma}}_{in} + \hat{\mathbf{\Gamma}}_{in}\hat{\mathbf{L}}_{in} = \overset{\vartriangle}{\hat{\mathbf{\Gamma}}} - \hat{\mathbf{L}}_{in}^{T}(\hat{\mathbf{\Gamma}} - \hat{\mathbf{\Gamma}}_{in}) - (\hat{\mathbf{\Gamma}} - \hat{\mathbf{\Gamma}}_{in})\hat{\mathbf{L}}_{in} - \\
&\quad - \hat{\mathbf{D}}_{in} = \overset{\vartriangle}{\hat{\mathbf{\Gamma}}} - \hat{\mathbf{L}}_{in}^{T}\hat{\mathbf{\Gamma}}_{el} - \hat{\mathbf{\Gamma}}_{el}\hat{\mathbf{L}}_{in} - \hat{\mathbf{D}}_{in} = \overset{\vartriangle}{\hat{\mathbf{\Gamma}}} - \hat{\mathbf{L}}_{in}^{T}\frac{1}{2}(\hat{\mathbf{C}}_{el} - \mathbf{I}) - \frac{1}{2}(\hat{\mathbf{C}}_{el} - \mathbf{I})\hat{\mathbf{L}}_{in} - \hat{\mathbf{D}}_{in} = \\
&\quad = \overset{\vartriangle}{\hat{\mathbf{\Gamma}}} - \frac{1}{2}\hat{\mathbf{L}}_{in}^{T}\hat{\mathbf{C}}_{el} + \frac{1}{2}\hat{\mathbf{L}}_{in}^{T} - \frac{1}{2}\hat{\mathbf{C}}_{el}\hat{\mathbf{L}}_{in} + \frac{1}{2}\hat{\mathbf{L}}_{in} - \hat{\mathbf{D}}_{in} = \overset{\vartriangle}{\hat{\mathbf{\Gamma}}} - \frac{1}{2}\hat{\mathbf{L}}_{in}^{T}\hat{\mathbf{C}}_{el} - \frac{1}{2}\hat{\mathbf{C}}_{el}\hat{\mathbf{L}}_{in} + \hat{\mathbf{D}}_{in} - \hat{\mathbf{D}}_{in} = \\
&\quad = \overset{\vartriangle}{\hat{\mathbf{\Gamma}}} - \frac{1}{2}\hat{\mathbf{L}}_{in}^{T}\hat{\mathbf{C}}_{el} - \frac{1}{2}\hat{\mathbf{C}}_{el}\hat{\mathbf{L}}_{in}
\end{aligned}$$

Replacing the elastic deformation rate tensor $\dot{\hat{\mathbf{\Gamma}}}_{el}$ by the corresponding formulation $(\overset{\vartriangle}{\hat{\mathbf{\Gamma}}} - \frac{1}{2}\hat{\mathbf{L}}_{in}^{T}\hat{\mathbf{C}}_{el} - \frac{1}{2}\hat{\mathbf{C}}_{el}\hat{\mathbf{L}}_{in})$ leads to the following expression of the Clausius Duhem inequality:

$$\begin{aligned}
&\left(\hat{\mathbf{T}} - \mathbf{F}_{in}\frac{\partial \Psi_{iso}^{\infty}(\mathbf{E})}{\partial \mathbf{E}}\mathbf{F}_{in}^{T} - \mathbf{F}_{in}\frac{\partial \Psi_{vol}^{\infty}(\mathbf{E})}{\partial \mathbf{E}}\mathbf{F}_{in}^{T} - \frac{\partial \hat{\Psi}_{iso}^{ov}(\hat{\mathbf{\Gamma}}_{el})}{\partial \hat{\mathbf{\Gamma}}_{el}} - \frac{\partial \hat{\Psi}_{vol}^{ov}(\hat{\mathbf{\Gamma}}_{el})}{\partial \hat{\mathbf{\Gamma}}_{el}}\right) : \overset{\vartriangle}{\hat{\mathbf{\Gamma}}} + \\
&\quad + \frac{1}{2}\frac{\partial \hat{\Psi}_{iso}^{ov}(\hat{\mathbf{\Gamma}}_{el})}{\partial \hat{\mathbf{\Gamma}}_{el}} : \left(\hat{\mathbf{L}}_{in}^{T}\hat{\mathbf{C}}_{el} + \hat{\mathbf{C}}_{el}\hat{\mathbf{L}}_{in}\right) + \frac{1}{2}\frac{\partial \hat{\Psi}_{vol}^{ov}(\hat{\mathbf{\Gamma}}_{el})}{\partial \hat{\mathbf{\Gamma}}_{el}} : \left(\hat{\mathbf{L}}_{in}^{T}\hat{\mathbf{C}}_{el} + \hat{\mathbf{C}}_{el}\hat{\mathbf{L}}_{in}\right) \geq 0
\end{aligned} \tag{2.98}$$

Considering only the isochoric part of the free energy per unit volume for the overstress and using $\mathbf{A} : \mathbf{B} = Sp(\mathbf{A}^T\mathbf{B})$ leads to:

$$\frac{\partial \hat{\Psi}^{ov}_{iso}(\hat{\mathbf{\Gamma}}_{el})}{\partial \hat{\mathbf{\Gamma}}_{el}} : \left(\hat{\mathbf{L}}^T_{in}\hat{\mathbf{C}}_{el} + \hat{\mathbf{C}}_{el}\hat{\mathbf{L}}_{in} \right) = Sp\left(\frac{\partial \hat{\Psi}^{ov}_{iso}(\hat{\mathbf{\Gamma}}_{el})}{\partial \hat{\mathbf{\Gamma}}_{el}} \hat{\mathbf{L}}^T_{in}\hat{\mathbf{C}}_{el} + \frac{\partial \hat{\Psi}^{ov}_{iso}(\hat{\mathbf{\Gamma}}_{el})}{\partial \hat{\mathbf{\Gamma}}_{el}} \hat{\mathbf{C}}_{el}\hat{\mathbf{L}}_{in} \right) \tag{2.99}$$

Using $Sp(\mathbf{AB}) = Sp(\mathbf{BA})$, Eq. 2.99 results in:

$$Sp\left(\frac{\partial \hat{\Psi}^{ov}_{iso}(\hat{\mathbf{\Gamma}}_{el})}{\partial \hat{\mathbf{\Gamma}}_{el}} \hat{\mathbf{L}}^T_{in}\hat{\mathbf{C}}_{el} + \frac{\partial \hat{\Psi}^{ov}_{iso}(\hat{\mathbf{\Gamma}}_{el})}{\partial \hat{\mathbf{\Gamma}}_{el}} \hat{\mathbf{C}}_{el}\hat{\mathbf{L}}_{in} \right) = Sp\left(\hat{\mathbf{C}}_{el} \frac{\partial \hat{\Psi}^{ov}_{iso}(\hat{\mathbf{\Gamma}}_{el})}{\partial \hat{\mathbf{\Gamma}}_{el}} \hat{\mathbf{L}}^T_{in} + \frac{\partial \hat{\Psi}^{ov}_{iso}(\hat{\mathbf{\Gamma}}_{el})}{\partial \hat{\mathbf{\Gamma}}_{el}} \hat{\mathbf{C}}_{el}\hat{\mathbf{L}}_{in} \right) \tag{2.100}$$

Under the assumption that $\hat{\Psi}^{ov}_{iso}(\mathrm{I}_{\hat{\boldsymbol{C}}_{el}}, \mathrm{II}_{\hat{\boldsymbol{C}}_{el}}, \mathrm{III}_{\hat{\boldsymbol{C}}_{el}})$ is an isotropic tensor function which only depends on the invariants of $\hat{\mathbf{C}}_{el}$ (with $\hat{\mathbf{C}}_{el} = \hat{\mathbf{\Gamma}}_{el}$), the derivative of the isochoric part of the free energy per unit volume for the overstress can be expressed as:

$$\frac{\partial \hat{\Psi}^{ov}_{iso}(\hat{\mathbf{\Gamma}}_{el})}{\partial \hat{\mathbf{\Gamma}}_{el}} = \alpha(...)\mathbf{1} + \beta(...)\hat{\mathbf{C}}_{el} + \gamma(...)\hat{\mathbf{C}}^2_{el} + ... + \omega(...)\hat{\mathbf{C}}^n_{el} \tag{2.101}$$

By means of Eq. 2.101, the following relation can be established

$$\hat{\mathbf{C}}_{el} \frac{\partial \hat{\Psi}^{ov}_{iso}(\hat{\mathbf{\Gamma}}_{el})}{\partial \hat{\mathbf{\Gamma}}_{el}} = \frac{\partial \hat{\Psi}^{ov}_{iso}(\hat{\mathbf{\Gamma}}_{el})}{\partial \hat{\mathbf{\Gamma}}_{el}} \hat{\mathbf{C}}_{el} \tag{2.102}$$

and Eq. 2.100 can be rearranged to

$$\begin{aligned} &Sp\left(\hat{\mathbf{C}}_{el} \frac{\partial \hat{\Psi}^{ov}_{iso}(\hat{\mathbf{\Gamma}}_{el})}{\partial \hat{\mathbf{\Gamma}}_{el}} \hat{\mathbf{L}}^T_{in} + \frac{\partial \hat{\Psi}^{ov}_{iso}(\hat{\mathbf{\Gamma}}_{el})}{\partial \hat{\mathbf{\Gamma}}_{el}} \hat{\mathbf{C}}_{el}\hat{\mathbf{L}}_{in} \right) = \hat{\mathbf{C}}_{el} \frac{\partial \hat{\Psi}^{ov}_{iso}(\hat{\mathbf{\Gamma}}_{el})}{\partial \hat{\mathbf{\Gamma}}_{el}} : \left(\hat{\mathbf{L}}^T_{in} + \hat{\mathbf{L}}_{in} \right) = \\ &2\hat{\mathbf{C}}_{el} \frac{\partial \hat{\Psi}^{ov}_{iso}(\hat{\mathbf{\Gamma}}_{el})}{\partial \hat{\mathbf{\Gamma}}_{el}} : \hat{\mathbf{D}}_{in} \end{aligned} \tag{2.103}$$

As the same relations hold. for the volumetric part of the free energy per unit volume for the overstress, the total formulation of the Clausius Duhem inequality yields:

$$\begin{aligned} &\left(\hat{\mathbf{T}} - \mathbf{F}_{in} \frac{\partial \Psi^{\infty}_{iso}(\mathbf{E})}{\partial \mathbf{E}} \mathbf{F}^T_{in} - \mathbf{F}_{in} \frac{\partial \Psi^{\infty}_{vol}(\mathbf{E})}{\partial \mathbf{E}} \mathbf{F}^T_{in} - \frac{\partial \hat{\Psi}^{ov}_{iso}(\hat{\mathbf{\Gamma}}_{el})}{\partial \hat{\mathbf{\Gamma}}_{el}} - \frac{\partial \hat{\Psi}^{ov}_{vol}(\hat{\mathbf{\Gamma}}_{el})}{\partial \hat{\mathbf{\Gamma}}_{el}} \right) : \overset{\Delta}{\hat{\mathbf{\Gamma}}} + \\ &+ \hat{\mathbf{C}}_{el} \left(\frac{\partial \hat{\Psi}^{ov}_{iso}(\hat{\mathbf{\Gamma}}_{el})}{\partial \hat{\mathbf{\Gamma}}_{el}} + \frac{\partial \hat{\Psi}^{ov}_{vol}(\hat{\mathbf{\Gamma}}_{el})}{\partial \hat{\mathbf{\Gamma}}_{el}} \right) : \hat{\mathbf{D}}_{in} \geq 0 \end{aligned} \tag{2.104}$$

Since the variables $\overset{\Delta}{\hat{\mathbf{\Gamma}}}$ and $\hat{\mathbf{D}}_{in}$ are independent of each other, Eq. 2.104 is fulfilled, if the first term in brackets is zero, and if the second part is guaranteed to be greater than zero. Setting the first bracket of 2.104 equal to zero leads to the formulation of the stress:

$$\hat{\mathbf{T}} = \mathbf{F}_{in} \frac{\partial \Psi^{\infty}_{iso}(\mathbf{E})}{\partial \mathbf{E}} \mathbf{F}^T_{in} + \mathbf{F}_{in} \frac{\partial \Psi^{\infty}_{vol}(\mathbf{E})}{\partial \mathbf{E}} \mathbf{F}^T_{in} + \frac{\partial \hat{\Psi}^{ov}_{iso}(\hat{\mathbf{\Gamma}}_{el})}{\partial \hat{\mathbf{\Gamma}}_{el}} + \frac{\partial \hat{\Psi}^{ov}_{vol}(\hat{\mathbf{\Gamma}}_{el})}{\partial \hat{\mathbf{\Gamma}}_{el}} \tag{2.105}$$

The second part of Eq. 2.104 must be greater than or equal to zero and thus leads to the dissipation inequality:

$$\hat{\mathbf{C}}_{el} \left(\frac{\partial \hat{\Psi}^{ov}_{iso}(\hat{\mathbf{\Gamma}}_{el})}{\partial \hat{\mathbf{\Gamma}}_{el}} + \frac{\partial \hat{\Psi}^{ov}_{vol}(\hat{\mathbf{\Gamma}}_{el})}{\partial \hat{\mathbf{\Gamma}}_{el}} \right) : \hat{\mathbf{D}}_{in} = \hat{\mathbf{C}}_{el}\hat{\mathbf{T}}^{ov} : \hat{\mathbf{D}}_{in} \geq 0 \tag{2.106}$$

The easiest way to fulfill this inequality is to transform it into a quadratic form by equating $\hat{\mathbf{D}}_{in}$ with a multiple of $\hat{\mathbf{C}}_{el}\hat{\mathbf{T}}^{ov}$. With the proportionality factor η, which must always be positive, the dissipation inequality thus results in:

$$\hat{\mathbf{D}}_{in} = \frac{1}{\eta}\hat{\mathbf{C}}_{el}\hat{\mathbf{T}}^{ov} \tag{2.107}$$

The factor η can depend on the thermomechanical process history and must be greater than zero. Its dimension is stress times time and it can be interpreted as a viscosity function (unit: [MPa·s]).

2.2.7.2. Transformation to the Reference Configuration

To obtain the desired total Lagrange formulation, Eq. 2.105 and 2.107 must be transformed back to the reference configuration. In this operation, the transformation rules of the concept of dual variables are applied again. Due to the formulations depending on the co- and contravariant basis systems, the transformation rules for stress and deformation rate are different (compare push forward and pull back operations in Sec. 2.1.1.1). The Olydroyd deformation rate, defined in the intermediate configuration, is considerably simplified in the reference configuration. The stress on the reference configuration results in the following:

$$\mathbf{T} = \mathbf{F}_{in}^{-1}\hat{\mathbf{T}}\mathbf{F}_{in}^{-T} = \frac{\partial\hat{\Psi}_{iso}^{\infty}(\mathbf{E})}{\partial\mathbf{E}} + \mathbf{F}_{in}^{-1}\frac{\partial\hat{\Psi}_{iso}^{ov}(\hat{\mathbf{\Gamma}}_{el})}{\partial\hat{\mathbf{\Gamma}}_{el}}\mathbf{F}_{in}^{-T} + \frac{\partial\hat{\Psi}_{vol}^{\infty}(\mathbf{E})}{\partial\mathbf{E}} + \mathbf{F}_{in}^{-1}\frac{\partial\hat{\Psi}_{vol}^{ov}(\hat{\mathbf{\Gamma}}_{el})}{\partial\hat{\mathbf{\Gamma}}_{el}}\mathbf{F}_{in}^{-T} \tag{2.108}$$

Using $\mathbf{F}_{in}^{T}\hat{\mathbf{D}}_{in}\mathbf{F}_{in} = \mathbf{F}_{in}^{T}\overset{\triangle}{\hat{\mathbf{\Gamma}}}_{in}\mathbf{F}_{in} = \frac{1}{2}\dot{\mathbf{C}}_{in}$, reduces the Oldroyd derivative of the inelastic stretch tensor, holding for the intermediate configuration, to an ordinary time-derivative, Eq. 2.107 yields:

$$\dot{\mathbf{C}}_{in} = 2\mathbf{F}_{in}^{T}\hat{\mathbf{D}}_{in}\mathbf{F}_{in} = \frac{2}{\eta}\mathbf{F}_{in}^{T}\hat{\mathbf{C}}_{el}\hat{\mathbf{T}}^{ov}\mathbf{F}_{in} = \frac{2}{\eta}\left(\mathbf{F}_{in}^{T}\mathbf{F}_{el}^{T}\mathbf{F}_{el}\mathbf{F}_{in}\right)\left(\mathbf{F}_{in}^{-1}\hat{\mathbf{T}}^{ov}\mathbf{F}_{in}^{-T}\right)\left(\mathbf{F}_{in}^{T}\mathbf{F}_{in}\right) = \frac{2}{\eta}\mathbf{C}\mathbf{T}^{ov}\mathbf{C}_{in} \tag{2.109}$$

The overstress $\mathbf{T}^{ov}$ yields $\mathbf{T}^{ov} = \mathbf{F}_{in}^{-1}\frac{\partial\hat{\Psi}_{iso}^{ov}(\hat{\mathbf{\Gamma}}_{el})}{\partial\hat{\mathbf{\Gamma}}_{el}}\mathbf{F}_{in}^{-T} + \mathbf{F}_{in}^{-1}\frac{\partial\hat{\Psi}_{vol}^{ov}(\hat{\mathbf{\Gamma}}_{el})}{\partial\hat{\mathbf{\Gamma}}_{el}}\mathbf{F}_{in}^{-T}$.

2.2.7.3. Invariant Expression

Since $\hat{\Psi}_{iso}^{ov}(\hat{\mathbf{\Gamma}}_{el})$, $\hat{\Psi}_{vol}^{ov}(\hat{\mathbf{\Gamma}}_{el})$, $\Psi_{iso}^{\infty}(\mathbf{E})$ and $\Psi_{vol}^{\infty}(\mathbf{E})$ are isotropic tensor functions, they can be represented in terms of the invariants of the right Cauchy Green tensor $\mathbf{C}$ and the elastic Cauchy Green tensor $\hat{\mathbf{C}}_{el}$. This thesis solely considers energy potentials that depend on the first invariant, which leads to the following expression of the total stress.

$$\mathbf{T} = 2\frac{\partial\Psi_{iso}^{\infty}(\mathrm{I}_{\bar{\mathbf{C}}})}{\partial\mathbf{C}} + 2\frac{\partial\Psi_{vol}^{\infty}(J)}{\partial\mathbf{C}} + 2\mathbf{F}_{in}^{-1}\frac{\partial\hat{\Psi}_{iso}^{ov}(\mathrm{I}_{\hat{\bar{\mathbf{C}}}_{el}})}{\partial\hat{\mathbf{C}}_{el}}\mathbf{F}_{in}^{-T} + 2\mathbf{F}_{in}^{-1}\frac{\partial\hat{\Psi}_{vol}^{ov}(\hat{J}_{el})}{\partial\hat{\mathbf{C}}_{el}}\mathbf{F}_{in}^{-T} \tag{2.110}$$

The corresponding formulation of the evolution equation yields:

$$\dot{\mathbf{C}}_{in} = \frac{2}{\eta}\mathbf{C}\left(\mathbf{F}_{in}^{-1}\frac{\partial\hat{\Psi}_{iso}^{ov}(\mathrm{I}_{\hat{\bar{\mathbf{C}}}_{el}})}{\partial\hat{\mathbf{C}}_{el}}\mathbf{F}_{in}^{-T} + \mathbf{F}_{in}^{-1}\frac{\partial\hat{\Psi}_{vol}^{ov}(\hat{J}_{el})}{\partial\hat{\mathbf{C}}_{el}}\mathbf{F}_{in}^{-T}\right)\mathbf{C}_{in} \tag{2.111}$$

To carry out the derivative of the energy potentials with respect to the invariants, the following relations are used [241]:

$$\frac{\partial\Psi_{iso}(\mathrm{I}_{\bar{\mathbf{C}}})}{\partial\mathbf{C}} = \frac{\partial\Psi_{iso}(\mathrm{I}_{\bar{\mathbf{C}}})}{\partial\mathrm{I}_{\bar{\mathbf{C}}}}\frac{\partial\mathrm{I}_{\bar{\mathbf{C}}}}{\partial\bar{\mathbf{C}}} : \frac{\partial\bar{\mathbf{C}}}{\partial\mathbf{C}} \tag{2.112}$$

$$\frac{\partial \Psi_{vol}(J)}{\partial \mathbf{C}} = \frac{\partial \Psi_{vol}(J)}{\partial J}\frac{\partial J}{\partial \mathbf{C}} \tag{2.113}$$

Following Miehe [181] and Simo and Hughes [241], the directional derivative (Gateaux derivative) of the right Cauchy Green tensor with respect to its isochoric part yields:

$$\frac{\partial \bar{\mathbf{C}}}{\partial \mathbf{C}} = J^{-2/3}\Big[\mathbb{1} - \frac{1}{3}\mathbf{C}\otimes\mathbf{C}^{-1}\Big] \tag{2.114}$$

The derivatives of the invariatants of the right Cauchy Green tensor with respect to the right Cauchy Green tensor, yield [131, 241, 48]:

$$\frac{\partial \mathrm{I}_{\mathbf{C}}}{\partial \mathbf{C}} = \mathbf{1} \tag{2.115}$$

$$\frac{\partial \mathrm{II}_{\mathbf{C}}}{\partial \mathbf{C}} = \mathrm{I}_{\mathbf{C}}\mathbf{1} - \mathbf{C} \tag{2.116}$$

$$\frac{\partial \mathrm{III}_{\mathbf{C}}}{\partial \mathbf{C}} = \mathrm{III}_{\mathbf{C}}\mathbf{C}^{-1} \tag{2.117}$$

$$\frac{\partial J}{\partial \mathbf{C}} = \frac{J}{2}\mathbf{C}^{-1} \tag{2.118}$$

Applying Eq. 2.112, 2.113, 2.114, and the derivatives of the invariants to Eq. 2.110, and 2.111, yields:

$$\begin{aligned}\mathbf{T} = {} & 2J^{-2/3}\frac{\partial \Psi^{\infty}_{iso}(\mathrm{I}_{\bar{\mathbf{C}}})}{\partial \mathrm{I}_{\bar{\mathbf{C}}}}\Big[\mathbf{1} - \frac{1}{3}\Big(\mathbf{C}:\mathbf{1}\Big)\mathbf{C}^{-1}\Big] + 2\hat{J}_{el}^{-2/3}\frac{\partial \hat{\Psi}^{ov}_{iso}(\mathrm{I}_{\hat{\bar{\mathbf{C}}}_{el}})}{\partial \mathrm{I}_{\hat{\bar{\mathbf{C}}}_{el}}}\Big[\mathbf{C}_{in}^{-1} - \frac{1}{3}\Big(\mathbf{C}:\mathbf{C}_{in}^{-1}\Big)\mathbf{C}^{-1}\Big] + \\ & + \Big[\frac{\partial \Psi^{\infty}_{vol}(J)}{\partial J}J + \frac{\partial \hat{\Psi}^{ov}_{vol}(\hat{J}_{el})}{\partial \hat{J}_{el}}\hat{J}_{el}\Big]\mathbf{C}^{-1}\end{aligned} \tag{2.119}$$

Here, $(\mathbf{C}:\mathbf{1}) = \mathrm{I}_{\mathbf{C}}$, and $(\mathbf{C}:\mathbf{C}_{in}^{-1}) = \mathrm{I}_{\hat{\mathbf{C}}_{el}}$. When introducing a volumetric and deviatoric split for the flow rule and thus dividing the viscosity into shape-changing and volume-changing components, it remains essential to uphold the dissipation inequality. Following the approach of Justine [149], a proportionality between the volumetric part, denoted as η_V, and the deviatoric part, represented by η_D, is assumed. It is crucial to note that this relationship between them must always be positive.

$$\dot{\mathbf{C}}_{in} = \frac{4}{\eta_D}\hat{J}_{el}^{-2/3}\frac{\partial \hat{\Psi}^{ov}_{iso}(\mathrm{I}_{\hat{\bar{\mathbf{C}}}_{el}})}{\partial \mathrm{I}_{\hat{\bar{\mathbf{C}}}_{el}}}\Big[\mathbf{C} - \frac{1}{3}\Big(\mathbf{C}:\mathbf{C}_{in}^{-1}\Big)\mathbf{C}_{in}\Big] + \frac{2}{\eta_V}\hat{J}_{el}\Big[\frac{\partial \hat{\Psi}^{ov}_{vol}(\hat{J}_{el})}{\partial J_{el}}\Big]\mathbf{C}_{in} \tag{2.120}$$

The viscosities must follow the relation $\eta_V = \alpha\eta_D$ with $\alpha > 0$ (cf. Justine [149]).

2.2.7.4. Temperature Expansion

In the context of isothermal processes, it becomes essential to account for temperature-related effects primarily through the viscosity function and the deformation gradient. To establish a consistent framework, considering deformations due to temperature, the deformation gradient is partitioned into a mechanical segment and a thermal counterpart (Lion [171]):

$$\mathbf{F} = \mathbf{F}_{\theta}\mathbf{F}_{M} \tag{2.121}$$

The derivation of the mechanical stretch tensor stems from the mechanical part of the deformation gradient, as elucidated by the following equation:

$$\mathbf{C}_M = \mathbf{F}_M^T \mathbf{F}_M \tag{2.122}$$

The thermal component is computed in advance, guided by a priori considerations, while the mechanical part is subsequently substituted.

$$\mathbf{T}_M = 2J_M^{-2/3} \frac{\partial \Psi_{iso}^{\infty}(\mathrm{I}_{\bar{\mathbf{C}}})}{\partial \mathrm{I}_{\bar{\mathbf{C}}}} \Big[\mathbf{1} - \frac{1}{3}\Big(\mathbf{C}_M : \mathbf{1}\Big)\mathbf{C}_M^{-1}\Big] + 2\hat{J}_{el}^{-2/3} \frac{\partial \hat{\Psi}_{iso}^{ov}(\mathrm{I}_{\hat{\bar{\mathbf{C}}}_{el}})}{\partial \mathrm{I}_{\hat{\bar{\mathbf{C}}}_{el}}} \Big[\mathbf{C}_{in}^{-1} - \frac{1}{3}\Big(\mathbf{C}_M : \mathbf{C}_{in}^{-1}\Big)\mathbf{C}_M^{-1}\Big] +$$
$$+ \Big[\frac{\partial \Psi_{vol}^{\infty}(J_M)}{\partial J_M} J_M + \frac{\partial \hat{\Psi}_{vol}^{ov}(\hat{J}_{el})}{\partial \hat{J}_{el}} \hat{J}_{el}\Big] \mathbf{C}_M^{-1} \tag{2.123}$$

The extension of the evolution equation to encompass thermal processes yields a comprehensive representation of the system's behavior in response to different, constant temperatures.

$$\dot{\mathbf{C}}_{in} = \frac{4}{\eta_D} \hat{J}_{el}^{-2/3} \frac{\partial \hat{\Psi}_{iso}^{ov}(\mathrm{I}_{\hat{\bar{\mathbf{C}}}_{el}})}{\partial \mathrm{I}_{\hat{\bar{\mathbf{C}}}_{el}}} \Big[\mathbf{C}_M - \frac{1}{3}\Big(\mathbf{C}_M : \mathbf{C}_{in}^{-1}\Big)\mathbf{C}_{in}\Big] + \frac{2}{\eta_V} \Big[\frac{\partial \hat{\Psi}_{vol}^{ov}(\hat{J}_{el})}{\partial \hat{J}_{el}} \hat{J}_{el}\Big] \mathbf{C}_{in} \tag{2.124}$$

2.3. Numerical Modeling

The theory of viscoelasticity is guided by time-dependent material behavior, which is described mathematically utilizing differential equations. In addition to analytical approaches that lead to an explicit solution, numerical methods for solving these differential equations approximate the solution by specifying functional values at specific points. An exact, explicit solution is sometimes very time-consuming and not always possible. Numerical solution methods are, therefore, generally used to solve time-dependent material equations in the context of structural mechanics.

A method recommended by Middendorf [180], Scheffer [225] for solving models of finite viscoelasticity is the implicit Euler method. This method is used for the numerical integration of the material equations in this work. Furthermore, Newton's method, based on the linear evolution of a Taylor series, is utilized to solve the equations for each iteration step. Together, these methods represent a powerful tool for solving differential equations in the context of material modeling.

Another problem in material modeling is determining the material parameters that minimize the error between model calculation and experiment. This parameter identification is a difficult task for models with many parameters, and within this thesis, it is solved using a global optimization algorithm.

2.3.1. Euler Backward Method

The Euler backward method is an implicit method for solving differential equations. In contrast to explicit methods that solve the individual approximations using an explicit formula from the approximation of the previous step, implicit methods don't use explicit formulas but relate the approximations of the individual steps by an equation. Compared to explicit methods, the advantage of implicit methods is the larger area of stability with the same accuracy. However, a further approximation method, such as the Newton method, is required to solve this equation in every step. The basic formulas and relations of the Euler backward method are presented

below. For more detailed information, the interested reader is referred to Butcher [37], Arens et al. [9].

Starting with the ordinary differential equation

$$\frac{dy}{dt} = f(t, y(t)) \tag{2.125}$$

where $y(t_0) = y_0$ holds and integrating Eq. 2.125 within the limits t_n to $t_{n+1} = t_n + h$, yields

$$y(t_{n+1}) - y(t_n) = \int_{t_n}^{t_{n+1}} f(t, y(t))dt, \tag{2.126}$$

wich can be approximately written as

$$y(t_{n+1}) - y(t_n) \approx hf(t_{n+1}, y(t_{n+1})). \tag{2.127}$$

Rearranging Eq. 2.127 and using the big O-notation, that represents the local truncation error $O(h^2)$, leads to

$$y(t_{n+1}) = y(t_n) + hf(t_{n+1}, y(t_{n+1})) + O(h^2). \tag{2.128}$$

Reordering Eq. 2.128 results in the following iteration-equation for the sequence of approximations y_n at t_n:

$$f(t_{n+1}, y_{n+1}) = \frac{y_{n+1} - y_n}{h} \tag{2.129}$$

Like the explicit Euler method ($y(t_{n+1}) - y(t_n) \approx hf(t_n, y(t_n))$), the implicit method has a convergence order of 1 but has a much larger stability region.

2.3.2. Taylor Series

The Taylor series aims to improve the approximation of a function through linearization using polynomials of a higher degree. Assume a polynomial with the properties

$$f^{(k)}(x_0) = p_n^{(k)}(x_0) \tag{2.130}$$

for the function value $k = 0$ and the derivatives, of order $k = 1, ..., n$ at the point x_0. Then, for an n-times continuously differentiable function f, a Taylor polynomial of degree n can be formed around the development point x_0 ($x \in \mathbb{R}$):

$$p_n(x) = \sum_{k=0}^{n} \frac{f^{(k)}(x_0)}{k!}(x - x_0)^k \tag{2.131}$$

For this Taylor polynomial and the function under consideration, the function value and derivatives match up to the developed degree n. $f^{(k)}(x_0) = p_n^{(k)}(x_0)$ to the development point x_0. To map the gradient of a function at a specific point, a development up to the first derivative, which corresponds to a series developed up to the linear element, is therefore sufficient.

$$p_1(x) = \frac{f^{(0)}(x_0)}{1}(x - x_0)^0 + \frac{f^{(1)}(x_0)}{1}(x - x_0)^1 = f(x_0) + f'(x_0)(x - x_0) \tag{2.132}$$

For further details the reader is referred to Arens et al. [9].

2.3.3. Newton's Method

The solution of an equation in real numbers, which can be summarized as a zero-point task $f(x) = 0$, is possible in closed form only in exceptional cases. In all other cases, the problem must be solved numerically. The most frequently used numerical method for solving non-linear equations is the Newton's method.

Using Eq. 2.132, which corresponds to a linearization of the function $f(x)$ around the point x_0, and transfering it to the zero point task, results in

$$f(x_0) + f'(x_0)(x - x_0) = 0. \tag{2.133}$$

Assuming that f' is different from zero, the following value x_1 results from the initial value x_0

$$x_1 = x_0 - \frac{f(x_0)}{f'(x_0)} \tag{2.134}$$

A repetition of this procedure leads to the recursive sequence

$$x^{k+1} = x^k - \frac{f(x^k)}{f'(x^k)}, \tag{2.135}$$

where $(\,)^k$ describes the preceding iteration step, $(\,)^{k+1}$ the following iteration step, and $n \in \mathbb{N}$ applies. This iteration procedure now approaches the solution step by step.

This method can solve the equation representing the approximations of the individual steps inside the implicit Euler method. Therefore, if this concept is transferred to the formulation of the Euler backward method, the residual $\Xi(y_{n+1})$ must first be set up, which for the Newton's method is treated like the function $f(x_n)$ in Eq. 2.133. First, Eq. 2.129 is converted accordingly:

$$\Xi(y_{n+1}) = y_{n+1} - y_n - hf(t_{n+1}, y_{n+1}) = 0 \tag{2.136}$$

The residual $\Xi(y_{n+1})$ can be approximated with a Taylor series expansion. Ξ is linearized around y^k_{n+1} cancelling the Taylor series after the linear element:

$$\Xi(y^{k+1}_{n+1}) \approx \Xi(y^k_{n+1}) + \frac{\partial \Xi(y^k_{n+1})}{\partial y^k_{n+1}} \left(y^{k+1}_{n+1} - y^k_{n+1} \right) = 0 \tag{2.137}$$

Applying Newton's method, Eq. 2.137 is rearranged in such a way that it equals the form of Eq. 2.133 while the function $f(x^k)$ is replaced by the residuum $\Xi(y^k_{n+1})$ and x^k by y^k_{n+1}. Finally, the following relationship holds for the solution of the implicit Euler method:

$$y^{k+1}_{n+1} = y^k_{n+1} - \frac{\Xi(y^k_{n+1})}{\frac{\partial \Xi(y^k_{n+1})}{\partial y^k_{n+1}}} \tag{2.138}$$

Subsequently, a small example determining the zeros of the function $f(x) = 5x^2 - 5$ is employed to illustrate the functionality of Newton's method. The zeros $[x_1, x_2] = \pm\sqrt{1}$ are obtained analytically. The following algorithm is implemented in Matlab:

```
1
2           x = [-4.5;4.5];
3           x_old = 10;
4
5           while abs(x_old-x) > 10^-5
6
7           R = 5*x^2-5;
8           dR = 10*x;
9
10          x_old = x;
11          x = x - (R)/(dR);
12
13          end
```

The letter R denotes the residual whose zeros are to be determined (in this case, it corresponds to the function), and dR denotes the analytical derivative of the residual or the function. In Fig. 2.11, the iterations of the algorithm are graphically illustrated. The algorithm begins with a user-specific starting point and calculates the residual value and its derivative at this point. A tangent is then formed at the point of the function, and its intersection with the zero line (function value equal to 0) is determined. This intersection point represents an update for the starting point. If this update differs from the starting point by an amount less than a previously defined tolerance limit (in this case, 10^{-5}), the algorithm is canceled. If the difference exceeds the tolerance, the algorithm continues until the value falls below the limit.

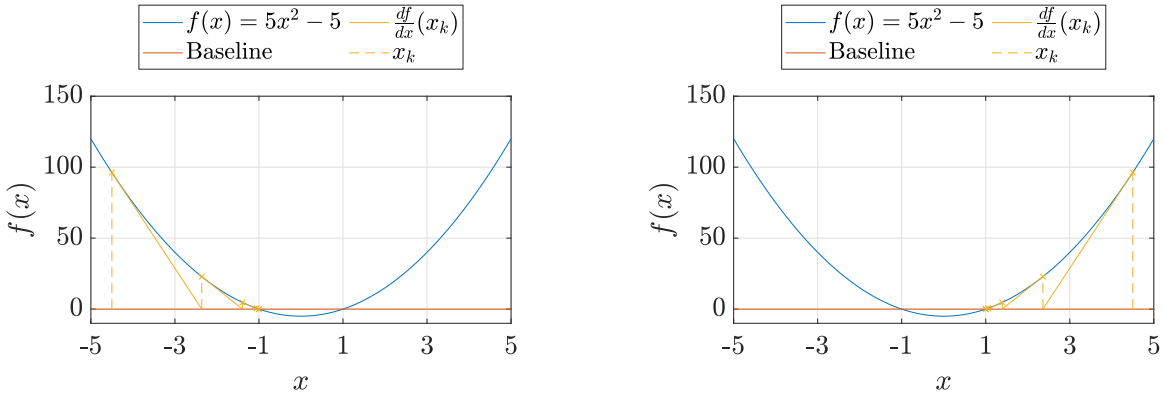

Figure 2.11.: Newton Raphson Algorithm; Starting Value -4.5 (left), 4.5 (right)

Fig. 2.11 shows the functionality of the algorithm for the function $f(x) = 5x^2 - 5$. The algorithm comes to the same solution as the analytical calculation. However, depending on the choice of the starting value, the algorithm converges to different solutions, while the accuracy of the solution depends on the chosen tolerance. However, the presented example is designed only for demonstration purposes and does not serve as the basis for a sound discussion of the algorithm's functionality. Nevertheless, it should be remembered that the algorithm's solutions strongly depend on the choice of the starting value.

2.4. Parameter Identification - Optimization

When modeling physical problems, the application problems are usually idealized, i.e. approximated using mathematical formulations. This approximation leads to systems with unknowns that can be equated with material parameters in material modeling. In order to be able to make the best possible selection of the corresponding parameters, it is necessary to formulate a so-called target function f, which depends on the unknowns x and evaluates the system by describing the error between measured variables and calculations. The search for the best possible combination of the unknowns x results in the mathematical problem of minimizing the function value $f(x)$ among all x. Taking into account the restrictions that the vector x of the unknowns is finite-dimensional and only a finite number of constraints have to be considered, the following non-linear minimization problem arises

$$
\begin{array}{lllll}
inf & f(x) & & & \\
x: & g_i(x) \leq 0 & for & i = 1, 2, ..., p \\
& g_j(x) = 0 & for & j = p+1, p+2, ..., m \\
& x \in \mathcal{B} &
\end{array}
$$

where for the index sets $I_1 = \{1, ..., p\}$ and $I_2 = \{p+1, ..., m\}$ with $0 \leq p \leq m < \infty$ and for the unknowns $x \in \mathbb{R}^n, \mathcal{B} \subset \mathbb{R}^{\setminus}$ [142] hold.

2.4.1. Global Optimization

For solving problems with multiple local minima, using global optimization algorithms incorporating local solvers is a prevalent approach [95]. With the *globalsearch* algorithm, the software *Matlab* provides a powerful tool for this purpose. It combines a heuristic search method and a local gradient-based solver incorporated in a multi-start procedure to achieve both advantages by avoiding their disadvantages. A multi-start procedure generally searches for a global solution by starting a local solver from multiple, uniformly distributed start points. Using the *globalsearch* algorithm decreases the number of potential starting points considerably by employing particular constraints. [258]

The heuristic search method is carried out by the *scattersearch* function, a metaheuristic algorithm that generates a population of starting points whose elements are maintained and updated from iteration to iteration. Deterministic combinations of previous members of the population generate new elements. [116]

2.4.2. Local Solver - fmincon

fmincon (function minimization under constraints) is a sophisticated optimization solver that employs a combination of optimization algorithms and constraint-handling techniques to efficiently find solutions to a given objective function under a set of equality and inequality constraints. It adapts its strategy based on the problem structure and user-defined options to achieve convergence to a feasible and optimal solution. There are several optimization algorithms that can be chosen. Within this work the interior point technique [38, 39, 262] is used.

2.5. Materials

This chapter provides a brief overview of the materials covered in the thesis, which aims to contribute to the description of laminated glass in its broken state. The individual components of LSG glass interlayer are first described individually, followed by a detailed analysis of the product laminated glass.
Solids can be divided into three material groups: metals, ceramics, and polymers. These groups can be characterized according to their way of connecting the atoms inside the material. Metals use metallic bonds, ceramics use ionic bonds, and polymers use covalent bonds [221]. These different bond types and the resulting different arrangements at the molecular level result in different material properties. Glass and polyvinyl butyral are polymers, which is why the third material group, the polymers, will be discussed in more detail in the following.

2.5.1. Polymers

Polymers can be characterized at different scales (compare Fig. 2.12). At the micro level, they consist of monomers formed from groups of atoms. At the meso level, they consist of molecular chains linked together by connecting the individual monomers via covalent bonds. At the macro level, they form branched structures of molecular chains linked via primary and or secondary bonds. The position and conformation of the polymer chains depend on the micro Brownian motion [234].

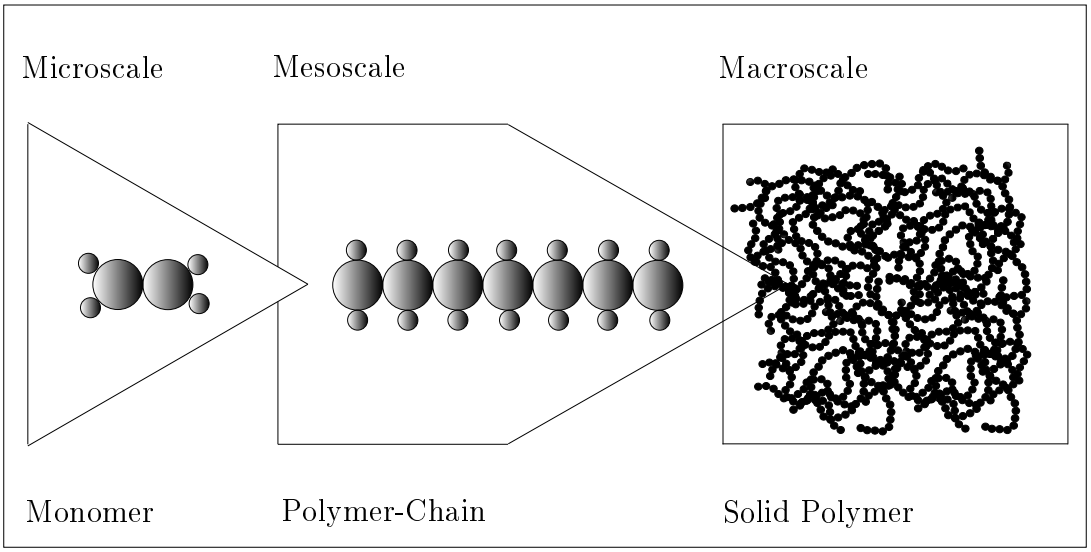

Figure 2.12.: Structure of a Polymer at different scales, after Bergström [24]

2.5.1.1. Syntheses of Polymers

The synthetic form of polymers is called polymerization and occurs when the monomers' functionality is at least two. It consists of polyaddition (free radical, ionic, coordination) and polycondensation [35]. In the case of an addition, growth occurs via addition reactions, and in the case of condensation, via condensation reactions in which one molecule is split off at a time. However, polycondensation usually proceeds as a step reaction and polyaddition as a chain reaction [215]. The step reaction consists of successive reactions between functional groups of the reactants. A reactive center initiates the chain reaction and entails a progressive propagation

that is terminated only after the destruction of the reactive center. The functionality of the monomers determines whether the polymer is crosslinked or not. Examples for the simulation of the synthetic form of polymers can be found in Mark [177].

2.5.1.2. Structures of Polymers

Polymers can be divided into the subgroups of crosslinked ones (elastomers or thermosets) and non-crosslinked ones (thermoplastics) [234, 24] (cf. Fig. 2.13), both having polymer chains with primary (covalent) bonds. The bonds between the individual polymer chains, on the other hand, are partly primary and partly secondary (van der Waals, hydrogen, dipoles) within the group of elastomers and thermosets, and exclusively secondary within the group of thermoplastics [35]. However, Elastomers have lower crosslinking than thermosets, resulting in fewer primary bonds. Crosslinked and non-cross-linked polymers can also be divided into amorphous and semi-crystalline according to their degree of crystallinity [234].

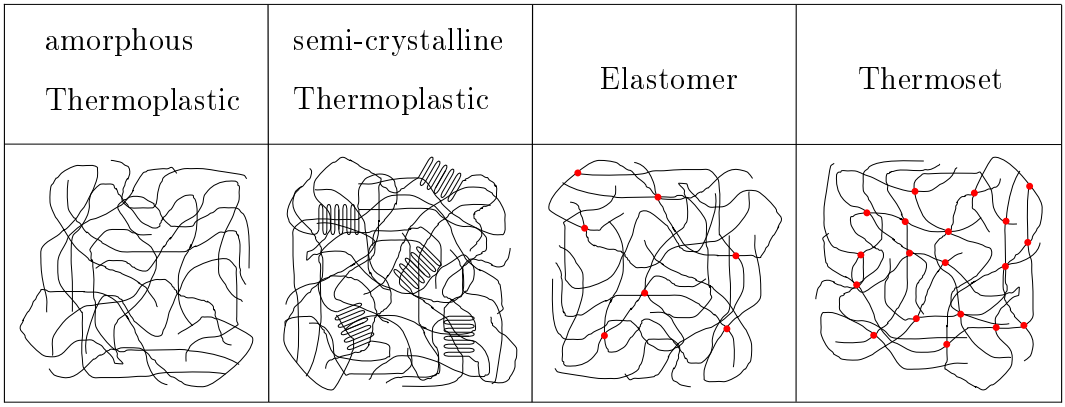

Figure 2.13.: Structures of Polymers, after Domininghaus [96]

2.5.1.3. Aggregate States of Polymers

The aggregate states are closely related to the glass transition, melting and flow temperatures, and the associated molecular mobility. The glass transition temperature T_g describes the transition from the entropy-elastic (rubber state) to the energy-elastic (glass state), the melting temperature T_m describes the melting of the crystalline phases, the flow temperature T_f describes the loosening of the entanglements of the macromolecules. The crystals are solid up to the melting temperature. The Mirko-Brownian motion thaws in the glass transition region and fully develops in the rubber and melt states. In contrast to amorphous polymers, semi-crystalline polymers exhibit individual relaxation processes coupled to the crystalline regions, each characterized by a decrease in stiffness. Furthermore, semi-crystalline polymers generally exhibit higher strengths. [234, 215, 177, 35].

2.5.2. Standard PVB

Standard PVB is the most commonly used material for LG interlayers. It consists of PVB resin (75 [%]), additives (<1 [%]), and plasticizers (25 [%]). The higher the proportion of plasticizer, the more the glass transition temperature is reduced. The material is created by chain polymerization of vinyl acetate, hydrolysis to polyvinyl alcohol, and acetalization with butyraldehyde. It has no crosslinks and is considered an amorphous thermoplastic. Like polymers in general, the stochastic arrangement of the polymer chains leads to isotropic material

behavior. Furthermore, above the glass transition temperature, it shows purely viscoelastic behavior.[159, 231]

The PVB used in this work is manufactured by the interlayer-company Kuraray and has the product-specific name Trosifol®UltraClear - B200NR. It shows isotropic [103, 231, 165], purely viscoelastic [165, 231] material behavior and is strongly time, temperature- [165, 103, 161] and even moisture-dependent [31]. Its glass-transition temperature is around 25 [°C] [165, 103, 162, 231], and within the glass transition region and above, it shows nearly incompressible behavior ($\nu \approx 0.47$ [-] at room temperature) [165], however, the values of the Poisson's ratio strongly depend on the temperature, taking on values from 0.4 [-] up to 0.49 [-] [231]. Dynamic Scanning Calorimetry (DSC) and DMTA tests showed that PVB is a rheological simple material [163]. The strain range, the linear viscoelastic theory can be applied in, is limited to 0.5 [%] in the energy-elastic and 35 [%] in the entropy-elastic range [230, 104, 233]. Beyond the linearity limits, the material behavior is governed by non-linear viscoelasticity [231]. Its elongation at breakage strongly depends on the strain rate and can achieve values from 210 [%] up to 300 [%], and the stress at breakage is 25 [MPa] [165]. Its properties are generally not influenced by the lamination process [103].

2.5.3. Glass

Nowadays, glass is mainly produced in the so-called float process. In this process, the raw materials quartz sand (60 [%]), lime and dolomite (20 [%]), and sodium carbonate (20 [%]) are first melted in a melting tank. The molten glass is then fed into a tin bath, where the floating melt spreads evenly and is drawn into the cooling area via laterally mounted gear wheels. The speed of the drawing process determines the glass thickness. As soon as the cooling process is completed, the glass can be further processed [239, 227]. Fig. 2.14 shows the procedure.

After reaching the melting point, all atomic bonds of the raw material break. The energy added by heat corresponds to the atomic bonding energy. In the liquid state, the glass then behaves like a Newtonian fluid. The viscosity is determined by the intermolecular interactions (friction) and prevents or delays a crystalline arrangement of the molecules during cooling. The speed of the cooling process, therefore, determines the arrangement of the molecules. The glass transition slows down the molecular dynamics and, therefore, leads to the state of an amorphous, disordered solid, also called supercooled melt [245].

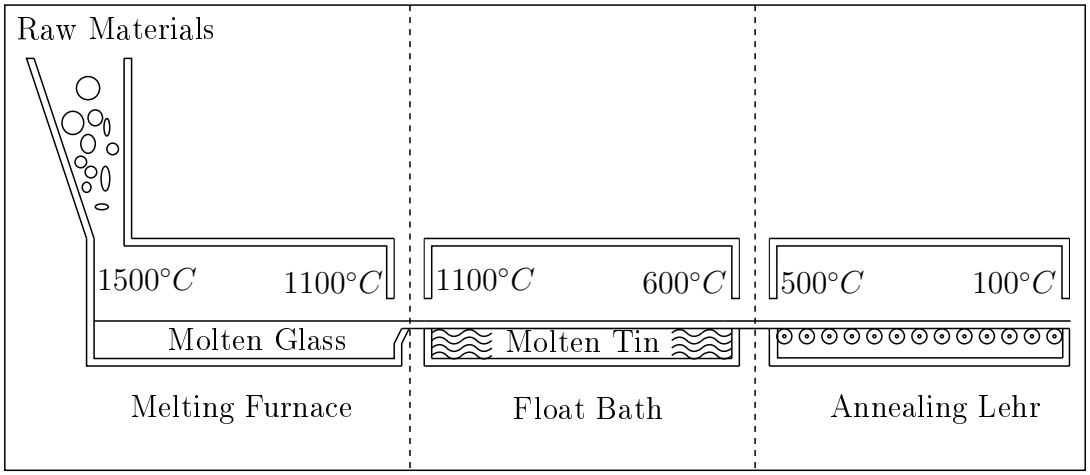

Figure 2.14.: Float Process, after Schneider et al. [227]

In a further process step, the glass is tempered, preventing subcritical crack growth in the stress-free glass and reducing the effect of surface damage [229]. The tempering process leads to

compressive stresses on the surface and tensile stresses inside the glass. Tensile and compressive stresses are in equilibrium.

There are two ways of tempering. Either thermally, by heating the base glass to about 100 [°C] above T_g and then rapidly cooling it by blowing in the air, leading to a residual stress contribution corresponding to the parabolic temperature profile. Alternatively, chemically, the tempering occurs via the near-surface ion exchange of alkali ions, brought about by storing the glass sheet in a molten salt bath. [239, 227]. A comparison of the resulting residual stress, induced by thermal and chemical prestressing, is shown in Fig. 2.15.

In this way, different essential products can be distinguished. They start with annealed glass [82, 83], which is obtained from sodium silicate by the float process. At this point, there are other base products, but these will not be considered here. Thermally toughened glass (TTG) [72, 73] and heat strengthened glass (HTG) [78, 79] can be produced from the basis glass by thermal tempering, or chemically tempered glass (CTG) [74, 75] by chemical tempering. The difference in the production of HTG and TTG is the cooling rate during the tempering process. TTG is cooled rapidly, resulting in high residual stresses, while HTG is cooled more slowly, resulting in lower residual stresses.

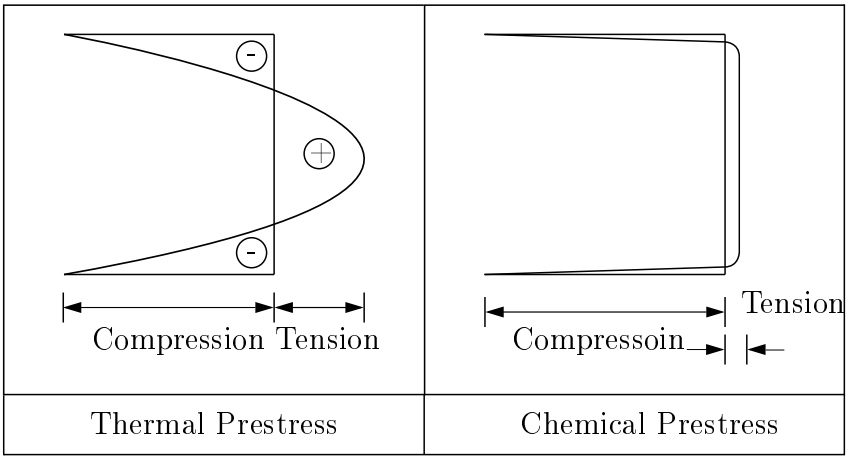

Figure 2.15.: Residual Stresses Induced by Thermal and Chemical Prestressing

The different tempering processes introduce different residual stresses and thus produce different elastic energy densities. The elastic energy density and the glass thickness are decisive for the fracture structure of glass [207, 208]. Different prestressed glasses, therefore, also exhibit different fracture patterns. The higher the internal elastic energy, the finer the fracture pattern (cf. Fig. 2.16).

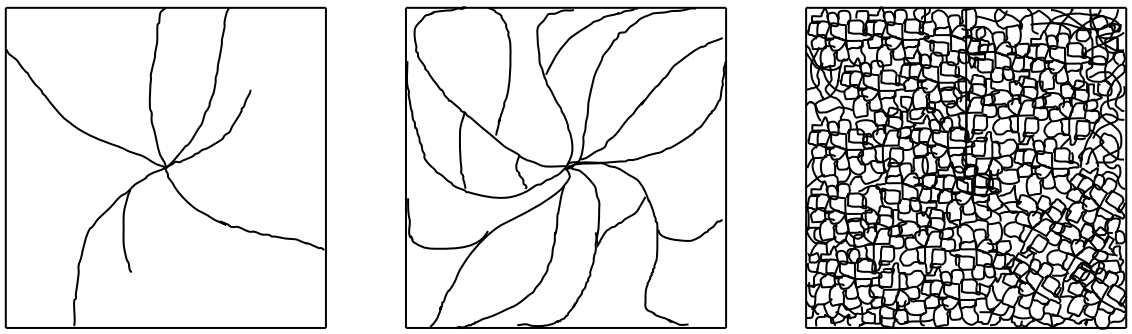

Figure 2.16.: Different Fracture Patterns for different Levels of Prestress

2.5.4. Laminated Glass

Laminated glass (cf. Fig. 2.17) is defined by DIN EN ISO 12543-1:2022-03 [85]:

Definition 1. *as an assembly consisting of a glass pane with one or more panes of glass and/or glazing material made of plastic, interconnected by one or more intermediate layers*

The manufacturing process of laminated glass comprises two stages in which the bond between the interlayer and the glass is produced. A vacuum or roll pre-laminate is produced after cleaning the glass and conditioning the interlayer. The choice of the pre-bonding process depends on the interlayer material. In vacuum pre-laminating, the air between the individual layers of the laminate is removed utilizing a vacuum bag or circulating hoses. In roll pre-laminating, the laminate is rolled together using heated rolls. The main composite is then usually produced in an autoclave, where the laminate is pressed together at a temperature of approx. 140 [$°C$] under the pressure of approx. 12 - 14 [bar]. For some interlayers, it is also possible to produce the main composite in a vacuum process [239, 227].

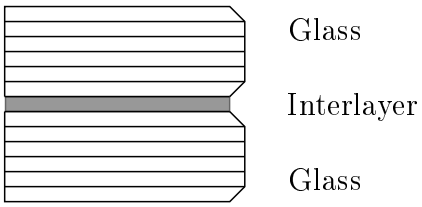

Figure 2.17.: Principle Sketch of a Laminated Glass

The basic properties and requirements for laminated glass are regulated by DIN EN ISO 12543-3:2022-03 [87]. If a laminated glass with an interlayer of PVB meets the requirements of DIN EN ISO 12543-2:2022-03 [86], it may be called laminated safety glass. The requirements include properties of the interlayer that must be met after testing in accordance with DIN EN ISO 527-3:2019-02 [92] as well as requirements for breakage and adhesion behavior in the soft body impact tests [76].

2.6. Experiments

For the experimental investigation of polymers, several properties must be considered. In particular, sensitivity to temperature and humidity requires special attention and leads to strict test conditions. Furthermore, investigating the time-dependent behavior under large deformations demands precise requirements for the measuring instruments. The following sections briefly introduce the corresponding test equipment required to take account of the complex and highly sensitive material behavior.

2.6.1. General Polymer Testing

There are various standards by which regulations for polymer testing are defined. The regulations can be divided into conditioning [89], testing in the intact state (tensile properties [90, 91, 92], creep properties [84], dynamic behavior [93, 137, 136]) and tests of material failure (tear propagation tests).

The climate for conditioning and testing is defined as 23±1 [$°C$] and 50±5 [%rH] for class 1, and 23±2 [$°C$] and 50±10 [%rH] for class 2, respectively [89]. For tensile tests, the testing

machine must meet the requirements specified by ISO 7500-1:2018-02 [138] (force measuring device class 1) and ISO 9513:2012-12 [139] and also comply with the tolerances specified by DIN EN ISO 527-1:2019-12 [90]. The extensometer must comply with class 1 according to ISO 9513:2012-12 [139]. Possible specimen geometries are presented in [92].

The exceptional standard tailored to PVB [77] aims to test the stiffness properties in the low strain range to determine the shear bond of laminated safety glass. A standard for testing PVB in the finite strain range has yet to be created.

2.6.2. Experimental Setup

In this chapter, the test instruments selected in accordance with the requirements of Sec. 2.6.1 are presented. These instruments include a punching machine for producing the test specimens, a climate chamber for conditioning the test specimens, a climate container with a constantly controlled temperature, a universal testing machine, and corresponding measuring sensors to measure force, displacement, temperature, and humidity.

2.6.2.1. Specimens Geometry

Two different specimen geometries were used, shown in Figure 2.18. Below, the left-hand geometry is referred to as Type A, the right-hand geometry as Type B. Specimen Type B equals Type 4 within DIN EN ISO 527-3:2019-02 [92], Type A was developed by Becker [18] for thermoplastic materials exposed to high strain rates and has already been used by several researchers for investigations on PVB [165, 162, 30, 231].

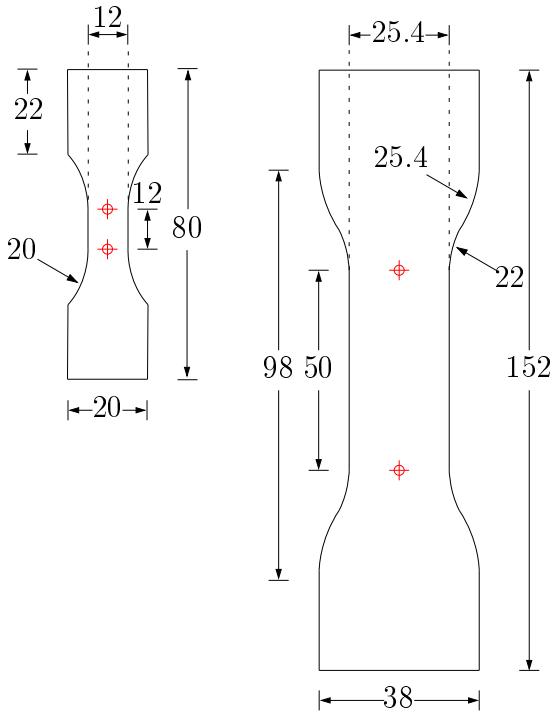

Figure 2.18.: Specimens geometry: Specimen *Typ A* (left); Specimen *Type B* (right); thickness of both Specimens is 1.52 [mm] and the unit within the drawing [mm]

2.6.2.2. Stamping Machine

The type A test specimens were punched out of a PVB roll. A mechanical press (Fig. 2.19 left) and a cutting die (Fig. 2.19 right) with the dimensions of the geometry of Becker [18], both

manufactured by the company *Star cutting technology*, were used for this purpose.

Figure 2.19.: Stamping machine setup from from Star cutting technology

2.6.2.3. Universal testing machine

A single-column material testing machine (Fig. 2.20) from ZwickRoell (Z2.5 zwickiLine) is used for testing. The maximum reachable force is 2.5 [kN], achieving testing velocities from 0.001 to 800 [mm/min].

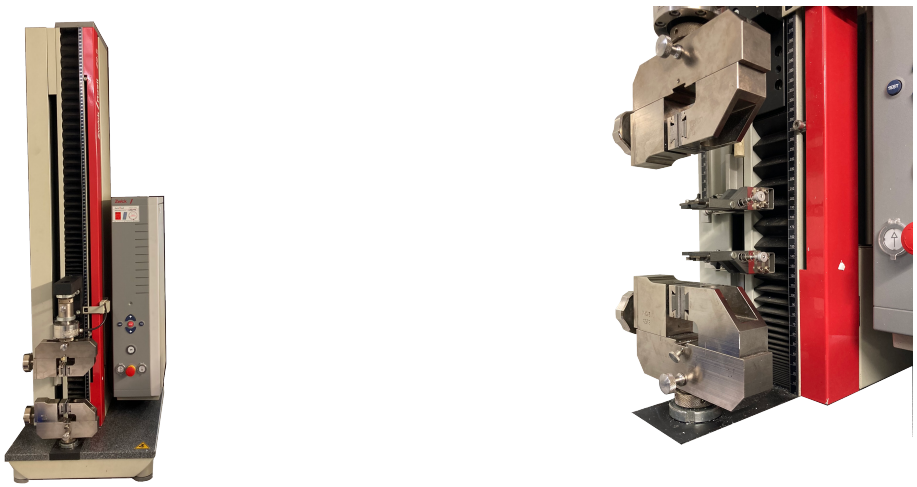

Figure 2.20.: Universal testing machine Z2.5 from ZwickRoell GmbH & Co. KG

2.6.2.4. Mechanical Clamping Device

The symmetrically gripping screw grips are single-sided closing grips for static and quasi-static tensile tests. They clamp up to a test force of 2.5 [kN] and are suitable for tests in a temperature range from -70 to 250 [$°C$]. The minimum initial gauge length L_0 is 5 [mm], and the specimen thickness must not exceed 18 [mm].

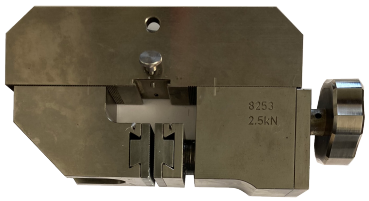

Figure 2.21.: Mechanical Clamping Device from ZwickRoell GmbH & Co. KG, article number 316322

2.6.2.5. Mechanical Sensors

Force Transducer The force transducer converts the physical quantity of force into an electrically measurable voltage. It consists of a mechanical deformation body with bonded strain gauges and strain-dependent electrical resistors, which are connected to form a measuring bridge. The value of the measuring voltage at the output of the bridge circuit is analogous to the force (F) to be measured, which acts on the deformation body and the entire force transducer system—the sign of the measurement voltage changes with the direction of the load. It has a nominal force F_{nom} of 2.5 [kN] and is designed for a temperature range of -20 to 60 [$°C$] with an accuracy class 1 from 0.2 [%] of F_{nom} (from 5 [N]) and accuracy class 0.5 from 1 [%] of F_{nom} (from 25 [N]).

Displacement Transducer The extensometer is a distance-measuring system that determines the change in length between two points. Its basis is a precision guide profile with two weight-compensated measuring carriages. The measuring system is designed for significant changes in length with ordinary measuring resolution. It determines the change in length between the probes by running the measuring slides on two precision columns, using particularly smooth-running guide elements. This setup ensures low-force transmission of the change in length and minimizes transmission errors. Counterweights balance the mass of the measuring slides. The extensometer measures from a deformation of 2 mm with the accuracy required by DIN EN ISO 527-1:2019-12 [90], which corresponds to class 1 according to ISO 9513:2012-12 [139], with a resolution of 0.003 [mm/pulse]. The initial gauge length must be between 10 and 200 [mm], and the cross-section of the sample must not exceed 60 [mm] in width and 20 [mm] in thickness. The ambient temperature during the test must be between 10 and 35 [$°C$]. The extensometer measures up to a deformed length of 800 [mm], whereby the minimum tensile force transferred from the grips to the specimens is a maximum of 0.2 [N].

Figure 2.22.: Force Transducer from A.S.T GmbH (left); Displacement Transducer from ZwickRoell GmbH & Co. KG, article number 024895 (right))

2.6.2.6. Temperature Sensors

Thermoelement The temperature was constantly tracked by a sensor of the *Thermoelement Typ K* type, which consists of (+) leg made from Nickel-Chrom and a (-) leg made from Nickel-Aluminium.

Climate Sensor To ensure the repeatability of the tests, temperature and relative humidity were constantly tracked by the use of the temperature-humidity USB meter, Voltcraft DL-121TH. The sensor covers a temperature range of -40 to 70 [$°C$] and a humidity range of 0 - 100 [%] and records up to 16000 data points. The recording is in a measuring interval of 2 [s] to 24 [h] with an accuracy of ± 1 [$°C$] for temperature and ± 3 [%rH] for humidity with a resolution of 0.1 ([$°C$], [%rH]).

Figure 2.23.: Thermoelement Typ K (left); Climate Sensor from Voltcraft, model DL-121TH (right))

2.6.2.7. Climatic Environment

Climatic Chamber Binder's Model MKF 720 (cf. Fig 2.24) was selected for the conditioning of the specimens. It is a dynamic climate chamber engineered for precise control in experiments and tests involving rapid temperature changes and humidity regulation. With temperatures ranging from -40 to 180 [$°C$], this chamber is able to create extremely cold and hot environments, accommodating diverse testing scenarios. Furthermore, its humidity control capabilities range from 10 to 98 [%rH], ensuring the maintenance of specific humidity conditions.

To facilitate humidity regulation, the MKF 720 comes equipped with an integrated 20-liter water reservoir. This reservoir serves to sustain humidity levels within the chamber during testing. Moreover, it provides four potential-free switching contacts, offering flexibility for controlling external devices or monitoring test conditions. It also features programmable condensation protection for samples, ensuring that test samples within the chamber are safeguarded from issues related to condensation, thereby upholding the reliability and accuracy of test results.

Climatic Container Within the climatic container, temperatures between 10 to 50 [$°C$] can be adjusted for theoretically any load duration. (climate homogeneity measurements are continuously taken during each experimental run at two points within the air of the climate chamber and at one point on each test specimen). The temperature precision of the climate chambers is ± 1 [$°C$].

Figure 2.24.: Climatic chamber for conditioning of the specimens (left); Climatic container for testing the specimens (right))

3. Experiments

This chapter describes the conditioning and preparation of the specimens, the different test specifications, and the experimental investigations. In general, the chapter is divided into two parts. The first part contains a detailed characterization of the time-dependent behavior of PVB under large deformations. The second part intends to describe the behavior of PVB under large deformations for a long loading duration using a simplified approach.

The first part can be divided again into several phenomena. It is distinguished between a loading process carried out until failure, a loading process followed by unloading, and a loading process followed by relaxation. The strain rate tensor $\mathbf{D}$ characterizes these processes. The stretch rate is greater than zero for the loading, smaller than zero for the unloading, and equal to zero for the relaxation process. According to these processes, three test prescriptions are defined. The first prescription (constant positive strain rate) represents a constant uniaxial tensile loading under seven different strain rates until failure. The results serve as a reference point for determining a suitable unloading point. For this point, it must be ensured, on the one hand, that the material does not fail and, on the other hand, that as much of the loading process as possible is represented. These tests are followed by uniaxial tensile tests with loading up to a maximum defined by the fracture tests and subsequent unloading. The third and final part of the tests consists of relaxation tests (loading process followed by a strain rate equal to 0) at three different strain rates and various loading levels, lasting from one to twelve hours.

To be used within an engineering approach, a test specification should be defined as simple and practicable as possible and provide maximum information about the material behavior for a reasonable test duration. The one chosen is the so-called staircase test, commonly used to determine the infinite stiffness of elastomers. The test contains loading and unloading branches, each loaded at an identical strain rate. However, this test is interrupted at certain strain levels by individual breakpoints at which the strain is held constant for five minutes. The duration is again chosen so that the test can be run in an adequate time frame, but the relaxation behavior can be characterized as accurately as possible.

The results of the uniaxial tension tests until failure, the cyclic, and the relaxation tests will be presented in Pauli and Siebert [200], which has been submitted to the journal Glass Structures & Engineering and is accepted but not published so far.

3.1. Specimen Preparation and Conditioning

The tests can be divided into two test series, with different test specimen geometries used for each series (compare Sec. 2.6.2.1). The production and conditioning of the test specimens are described separately below according to these series.

3.1.1. Test Series One - Geometry Type A

The PVB film with a thickness of 1.52 [mm] was delivered on a roll and stored in a plastic film in a laboratory environment. A separating layer prevented the film from sticking together on the roll. Sheets from this roll were used to punch out test specimens using a stamp and a cutter with the geometry type A (compare Sec. 2.6.2.2) and conditioned within a climatic chamber

(compare Sec. 2.6.2). Within the conditioning process, the temperature was increased to 50 [$°C$] at a constant relative humidity of 30 [%rH] and was maintained under these conditions for 1 hour. Subsequently, the temperature was decreased at a cooling rate of 2.5 [$°C/h$], and the humidity was increased at a humidity rate of 1.67 [%rH/h]. After the temperature reached 20 [$°C$] and the humidity reached 50 [%rH], this condition was sustained for a minimum of 12 [h]. However, the test specimens were not subjected to a lamination process with increased temperature and pressure, as Elzière [103], Schuster [231] found that this did not affect the material behavior.

3.1.2. Test Series Two - Geometry Type B

The PVB film was delivered as pre-cut test specimens (type B) with a thickness of 1.52 mm. The test specimens used in this work were first heated to 50 [$°C$], cooled slowly to 23 [$°C$], and then kept at a constant 23 [$°C$] for 12 [h].

3.2. Test Procedures

Just as the previous chapter was divided into the two test series, the test instructions presented below are shown separately for the two series.

3.2.1. Test Series One - Geometry Type A

For the testing phase, specimens were extracted from the climatic chamber and individually transferred to the container where the tests were carried out. It maintained a constant temperature of 20±1 [$°C$], with humidity variations of 65+/-5 [%rH]. Temperature and humidity were constantly tracked by a Thermoelement K sensor and the Voltcraft DL-121TH (cf. Sec. 2.6.2.6). Pliers, stored at 20±1 [$°C$], were used to install the specimens to prevent handcontact-induced heating. Each sample was initially clamped in the upper clamp (cf. Sec. 2.6.2.4) before the machine's starting position was approached. After reaching a distance of 36 [mm] between the clamps, the lower part of the specimen was fixed. By tightening the clamps, the samples buckled in the middle. A pre-force of 5 [N] was applied at a speed of 50 [mm/min] (controlled via the crosshead) to straighten the specimen. Subsequently, the extensometer clamps (Sec. 2.6.2.5) were attached and centered at a 12 [mm] distance, and the test was started. The distance between the two clamps constantly controlled the testing speed.

Different scenarios were investigated to characterize the time-dependent behavior of PVB under large deformations utilizing the strain rate, in the following expressed in terms of the strain rate tensor $\mathbf{D}$, as the driving quantity:

1. Influence of Displacement Transducer: It is checked whether the mechanical clamps of the displacement transducer influence the material's behavior in the intact state or its failure.

2. Rate-dependent Behavior: The stress response under varying strain rates is investigated.

3. Relaxation Behavior: The relaxation behavior concerning different strain levels approached from different strain rates is explored.

4. Hysteresis Behavior: Examining hysteresis behavior reveals the energy dissipation characteristics of laminated safety glass [103].

3.2.1.1. Influence of Displacement Transducer

These tests were carried out at a velocity of 50 [mm/min] until failure of the specimen was reached. Three tests with and without clamps attached were carried out. Failure was defined as a drop in force of 80 percent compared to the maximum measured force. In contrast to the other specimens tested within series A, the ones utilized for checking the influence of the displacement transducer did not undergo particular conditioning. However, they were all stored in the same climate for more than 24 hours.

3.2.1.2. Tests until Failure

The graphical representation in Fig. 3.1 provides a clear visualization of the applied strains concerning time for the seven test series conducted until failure. Besides the standard scale, a logarithmic scale is presented to enhance precision and clarity. The curves in Fig. 3.1 are presented up to a strain level of 300 [%] for clarity and ease of representation. It is essential to emphasize that no specific strain limit was defined within the test specification. The procedure was continued in each test until the specimen reached the point of failure. Failure was defined as a drop in force of 80 percent compared to the maximum measured force. The legends in the two graphs of Fig. 3.1 show the strain rates in [1/s] applied in the respective test series.

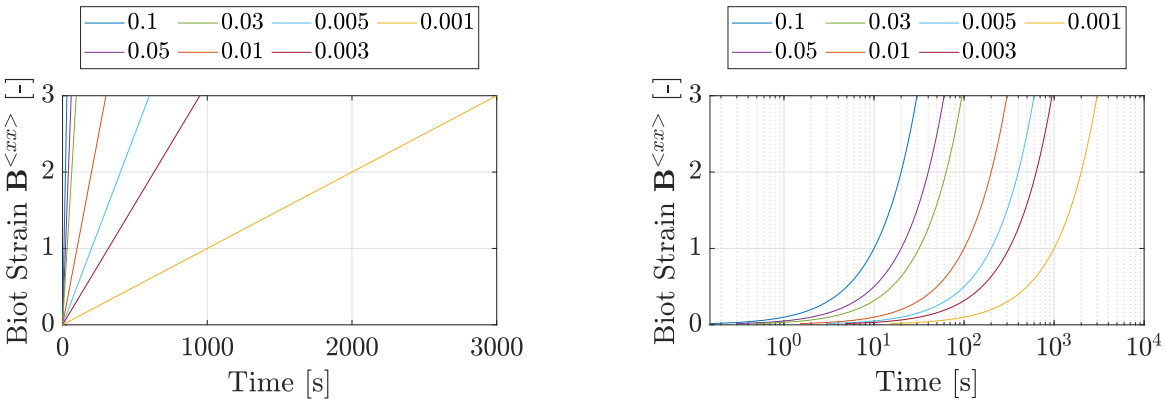

Figure 3.1.: Test Procedures: Tension until Failure

3.2.1.3. Cyclic Tests

Fig. 3.2 and 3.3 outline the specific protocols employed for the cyclic tests, depicted in standard and logarithmic scales. The general procedure is to achieve a particular strain level by utilizing a specific strain rate and then releasing the strain with the same strain rate until a lower force limit is reached. The stress, particularly the difference between the loading and unloading branches, is measured throughout the test. Three distinct strain rates (0.1 [1/s], 0.01 [1/s], 0.001 [1/s]) were explored. For each strain rate, the turning point of the hysteresis was consistently set at a strain level of 150 [%]. For the middle strain rate of 0.01 [1/s], the strain levels 50, 100, and 200 [%] were additionally chosen as turning points of the hysteresis. All tests were intentionally concluded when a force of 1 [N] was achieved. This limit ensured the specimens remained consistently under tensile stress throughout the testing process, providing reliable and controlled experiment conditions.

The legends in the two graphs of Fig. 3.2 show the strain rates in [1/s] applied in the respective test series, and the legends in the two graphs of Fig. 3.3 show the strain levels in [%] applied in the respective test series regarding relaxation.

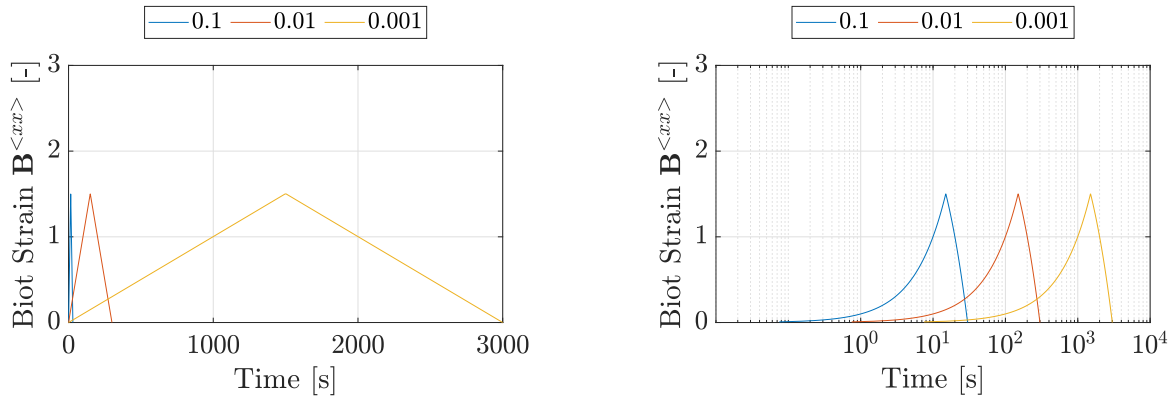

Figure 3.2.: Test Procedure: Cyclic Tests at different Strain Rates

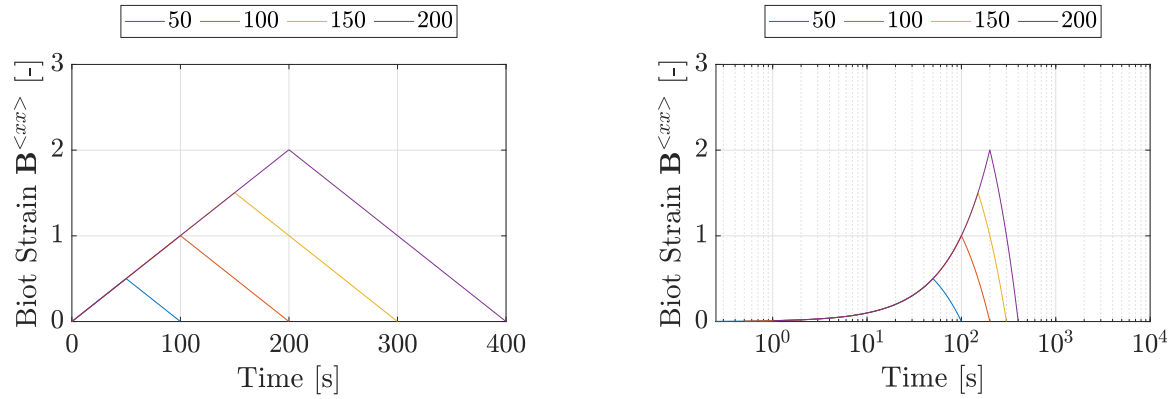

Figure 3.3.: Test Procedure: Cyclic Tests at the same Strain Rate

3.2.1.4. Relaxation Tests

Fig. 3.4 and 3.5 show the different test specifications for the relaxation tests in standard and logarithmic scales. The general procedure is to achieve a particular strain level by utilizing a specific strain rate and holding the strain level for a respective amount of time. The stress, particularly the decay in stress, is then measured throughout the whole test. They encompass a total of six distinct procedures, with three different strain rates (0.1 [1/s], 0.01 [1/s], 0.001 [1/s]) and four various strain levels (50 [%], 100 [%], 150 [%], 200 [%]). The middle strain rate (0.01 [1/s]) is explored at all four strain levels, the high strain rate (0.1 [1/s]) at a level of 100 [%] and the low strain rate (0.001 [1/s]) at a level of 200 [%]. All tests are carried out for three durations: one hour, three hours, and 12 hours. These durations were chosen to analyze the stress relief in different sections.

The legends in the two graphs of Fig. 3.4 show the strain rates in [1/s] applied in the respective test series, and the legends in the two graphs of Fig. 3.5 show the strain levels in [%] applied in the respective test series regarding relaxation. In both figures, the triangle, the circle, and the square indicate the duration of the particular relaxation process.

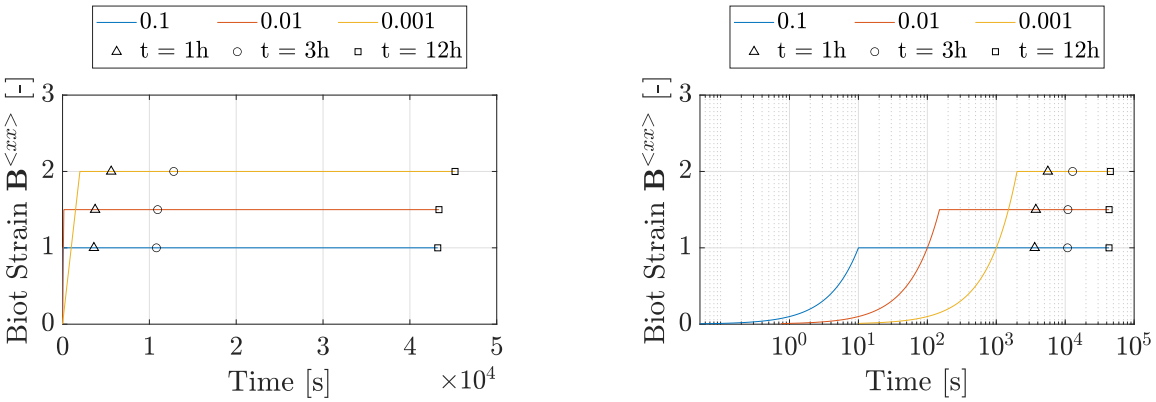

Figure 3.4.: Test Procedure: Relaxation Tests at different Strain Rates

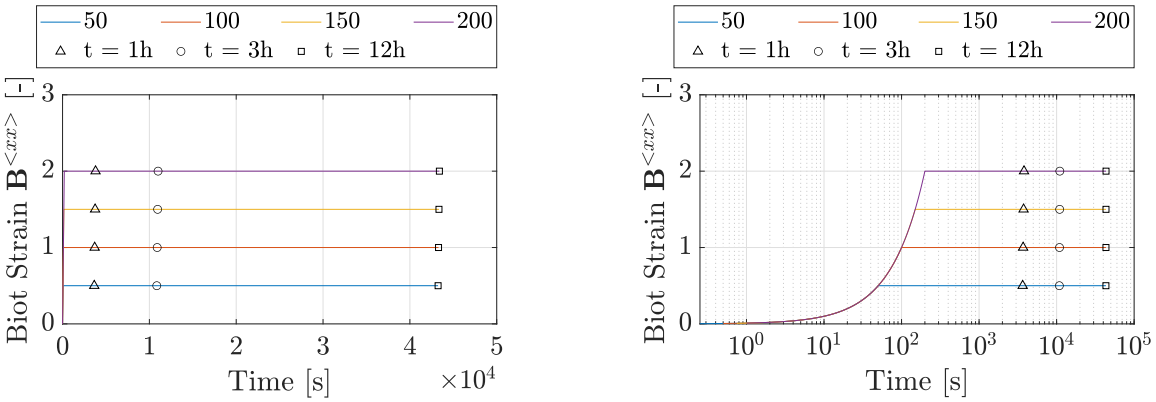

Figure 3.5.: Test Procedure: Relaxation tests at the same Strain Rate

3.2.2. Test Series Two - Geometry Type B

Each sample was initially attached with the upper clamp before the machine approached its starting position. After reaching a distance of 98 mm between the clamps, the lower part of the specimen was fixed. By tightening the clamps, the samples buckled in the middle. A pre-force of 5 N was applied at a speed of 50 [mm/min] (controlled via the crosshead) to straighten the specimen. Subsequently, the extensometer clamps were attached and centered at 50 mm, and the test started. The distance between the two clamps controlled the velocity during the whole experiment. Temperature and relative humidity were constantly tracked by the use of the temperature-humidity USB meter, Voltcraft DL-121TH (cf. Sec. 2.6.2).

The performed test is called the "staircase test" in the following, as its test procedure reminds of a staircase. Usually, this test serves to evaluate the equilibrium response of polymeric materials, mostly elastomers Bergström and Boyce [cf. 25]. With a displacement-controlled constant strain rate of 0.01 [1/s], the specimen is loaded to a defined maximum value of 190 % technical strain and then unloaded until reaching a force of 5 N. Several holding steps are defined on the loading and unloading paths during this cycle. Within these steps, the current strain is held constant for 5 min. Fig. 3.6 shows the test procedure with all defined steps in graphical and tabular form.

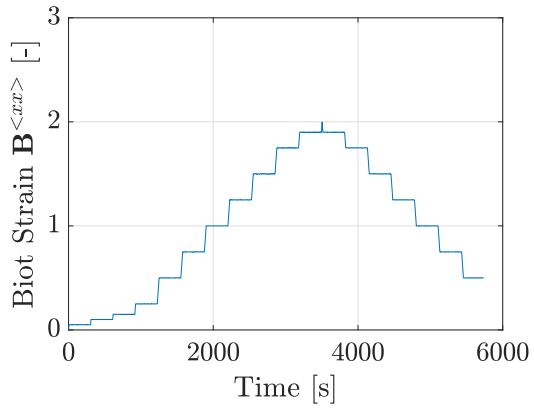

$\mathbf{B}^{<xx>}$ [%]	holding time [s]	$\mathbf{B}^{<xx>}$ [%]	holding time [s]
5	300	100	300
10	300	125	300
15	300	150	300
25	300	175	300
50	300	190	300
75	300		

Figure 3.6.: Test Procedure: Staircase Test

3.3. Test Results

The results of each procedure are presented below. This section shows only the mean value of the single tests. The Appendix depicts a detailed representation of all the tests, including mean value and standard deviation (cf. App. A). Some of the results of the tension tests until failure, the cyclic, and the relaxation tests already have been published in Pauli and Siebert [200].

3.3.1. Control Tests

Fig. 3.7 shows the result of the control tests carried out at a constant crosshead velocity of 50 [mm/min] with and without attaching the clamps of the displacement transducer. Both tests were carried out three times. On the left side, the stress-strain course is shown, and on the right side, the points of failure are presented. For each specification, three repetitions were conducted (cf. App. A.1). A look at Fig. 3.7 shows very clearly that the clamps of the extensometer do not influence the behavior of the sample.

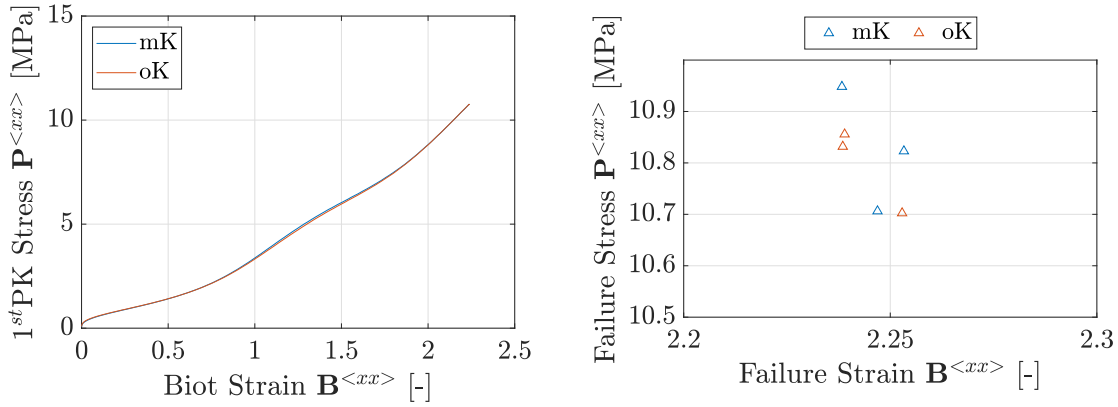

Figure 3.7.: Mean values for tests with and without clamps (left); points of failure (right)

3.3.2. Tension-Tests until Failure

Uniaxial tensile tests were carried out at seven different strain rates (according to the test specification, shown in Fig. 3.1) to investigate the rate dependence of standard PVB. The

results show that the observed material behavior can be divided into three sections. The first section contains an initial stiffness that increases with increasing strain rate. It follows a region of low stiffness, comparable to a flow plateau, limited to a specific stress level. Above this stress level, there is a sharp increase in stiffness. However, due to the greater initial stiffness of the curves with the higher strain rate tests, the stress increase occurs at locations of different strains. However, the sharp stiffness increase (3rd section) is almost parallel for all strain rates. Fig. 3.8 shows the test results for seven different strain rates [1/s] until the failure of the specimen. For each specification, a minimum of five repetitions were conducted (cf. App. A.2).

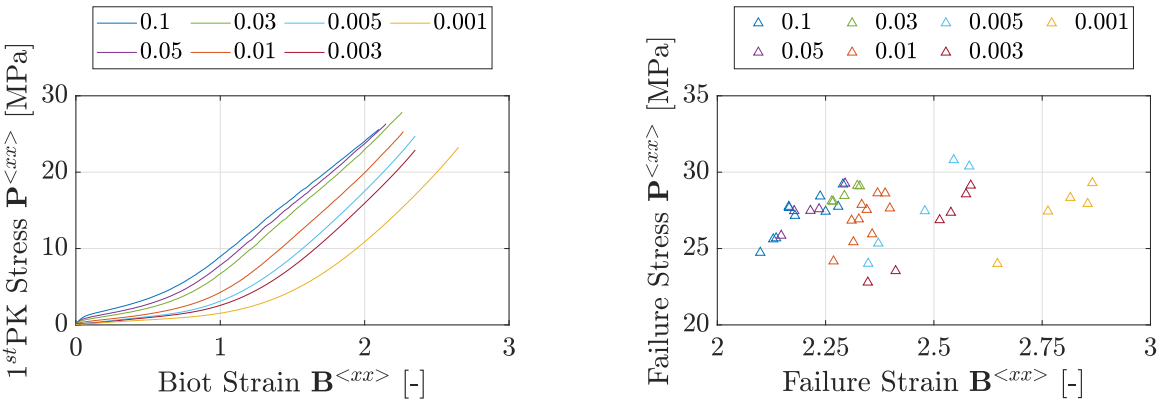

Figure 3.8.: Mean values for different strain rates (left); points of failure (right)

Fig. 3.9 shows respective boxplots for the stresses and strains at failure, considering the results for each strain rate separately and the sum of all results. The boxes limited by the 25th, indicated by the bottom, and the 75th percentile, marked by the top, represent the interquartile range of each sample. The horizontal line in between each box represents the median of the sample. Two whiskers extend the boxes by 1.5 times the interquartile range upwards and downwards. All values outside the range of the whiskers are indicated as outliers.

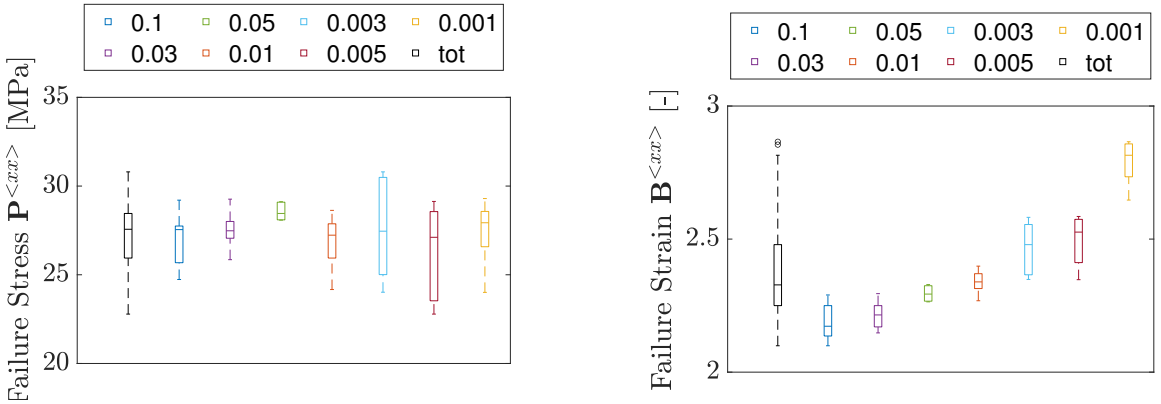

Figure 3.9.: Box plots of stresses at failure (left); box plots of strains at failure (right)

Looking at the failure conditions of the test specimens in Fig. 3.8 (right), it is noticeable that the elongation at fracture reduces with increasing strain rate. Still, the stress at fracture stays almost constant. These observations are clearly confirmed by the box plots.

3.3.2.1. Evaluation of Failure

Besides the material's intact state, the failure is to be evaluated. Knowing the probability distribution of the test data is crucial to assess a particular failure criterion on a design level.

For this purpose, the *Kolmogorov Smirnov Test* (KS-test) is utilized. It is a statistical test to check whether a random variable follows a postulated distribution. If used as a two-sided hypothesis test, the KS-test consists of the null hypothesis, stating that the random variable follows a distinct distribution, and the alternative hypothesis, saying that it does not. The test compares the cumulative density functions of the test data and the postulated distribution. It returns the probability p of observing a test statistic as extreme as, or more extreme than, the observed value under the null hypothesis. Small values of p cast doubt on the validity of the null hypothesis. Based on a significance level denoted by α, the test decides whether to reject the null hypothesis. The test fails to reject the null hypothesis for p values above the α-significance level.

It is important to note that the data is evaluated together, not separately, for the particular strain rate. For all evaluations, the data is categorized into 20 bins, each containing the values of a specific interval.

Failure - 1^{st}PK Stress A look at Fig 3.8, the stress at the failure level appears almost horizontal with only a small scattering in the vertical direction. This observation seems promising for the derivation of a failure criterion. In this respect, the categorized data is displayed utilizing a cumulative and probability density representation to assess the stress values at failure further. Various distributions are used to approximate the data. Fig. 3.10 illustrated the distribution of the test results and the respective distribution functions to evaluate the sample distribution.

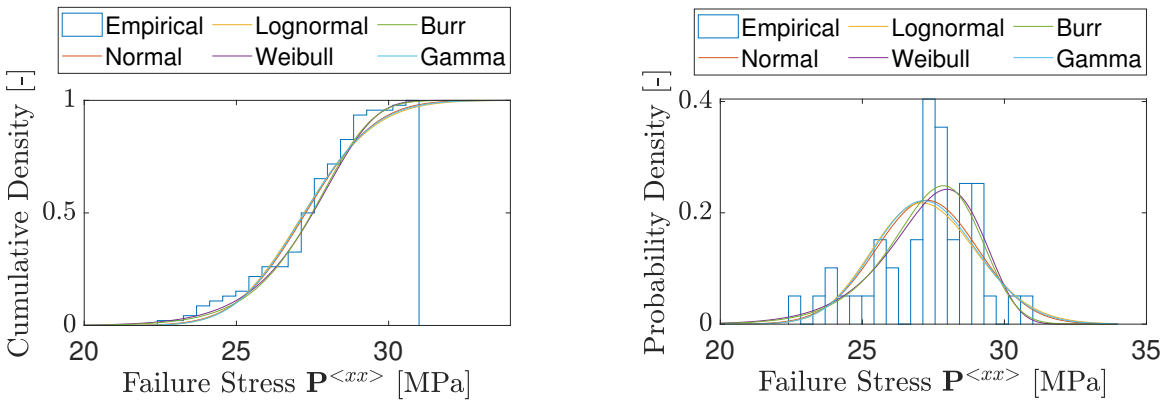

Figure 3.10.: Statistical evaluation of the stresses at failure

Visually, all distributions are able to approximate the data, although the *Burr* and the *Weibull* distribution appear to be the most promising.

After visual evaluation of the data's distribution, the data is analyzed analytical using the KS-test function implemented in Matlab. Parameter h indicates if the test rejects the null hypothesis or not (reject $h = 1$), parameter p returns the probability of the data following the respective distribution. Tab. 3.1 displays the results of the KS-test in columns one and two and the fit parameters of the particular distribution function in columns three to five. The analytical evaluation of the individual distributions confirms the findings obtained from the visual assessment. The test data could, at a significance level of 5 [%], correspond to each of the tested distributions, whereby it is most likely that the data follow the Weibull or Burr distribution.

A *Quantil-Quantil-Plot* (QQ-plot) helps visually evaluate the respective distributions more precisely as the inspection of the PDF and CDF plots. This plot displays the quantiles of the sample data against the theoretical quantiles of a particular distribution. If the data distribution follows a linear course, it is assumed to follow the respective theoretical distribution. Within

Table 3.1.: Results for KS-test at a significance level of 5 % and fit parameters for distribution functions

Distribution	h [-]	p [%]	p_1	p_2	p_3
Normal	0	12.46	27.2761	1.7928	
Lognormal	0	8.23			
Weibull	0	52.62	28.0646	18.4657	
Burr	0	47.32	31.0003	20.0227	8.0538
Gamma	0	9.36	229.1297	0.1190	

the plot (compare Fig. 3.11), the data points are displayed by a plus sign marker('+'), and the theoretical distribution by a straight line, consisting of two parts. The first part, depicted as a solid line, connects the first and third quartiles of the data. The second part, represented by a dashed reference line, displays the data outside the interval limited by the first and third quartiles.

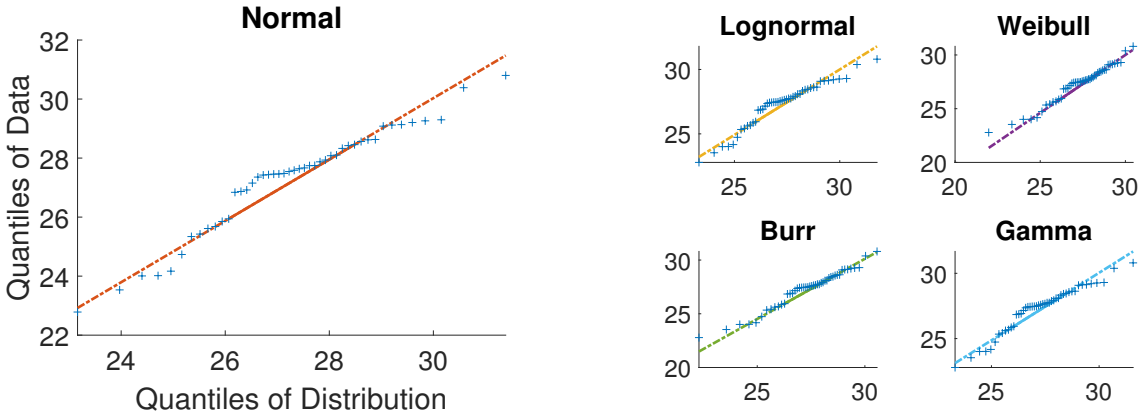

Figure 3.11.: QQ-plots of the stresses at failure

Again, the evaluation of the QQ-plot confirms the conclusions drawn from the first visual inspection and the analytical assessment.

Failure - Biot Strain The problem with choosing the 1^{st}PK stress as a failure criterion is that the stress increase concerning strain increase is not considered. As the Biot strain incorporated the actual length of the stressed body, this problem does not appear. Again, to evaluate the strains at failure, the data's cumulative and probability density representation is plotted together with the same contribution functions used for evaluating the stresses.

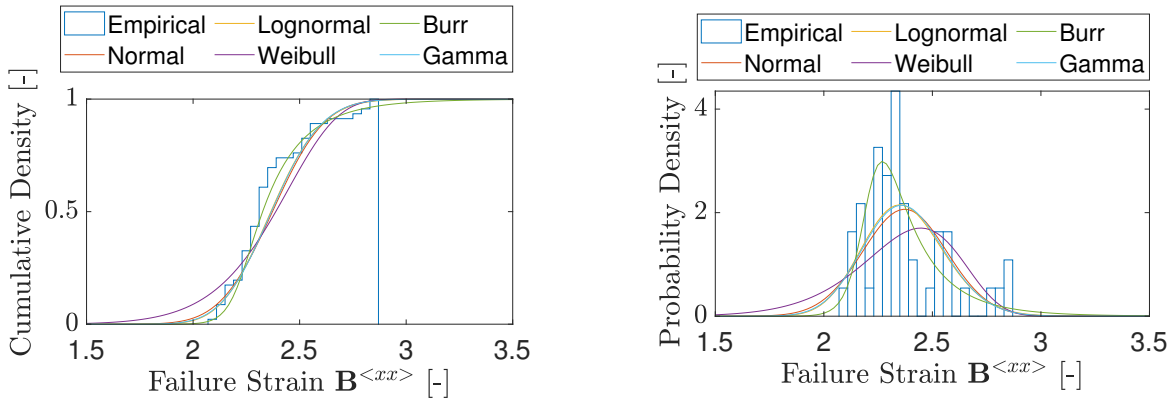

Figure 3.12.: Statistical evaluation of the strains at failure

The first visual inspection of Fig. 3.12, as well as the analytical evaluation, represented in Tab. 3.2, reveal that, except the Weibull distribution, all distributions might represent the test data. However, the Burr distribution appears to be by far the most promising. It is interesting to note that all distributions that assume the null hypothesis are at the same level, except the Burr distribution, which has a strikingly higher value. The conclusion drawn from Fig. 3.12 and Tab. 3.2 are confirmed by Fig. 3.13, representing the QQ-plots of the considered distribution functions concerning the failure strains.

Table 3.2.: Results for KS-test at a significance level of 5 % and fit parameters for distribution functions

Distribution	h [-]	p [%]	p_1	p_2	p_3
Normal	0	10.38	2.3724	0.1931	
Lognormal	0	17.06	0.8608	0.0787	
Weibull	1	4.27	2.4662	11.3642	
Burr	0	97.45	2.2143	46.6722	0.2889
Gamma	0	14.52	161.7556	0.0147	

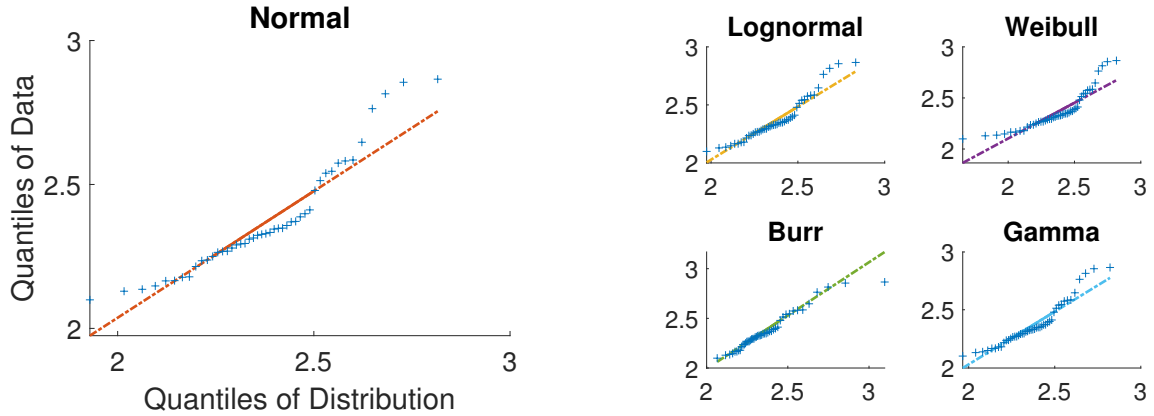

Figure 3.13.: QQ-plots of the strains at failure

Failure - Cauchy Stress Choosing the Cauchy stress for the failure criterion appears to combine the advantages of the 1^{st}PK stress and the Biot strain, as it is stress-based and considers

the actual length of the stressed body. Fig. 3.14 and Tab. 3.3 show that all distribution functions can represent the test data. Interestingly, all distributions display a high probability except for the Weibull distribution. The QQ-plot (Fig. 3.15) underlines the considerations drawn from the first visual inspection and the analytcal evaluation of the test data.

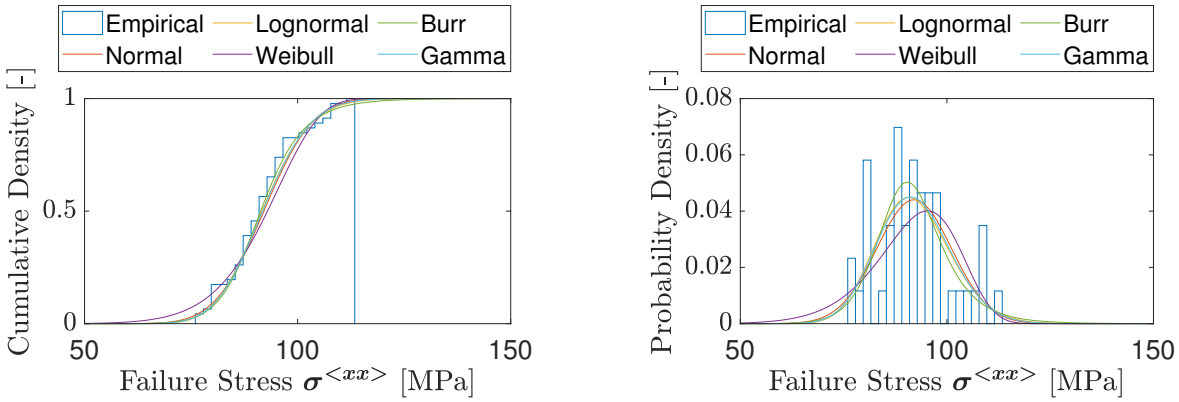

Figure 3.14.: Statistical evaluation of the Cauchy stresses at failure

Table 3.3.: Results for KS-test at a significance level of 5 % and fit parameters for distribution functions

Distribution	h [-]	p [%]	p_1	p_2	p_3
Normal	0	47.17	92.0727	9.0528	
Lognormal	0	61.90	4.5179	0.0974	
Weibull	0	14.13	96.2429	10.4475	
Burr	0	88.79	90.0523	19.4287	0.8264
Gamma	0	59.45	107.3603	0.8576	

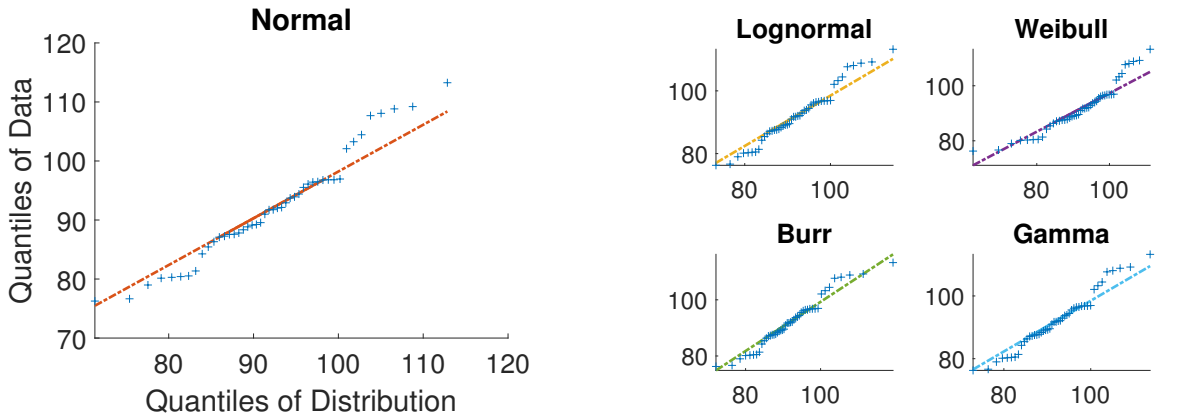

Figure 3.15.: QQ-plots of the Cauchy stresses at failure

3.3.2.2. Comparison with Results from Literature

This section compares the test results with various results from the literature to categorize their quality. However, the comparison is made without judgment, as this will only be made

in the discussion. Fig.'s 3.16, 3.17, and 3.18 show a selection of the tensile test results up to failure from the previous section and test results from the literature. The results from the literature are then described in detail. All considered curves are presented concerning First Piola Kirchhoff or Cauchy stresses and Biot strains to create an equal basis for comparison. Material incompressibility was assumed to simplify this conversion.

Bennison et al. [22] investigated various interlayers within the context of laminated glass for blast mitigation. To this end, uniaxial tension tests were conducted on Polyvinyl Butyral and SentryGlas®, employing a servo-hydraulic test machine. The PVB utilized in the study was of the Butacide®, configured in a dog-bone geometry. Digital recording of specimen deformation was performed concurrently with synchronized documentation of the applied load. Strain rates examined encompassed 0.07, 0.7, 8, and 80 [1/s]. However, pertinent details regarding the control of test velocity and climatic conditions during testing remain undisclosed. Fig. 3.16 (right) shows the test results for the strain rates 0.07 and 0.7.

Hooper et al. [134] examined the mechanical behavior of PVB across varying strain magnitudes and rates. Type 2 specimens, as delineated in BS ISO 37:2005 [36], were cut from a sheet of PVB (Solutia product number RB-41). Uniaxial tensile tests were executed using the Instron "VHS" high strain-rate test machine. They explored strain rates ranging from 0.2 to 400 [1/s] without further information on the control of the test velocity. Force measurements were obtained through a piezoelectric load cell (Model 222B manufactured by PCB Piezotronics Inc). At the same time, deformation tracking employed an optical measurement system evaluated by the OpenCV computer vision library. The ambient room temperature for testing was 25 ± 3 [$°C$], although information regarding humidity levels is unavailable. The test result for a strain rate of 0.2 [1/s] is illustrated in Fig. 3.16 (right).

Xu et al. [270] investigated the temperature and strain rate-dependent response of Polyvinyl Butyral (PVB) under uniaxial tension. Dumbbell-shaped specimens with a thickness of 1.52 [mm], conforming to the specifications outlined in DIN 53504:2017-03 [71], were subjected to testing at various strain rates: 1, 0.1, 0.01, 0.001 [1/s], corresponding to testing velocities of 1.56, 15.6, 156, and 1560 [mm/min]. Different temperatures (-10, 0, 10, 23, 40, 55, 70 [$°C$] ASTM D1349-99:2005 [12]) were explored, with a specific emphasis on a temperature of 23 [$°C$] for this thesis. The humidity was not controlled and, therefore, varied from 20 to 30 [%rH]. The hydraulic testing machine "INSTRON 8872" was employed for the experiments, along with a temperature controller and a CCD (Charged-coupled Device) camera for data acquisition. The PVB used was not further specified.

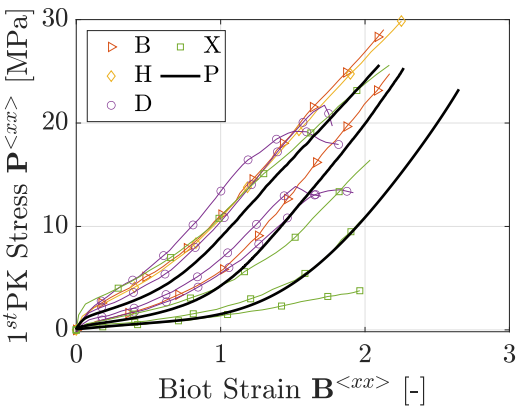

Figure 3.16.: "B" = Bennison: 0.07, 0.7 [1/s]; "H" = Hooper: 0.2 [1/s]; "D" = Del Linz: 0.01, 0.02, 0.1, 0.2 [1/s]; "X" = Xu: 0.001, 0.01, 0.1, 1 [1/s]; "P" = Pauli: 0.001, 0.01, 0.1 [1/s]

Del Linz et al. [64] investigated the material response of the PVB Saflex®RB41 in Blast Loading Situations. They utilized dogbone specimens according to BS ISO 37:2005 [36] with a thickness of 1.52 mm manufactured using a cutting die. They used a single column 1 kN Zwick tensile testing machine to apply strain rates of 0.01 [1/s], 0.02 [1/s], 0.1 [1/s], 0.2 [1/s] at a temperature of 20 [$°C$]. The inbuilt force sensor measured the force during the test; the displacement was tracked optically similarly to that used by Hooper et al. [134].

Iwasaki and Sato [140] explored the interface fracture toughness of Polyvinyl Butyral (PVB)/glass under high strain rates using high and low-speed tensile tests. The 0.76 mm thick sheet of S-LEC^{TM} interlayer film from Sekisui Chemical Co. Ltd. was cut into the dogbone configuration (JIS 2), following the guidelines stipulated in JIS K 7113:1995 [145]. Additionally, the PVB films underwent conditioning at 130 [$°C$] for one hour within a vacuum bag. They conducted the uniaxial tension tests utilizing the "LSC-05/300" test apparatus. They measured the deformations using the optical extensometer "SS-220D," both manufactured by Tokyo Testing Machine Inc. Strain rates examined encompassed 0.0067, 0.033, 0.067, 0.13, and 0.2, corresponding to testing velocities of 10, 50, 100, 200, and 300 mm/min, respectively. However, there is no information regarding the control of test velocity and the climatic conditions during testing. Fig. 3.16 (left) shows the test results for the strain rates 0.0067, 0.067, and 0.2 [1/s].

Liu et al. [172] conducted an experimental study on the mechanical behavior of PVB under various loading conditions. They used a Zwick Roell Z5 testing machine with a 5kN KPA-Z load cell, engineered by A.S.T. GmbH Dresden to track the force and an optical measurement system consisting of a cold light illuminator and a CCD (Charge-coupled Device) camera to track the displacement. They utilized dumbbell-shaped specimens JIS K 7113:1995 [145] with a thickness of 0.76 and investigated testing velocities of 10, 50, 100, and 200 mm/min corresponding to the strain rates 0.004, 0.02, 0.04, 0.08 [1/s].

Kuntsche [165] conducted a series of uniaxial tension tests at various displacement velocities (5, 50, 200, 6000, 60000, 210000 [mm/min]) on specimens of PVB BG sheets manufactured by *kuraray europe gmbh*, cut in the geometry proposed by Becker [18] (cf. specimen *Typ A*). He executed the tests under controlled conditions with a temperature maintained at 22-23 [$°C$] and a relative humidity of 30-50 [%rH]. Notably, the specimens were conditioned in a climatic box until just before the commencement of the test. In this study, the universal testing machine utilized was the "Zwick Z050 THW," equipped with the Load cell "Zwick Roell Xforce K 50 kN" and pneumatic wedge clamping jaws "TH175" from "Grip Engineering." Displacement measurement was facilitated by the video extensometer "uEye UI-2280SE." Dynamic tensile tests were conducted at Fraunhofer LBF using the high-speed testing machine Zwick Amsler HTM 5020, employing manual wedge clamping jaws as the clamping tool. Video extensometry during dynamic tests involved a black and white high-speed camera operating at 10000 fps with a resolution of 260 $\times$ 1060 pixels.

Knight et al. [152] explored the mechanical behavior of laminated glass polymer interlayer subjected to environmental effects. They conducted experiments on 0.76 mm thick Saflex/Standard Clear Type IV specimens of ASTM D638-10:2010 [13]. They utilized a temperature control chamber to adjust the test temperature and maintain isothermal conditions during mechanical testing. The quasi-static tensile testing was conducted using an electromechanical static testing frame with load cells and a Linear Variable Differential Transformer (LVDT). They tracked the deformation during the tests using a high-resolution camera. Within this thesis, only the tests at room temperature without environmental influences at a testing speed of 2 [in/s], with an initial strain rate of 0.333 [1/s] and a final strain rate of 0.09 [1/s], are further considered.

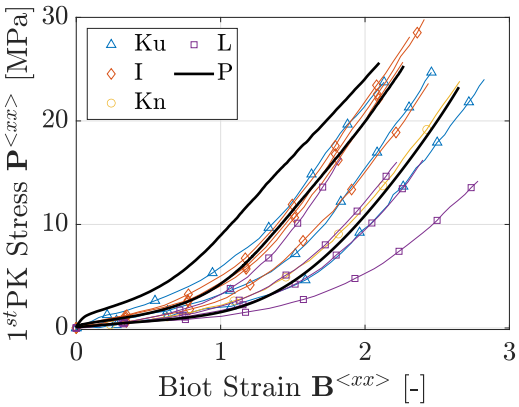

Figure 3.17.: "Ku" = Kuntsche: 5, 50, 200 [mm/min]; "I" = Iwasaki: 10, 50, 100, 200 [mm/min]; "Kn" = Knight: 50 [mm/min]; "L" = Liu: 10, 50, 100, 200 [mm/min]; "P" = Pauli: 0.001, 0.01, 0.1 [1/s]

Centelles et al. [43] investigated the mechanical properties of laminated glass interlayers subjected to aging utilizing tensile tests on cured and virgin specimens. In addition to other interlayers, they investigated BG-R 20, corresponding to the B200NR used in this work. The specimens were extracted from an interlayer sheet utilizing a cutting die with the shape according to ASTM D638-10:2010 [13]. They used a Zwick Roell tensile testing machine to apply displacement rates of 10, 50, and 100 [mm/min] at a temperature of 24 [$°C$].

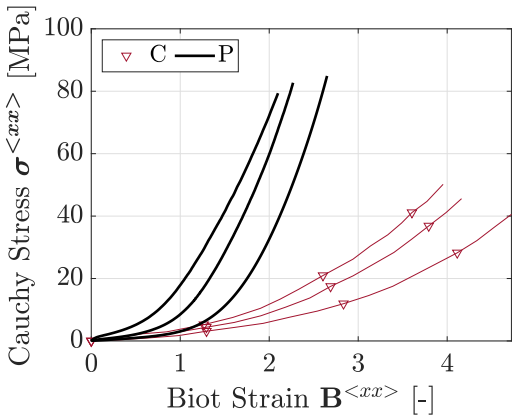

Figure 3.18.: "C" = Centelles: 10, 50, 100 [mm/min]; "P" = Pauli: 0.001, 0.01, 0.1 [1/s]

3.3.3. Cyclic-Tests

The cyclic tests involved loading at three different, constant strain rates up to a particular strain and subsequent unloading at the same strain rate. However, the unloading was limited to a residual force of 1 [N] to ensure that the specimen was constantly under tension and no stability problems arose. Besides the strain rates, the strain levels, which signal the end of loading and the beginning of unloading, were varied. For the strain rate 0.01 [1/s], the strain levels 50, 100, 150, and 200 [%] were investigated, and for the strain rates 0.1 and 0.001 [1/s], the level 150 [%] (cf. Fig. 3.2.1.3). Fig. 3.19 presents the mean values from at least three specimens for each test according to the respective specification.

Combined with the findings from the fracture tests, which showed a greater stiffness for higher strain rates and an increase in stiffness for higher strains, this observation leads to the logical conclusion that the hystereses are open further for higher strain rates and at higher strain levels. Since the area of a hysteresis represents the energy dissipated by the material,

this finding suggests that the material dissipates increasingly more energy under loads with increasing strain rates and up to higher strain levels. In addition to that, it could be observed that a residual deformation within the sample remained after the test was completed. This deformation was restored almost completely within approximately one hour after releasing the specimen, intending that there was no plastic deformation. This observation was also made by Kuntsche [165] and Schuster [231].

Fig. 3.19 shows the mean values of the test results for the strain rate 0.01 [1/s] loaded to the strain levels 50, 100, 150, and 200 [%], as well as the strain rates 0.1 [1/s] and 0.001 [1/s] loaded to a strain level of 150 [%].

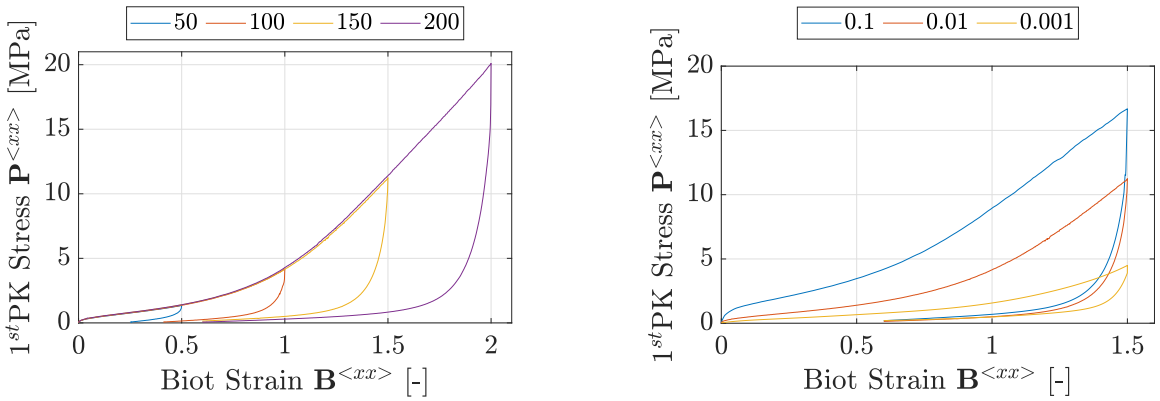

Figure 3.19.: Mean values for different strain levels (left) and different strain rates (right)

3.3.3.1. Comparison with Results from Literature

Elzière [103] conducted cyclic tests with controlled displacement speed at varying temperatures (10, 20, 30, 50, 70 [$°C$]) and strain rates (0.001, 0.01, 0.1, 1 [1/s]) on PVB. He did not provide specific details regarding the type and manufacturer of the PVB employed in the study. To align the outcomes of this thesis with Elzière [103]'s findings, only the temperature of 20 [$°C$] is considered. The experimental apparatus comprised a Zwick "Hamsler HC25" hydraulic machine equipped with a 1 kN load cell and an "Instron 5565" with a 100 N load cell for tests with a highly soft material response. A closed cabinet and the Eurother Automation thermoregulator (model 2216L) maintained the temperature regulation during testing. Notably, humidity levels were neither regulated nor monitored, with an assumed range of 20 to 50 [%rH]. Deformation of the specimen and the clamp displacement were measured utilizing a video extensometer featuring the Baumer BM20 camera.

No permanent deformation was observed after the test, even for low temperatures and high strain rates. Fig. 3.20 compares the test results presented by Elzière [103] for the strain rates 0.001, 0.01, and 0.1 at a respective strain level of 200 [%] with the tests at the strain rates 0.001 and 0.1 [1/s] to a strain level of 150 [%] and the strain rate of 0.01 [1/s] to a level of 200 [%] conducted within this thesis.

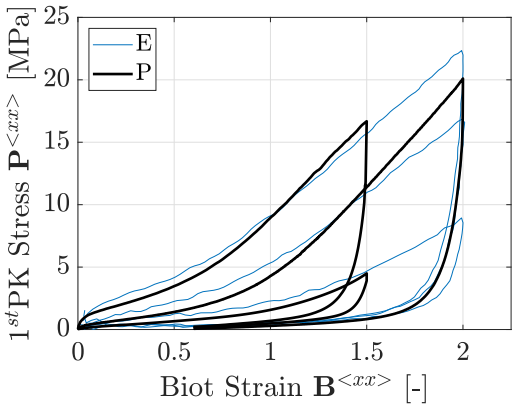

Figure 3.20.: "E" = Elziere: 0.001, 0.01, 0.1 [1/s]; "P" = Pauli: 0.001, 0.01, 0.1 [1/s]

3.3.4. Relaxation-Tests

By loading the specimens at a constant strain rate up to a particular strain level and keeping the strain constant at this level for specific times, the relaxation tests aim to investigate the material behavior at a constant strain level concerning time. These tests aimed to measure the decrease in stiffness as a function of time. For this purpose, three specific intervals were selected, and the behavior of the stress as a function of time was investigated. The first interval extends from the beginning of the holding phase up to one hour, the second describes the behavior between one and three hours, and the third includes the behavior from three hours to a duration of 12 hours.

According to the specifications, three different strain rates and four various strain levels were investigated (cf. Fig. 3.4 and Fig. 3.5). The same qualitative behavior, consisting of a steep stiffness loss at the beginning and an almost horizontal course at later times, could be observed for all configurations. The qualitative behavior can be differentiated according to the three-time intervals. The first interval represents the most loss in stiffness, followed by the second interval, which can be seen as a transition between the first and the last section, and the last interval with a nearly horizontal curve. However, higher initial strain levels appear to cause a steeper course and a greater inclination at later times. This behavior becomes especially apparent when looking at the logarithmic representation of the test results. In general, all test results look qualitatively similar.

Concerning the number of specimens per test set, the following must be noted: Of course, every test that lasts 12 hours also includes the tests that last one or three hours. However, this does not apply the other way around. For this reason, there are more test repetitions for the shorter durations and, consequently, different mean values. For tests with a one-hour duration, at least five repetitions were conducted; for the tests with a three-hour duration, at least three tests were conducted; for the tests with 12 hours duration, at least two tests were conducted (cf. A. A.4).

Similar to the cyclic tests, a residual deformation was left in the specimens after removing them from the test apparatus. Again, this deformation was restored almost completely within approximately one hour after releasing the specimen [165, 231].

Fig. 3.21 shows the test results for a strain rate of 0.01 [1/s] at the four different strain levels 50, 100, 150 and 200 [%], presented in standard and logarithmic representation. Fig. 3.22 shows the test results for strain rates of 0.001, 0.01, 0.1 [1/s] at a strain level of 150 [%], presented in standard and logarithmic representation.

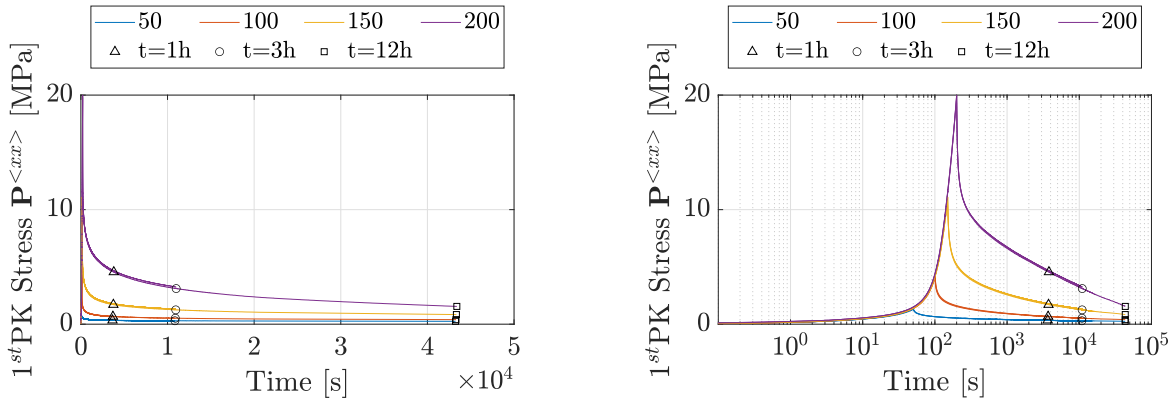

Figure 3.21.: Mean values of different strain levels in standard (left) and logarithmic representation (right)

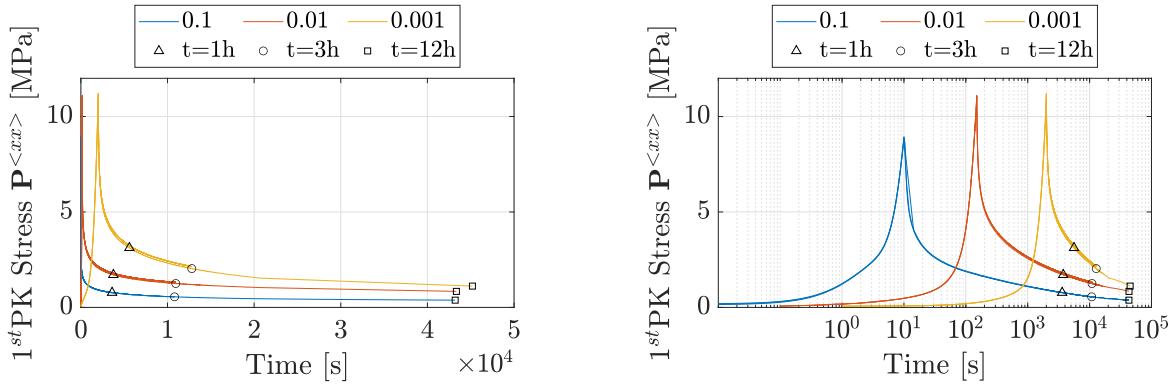

Figure 3.22.: Mean values of different strain rates in standard (left) and logarithmic representation (right)

3.3.4.1. Comparison with Results from Literature

Schuster [231] conducted relaxation tests on various laminated glass interlayers utilizing the specimen geometry recommended by Becker [18]. However, for this discussion, only the results of the Saflex RB41 interlayer, comparable to the B200 NR explored within this thesis, are considered. Before testing, all specimens underwent conditioning at 100 [$°C$] for one hour and subsequently storage at the respective testing climate for a minimum of 12 [h]. The experimental setup featured a Zwick Roell Z050 universal testing machine with a load cell integrated into the Zwick (50 kN, 0.2% relative uncertainty, class 0.5 according to DIN EN ISO 7500-1:2018-06 [94]). Deformation measurements were recorded using the Vic-Gauge-2D camera system from Isi-sys GmbH. The tests were conducted within a climatic chamber to ensure precise control over temperature and humidity. The considered testing conditions were 20 [$°C$] and 50 [%rH]. The specimens were clamped using hydraulic jaws and subjected to a tensile force at a displacement rate of 400 [mm/min] up to 50, 100, and 125 [mm] deformations. Subsequently, these displacement levels were held constant for 1-2 [h].

Elzière [103] conducted a relaxation experiment at 20 [$°C$] loaded at a strain rate of 1 [1/s] up to a strain level of 50 [%] holding the applied strain for 1000 [s]. He utilized the test apparatus described in Sec. 3.3.3.1.

Fig. 3.23 shows the comparison of the relaxation tests conducted in this thesis and the results of Schuster [231] and Elzière [103]. As the longest duration of the tests from the literature was two hours, the relaxation tests from this thesis are only presented for three hours. Furthermore,

assuming incompressibility, the test results from this thesis are transformed to Cauchy stresses to match the presented configuration of the literature results.

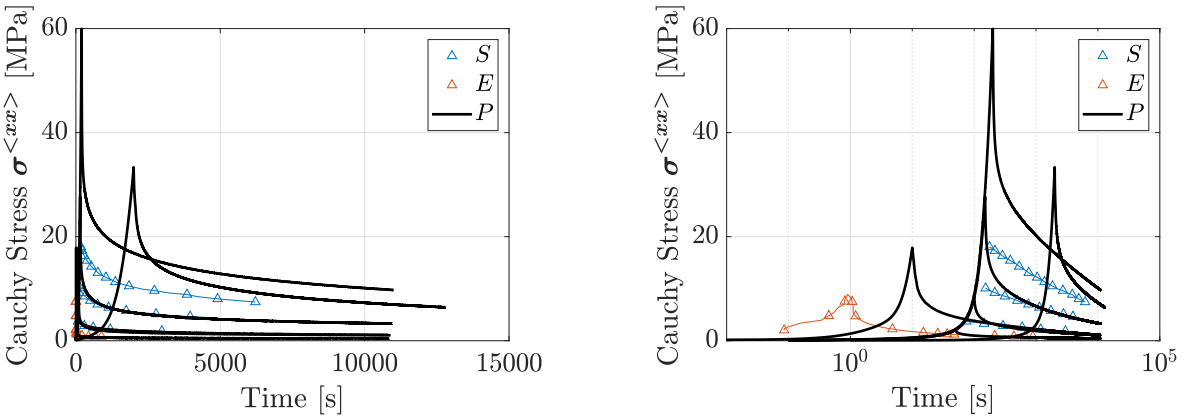

Figure 3.23.: "S" = Schuster; "E" = Elziere; "P" = Pauli

3.3.4.2. Summary of Experiments

Fig. 3.24 shows the results of all cyclic and relaxation tests and the tests until failure at the respective strain rate. Firstly, it is evident that the mean values of the individual tests match each other excellently despite the fluctuations in humidity in the test container. Furthermore, it is interesting that the stress drop over time, shown in the diagram as a vertical curve, approximately spans the height of the associated hysteresis (cf. Fig. 3.24 (left)).

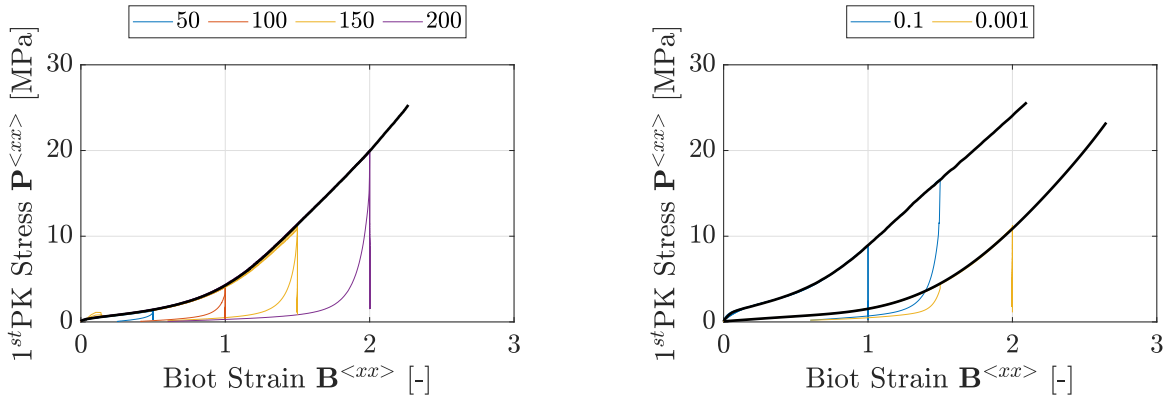

Figure 3.24.: Summary of all cyclic and relaxation tests and the tests until failure at the corresponding strain rate

3.3.5. Staircase-Tests

Fig. 3.25 shows the mean values of 5 tests along for the measure 1^{st}Piola Kirchhoff stress over the corresponding Biot strains (left), and the stresses over time (right). The test results and the evaluation procedure already have been published in [199].

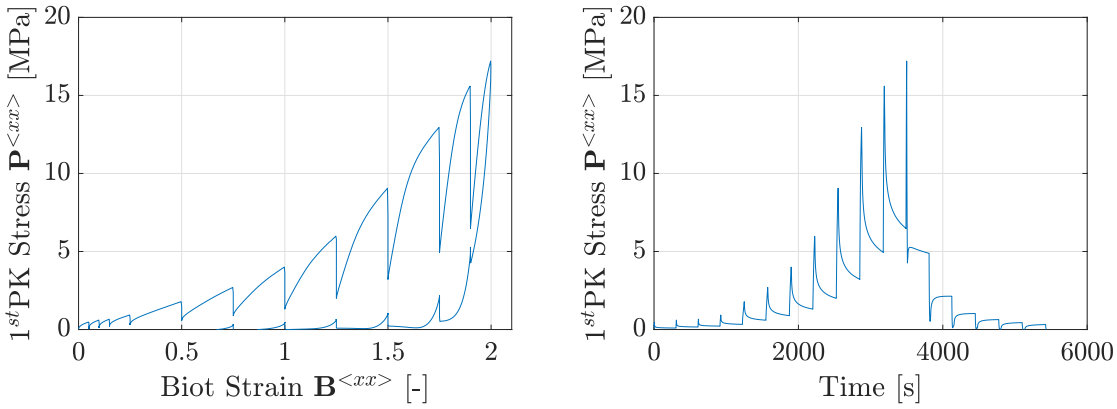

Figure 3.25.: Results of Staircase-Test: Stress over Strain (left), Stress over Time (right)

3.3.5.1. Evaluation of the Staircase Test

The experiments were conducted at a temperature of 21.5±1 [$°C$] and a relative humidity range of 42.5±7.5 [%]. Notably, a noticeable buckling phenomenon manifested within the specimens during the unloading phase, rendering the steps of strain decrease during the unloading cycle unsuitable for validation purposes. Nonetheless, the relaxation characteristics observed during the holding stages remained analyzable. Consequently, by considering both loading and unloading cycles, it became feasible to derive an *equilibrium curve* a theoretical state of material equilibrium governed by elastic principles.

A closer look at Fig. 3.25 shows that the material behavior on the loading branch is different compared to the behavior on the unloading branch. The specimens relax during the holding steps on the loading branch, and the stress decreases - however, the stress increases during the holding steps on the unloading branch. The vertical lines in Fig. 3.25 (left) show the total stress increase and decrease. Plotted over time (cf. Fig. 3.25 (right)), these vertical lines show the course of the decaying and increasing curves. As the loading and unloading path steps are, on purpose, at the same strain value, grouping each holding step at the same strain value in pairs of two (one loading to one unloading part) is reasonable.

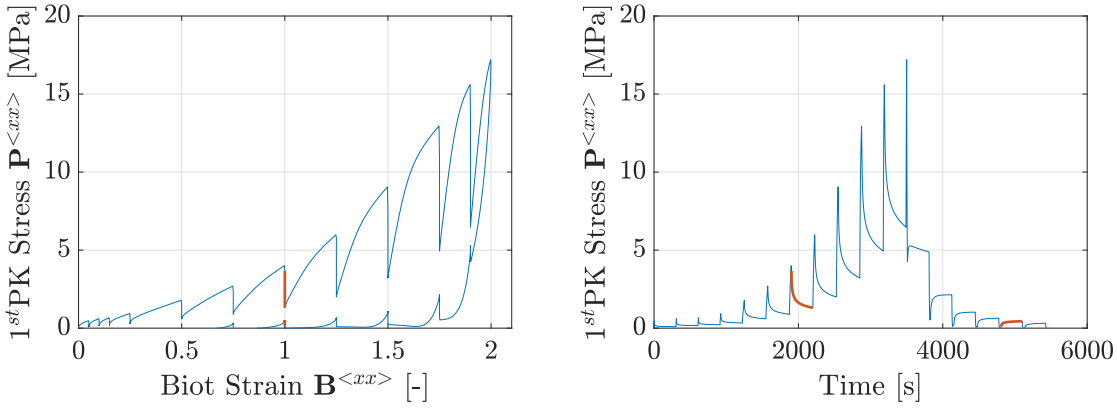

Figure 3.26.: Results of Staircase-Test: Stress over Strain (left), Stress over Time (right); location marked for exemplary evaluation

The pair of related stress increases and decreases at strain step 100 [%] is considered isolated to gather a better understanding (cf. Fig. 3.26). The corresponding stress values of the vertical lines are plotted against the time axis. For a more straightforward presentation, the starting point of both lines is chosen at a fictitious time t = 0 [s] (cf. Fig. 3.27).

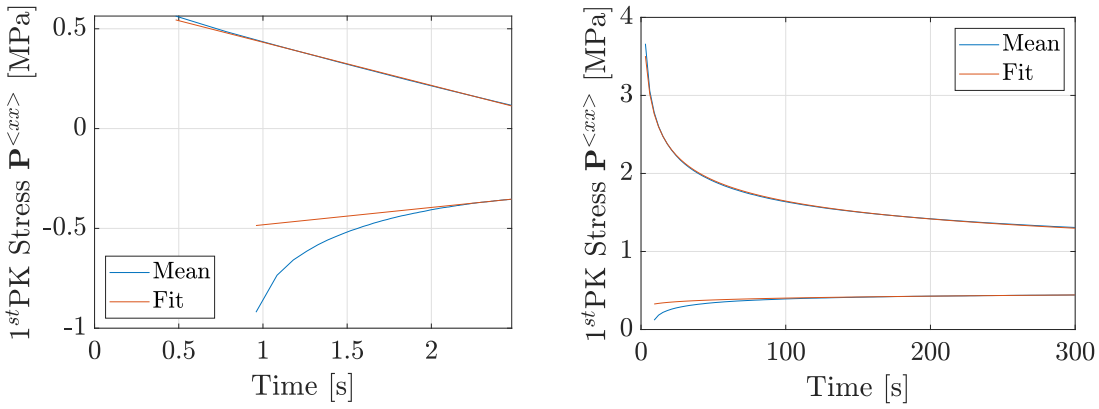

Figure 3.27.: Curve-Fit of relaxation pair: double logarithmic scale (left); normal scale (right)

Considering a double logarithmic presentation (cf. Fig. 3.27 (left)), the curve on the loading branch (upper curve) shows an almost linear course and the curve on the unloading branch shows a nonlinear course in the beginning, but tends to a linear course at a later timestep.

According to the theory of viscoelasticity, the rate-dependent hysteresis gets smaller and smaller if the strain rate gets lower until it ends up in a single curve. According to this theory, the curves on the loading and unloading paths are supposed to meet at some point in time, which is considered to lie on the equilibrium curve.

The loading and unloading curves are fitted to a polynomial function of the first order to anticipate the courses for longer load durations and find the points on the equilibrium curve. Since the behavior of the curve on the unloading branch shows only linear behavior at the end of the holding cycle, the inclination at this point is used to extrapolate the course. Employing the polynomial functions received by the fitting procedure, the intersection of the increasing and decreasing stress curves is calculated (cf. Fig. 3.28 (left)). This procedure is repeated for all pairs of increasing and decreasing stress curves, leading to the representation of the equilibrium curve. Fig. 3.28 (right) shows the points on the equilibrium curve within the total stress over strain curve.

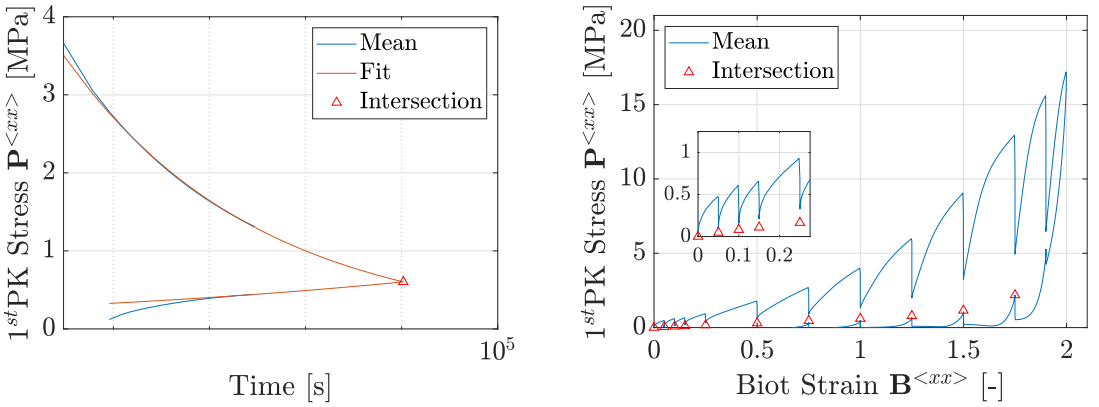

Figure 3.28.: Intersection of exemplary point on logarithmic time scale (left), Plot of intersection points within initial stress strain curve (right)

Notably, only data pairs corresponding to strains equal to or greater than 75 [%] were subjected to the outlined procedure. Values below this threshold were approximated as the mean between the lowest stress value of the relaxation curve and zero stress because the test stopped at a strain level of 75 [%] on the unloading path. Additionally, the data point at 190% strain was excluded from evaluation due to erratic behavior observed in the unloading curve. Nevertheless, the curve is extrapolated linearly to ensure a robust database for material model

calibration (cf. Fig. 3.29 (left)). This extrapolation involves calculating the slope between the last and penultimate intersection points, deriving additional stress points to a final strain of 300%. Subsequently, a fourth-order polynomial function is fitted to the intersection points and evaluated at evenly distributed linear points to serve as a comprehensive database for material model calibration (cf. Fig. 3.29 (right)).

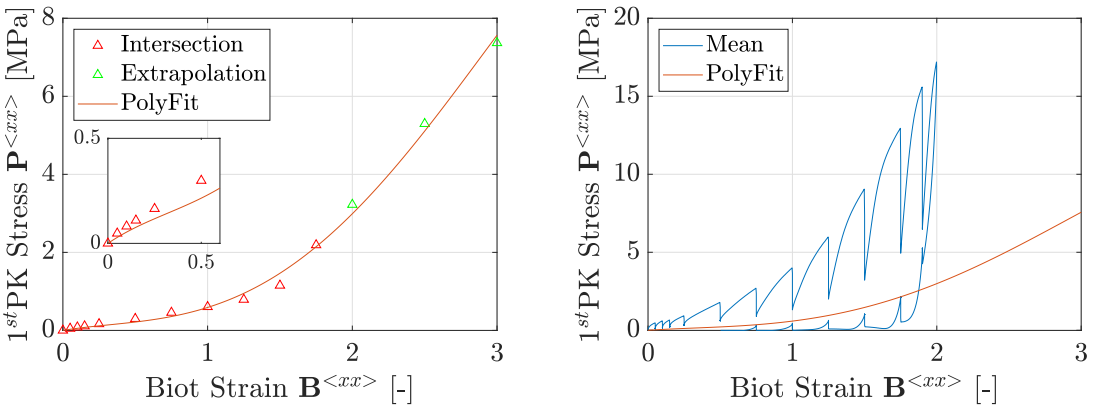

Figure 3.29.: Extrapolation of Intersection Points (left), Poly-Fit within Mean of Measurement (right)

4. Modeling

The phenomena observed in the presented experiments are now to be described with the help of the mechanical equations and material models from Sec. 2.2 and analyzed using the numerical methods presented in Sec. 4.3 are calculated. For this purpose, a three-dimensional, compressible material model of finite viscoelasticity, based on the framework presented in Sec. 2.2.7, is formulated. The relations within the viscosity functions that represent the time-dependent behavior are based on considerations of [171, 235, 225]. However, contrary to the micromechanical formulation, which the models designed for thermoplastics, from chapter 1.2.4, are based on, this model is phenomenologically motivated [169].

The model is reduced to the uniaxial state for the calibration and recalculation of the tests. This procedure considerably speeds up the parameter identification process and is common practice in material modeling [235, 225]. In addition, the kinematic constraint of incompressibility is applied, based on the observations of [165], who determined the Poisson's ratio at room temperature to be nearly 0.5. This boundary condition replaces the volumetric potentials with a Lagrange multiplier formulation. The implemented model is then validated using examples from the literature and analytical solutions.

The required material parameters are calibrated using the test data, and the tests are recalculated based on the validated model. In addition, the model is validated on tests not included in the parameter identification process.

The model already has been presented in Pauli and Siebert [200].

4.1. Model Construction

The model's description is based on the rheological concept of a single Maxwell element, which consists of a spring connected in series with a damper. A spring parallel to the Maxwell element representing the material's infinity stiffness is not employed. This assumption differs from the formulation of the generalized Maxwell model consisting of several Maxwell elements parallel to a single spring, which was used in the literature for the description of PVB [165, 159, 30]. However, omitting the infinity stiffness goes along with the chemical properties of thermoplastics, which do not show any residual stiffness for processes of infinite duration.

The general concept of the Maxwell element illustrates the functionality of linear viscoelasticity and can be transferred to finite viscoelasticity. However, caution is required when describing the kinematics in the case of large deformations. The equations for both theories are listed below to illustrate the parallels and differences between the linear and finite theories and thus demonstrate the transfer from small to large deformations. In both cases, the strain is the control variable. Subsequently, the individual elements of the model formulation developed in this thesis are derived individually and combined.

The kinematics for small deformations follow the linearized Green Lagrange strain tensor $\mathbf{e} = \frac{1}{2}[\mathbf{H} + \mathbf{H}^T]$. Following the rheological model (cf. Fig. 4.1), this is divided additively into an elastic $\mathbf{e}_{el}$ and inelastic part $\mathbf{e}_{in}$.

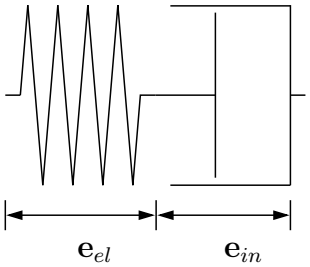

Figure 4.1.: Maxwell Element - small Deformations

The stress within the Maxwell element depends on the applied strain, which in turn depends on time. Therefore, the description of the stress leads to a system consisting of the stress equation and a differential equation that describes the time-dependent kinematics within the Maxwell element. This differential equation is derived from the dissipation inequality and can be solved analytically by integration in the case of small deformations.

Reducing the stress of the three parameter Maxwell model, represented in Eq. 2.71, to the stress of a single Maxwell element following the same evolution equation (Eq. 2.69), leads to implicit description of linear viscoelasticity:

$$\sigma = E_{el}(\varepsilon - \varepsilon_{in}) \tag{4.1}$$

$$\dot{\varepsilon}_{in} = \frac{1}{\eta} E_{el}(\varepsilon - \varepsilon_{in}) \tag{4.2}$$

The explicit formulation of the Maxwell element (Eq. 2.77) leads to the following stress expression

$$\sigma = \int_{s=0}^{s=t} E_{el} e^{-\frac{t-s}{\tau}} \frac{d\varepsilon(s)}{ds} ds, \tag{4.3}$$

where the Kernel function $E_R(t-s) = E_{el} e^{-\frac{t-s}{\tau}}$, presented in Eq. 2.78, corresponds to the relaxation modulus which is utilized within the *Prony series*, commonly used to describe the time-dependent behavior of PVB within the regime of small deformations.

Considering large deformations, however, linearizing the Green Lagrange strain tensor and, therefore, a simple additive split is no longer possible. Following the general framework presented in Sec. 2.2.7, the additive split of the deformation is now formulated on a fictive intermediate configuration between reference and current state. The strain tensor $\hat{\mathbf{\Gamma}} = \frac{1}{2}\left(\mathbf{F}_{el}^T\mathbf{F}_{el} - \mathbf{F}_{in}^{-T}\mathbf{F}_{in}^{-1}\right) = \hat{\mathbf{\Gamma}}_{el} + \hat{\mathbf{\Gamma}}_{in}$ results in an elastic part of the Green type $\hat{\mathbf{\Gamma}}_{el} = \frac{1}{2}\left(\mathbf{F}_{el}^T\mathbf{F}_{el} - \mathbf{1}\right)$, and an inelastic part of the Almansi type $\hat{\mathbf{\Gamma}}_{in} = \frac{1}{2}\left(\mathbf{1} - \mathbf{F}_{in}^{-T}\mathbf{F}_{in}^{-1}\right)$. The corresponding rheological model is presented in Fig. 4.2.

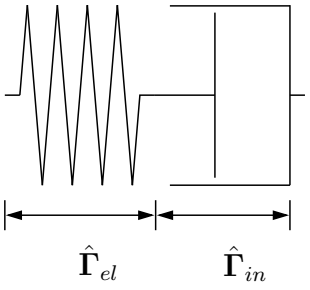

Figure 4.2.: Maxwell Element - large Deformations

The formulation of the theory of finite viscoelasticity results in the following system of equations consisting of the stress formulation (cf. Eq. 2.123) and the evolution equation (cf. Eq. 2.124):

$$\mathbf{T}_M = 2\hat{J}_{el}^{-2/3}\frac{\partial\hat{\Psi}_{iso}^{ov}(\mathrm{I}_{\hat{\boldsymbol{C}}_{el}})}{\partial\mathrm{I}_{\hat{\boldsymbol{C}}_{el}}}\Big[\boldsymbol{C}_{in}^{-1}-\frac{1}{3}\Big(\boldsymbol{C}_M:\boldsymbol{C}_{in}^{-1}\Big)\boldsymbol{C}_M^{-1}\Big]+\Big[\frac{\partial\hat{\Psi}_{vol}^{ov}(\hat{J}_{el})}{\partial\hat{J}_{el}}\hat{J}_{el}\Big]\boldsymbol{C}_M^{-1} \tag{4.4}$$

$$\dot{\mathbf{C}}_{in} = \frac{4}{\eta_D}\hat{J}_{el}^{-2/3}\frac{\partial\hat{\Psi}_{iso}^{ov}(\mathrm{I}_{\hat{\boldsymbol{C}}_{el}})}{\partial\mathrm{I}_{\hat{\boldsymbol{C}}_{el}}}\Big[\boldsymbol{C}_M-\frac{1}{3}\Big(\boldsymbol{C}_M:\boldsymbol{C}_{in}^{-1}\Big)\boldsymbol{C}_{in}\Big]+\frac{2}{\eta_V}\Big[\frac{\partial\hat{\Psi}_{vol}^{ov}(\hat{J}_{el})}{\partial\hat{J}_{el}}\hat{J}_{el}\Big]\boldsymbol{C}_{in} \tag{4.5}$$

Following the rheological considerations of the generalized Maxwell model, which contains a series of single Maxwell elements, leads to the total stress equal to the sum of particular stress portions, each following a respective evolution equation. Transferring a single Maxwell element to a series of Maxwell elements applies to small deformations in the same way as for large deformations. Concerning finite viscoelasticity, the following system of equations arises:

$$\mathbf{T}_M = \sum_{i=1}^{n}\Big\{2\hat{J}_{el}^{-2/3,(i)}\frac{\partial\hat{\Psi}_{iso}^{ov,(i)}(\mathrm{I}_{\hat{\boldsymbol{C}}_{el}^{(i)}})}{\partial\mathrm{I}_{\hat{\mathbf{C}}_{el}^{(i)}}}\Big[\Big(\mathbf{C}_{in}^{-1,(i)}-\frac{1}{3}\Big(\mathbf{C}_M:\mathbf{C}_{in}^{-1,(i)}\Big)\mathbf{C}_M^{-1}\Big]+\Big[\frac{\partial\hat{\Psi}_{vol}^{ov,(i)}(\hat{J}_{el}^{(i)})}{\partial\hat{J}_{el}^{(i)}}\hat{J}_{el}^{(i)}\Big]\mathbf{C}_M^{-1}\Big\}$$

$$\dot{\mathbf{C}}_{in}^{(i)} = \frac{4}{\eta_D}\hat{J}_{el}^{-2/3,(i)}\frac{\partial\hat{\Psi}_{iso}^{ov,(i)}(\mathrm{I}_{\hat{\boldsymbol{C}}_{el}^{(i)}})}{\partial\mathrm{I}_{\hat{\boldsymbol{C}}_{el}^{(i)}}}\Big[\boldsymbol{C}_M-\frac{1}{3}\Big(\boldsymbol{C}_M:\boldsymbol{C}_{in}^{-1,(i)}\Big)\boldsymbol{C}_{in}^{(i)}\Big]+\frac{2}{\eta_V}\Big[\frac{\partial\hat{\Psi}_{vol}^{ov,(i)}(\hat{J}_{el}^{(i)})}{\partial\hat{J}_{el}^{(i)}}\hat{J}_{el}^{(i)}\Big]\boldsymbol{C}_{in}^{(i)}$$

Within this system of equations, the formulation of the potentials and the viscosities is variable. Furthermore, the number of elements within the sum is freely selectable.

The following selection of the hyperelastic potential functions is based on the possibilities presented in Sec. 2.2.1, and together with the viscosity formulation and the number of elements, aims that the model describes the characteristic observations made during the experiments in the best possible way. Furthermore, the model follows the concept established by Bergström and Boyce [25], Boyce et al. [33, 34], and the selected potentials and viscosity function are categorized into a multi-network consisting of three single networks, A, B, and C, each corresponding to characteristics on a molecular level. However, in this case, the characteristic of each network is based on phenomenological considerations rather than micromechanics.

The main findings from the experimental investigations can be categorized according to the strain rate tensor, the driving quantity, and the corresponding testing procedures. The investigation of the strain-rate-dependent behavior revealed a rate-dependent initial stiffness, followed by a decrease in stiffness in the regime of moderate deformations and a considerable hardening concerning large strains. The cyclic experiments exposed a decisive difference in stiffness for loading and unloading, with unloading showing a much softer material response. The relaxation processes revealed a sharp drop in stiffness within the first seconds after reaching the holding strain level. This drop was followed by a transition region concerning moderate durations and a continuous but weak decline in stiffness for long durations. However, the inclination within the regime of long durations strongly depends on the strain level approached in the relaxation process.

With the Neo Hookean and the Yeoh potential, two functions based on the first invariant of the Cauchy Green tensor are selected, a reasonable assumption concerning the experiments conducted in the uniaxial stress state. The Yeoh potential, following a polynomial description of higher order compared to the Neo Hooken model, shows higher accuracy, with the disadvantage of a more complex formulation. However, in general, both potentials show similar computation time and convergence performance.

The viscosity functions within the model are characterized by shear modulus and relaxation time, enriched by particular tensor functions based on internal mechanisms (cf. [169, 214, 236]). Individual relaxation times are generally classified into several decades to ensure a smooth progression across a broad time scale. They are characterized by different relaxation times and incorporate internal mechanisms. There are several mechanisms that all elements have in common. However, some are individually engineered for selected elements only. The common features are introduced briefly in the following section. The individual components will be picked up at their respective locations in the description of the single elements.

The first scalar-valued tensor function (cf. Eq. 4.6) that is applied to all three networks amplifies the viscosity as strains intensify gradually. This approach enhances viscosity in the regime of increasing strains and was also used by Sedlan and Haupt [236] and Lion [171].

$$f(||\mathbf{C}_M||) = \mu\Big(\frac{||\mathbf{C}_M||}{\sqrt{3}}\Big)^{\chi} \tag{4.6}$$

Fig. 4.3 shows an example for Eq. 4.6 for values of $\mathbf{C_M} = [1.7321 : 9.0123]$, values for $\chi = [0.1; 1; 2; 5; 10]$, and $\mu = 10$. The graph emphasizes the influence of the tensor function on the shear modulus μ with respect to the stretch λ, considering incompressible material behavior and an uniaxial stress state.

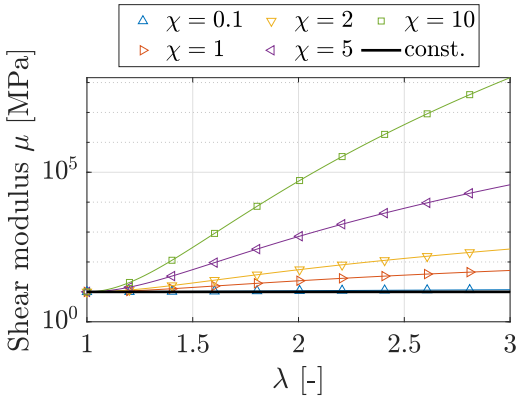

Figure 4.3.: Examplary calculation for the first viscosity element

A further key element is the utilization of a signum function, dependent on the Frobenius scalar product $\mathbf{D}_M : \mathbf{C}_M$ of the deformation rate tensor $\mathbf{D}_M$ and the right Cauchy Green tensor $\mathbf{C}_M$. This scalar-valued tensor function enables a different material response for loading and unloading behaviors. This procedural concept is a crucial element for capturing the observed hystereses and was recommended by Bergström [23].

$$f(\mathbf{C}_M, \mathbf{D}_M) = \tau\frac{1}{2}\Big(1 + sign(\mathbf{D}_M : \mathbf{C}_M)\Big) \tag{4.7}$$

Fig. 4.4 presents an exemplary calculation for Eq. 4.7 considering values for $(\mathbf{D}_M : \mathbf{C}_M) = [1]$ for $t = [0 : 100]$ and $(\mathbf{D}_M : \mathbf{C}_M) = [-1]$ for $t = [101 : 200]$ to illustrate the behavior of the signums function regarding the relaxation time. The unaffected relaxation time τ equals constantly 100 [s] while the tensor function forces the relaxatio time to take the value zero for processes with negative values of the trace of the strain rate tensor.

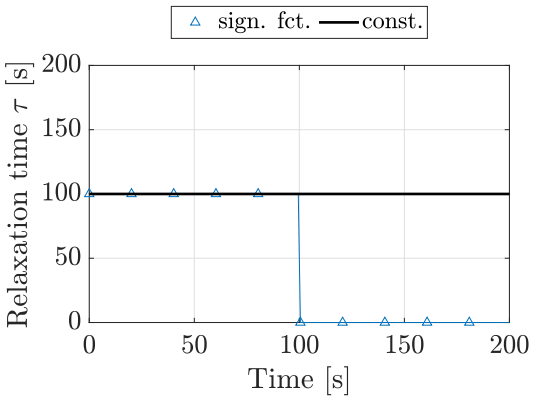

Figure 4.4.: Examplary calculation for the second viscosity element

The last key element that is shared by all networks is a scalar-valued tensor function that utilized a formulation based on an exponential function. It depends on the Frobenius norm of the deformation rate tensor $\mathbf{D}_M$ and captures the rate dependency on the unloading paths. This element was also used by Scheffer et al. [226].

$$f(||\mathbf{D}_M||) = \tau + exp\Big(\zeta||\mathbf{D}_M||\Big)\xi \tag{4.8}$$

Fig. 4.5 shows the impact of the third tensor function on the relaxtion time, utilizing parameter values $\xi = [1, 5, 10, 20, 50]$ considering $||(D)|| = [1]$.

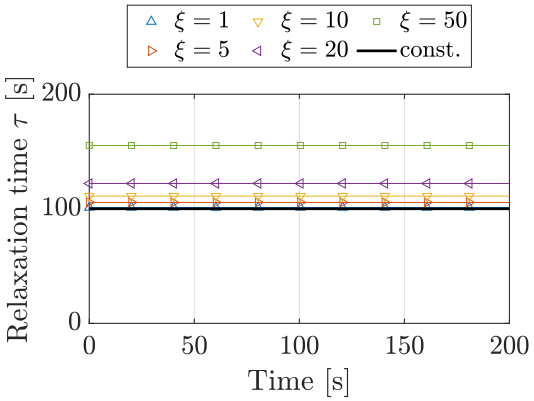

Figure 4.5.: Examplary calculation for the third viscosity element

These features are designed for one particular temperature and are only valid for this temperature. However, although it is not utilized within this work, the structure to consider different temperatures is already introduced by incorporating a temperature-dependent viscosity parameter denoted as η_0, as outlined in the works of Lion [171], Heimes [127]. This parameter is implemented in every network and plays a crucial role in capturing the impact of temperature variations on the material's behavior. However, it is essential to notice that these considerations hold for various isothermal temperature processes without considering entropy.

As described in the last paragraphs, the model structure and the respective features serve as the fundamental framework for each network (cf. Eq. 4.4 and Eq. 4.4). However, in certain instances, this structure is subject to modifications. Consequently, the following sections provide individual and detailed descriptions of each network.

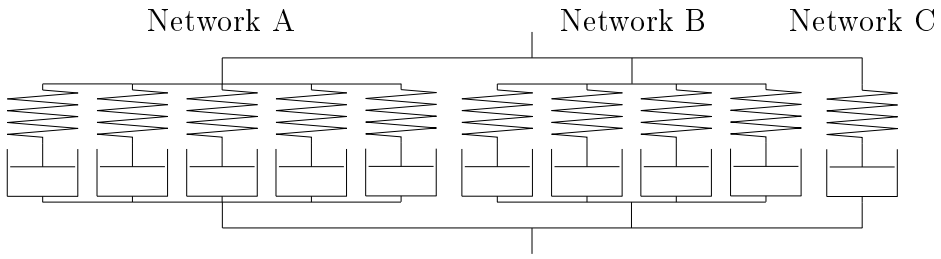

Figure 4.6.: Rheological elements of the Network Model

Network A mainly describes the initial, time-dependent stiffness and the material softening in the region of moderate deformations. Its elastic response follows the Neo-Hookean potential, and besides the mechanisms described in the last paragraph, each viscosity function is enriched by a scalar-valued tensor function, which aligns with the approach proposed by [169] to facilitate the rapid decay of initial stiffness within the region of moderate deformations. It dependes on the 2^{nd}PK stress tensor and results in:

$$f(||\mathbf{T}_M||) = \tau exp\Big(-\frac{||\mathbf{T}_M||}{s_0}\Big) \tag{4.9}$$

It employs an exponential function coupled with a stress threshold that, when surpassed, decreases viscosity, resulting in a reduced initial stiffness. To illustrate the functionality of the tensor function, described in Eq. 4.9, an example is depicted in Fig. 4.7. It shows the course of a relaxation time τ with respect to a stress tensor of $||\mathbf{T}_M|| = [0 : 50]$ and values for $s_0 = [1; 5; 10; 20; 50]$.

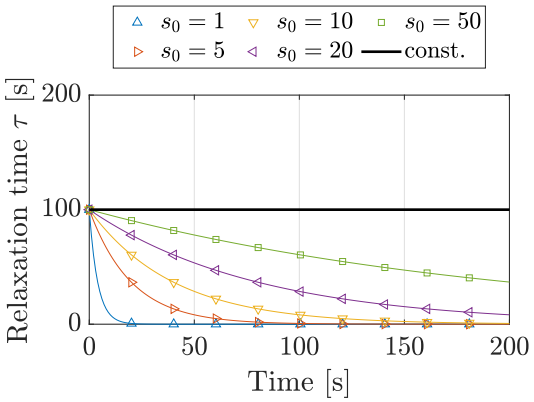

Figure 4.7.: Examplary calculation for the fourth viscosity element

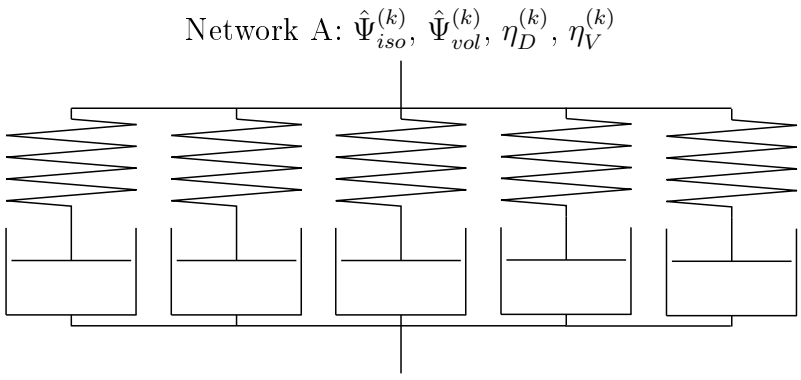

Figure 4.8.: Rheological elements of Network A

The potential and viscosity function of network A apply for first five (k=1 to 5) Maxwell element of the model (cf. 4.6) and are presented below.

$$\hat{\Psi}_{iso}^{(k)} = \frac{\mu^{(k)}}{2}(\mathrm{I}_{\hat{\mathbf{C}}_{el}^{(k)}} - 3)$$
$$\hat{\Psi}_{vol}^{(k)} = \frac{\kappa^{(k)}}{2}(\hat{J}_{el}^{(k)} - 1)^2$$
$$\eta_D^{(k)} = \eta_0^{(k)}\mu^{(k)}\Big(\frac{||\mathbf{C}_M||}{\sqrt{3}}\Big)^{\chi^{(k)}}\Big[\frac{1}{2}\tau^{(k)}exp\Big(-\frac{||\mathbf{T}_M||}{s_0^{(k)}}\Big)\Big(1 + sign(\mathbf{D}_M : \mathbf{C}_M)\Big) + exp\Big(\zeta^{(k)}||\mathbf{D}_M||\Big)\xi^{(k)}\Big]$$
$$\eta_V^{(k)} = \eta_D^{(k)}\frac{\kappa^{(k)}}{\mu^{(k)}}$$

Network B is supposed to describe the material behavior over long durations, which is why the larger relaxation times are assigned to it. Moreover, the viscosity function only contains the essential elements (tensorfunction 1 - 3) described in the introduction of the general model structure. The Neo-Hookean potential covers the elastic response.

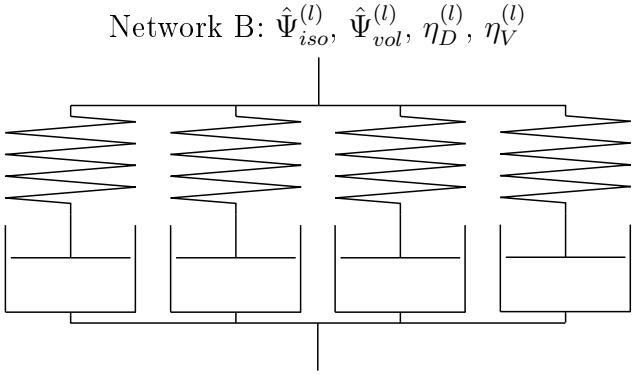

Figure 4.9.: Rheological elements of Network B

The potential and viscosity function of network B apply the Maxwell elements six to nine (l=1 to 4) of the model (cf. 4.6) and are presented below.

$$\hat{\Psi}_{iso}^{(l)} = \frac{\mu^{(l)}}{2}(\mathrm{I}_{\hat{\mathbf{C}}_{el}^{(l)}} - 3)$$
$$\hat{\Psi}_{vol}^{(l)} = \frac{\kappa^{(l)}}{2}(\hat{J}_{el}^{(l)} - 1)^2$$
$$\eta_D^{(l)} = \eta_0^{(l)}\mu^{(l)}\Big(\frac{||\mathbf{C}_M||}{\sqrt{3}}\Big)^{\chi^{(l)}}\Big[\frac{1}{2}\tau^{(l)} \cdot \Big(1 + sign(\mathbf{D}_M : \mathbf{C}_M)\Big) + exp\Big(\zeta^{(l)}||\mathbf{D}_M||\Big)\xi^{(l)}\Big]$$
$$\eta_V^{(l)} = \eta_D^{(l)}\frac{\kappa^{(l)}}{\mu^{(l)}}$$

Network C adopts a modified Yeoh potential, with coefficients C_{10} and C_{20} set to zero [226]. This modification is utilized to reduce the influence of network C on the material response in the area of small and moderate deformations to a minimum. A further essential addition to Network C is the enrichment of the viscosity function by a further scalar-valued tensor function depending on $\mathbf{D}_M$. This function is designed to significantly reduce the viscosity during relaxation processes.

$$f(||\mathbf{D}_M||) = \tau\Big|1 - exp(||\mathbf{D}_M||)\Big| \tag{4.10}$$

The mechanism of Eq. 4.10 ensures that the stress response of Network C is not overestimated, even though a considerable large relaxation time is assigned to it. Fig. 4.10 illustrates the impact of the tensor functino on the relaxation time, considering $||\mathbf{D}|| = [1]$ for the time $t = [0 : 100]$, and $||\mathbf{D}|| = [0]$ for the time $t = [101 : 200]$.

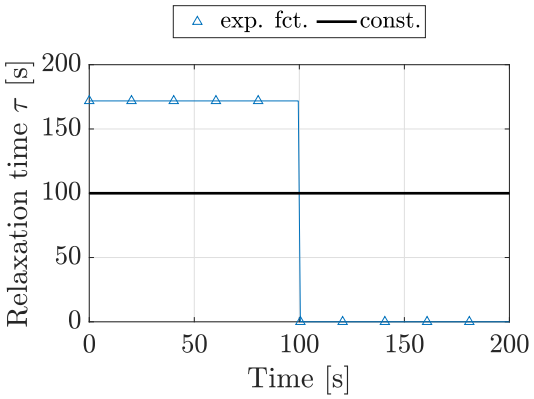

Figure 4.10.: Examplary calculation for the fifth viscosity element

Network C: $\hat{\Psi}_{iso}^{(m)}$, $\hat{\Psi}_{vol}^{(m)}$, $\eta_D^{(m)}$, $\eta_V^{(m)}$

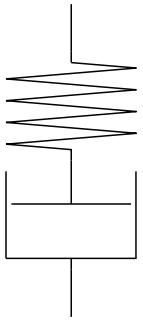

Figure 4.11.: Network C

The potential and viscosity function of network C apply to the 10^{th} Maxwell element (m=1) of the model (cf. 4.6) and are presented below.

$$\hat{\Psi}_{iso}^{(m)} = C_{30}^{(m)}(\mathrm{I}_{\hat{\mathbf{C}}_{el}^{(m)}} - 3)^3$$

$$\hat{\Psi}_{vol}^{(m)} = \frac{\kappa^{(m)}}{2}(\hat{J}_{el}^{(m)} - 1)^2$$

$$\eta_D^{(m)} = \eta_0^{(m)}\mu^{(m)}\left(\frac{||\mathbf{C}_M||}{\sqrt{3}}\right)^{\chi^{(m)}}\left[\frac{1}{2}\tau^{(m)} \cdot \left(1 + sign(\mathbf{D}_M : \mathbf{C}_M)\right) \cdot \left|1 - \gamma^{(m)}exp(||\mathbf{D}_M||)\right| + \right.$$
$$\left. + exp\left(\zeta^{(m)}||\mathbf{D}_M||\right)\xi^{(m)}\right]$$

$$\eta_V^{(m)} = \eta_D^{(m)}\frac{\kappa^{(m)}}{\mu^{(m)}}$$

In summary, with its diverse potential functions and carefully engineered viscosity mechanisms, this multi-network model presents a robust and adaptable framework for describing the time- and temperature-dependent material behavior of PVB at large strains.

Finally, the complete model consists of the sum of single stress elements and their respective evolution equations according to the single networks: Network A consists of 5 elements, network B consists of 4 elements, and Network C consists of 1 element.

$$\mathbf{T}_M = \sum_{k=1}^{5}\Big\{\hat{J}_{el}^{-2/3,(k)}\mu^{(k)}\Big[\Big(\mathbf{C}_{in}^{-1,(k)} - \frac{1}{3}\Big(\mathbf{C}_M : \mathbf{C}_{in}^{-1,(k)}\Big)\mathbf{C}_M^{-1}\Big] + \kappa^{(k)}\Big[(\hat{J}_{el}^{(k)} - 1)\hat{J}_{el}^{(k)}\Big]\mathbf{C}_M^{-1}\Big\}$$
$$+ \sum_{l=1}^{4}\Big\{\hat{J}_{el}^{-2/3,(l)}\mu^{(l)}\Big[\Big(\mathbf{C}_{in}^{-1,(l)} - \frac{1}{3}\Big(\mathbf{C}_M : \mathbf{C}_{in}^{-1,(l)}\Big)\mathbf{C}_M^{-1}\Big] + \kappa^{(l)}\Big[(\hat{J}_{el}^{(l)} - 1)\hat{J}_{el}^{(l)}\Big]\mathbf{C}_M^{-1}\Big\} +$$
$$+ 6\sum_{m=1}^{1}\Big\{\hat{J}_{el}^{-2/3,(m)}C_{30}^{(m)}(\mathrm{I}_{\hat{\mathbf{C}}_{el}^{(m)}} - 3)^2\Big[\Big(\mathbf{C}_{in}^{-1,(m)} - \frac{1}{3}\Big(\mathbf{C}_M : \mathbf{C}_{in}^{-1,(m)}\Big)\mathbf{C}_M^{-1}\Big] +$$
$$+ \kappa^{(m)}\Big[(\hat{J}_{el}^{(m)} - 1)\hat{J}_{el}^{(m)}\Big]\mathbf{C}_M^{-1}\Big\}$$

The evolution equations of the individual networks determined by the corresponding viscosity functions are presented below for each network (considering $\mu^{(m)} = 2C_{30}^{(m)}$).

$$\dot{\mathbf{C}}_{in}^{(k)} = \frac{2\hat{J}_{el}^{-2/3,(k)}\Big[\mathbf{C}_M - \frac{1}{3}\Big((\mathbf{C}_M : \mathbf{C}_{in}^{-1,(k)})\mathbf{C}_{in}^{(k)}\Big)\Big] + 2\mu^{(k)}\Big[(\hat{J}_{el}^{(k)} - 1)\hat{J}_{el}^{(k)}\Big]\mathbf{C}_{in}^{(k)}}{\eta_0^{(k)}\Big(\frac{||\mathbf{C}_M||}{\sqrt{3}}\Big)^{\chi^{(k)}}\Big[\frac{1}{2}\tau^{(k)}exp\Big(-\frac{||\mathbf{T}_M||}{s_0^{(k)}}\Big)\Big(1 + sign(\mathbf{D}_M : \mathbf{C}_M)\Big) + exp\Big(\zeta^{(k)}||\mathbf{D}_M||\Big)\xi^{(k)}\Big]}$$

$$\dot{\mathbf{C}}_{in}^{(l)} = \frac{2\hat{J}_{el}^{-2/3,(l)}\Big[\mathbf{C}_M - \frac{1}{3}\Big((\mathbf{C}_M : \mathbf{C}_{in}^{-1,(l)})\mathbf{C}_{in}^{(l)}\Big)\Big] + 2\mu^{(l)}\Big[(\hat{J}_{el}^{(l)} - 1)\hat{J}_{el}^{(l)}\Big]\mathbf{C}_{in}^{(l)}}{\eta_0^{(l)}\Big(\frac{||\mathbf{C}_M||}{\sqrt{3}}\Big)^{\chi^{(l)}}\Big[\frac{1}{2}\tau^{(l)} \cdot \Big(1 + sign(\mathbf{D}_M : \mathbf{C}_M)\Big) + exp\Big(\zeta^{(l)}||\mathbf{D}_M||\Big)\xi^{(l)}\Big]}$$

$$\dot{\mathbf{C}}_{in}^{(m)} =$$
$$= \frac{6(\mathrm{I}_{\hat{\mathbf{C}}_{el,m}} - 3)^2\hat{J}_{el}^{-2/3,(m)}\Big[\mathbf{C}_M - \frac{1}{3}\Big((\mathbf{C}_M : \mathbf{C}_{in}^{-1,(m)})\mathbf{C}_{in}^{(m)}\Big)\Big] + 2\mu^{(m)}\Big[(\hat{J}_{el}^{(m)} - 1)\hat{J}_{el}^{(m)}\Big]\mathbf{C}_{in}^{(m)}}{\eta_0^{(m)}\Big(\frac{||\mathbf{C}_M||}{\sqrt{3}}\Big)^{\chi^{(m)}}\Big[\frac{1}{2}\tau^{(m)} \cdot \Big(1 + sign(\mathbf{D}_M : \mathbf{C}_M)\Big) \cdot \Big|1 - \gamma^{(m)}exp(||\mathbf{D}_M||)\Big| + exp\Big(\zeta^{(m)}||\mathbf{D}_M||\Big)\xi^{(m)}\Big]}$$

In order to implement the material model in an FE code, it is useful to bear in mind the primary considerations of the finite element method, which is based on the principle of virtual work. There are several ways to approach the virtual work formulation. However, in the following, the derivation based on the potential energy is depicted briefly. The following derivation is extracted from Bonet and Wood [29], de Borst et al. [63]. The total potential energy at the stationary point ϕ reads

$$\Pi(\phi) = \int_V \Psi(\mathbf{C})dV - \int_V \tilde{\mathbf{b}}_R \cdot \phi dV - \int_{\partial V} \tilde{\mathbf{t}}_R \cdot \phi dA, \tag{4.11}$$

and the derivative of Eq. 4.11 in the arbitrary direction $\delta\mathbf{v}$ (subsequently assumed to be a virtual velocity) results in the expression of the virtual work

$$D\Pi(\phi)[\delta\mathbf{v}] = \int_V \mathbf{T} : D\mathbf{E}[\delta\mathbf{v}]dV - \int_V \tilde{\mathbf{b}}_R \cdot \delta\mathbf{v}dV - \int_A \tilde{\mathbf{t}}_R \cdot \delta\mathbf{v}dA = 0, \tag{4.12}$$

which can be split into an internal and external part

$$D\Pi(\phi)[\delta\mathbf{v}] = \delta W(\phi, \delta\mathbf{v}) = \delta W_{int}(\phi, \delta\mathbf{v}) + W_{ext}(\phi, \delta\mathbf{v}) \tag{4.13}$$

In order to solve the problem of virtual work numerically using the Newton-Raphson Method, a linearization Eq. 4.13 is required. This linearization equals the derivative of the virtual work at the stationary point ϕ in the direction of the incremental change $\mathbf{u}$. After some reformulations, the linearized internal work in Lagrangian representation results in

$$D\delta W_{int}(\phi, \delta\mathbf{v})[u] = \int_V D\mathbf{E}[\delta\mathbf{v}] : \mathbb{C} : D\mathbf{E}[\mathbf{u}]dV + \int_V \mathbf{T} : [(\nabla_R \mathbf{u})^T \nabla_R \delta\mathbf{v}]dV. \tag{4.14}$$

Furthermore, assuming the body force $\tilde{\mathbf{b}}$ to be the gravity loading $\rho\tilde{\mathbf{g}}$, and the traction force $\tilde{\mathbf{t}}$ to be the uniform normal pressure p, the linearization of the external work yields

$$D\delta W_{ext}(\phi, \delta\mathbf{v})[u] = \int_V \rho_R \tilde{\mathbf{g}} \cdot \delta\mathbf{v} dV + \mathbf{F}^{-T}\Big[\int_a p\mathbf{n} \cdot \delta\mathbf{v} da\Big]\mathbf{F}^{-1}. \tag{4.15}$$

The linearization of the internal work leads to the stiffness matrix of the material

$$\mathbb{C} = \mathbb{C}^{ov}_{iso} + \mathbb{C}^{ov}_{vol}, \tag{4.16}$$

containing

$$\mathbb{C}^{ov}_{iso} = 2\frac{\partial \mathbf{T}^{ov}_{iso}(\mathbf{C}, \mathbf{C}_{in})}{\partial \mathbf{C}} = 2\frac{\partial \mathbf{T}^{ov}_{iso}}{\partial \mathbf{C}_{in}} : \frac{\partial \mathbf{C}_{in}}{\partial \mathbf{C}} + 2\frac{\mathbf{T}^{ov}_{iso}}{\partial \mathbf{C}}, \tag{4.17}$$

and

$$\mathbb{C}^{ov}_{vol} = 2\frac{\partial \mathbf{T}^{ov}_{vol}(\mathbf{C}, \mathbf{C}_{in})}{\partial \mathbf{C}} = 2\frac{\partial \mathbf{T}^{ov}_{vol}}{\partial \mathbf{C}_{in}} : \frac{\partial \mathbf{C}_{in}}{\partial \mathbf{C}} + 2\frac{\mathbf{T}^{ov}_{vol}}{\partial \mathbf{C}}. \tag{4.18}$$

The principles presented above represent the fundamental equations of the finite element method to give the reader an understanding of the point at which the material model presented starts. In order to implement this model in a commercial FE code (Ansys, Abaqus) using a user-defined material subroutine (UMat), the tangent operators must be written down and implemented. This operation is not be explained further. Instead, this work aims to provide a material model and the corresponding material parameters for PVB considering large deformations concerning time. For this purpose, only the evolution equation has to be linearized to describe the inelastic strain's incremental development. Under the simplified assumption of incompressibility, this operation is carried out in the following sections for the uniaxial stress state to create the basic framework for parameter identification.

4.2. Uniaxial Reduction and Numerical Implementation

For further investigations and parameter identification, the model is significantly simplified by assuming incompressible material behavior and reducing it to the uniaxial stress state. Based on these simplifications, the model structure is finally implemented numerically. Additionally only one temperature is considered and, therefore, $\mathbf{C}_M$ and $\mathbf{D}_M$ are equal to $\mathbf{C}$ and $\mathbf{D}$.

4.2.1. Incompressibility Constraint

So far, the model follows a compressible formulation, resulting in a strict separation into isochoric and volumetric parts. However, as investigated by [165] and [231] the Poisson's ratio of PVB is close to 0.5, and therefore, the assumption of incompressible material behavior is reasonable. Considering the incompressibility constraint prohibits changes in the volume of the material. Consequently, the determinant of the deformation gradient J must equal one. This assumption also holds for the elastic and the inelastic part of the deformation gradient ($J = J_{el} = J_{in} = 1$). Considering $J = 1$, the separation of the deformation gradient into volumetric and isochoric parts as presented in Eq. 2.17 becomes obsolete ($\mathbf{C} = \bar{\mathbf{C}}$), and in consequence, the derivative of the isochoric energy potential (compare Eq. 2.112) simplifies considerably:

$$\mathbf{T}_{iso} = 2\frac{\partial \Psi_{iso}(\mathrm{I}_{\mathbf{C}})}{\partial \mathbf{C}} = 2\frac{\partial \Psi_{iso}(\mathrm{I}_{\mathbf{C}})}{\partial \mathrm{I}_{\mathbf{C}}}\frac{\partial \mathrm{I}_{\mathbf{C}}}{\partial \mathbf{C}} : \frac{\partial \mathbf{C}}{\partial \mathbf{C}} = 2\frac{\partial \Psi_{iso}(\mathrm{I}_{\mathbf{C}})}{\partial \mathrm{I}_{\mathbf{C}}} \tag{4.19}$$

However, it is essential to note that the equilibrium requirements must still be satisfied. A common approach is replacing the hydrostatic stress derived from the volumetric part of the energy potential Ψ_{vol} by the Lagrange multiplier p. Following the Total Lagrange formulation, p, defined on the current configuration, is pulled back to the reference configuration (cf. Eq. 2.4).

$$\mathbf{T}_{vol} = p\mathbf{C}^{-1} \tag{4.20}$$

The sum of the isochoric and the volumetric part of the stress results in the following formulation of the total stress:

$$\mathbf{T} = \mathbf{T}_{iso} + \mathbf{T}_{vol} = 2\frac{\partial \hat{\Psi}^{ov}_{iso}(\mathrm{I}_{\hat{\mathbf{C}}_{el}})}{\partial \mathrm{I}_{\hat{\mathbf{C}}_{el}}}\mathbf{C}^{-1}_{in} + p\mathbf{C}^{-1}$$

Following the incompressibility constraint, which prohibits volumetric deformations, yields a deviatoric expression of the evolution equation. Based on this consideration, the volumetric part of Eq. 2.120 is erased, and the evolution equation for incompressible material behavior results in:

$$\dot{\mathbf{C}}_{in} = \frac{4}{\eta_D}\frac{\partial \hat{\Psi}^{ov}_{iso}(\mathrm{I}_{\hat{\mathbf{C}}_{el}})}{\partial \mathrm{I}_{\hat{\mathbf{C}}_{el}}}\Big[\mathbf{C} - \frac{1}{3}\Big(\mathbf{C} : \mathbf{C}^{-1}_{in}\Big)\mathbf{C}_{in}\Big]$$

The complete model structure considering the incompressibility constraint results in the following expression:

$$\mathbf{T} = \sum_{k=1}^{5}\Big\{\mu^{(k)}\mathbf{C}_{in}^{-1,(k)}\Big\} + \sum_{l=1}^{4}\Big\{\mu^{(l)}\mathbf{C}_{in}^{-1,(l)}\Big\} + 6\sum_{m=1}^{1}\Big\{C_{30}^{(m)}(\mathrm{I}_{\hat{\mathbf{C}}_{el}^{(m)}}-3)^2\mathbf{C}_{in}^{-1,(m)}\Big\} + p\mathbf{C}^{-1}$$

$$\dot{\mathbf{C}}_{in}^{(k)} = \frac{2\Big[\mathbf{C} - \frac{1}{3}\Big((\mathbf{C}:\mathbf{C}_{in}^{-1,(k)})\mathbf{C}_{in}^{(k)}\Big)\Big]}{\Big(\frac{||\mathbf{C}||}{\sqrt{3}}\Big)^{\chi^{(k)}}\Big[\frac{1}{2}\tau^{(k)}exp\big(-\frac{||\mathbf{T}||}{s_0^{(k)}}\big)\Big(1+sign(\mathbf{D}:\mathbf{C})\Big) + exp\Big(\zeta^{(k)}||\mathbf{D}||\Big)\xi^{(k)}\Big]}$$

$$\dot{\mathbf{C}}_{in}^{(l)} = \frac{2\Big[\mathbf{C} - \frac{1}{3}\Big((\mathbf{C}:\mathbf{C}_{in}^{-1,(l)})\mathbf{C}_{in}^{(l)}\Big)\Big]}{\Big(\frac{||\mathbf{C}||}{\sqrt{3}}\Big)^{\chi^{(l)}}\Big[\frac{1}{2}\tau^{(l)}\cdot\big(1+sign(\mathbf{D}:\mathbf{C})\Big) + exp\Big(\zeta^{(l)}||\mathbf{D}||\Big)\xi^{(l)}\Big]}$$

$$\dot{\mathbf{C}}_{in}^{(m)} = \frac{6(\mathrm{I}_{\hat{\mathbf{C}}_{el}^{(m)}}-3)^2\Big[\mathbf{C} - \frac{1}{3}\Big((\mathbf{C}:\mathbf{C}_{in}^{-1,(m)})\mathbf{C}_{in}^{(m)}\Big)\Big]}{\Big(\frac{||\mathbf{C}||}{\sqrt{3}}\Big)^{\chi^{(m)}}\Big[\frac{1}{2}\tau^{(m)}\cdot\Big(1+sign(\mathbf{D}:\mathbf{C})\Big)\cdot\Big|1-\gamma^{(m)}exp(||\mathbf{D}||)\Big| + exp\Big(\zeta^{(m)}||\mathbf{D}||\Big)\xi^{(m)}\Big]}$$

4.2.2. Uniaxial Reduction

This section reduces the model to the uniaxial stress state for further consideration and investigation. This simplification is beneficial because the tests are also based on uniaxial tests, and the uniaxial stress state plays a predominant role in considering the residual load-bearing capacity of LSG.

$$\mathbf{T}^{<xx>} = 2\frac{\partial\hat{\Psi}_{iso}^{ov}(\mathrm{I}_{\hat{\mathbf{C}}_{el}})}{\partial\mathrm{I}_{\hat{\mathbf{C}}_{el}}}\mathbf{C}_{in}^{-1,<xx>} + p\mathbf{C}^{-1,<xx>}$$

$$\dot{\mathbf{C}}_{in}^{<xx>} = \frac{4}{\eta}\frac{\partial\hat{\Psi}_{iso}^{ov}(\mathrm{I}_{\hat{\mathbf{C}}_{el}})}{\partial\mathrm{I}_{\hat{\mathbf{C}}_{el}}}\Big[\mathbf{C}^{<xx>} - \frac{1}{3}\Big((\mathbf{C}:\mathbf{C}_{in}^{-1})\mathbf{C}_{in}^{<xx>}\Big)\Big]$$

Satisfying equilibrium within the uniaxial stress state forces the stresses in the transversal direction to be equal to zero:

$$\mathbf{T}^{<yy>} = 2\frac{\partial\hat{\Psi}_{iso}^{ov}(\mathrm{I}_{\hat{\mathbf{C}}_{el}})}{\partial\mathrm{I}_{\hat{\mathbf{C}}_{el}}}\mathbf{C}_{in}^{-1,<yy>} + p\mathbf{C}^{-1,<yy>} = 0 \tag{4.21}$$

Utilizing this requirement leads to the expression of the Lagrange multiplier p in terms of the stress in the transversal direction:

$$p = -\Big(2\frac{\partial\hat{\Psi}_{iso}^{ov}(\mathrm{I}_{\hat{\mathbf{C}}_{el}})}{\partial\mathrm{I}_{\hat{\mathbf{C}}_{el}}}\mathbf{C}_{in}^{-1,<yy>}\mathbf{C}^{<yy>}\Big) \tag{4.22}$$

Using this expression of the Lagrange multiplier yields the stress in the loading direction:

$$\mathbf{T}^{<xx>} = 2\frac{\partial\hat{\Psi}_{iso}^{ov}(\mathrm{I}_{\hat{\mathbf{C}}_{el}})}{\partial\mathrm{I}_{\hat{\mathbf{C}}_{el}}}(\mathbf{C}_{in}^{-1,<xx>} - \mathbf{C}_{in}^{-1,<yy>}\mathbf{C}^{<yy>}\mathbf{C}^{-1,<xx>}) \tag{4.23}$$

The following presents the entries for the deformation gradient and right Cauchy Green stretch tensor, considering uniaxial tension. The entries of the deformation are equal to the principal stretches for the respective deformation state. Although they are not displayed here, the

volume-preserving property is also assigned to the elastic and inelastic deformation and stretch tensors, whose entries are principal stretches as well ($\lambda = \lambda_{el}\lambda_{in}$).

$$\mathbf{F} = \begin{bmatrix} \lambda & 0 & 0 \\ 0 & \frac{1}{\sqrt{\lambda}} & 0 \\ 0 & 0 & \frac{1}{\sqrt{\lambda}} \end{bmatrix} \qquad \mathbf{C} = \begin{bmatrix} \lambda^2 & 0 & 0 \\ 0 & \frac{1}{\lambda} & 0 \\ 0 & 0 & \frac{1}{\lambda} \end{bmatrix} \qquad \dot{\mathbf{C}}_{in} = \begin{bmatrix} 2\dot{\lambda}_{in}\lambda_{in} & 0 & 0 \\ 0 & -\frac{\dot{\lambda}_{in}}{\lambda_{in}^2} & 0 \\ 0 & 0 & -\frac{\dot{\lambda}_{in}}{\lambda_{in}^2} \end{bmatrix}$$

Considering these entries into the representation of the stress in uniaxial direction (cf. Eq. 4.23), yields:

$$\mathbf{T}^{<xx>} = 2\frac{\partial \hat{\Psi}^{ov}_{iso}(\mathrm{I}_{\hat{\mathbf{C}}_{el}})}{\partial \mathrm{I}_{\hat{\mathbf{C}}_{el}}}\Big(\frac{1}{\lambda_{in}^2} - \frac{\lambda_{in}}{\lambda^3}\Big) \tag{4.24}$$

Calculating the Frobenius scalar product of the right Cauchy Green tensor and the inverse of its inelastic part considering the uniaxial stress state ($\mathbf{C} : \mathbf{C}_{in}^{-1} = \frac{\lambda^2}{\lambda_{in}^2} + 2\frac{\lambda_{in}}{\lambda}$) leads to the following expression of the evolution equation:

$$\dot{\mathbf{C}}_{in}^{<xx>} = \frac{4}{\eta}\frac{\partial \hat{\Psi}^{ov}_{iso}(\mathrm{I}_{\hat{\mathbf{C}}_{el}})}{\partial \mathrm{I}_{\hat{\mathbf{C}}_{el}}}\Big[\lambda^2 - \frac{1}{3}\Big(\frac{\lambda^3 + 2\lambda_{in}^3}{\lambda}\Big)\Big] \tag{4.25}$$

Evaluating the first entry of the inelastic deformation rate tensor, $\dot{\mathbf{C}}_{in}^{<xx>}$, and considering Eq. 4.25, yields:

$$2\dot{\lambda}_{in}\lambda_{in} = \frac{4}{\eta}\frac{\partial \hat{\Psi}^{ov}_{iso}(\mathrm{I}_{\hat{\mathbf{C}}_{el}})}{\partial \mathrm{I}_{\hat{\mathbf{C}}_{el}}}\Big[\lambda^2 - \frac{1}{3}\Big(\frac{\lambda^3 + 2\lambda_{in,k}^3}{\lambda}\Big)\Big] \tag{4.26}$$

Solving Eq. 4.26 for $\dot{\lambda}_{in}$, yields:

$$\dot{\lambda}_{in} = \frac{2}{\eta}\frac{\partial \hat{\Psi}^{ov}_{iso}(\mathrm{I}_{\hat{\mathbf{C}}_{el}})}{\partial \mathrm{I}_{\hat{\mathbf{C}}_{el}}}\Big[\frac{\lambda^2}{\lambda_{in}} - \frac{1}{3}\frac{\lambda^3}{\lambda\lambda_{in}} - \frac{2}{3}\frac{\lambda_{in}^3}{\lambda\lambda_{in}}\Big] = \frac{4}{3}\frac{1}{\eta}\frac{\partial \hat{\Psi}^{ov}_{iso}(\mathrm{I}_{\hat{\mathbf{C}}_{el}})}{\partial \mathrm{I}_{\hat{\mathbf{C}}_{el}}}\Big[\frac{\lambda^2}{\lambda_{in}} - \frac{\lambda_{in}^2}{\lambda}\Big] \tag{4.27}$$

Transferring the general formulations of stress and the evolution equation considering incompressibility and assuming an uniaxial stress state leads to the equations of the model, to be numerically implemented in the following section:

$$\mathbf{T}^{<xx>} = \sum_{k=1}^{5}\mu^{(k)}\Big(\frac{1}{\lambda_{in}^{2,(k)}} - \frac{\lambda_{in}^{(k)}}{\lambda^3}\Big) + \sum_{l=1}^{4}\mu^{(l)}\Big(\frac{1}{\lambda_{in}^{2,(l)}} - \frac{\lambda_{in}^{(l)}}{\lambda^3}\Big) + 6\sum_{m=1}^{1}\Big\{C_{30}(\mathrm{I}_{\hat{\mathbf{C}}_{el}^{(m)}} - 3)^2\Big(\frac{1}{\lambda_{in}^{2,(m)}} - \frac{\lambda_{in}^{(m)}}{\lambda^3}\Big)\Big\}$$

$$\dot{\lambda}_{in}^{(k)} = \frac{2\Big[\lambda^2\frac{1}{\lambda_{in}^{(k)}} - \lambda_{in}^{2,(k)}\frac{1}{\lambda}\Big]}{3\Big(\frac{||\mathbf{C}||}{\sqrt{3}}\Big)^{\chi^{(k)}}\Big[\frac{1}{2}\tau^{(k)}exp\Big(-\frac{||\mathbf{T}||}{s_0^{(k)}}\Big)\Big(1 + sign(\mathbf{D} : \mathbf{C})\Big) + exp\Big(\zeta^{(k)}||\mathbf{D}||\Big)\xi^{(k)}\Big]}$$

$$\dot{\lambda}_{in}^{(l)} = \frac{2\Big[\lambda^2\frac{1}{\lambda_{in}^{(l)}} - \lambda_{in}^{2,(l)}\frac{1}{\lambda}\Big]}{3\Big(\frac{||\mathbf{C}||}{\sqrt{3}}\Big)^{\chi^{(l)}}\Big[\frac{1}{2}\tau^{(l)} \cdot \Big(1 + sign(\mathbf{D} : \mathbf{C})\Big) + exp\Big(\zeta^{(l)}||\mathbf{D}||\Big)\xi^{(l)}\Big]}$$

$$\dot{\lambda}_{in}^{(m)} = \frac{6(\mathrm{I}_{\hat{\mathbf{C}}_{el}^{(m)}} - 3)^2\Big[\lambda^2\frac{1}{\lambda_{in}^{(m)}} - \lambda_{in}^{2,(m)}\frac{1}{\lambda}\Big]}{3\Big(\frac{||\mathbf{C}||}{\sqrt{3}}\Big)^{\chi^{(m)}}\Big[\frac{1}{2}\tau^{(m)} \cdot \Big(1 + sign(\mathbf{D} : \mathbf{C})\Big) \cdot \Big|1 - \gamma^{(m)}exp(||\mathbf{D}||)\Big| + exp\Big(\zeta^{(m)}||\mathbf{D}||\Big)\xi^{(m)}\Big]}$$

4.2.3. Numerical Implementation

Based on the assumption of incompressibility, the equations for implementing the model for the uniaxial stress state are now derived. The individual evolution equations are integrated using the Euler backward method and then solved using the Newton method (cf. Sec. 2.3). The corresponding equations are first set up for a general potential function, depending on the first invariant of the right Cauchy Green tensor, and then transferred explicitly to the two potentials used in the model.

In the first step, the description of the Euler Backwards algorithm, presented in Eq. 2.129, is picked up and formulated for the inelastic stretch λ_{in}:

$$f(\lambda_{in,(n+1)}, t_{(n+1)}) = \frac{\lambda_{in,(n+1)} - \lambda_{in,(n)}}{\Delta t} \tag{4.28}$$

Utilizing the formulation of the evolution equation to express the function represented in Eq. 4.28 yields the following equation:

$$\frac{\lambda_{in,(n+1)} - \lambda_{in,(n)}}{\Delta t} = \frac{4}{3}\frac{1}{\eta}\frac{\partial \hat{\Psi}^{ov}_{iso}(\mathrm{I}_{\hat{\mathbf{C}}_{el}})}{\partial \mathrm{I}_{\hat{\mathbf{C}}_{el}}}\Big[\frac{\lambda^2_{(n+1)}}{\lambda_{in,(n+1)}} - \frac{\lambda^2_{in,(n+1)}}{\lambda_{(n+1)}}\Big] \tag{4.29}$$

The representation of Eq. 4.29 in terms of a residuum (cf. Eq. 2.136) yields:

$$\Xi(\lambda_{in,(n+1)}) = \lambda_{in,(n+1)} - \lambda_{in,(n)} - \frac{4}{3}\frac{1}{\eta}\frac{\partial \hat{\Psi}^{ov}_{iso}(\mathrm{I}_{\hat{\mathbf{C}}_{el}})}{\partial \mathrm{I}_{\hat{\mathbf{C}}_{el}}}\Big[\frac{\lambda^2_{(n+1)}}{\lambda_{in,(n+1)}} - \frac{\lambda^2_{in,(n+1)}}{\lambda_{(n+1)}}\Big)\Big] = 0 \tag{4.30}$$

Subsequently, Eq. 4.30 is expressed in terms of a Taylor series expansion, cut off after the linear part (cf. Eq. 2.137), utilizing the Newton Algorithm.

$$\Xi(\lambda^{(k+1)}_{in,(n+1)}) \approx \Xi(\lambda^{(k)}_{in,(n+1)}) + \frac{\partial \Xi(\lambda^{(k)}_{in,(n+1)})}{\partial \lambda^{(k)}_{in,(n+1)}}\Big(\lambda^{(k+1)}_{in,(n+1)} - \lambda^{(k)}_{in,(n+1)}\Big) = 0 \tag{4.31}$$

The derivative of the residuum with respect to the inelastic stretch λ_{in} leads to

$$\frac{\partial \Xi(\lambda^{(k)}_{in,(n+1)})}{\partial \lambda^{(k)}_{in,(n+1)}} = 1 + \frac{4}{3}\frac{1}{\eta}\frac{\partial \hat{\Psi}^{ov}_{iso}(\mathrm{I}_{\hat{\mathbf{C}}_{el}})}{\partial \mathrm{I}_{\hat{\mathbf{C}}_{el}}}\Big[\frac{\lambda^2_{(n+1)}}{\lambda^{2,(k)}_{in,(n+1)}} + 2\frac{\lambda^{(k)}_{in,(n+1)}}{\lambda_{(n+1)}}\Big] \tag{4.32}$$

and the final representation, in accordance with Eq. 2.138, results in:

$$\lambda^{(k+1)}_{in,(n+1)} = \lambda^{(k)}_{in,(n+1)} - \frac{\lambda^{(k)}_{in,(n+1)} - \lambda_{in,(n)} - \frac{4}{3}\frac{1}{\eta}\frac{\partial \hat{\Psi}^{ov}_{iso}(\mathrm{I}_{\hat{\mathbf{C}}_{el}})}{\partial \mathrm{I}_{\hat{\mathbf{C}}_{el}}}\Big[\frac{\lambda^2_{(n+1)}}{\lambda^{(k)}_{in,(n+1)}} - \frac{\lambda^{2,(k)}_{in,(n+1)}}{\lambda_{(n+1)}}\Big)\Big]}{1 + \frac{4}{3}\frac{1}{\eta}\frac{\partial \hat{\Psi}^{ov}_{iso}(\mathrm{I}_{\hat{\mathbf{C}}_{el}})}{\partial \mathrm{I}_{\hat{\mathbf{C}}_{el}}}\Big[\frac{\lambda^2_{(n+1)}}{\lambda^{2,(k)}_{in,(n+1)}} + 2\frac{\lambda^{(k)}_{in,(n+1)}}{\lambda_{(n+1)}}\Big]} \tag{4.33}$$

Neo Hooke The respective equations for the Neo Hookean potential, the basis of network A and B, are presented in the following. The respective residuum and its derivative are derived, being utilized according to Eq. 4.31 for the expression of the inelastic stretch, according to Eq. 4.33. The residuum results in:

$$\Xi(\lambda^{(k)}_{in,(n+1)}) = \lambda^{(k)}_{in,(n+1)} - \lambda^{(k)}_{in,(n)} - \mu\frac{2}{3}\frac{\Delta t}{\eta}\Big[\frac{\lambda^2_{(n+1)}}{\lambda^{(k)}_{in,(n+1)}} - \frac{\lambda^{2,(k)}_{in,(n+1)}}{\lambda_{(n+1)}}\Big)\Big] = 0 \tag{4.34}$$

and the derivative of the residuum yields:

$$\frac{\partial \Xi(\lambda_{in,(n+1)}^{(k)})}{\partial \lambda_{in,(n+1)}^{(k)}} = 1 + \mu \frac{2}{3} \frac{\Delta t}{\eta} \Big[\frac{\lambda_{(n+1)}^2}{\lambda_{in,(n+1)}^{2,(k)}} + 2 \frac{\lambda_{in,(n+1)}^{(k)}}{\lambda_{(n+1)}} \Big] \tag{4.35}$$

The final expression of the inelastic stretch based on the Neo Hookean potential, assuming incompressibility, for the uniaxial stress state leads to:

$$\lambda_{in,(n+1)}^{(k+1)} = \lambda_{in,(n+1)}^{(k)} - \frac{\lambda_{in,(n+1)}^{(k)} - \lambda_{in,(n)}^{(k)} - \mu \frac{2}{3} \frac{\Delta t}{\eta} \Big[\frac{\lambda_{(n+1)}^2}{\lambda_{in,(n+1)}^{(k)}} - \frac{\lambda_{in,(n+1)}^{2,(k)}}{\lambda_{(n+1)}} \Big) \Big]}{1 + \mu \frac{2}{3} \frac{\Delta t}{\eta} \Big[\frac{\lambda_{(n+1)}^2}{\lambda_{in,(n+1)}^{2,(k)}} + 2 \frac{\lambda_{in,(n+1)}^{(k)}}{\lambda_{(n+1)}} \Big]} \tag{4.36}$$

Yeoh The respective equations for the Yeoh potential, the basis of network C, is presented in the following. The respective residuum and its derivative are derived, being utilized according to Eq. 4.31 for the expression of the inelastic stretch, according to Eq. 4.33. The residuum results in:

$$\begin{aligned} \Xi(\lambda_{in,(n+1)}^{(k)}) &= \lambda_{in,(n+1)}^{(k)} - \lambda_{in,(n)}^{(k)} - \frac{4}{3} \frac{\Delta t}{\eta} \Big[3 C_{30} \Big(\frac{\lambda_{(n+1)}^2}{\lambda_{in,(n+1)}^{2,(k)}} + 2 \frac{\lambda_{in,(n+1)}^{(k)}}{\lambda_{(n+1)}} - 3 \Big)^2 \Big] \cdot \\ &\cdot \Big[\frac{\lambda_{(n+1)}^2}{\lambda_{in,(n+1)}^{(k)}} - \frac{\lambda_{in,(n+1)}^{2,(k)}}{\lambda_{(n+1)}} \Big] = 0 \end{aligned} \tag{4.37}$$

and the derivative of the residuum yields:

$$\begin{aligned} \frac{\partial \Xi(\lambda_{in,(n+1)}^{(k)})}{\partial \lambda_{in,(n+1)}^{(k)}} &= 1 + \frac{4}{3} \frac{\Delta t}{\eta} \Big[6 C_{30} \Big(- \frac{\lambda_{(n+1)}^2}{\lambda_{in,(n+1)}^{2,(k)}} - 2 \frac{\lambda_{in,(n+1)}^{(k)}}{\lambda_{(n+1)}} + 3 \Big) \cdot \\ &\cdot \Big(-2 \frac{\lambda_{(n+1)}^2}{\lambda_{in,(n+1)}^{3,(k)}} + \frac{2}{\lambda_{(n+1)}} \Big) \Big] \Big[\frac{\lambda_{(n+1)}^2}{\lambda_{in,(n+1)}^{(k)}} - \frac{\lambda_{in,(n+1)}^{2,(k)}}{\lambda_{(n+1)}} \Big] + \\ &+ \frac{4}{3} \frac{\Delta t}{\eta} \Big[-3 C_{30} \Big(\frac{\lambda_{(n+1)}^2}{\lambda_{in,(n+1)}^{2,(k)}} + 2 \frac{\lambda_{in,(n+1)}^{(k)}}{\lambda_{(n+1)}} - 3 \Big)^2 \Big] \cdot \Big[- \frac{\lambda_{(n+1)}^2}{\lambda_{in,(n+1)}^{2,(k)}} - 2 \frac{\lambda_{in,(n+1)}^{(k)}}{\lambda_{(n+1)}} \Big] \end{aligned} \tag{4.38}$$

The final expression of the inelastic stretch based on the Neo Hookean potential, assuming incompressibility, for the uniaxial stress state leads to:

$$\begin{aligned} \lambda_{in,(n+1)}^{(k+1)} &= \lambda_{in,(n+1)}^{(k)} - \Bigg\{ \lambda_{in,(n+1)}^{(k)} - \lambda_{in,(n)}^{(k)} - \frac{4}{3} \frac{\Delta t}{\eta} \Big[3 C_{30} \Big(\frac{\lambda_{(n+1)}^2}{\lambda_{in,(n+1)}^{2,(k)}} + 2 \frac{\lambda_{in,(n+1)}^{(k)}}{\lambda_{(n+1)}} - 3 \Big)^2 \Big] \cdot \\ &\cdot \Big[\frac{\lambda_{(n+1)}^2}{\lambda_{in,(n+1)}^{(k)}} - \frac{\lambda_{in,(n+1)}^{2,(k)}}{\lambda_{(n+1)}} \Big] \Big] \Bigg\} : \Bigg\{ 1 + \frac{4}{3} \frac{\Delta t}{\eta} \Big[6 C_{30} \Big(- \frac{\lambda_{(n+1)}^2}{\lambda_{in,(n+1)}^{2,(k)}} - 2 \frac{\lambda_{in,(n+1)}^{(k)}}{\lambda_{(n+1)}} + 3 \Big) \cdot \Big(-2 \frac{\lambda_{(n+1)}^2}{\lambda_{in,(n+1)}^{3,(k)}} + \frac{2}{\lambda_{(n+1)}} \Big) \Big] \cdot \\ &\cdot \Big[\frac{\lambda_{(n+1)}^2}{\lambda_{in,(n+1)}^{(k)}} - \frac{\lambda_{in,(n+1)}^{2,(k)}}{\lambda_{(n+1)}} \Big] + \frac{4}{3} \frac{\Delta t}{\eta} \Big[-3 C_{30} \Big(\frac{\lambda_{(n+1)}^2}{\lambda_{in,(n+1)}^{2,(k)}} + 2 \frac{\lambda_{in,(n+1)}^{(k)}}{\lambda_{(n+1)}} - 3 \Big)^2 \Big] \cdot \Big[- \frac{\lambda_{(n+1)}^2}{\lambda_{in,(n+1)}^{2,(k)}} - 2 \frac{\lambda_{in,(n+1)}^{(k)}}{\lambda_{(n+1)}} \Big] \Bigg\} \end{aligned} \tag{4.39}$$

Model Implementation Now that the structure of the material model has been derived, this section presents a brief representation of the implemented material model. The flow chart given in Fig. 4.12 emphasizes the implementation description, by presenting the numerical procedure exemplarily for Network A.

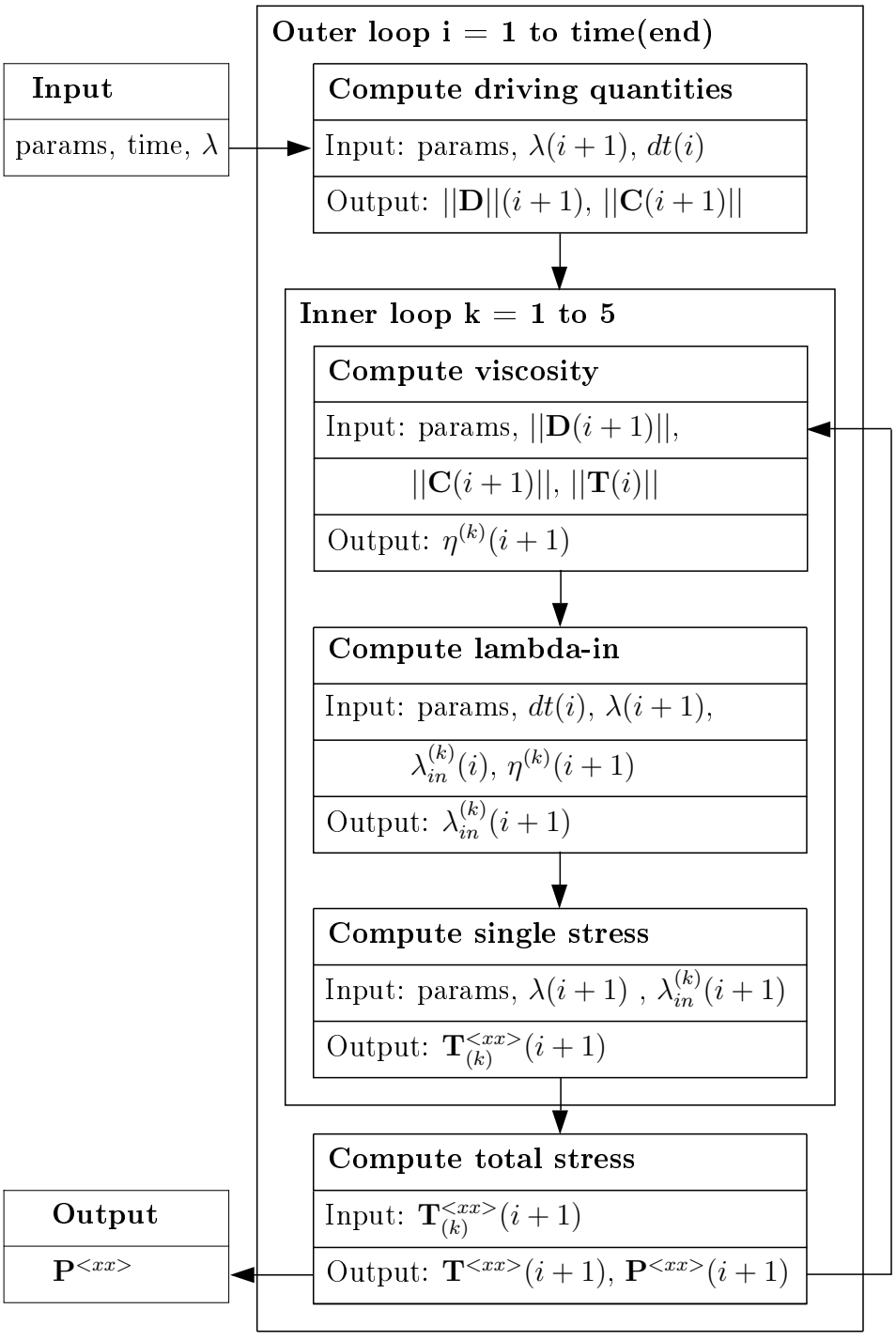

Figure 4.12.: Flow chart of exemplary implementation of Network A

The model receives two input vectors: one vector containing the individual material parameters, passed in whole in every iteration step, and a vector containing the applied strains and corresponding times passed iteratively entry by entry. The model iteration consists of one main loop, referred to below as the outer loop, which contains a loop for each of the individual networks, referred to below as the inner loop. Each inner loop consists of a viscosity function, an

evolution equation representing the inelastic stretch, and a stress equation. After each iteration within the main loop, the pre-dimensioned result vector, which contains the 2^{nd}PK stresses, is filled step by step with the sum of the single stresses. After the last iteration step of the outer loop, the 1^{st}PK output vector is calculated from the 2^{nd}PK vector.

Within an iteration of the outer loop, several iterations of the inner loops run, depending on the respective network. These individual iterations all follow the same sequence. Firstly, the viscosity function is called to transfer the input vectors to it. This function then returns a viscosity value, passed to the corresponding function of the evolution equation, which calculates an inelastic stretch and returns it. The inelastic stretch is then used to calculate the value of the 2^{nd}PK stress for the corresponding iteration of the inner loop. This procedure is carried out for each iteration of the inner loops until the total value of the 2^{nd}PK stress of the respective iteration step of the outer loop can be calculated. The outer loop, which performs the actions described in each iteration step, is then run through until the end of the input vector, which contains the strains and associated times, is reached. Finally, a 1^{st}PK vector is calculated from the 2^{nd}PK vector and passed as output.

4.3. Validation

This chapter aims to validate the numerical implementation of the viscoelastic evolution equation, which utilizes the Euler Backward formulation and Newton method and forms the foundation of the presented material model. Only differing in the explicit formulation of the evolution equation, the numerical formulation of linear, finite linear, and finite viscoelasticity follows the same structure. An example presented in [24] and shown in Tab. 4.1, serves as bench mark example. It is, therefore, solved for the problem of linear, finite linear, and finite viscoelasticity using the numerical structure implemented within this thesis, and the results are compared to analytical solutions and the ones presented in [24]. Furthermore, Sec. 4.3.3 provides an additional validation example concerning finite viscoelasticity.

Table 4.1.: Boundary conditions for the calculation example

τ [s]	E_{el}, μ_{el} [MPa]	E, μ [MPa]	$\dot{\boldsymbol{\varepsilon}}^{<xx>}$ [1/s]
0.1	0.8	0.2	± 0.5

4.3.1. Linear Viscoelasticity

To verify the presented algorithm, the problem of linear viscoelasticity for the one-dimensional case is solved exemplarily. The result is compared with the analytical solution and the solution of [24]. Considering Eq.'s 2.77 to 2.79 and, utilizing $\tau = \frac{\eta}{E}$, leads to the functional of the linear viscoelasticity

$$\sigma(t) = E \cdot \varepsilon(t) + \int_{s=0}^{s=t} e^{-\frac{t-s}{\tau}} E_{el} \frac{d\varepsilon(s)}{ds} ds,$$

and by considering a constant value of $\dot{\varepsilon}_0$, the loading path ($t = 0$ to $t = \frac{T}{2}$) leads to

$$\sigma(t) = E \cdot \varepsilon(t) + \dot{\varepsilon}_0 \eta \Big[1 - e^{-\frac{t}{\tau}}\Big],$$

and the unloading path ($t = \frac{T}{2}$ to $t = T$) results in

$$\sigma(t) = E \cdot \varepsilon(t) + \dot{\varepsilon}_0 \eta \left[2e^{\frac{\frac{T}{2}-t}{\tau}} - e^{-\frac{t}{\tau}} - 1 \right].$$

The solution of the loading and unloading path together form the analytical solution of the benchmark example considering linear viscoelasticity.

When calculating the numerical solution, time-dependent and -independent behavior are treated separately, and only the time-dependent part using the Euler Backwards formulation is implemented into the Newton-Raphson Algorithm. The relation within a single Maxwell element, considering the inelastic strain as internal variable, results in $\dot{\varepsilon}_{in} = \frac{E_{el}}{\eta}(\varepsilon - \varepsilon_{el})$, and the flow rule of linear viscoelasticity yields

$$\dot{\varepsilon}_{in} = \frac{\varepsilon_{in,(n+1)} - \varepsilon_{in,(n)}}{\Delta t} = \frac{1}{\tau} \left[\varepsilon_{(n+1)} - \varepsilon_{in,(n+1)} \right].$$

The residuum reads

$$\Xi(\varepsilon_{in,(n+1)}) = \varepsilon_{in,(n+1)} - \varepsilon_{in,(n)} - \frac{1}{\tau} \left[\varepsilon_{(n+1)} - \varepsilon_{in,(n+1)} \right] = 0,$$

and its derivation results in

$$\frac{\partial \Xi(\varepsilon^{(k)}_{in,(n+1)})}{\partial \varepsilon^{(k)}_{in,(n+1)}} = 1 + \frac{\Delta t}{\tau}.$$

The whole formulation of the linear viscoelastic evolution equation, utilizing the Newton method, yields:

$$\varepsilon^{(k+1)}_{in,(n+1)} = \varepsilon^{(k)}_{in,(n+1)} - \frac{\varepsilon^{(k)}_{in,(n+1)} - \varepsilon^{(k)}_{in,(n)} - \frac{1}{\tau} \left[\varepsilon_{(n+1)} - \varepsilon^{(k)}_{in,(n+1)} \right]}{1 + \frac{\Delta t}{\tau}}.$$

Fig. 4.13 shows the analytical, numerical, and solution derived from [24]. The small deviation of the result of the numerical solution compared to the other two shows that the code works correctly.

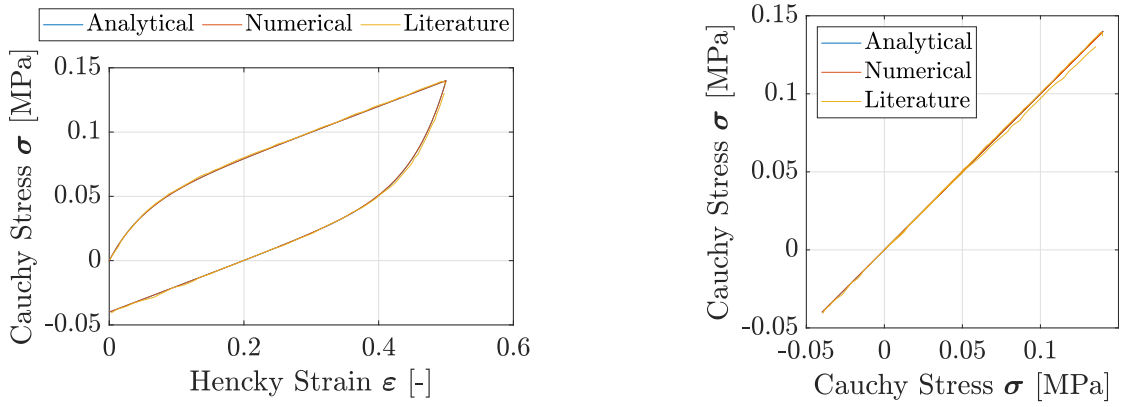

Figure 4.13.: Comparison of analytical, numerical ,and solution from [24] (left); Error with respect to the analytical solution (right)

4.3.2. Finite Linear Viscoelasticity

After the algorithm was very well applied to the problem of linear viscoelasticity, its applicability to the theory of finite linear viscoelasticity is now to be analyzed. For this purpose, the numerical calculation result is again compared with the analytical and Bergström's solutions [24].

Considering incompressible material behavior, the uniaxial stress state results in:

$$\boldsymbol{\sigma}^{<xx>} = 2\frac{\partial \Psi_{iso}(\mathrm{I}_{\mathbf{C}})}{\partial \mathrm{I}_{\mathbf{C}}}(\mathbf{C}^{<xx>} - \mathbf{C}^{<yy>}) = \mu(\lambda^2 - \frac{1}{\lambda})$$

The governing equation of the analytical approach describing finite, linear viscoelasticity follows the same principle like the one describing linear viscoelasticity. However, the stresses are derived from a hyperelastic Neo Hookean potential with the shear moduli μ_{el} and μ from Tab. 4.1. Replacing $E_{el}\frac{d\varepsilon(s)}{ds}$ by $\frac{d}{ds}\Big[\boldsymbol{\sigma}^{ov,<xx>}(s)\Big]$, and $E\cdot\varepsilon(t)$ by $\boldsymbol{\sigma}^{\infty,<xx>}(t)$, yields the governing equation:

$$\boldsymbol{\sigma}^{<xx>}(t) = \boldsymbol{\sigma}^{\infty,<xx>}(t) + \int_{s=0}^{s=t} e^{-\frac{t-s}{\tau}}\frac{d}{ds}\Big[\boldsymbol{\sigma}^{ov,<xx>}(s)\Big]ds$$

Integration by parts and further manipulating this expression leads to the semianalytical description of the problem of finite linear viscoelasticity (cf. B.2):

$$q(t+\Delta t) = \boldsymbol{\sigma}^{ov,<xx>}(t+\Delta t) - e^{-\frac{\Delta t}{\tau}}\int_{s=0}^{s=t}\frac{1}{\tau}\Big[e^{-\frac{t-s}{\tau}}\Big]\boldsymbol{\sigma}^{ov,<xx>}(s)ds - \boldsymbol{\sigma}^{ov,<xx>}(t)\Big[1-e^{-\frac{\Delta t}{\tau}}\Big] -$$

$$-\frac{\Delta\boldsymbol{\sigma}^{ov,<xx>}}{\Delta t}\Big[\Delta t - \tau + \tau e^{-\frac{\Delta t}{\tau}}\Big],$$

The total stress yields (cf. Eq. 2.90):

$$\boldsymbol{\sigma}^{<xx>} = \boldsymbol{\sigma}^{\infty,<xx>} + q.$$

The numerical approach includes the solution of Eq. 2.87 describing the evolution of the overstress within the theory of finite linear viscoelasticity. Solving the evolution equation again requires the Euler Backward integration scheme and a solution using Newton's method. The differential equation for the overstress in uniaxial stress considering incompressibility yields:

$$\dot{q} = \frac{q_{(n+1)} - q_{(n)}}{\Delta t} = \frac{d}{dt}\Big[\boldsymbol{\sigma}^{ov,<xx>}\Big]$$

The residuum for applying the Newton Raphson algorithm reads

$$\Xi(q^{(k)}_{(n+1)}) = q^{(k)}_{(n+1)} - q^{(k)}_{(n)} - \Delta t\Big(\frac{d}{dt}\Big[\boldsymbol{\sigma}^{ov,<xx>}\Big] - \frac{1}{\tau}q^{(k)}_{(n+1)}\Big) = 0,$$

and the derivation for the Neo Hookean potential results in

$$\frac{\partial\Xi(q^{(k)}_{(n+1)})}{\partial q^{(k)}_{(n+1)}} = 1 + \frac{\Delta t}{\tau},$$

leading to the following expression

$$q^{(k+1)}_{(n+1)} = q^{(k)}_{(n+1)} - \frac{q^{(k)}_{(n+1)} - q^{(k)}_{(n)} - \Delta t\Big(\frac{d}{dt}\Big[\boldsymbol{\sigma}^{ov,<xx>}\Big] - \frac{1}{\tau}q^{(k)}_{(n+1)}\Big)}{1+\frac{\Delta t}{\tau}}$$

which is solved iteratively using the Newton Raphson algorithm.

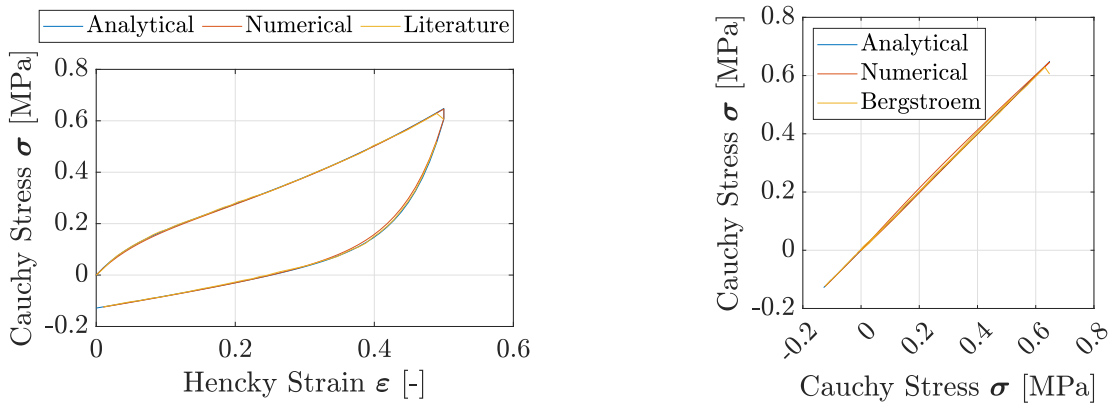

Figure 4.14.: Comparison of analytical, numerical ,and solution from [24] (left); Error with respect to the analytical solution (right)

Fig. 4.14 shows the results of the semi-analytical solution, the numerical solution, and the solution presented by [24]. The small deviation of the result of the implemented algorithm from the analytical solution and the one from [24], indicates that the code works properly, even considering hyperelastic material behavior.

4.3.3. Finite Viscoelasticity

Since the numerical algorithm successfully solves problems of linear and finite linear viscoelasticity, it is crucial to check its applicability to the problem of finite viscoelasticity. For this purpose, the benchmark example is solved numerically within the framework of finite viscoelasticity and compared to the solution of linear and finite linear viscoelasticity. An analytical solution of the non-linear differential equation is no longer possible.

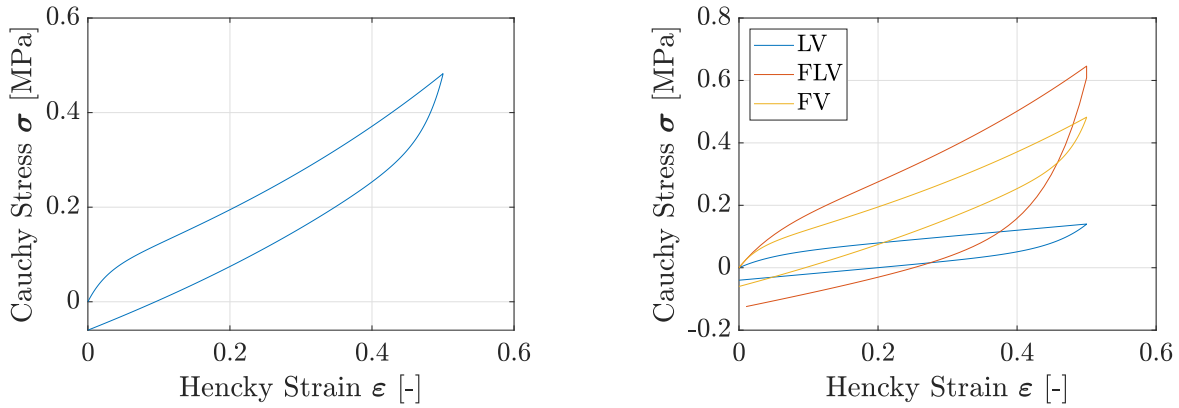

Figure 4.15.: Solution of example for finite viscoelastic approach (left); Comparison of results of linear viscoelastic, finite linear viscoelastic and finite viscoelastic approach for the benchmark example (right)

Fig. 4.15 shows the solutions of the benchmark example utilizing the three theories within the presented numerical framework. At first glance, the three solutions are strikingly different from one another. However, a closer look reveals some regularities. On the one hand, a comparison of finite viscoelasticity and finite linear viscoelasticity shows that both hystereses have a similar slope, which is consistent because both theories follow the same hyperelastic

potential. On the other hand, the linear and finite theories are similar regarding the shape and size of the hysteresis, which goes along with the fact that the finite theory emerges from the linear theory by extending it to large deformations. Overall, it is apparent that the observations are consistent with the underlying theory.

However, to verify the fundamental correctness of the numerical implementation of the material model, Sedlan's model [236], with its respective potentials, evolution equations, and viscosity functions presented below, is inserted into the model structure.

- Total Stress:

$$\mathbf{T} = \mathbf{T}_\infty + \sum_{k=1}^{n=3} \mathbf{T}_{ov}^{(k)} + p\mathbf{C}_M^{-1}$$

- Equilibrium Stress:

$$\mathbf{T}_\infty = [2C_{10} + 2C_{11}(\mathrm{II}_{\mathbf{C}_M} - 3) + 6C_{30}(\mathrm{I}_{\mathbf{C}_M} - 3)^2]\mathbf{1} - [2C_{01} + 2C_{11}(\mathrm{I}_{\mathbf{C}_M} - 3) + 4C_{02}(\mathrm{II}_{\mathbf{C}_M} - 3)]\mathbf{C}^{-1}\mathbf{C}^{-1}, \qquad \mathbf{T}_{ov}^{(k)} = 2\mu^{(k)}\mathbf{C}_{in}^{-1}$$

- Over Stress:

$$\dot{\mathbf{C}}_{in} = 4\frac{\mu^{(k)}}{\eta^{(k)}}\Big[\Big(\mathbf{C}_M - \frac{1}{3}\Big((\mathbf{C}_M : \mathbf{C}_{in}^{-1})\mathbf{C}_{in}\Big)\Big], \qquad \eta^{(k)} = \frac{\mu^{(k)}||\mathbf{C}||}{(1/2)\xi^{(k)}\sqrt{sp(\mathbf{C}^{-1}\dot{\mathbf{C}})^2} + \frac{1}{\tau^{(k)}}}$$

- Thixotropy:

$$\tau^{(k)} = \tau_{max}(1-q) + \tau_{min}q, \qquad \dot{q} = \xi\sqrt{sp(\mathbf{C}^{-1}\dot{\mathbf{C}})^2}(1-q) - \frac{1}{\tau q}\sqrt{q}, \qquad 0 \leq q < 1$$

In order to reproduce the model numerically, implementing a further differential equation describing the development of a structural variable intended to represent thixotropic effects is necessary. Thixotropy is a rheological phenomenon characterized by a time-dependent and reversible alteration in the viscosity of certain substances when subjected to mechanical agitation or shear forces. Materials exhibiting thixotropic behavior demonstrate a decrease in viscosity and an increase in fluidity under stress, only to revert to their higher viscosity state upon cessation of the applied force. This property is commonly observed in colloidal suspensions, gels, and certain fluids. Thixotropy finds application in various industrial sectors, such as the manufacturing of paints, where it facilitates improved application and spreading, as well as in biomedical contexts for the controlled flow characteristics of specific gel-like substances. For a more detailed description and further literature concerning this topic, the interested reader is referred to [235]. The following equations arise describing the structural variable.

The differential equation describing the evolution of the structural variable q yields:

$$\dot{q} = \frac{q_{(n+1)} - q_{(n)}}{\Delta t} = \xi|\mathbf{D}|(1 - q_{(n+1)}^{(k)}) - \frac{1}{\tau_q}q_{(n+1)}^{(k)} \tag{4.40}$$

For the numerical implementation, the residuum residuum of Eq. 4.40 must be derived. It reads:

$$\Xi(q_{(n+1)}^{(k)}) = q_{(n+1)}^{(k)} - q_{(n)}^{(k)} - \Delta t\Big(\xi|\mathbf{D}|(1 - q_{(n+1)}^{(k)}) - \frac{1}{\tau_q}q_{(n+1)}^{(k)}\Big) = 0$$

The derivation of the residuum results in

$$\frac{\partial \Xi(q_{(n+1)}^{(k)})}{\partial q_{(n+1)}^{(k)}} = 1 - \Delta t\Big(\xi|\mathbf{D}| - \frac{\Delta t}{\tau_q}\Big),$$

and leads to the following formulation for the Newton Raphson algorithm

$$q_{(n+1)}^{(k+1)} = q_{(n+1)}^{(k)} - \frac{q_{(n+1)}^{(k)} - q_{(n)}^{(k)} - \Delta t\Big(\xi|\mathbf{D}|(1 - q_{(n+1)}^{(k)}) - \frac{1}{\tau_q} q_{(n+1)}^{(k)}\Big)}{1 - \Delta t\Big(\xi|\mathbf{D}| - \frac{\Delta t}{\tau_q}\Big)}.$$

Thixotropic effects can be implemented into the viscosity function as process-dependent variables. Fig. 4.16 exemplarily shows the evolution of the structure variable concerning the parameters τ_q and ξ.

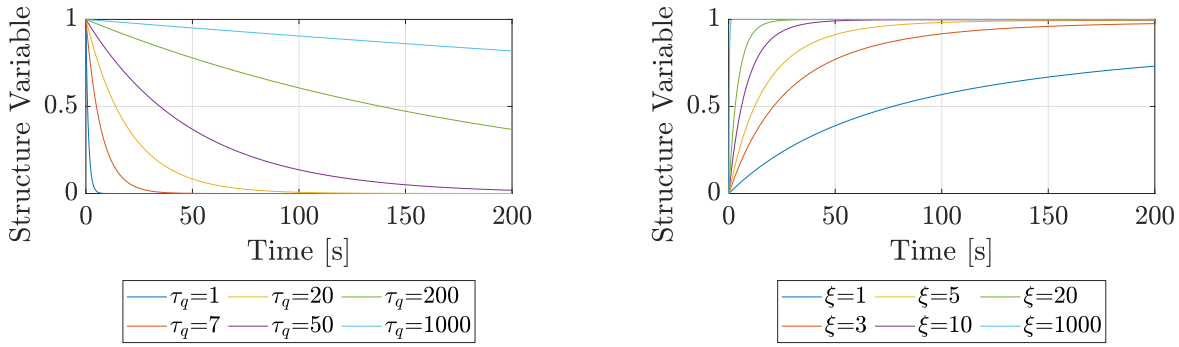

Figure 4.16.: Evaluation of the Structure Variable q for healing ($\mathbf{D} = 0$, $\xi = 10$) (left) and destruction ($\mathbf{D} \neq 0$, $\tau_q = 10000$) (right)

Tab. 4.2 and 4.3 present the material parameters identified by [236] for elastomeric materials:

Table 4.2.: Parameters for Equilibrium Response

C_{10} [MPa]	C_{01} [MPa]	C_{11} [MPa]	C_{02} [MPa]	C_{30} [MPa]
0.146	0.695	0.403	-0.657	0.019

Table 4.3.: Parameters for Non-Equilibrium Response and Damage Variable

k	$\mu^{(k)}$ [MPa]	$\xi^{(k)}$ [-]	$\tau_{max}^{(k)}$ [s]	$\tau_{min}^{(k)}$ [s]	ζ [-]	τ_q [s]
1	0.3	2	2e2	10	2.4	4e4
2	0.8	30	2e5	20		
3	0.3	10	2e4	20		

Three different regulations, taking into account different loading rates, relaxation, and unloading, were selected for verification of the material model. Fig. 4.17 ($\dot{\mathbf{B}}^{<xx>} = \pm 0.003$ [1/s]) and Fig. 4.18 ($\dot{\mathbf{B}}^{<xx>} = \pm 0.03$ [1/s]) show the result of a load with two cycles for two different

strain rates. Fig. 4.19 shows a simple cycle, interrupted by relaxation steps, comparable to the staircase tests from Ch. 3.3.5.

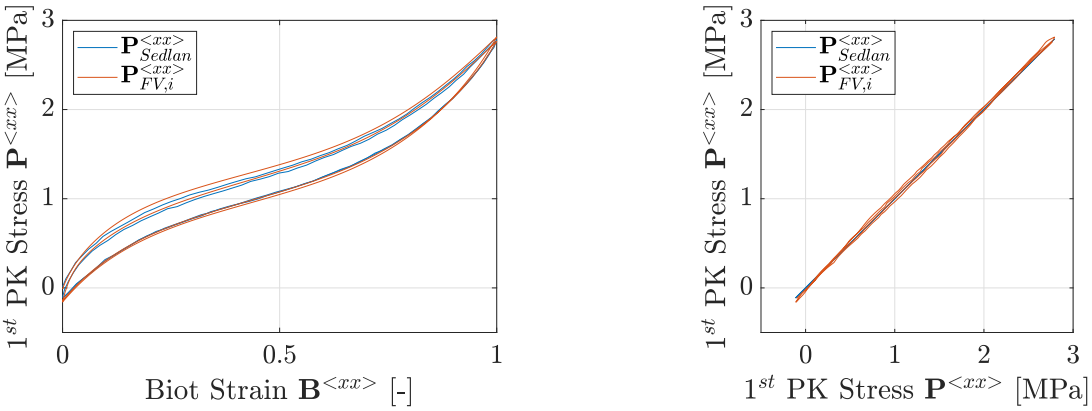

Figure 4.17.: Two Cycles with Strain Rate $\dot{\mathbf{B}}^{<xx>} = \pm 0.003$ [1/s] - Comparison (left), Error (right)

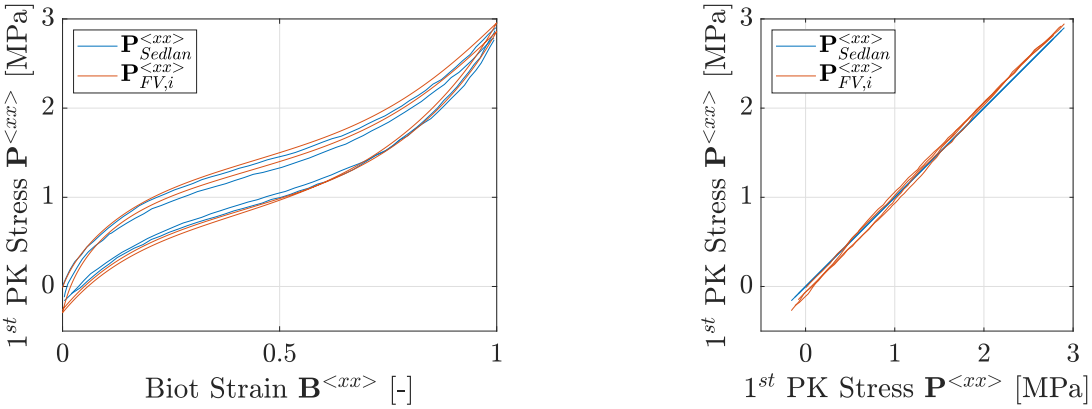

Figure 4.18.: Two Cycles with Strain Rate $\dot{\mathbf{B}}^{<xx>} = \pm 0.03$ [1/s] - Comparison (left), Error (right)

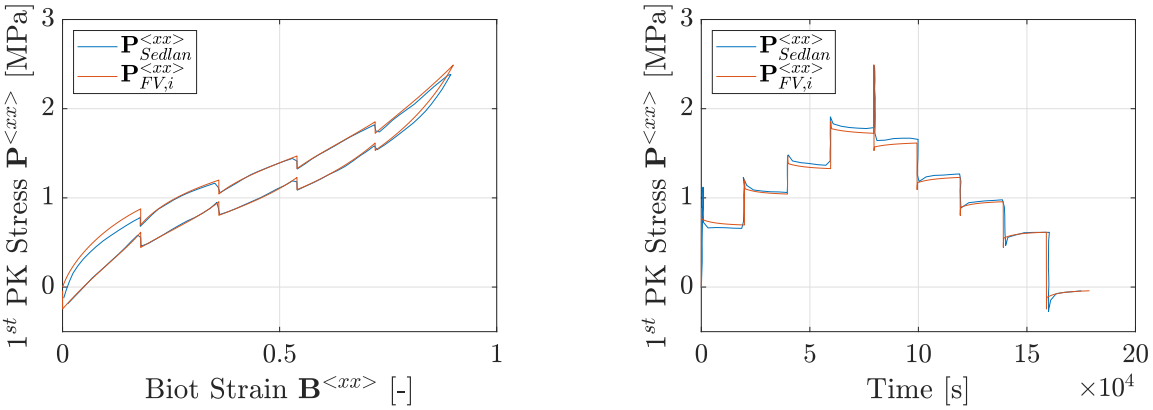

Figure 4.19.: One Cycle with Holding Steps - Stress over Strain (left), Stress over Time (right)

Fig.s 4.17 to 4.19 show excellent agreement between the calculations using the numerical structure implemented within this work and the results presented by [235] underlining the precise functionality of the numerical algorithm.

4.4. Investigations on the Viscosity Functions

After the construction, numerical implementation, and validation of the model within the previous sections, this section illustrates the behavior of the particular viscosity functions of the individual networks. The investigation follows the same phenomenologically motivated approach as the initial construction of the viscosity functions, utilizing the scalar tensor functions $||\mathbf{D}||$, $(\mathbf{D} : \mathbf{C})$, $||\mathbf{C}||$, $||\mathbf{T}||$ as process dependent variables and related material parameters. Goal of this examination is the evaluation of the The influence of these quantities. This description leads to three processes: Loading, unloading, and relaxation. Following these characteristic processes, six additional parameters have been introduced for the viscosity functions beyond the foundational components, relaxation time, and shear modulus, exerting influence over distinct loading modes. Different cases, constructed for every network, each involving the variation of one parameter while maintaining the remaining parameters constant, aim to represent these processes. Each case is illustrated in two particular plots. The first plot presents the constant viscosity unaffected by any process variables and the viscosities following the function of the particular network, influenced by the considered parameters. The second plot shows the stresses corresponding to constant and the varaying viscosities.

All three processes follow the same strain rate of $\dot{\mathbf{B}}^{<xx>} = 0.01$ [1/s]. However, the test with a single loading and the turning point of the cyclic tests, as well as the holding level of the relaxation tests, was at $\mathbf{B}^{<xx>} = 200$ [%]. For the constant parameters, particular values were chosen to illustrate the influence of the varied parameters in the best possible way.

4.4.1. Considerations regarding the loading behavior

Initially, an analysis of the network A with viscosity function

$$\eta_D = \eta_0 \mu \Big(\frac{||\mathbf{C}||}{\sqrt{3}}\Big)^{\chi} \Big[\frac{1}{2}\tau exp\Big(-\frac{||\mathbf{T}||}{\mathbf{s_0}}\Big)\Big(1 + sign(\mathbf{D} : \mathbf{C})\Big) + exp\Big(\zeta||\mathbf{D}||\Big)\xi\Big]$$

is conducted regarding the loading behavior with variations in the parameters s_0 (cf. Tab. 4.4) and χ (cf. Tab. 4.5). Firstly, a variation of χ, the parameter of the tensor function $f(\frac{||\mathbf{C}_M||}{)}$, keeping all other parameters constant at the values presented in Tab. 4.4, is carried out.

Table 4.4.: Exemplary Parameters for Network A, with varying χ

τ	μ	η_0	s_0	$\boldsymbol{\chi}$	ζ	ξ
100	25	1	2.5	**var.**	0.001	1.5

Depending on the size of χ, the magnitude of the viscosity function is increased with escalating deformation levels. The graphical representation distinctly illustrates that χ exerts negligible influence within the regime of small deformations, yet its impact becomes more pronounced with increasing distortions (cf. Fig. 4.20). Depending on the exponent value, distinct stress curves emerge. However, the influence of the stress barrier s_0, elaborated further in the subsequent paragraph, is evident in the plot.

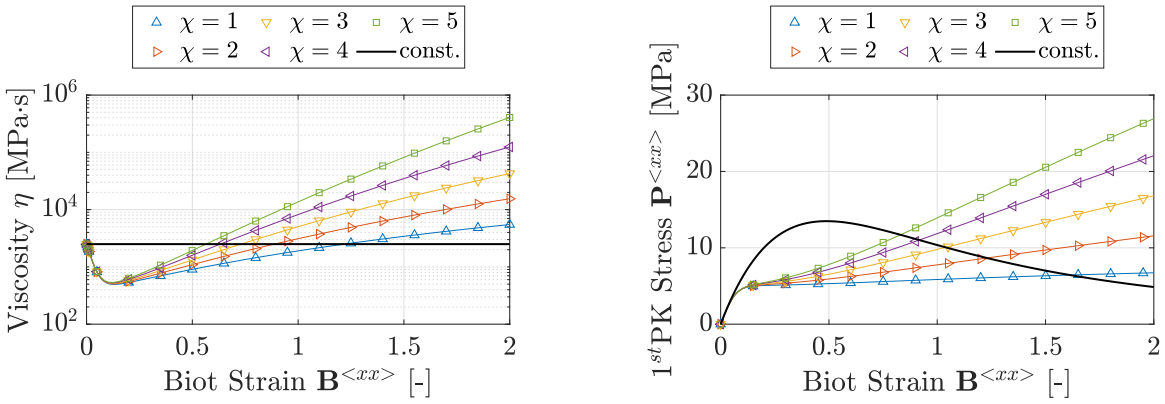

Figure 4.20.: Exemplary Calculation for the Network A, with varying χ; Viscosity (left), 1^{st}PK Stress (right)

The parameter s_0 functions as a stress barrier, significantly diminishing viscosity when a specific stress threshold is surpassed. This phenomenon is clearly observable in the graphs. Upon examining the stress curves, it becomes apparent that those incorporating stress barriers exhibit an initial stiffness identical to the stiffness of the constant viscosity curves. However, these curves rapidly plateau, resulting in an almost constant course as the stress exceeds a certain threshold. The slope of this plateau is, in turn, affected by the other parameters, which will not be further expounded upon in this discussion.

Table 4.5.: Exemplary Parameters for Network A, with varying s_0

τ	μ	η_0	$\mathbf{s_0}$	χ	ζ	ξ
100	25	1	**var.**	0	0.001	1.5

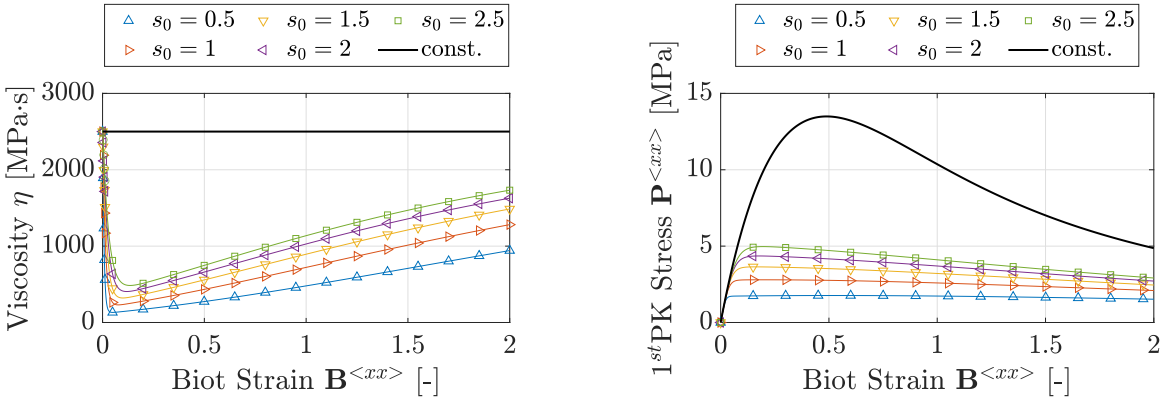

Figure 4.21.: Exemplary Calculation for the Network A, with varying s_0; Viscosity (left), 1^{st}PK Stress (right)

4.4.2. Considerations regarding the unloading behavior

A noteworthy phenomenon pertains to the disparate behaviors of the hysteresis on the loading and unloading paths. Specifically, the viscosity during loading exhibits a marked increase compared to unloading. A signum function was incorporated into the viscosity function, considerably diminishing viscosity for negative strain rates to depict this behavior with optimal precision. The influence of the relaxation time, τ, is nullified, and the viscosity is thus limited

to an exponential function contingent upon the parameters xi, zeta, and the norm of the strain rate tensor, which has a minor influence when considering other processes.

Although all networks utilize the formulation with the signum function, network B, with the respective viscosity function

$$\eta_D = \eta_0 \mu \Big(\frac{||\mathbf{C}||}{\sqrt{3}}\Big)^{\chi} \Big[\frac{1}{2}\tau \cdot \Big(1 + sign(\mathbf{D} : \mathbf{C})\Big) + exp\Big(\boldsymbol{\zeta} ||\mathbf{D}||\Big)\boldsymbol{\xi}\Big],$$

is chosen for the exemplary calculations.

ζ is multiplied with the norm of the distortion rate tensor, exerting a crucial influence on the exponent of the exponential function. Fig. 4.22 unmistakably delineates how the loading path of the hysteresis is particularly affected for varying ζ, with the relief path consistently converging towards zero.

Table 4.6.: Exemplary Parameters for Network B, with varying ζ

τ	μ	η_0	χ	$\boldsymbol{\zeta}$	ξ
100	25	1	0	**var.**	1.5

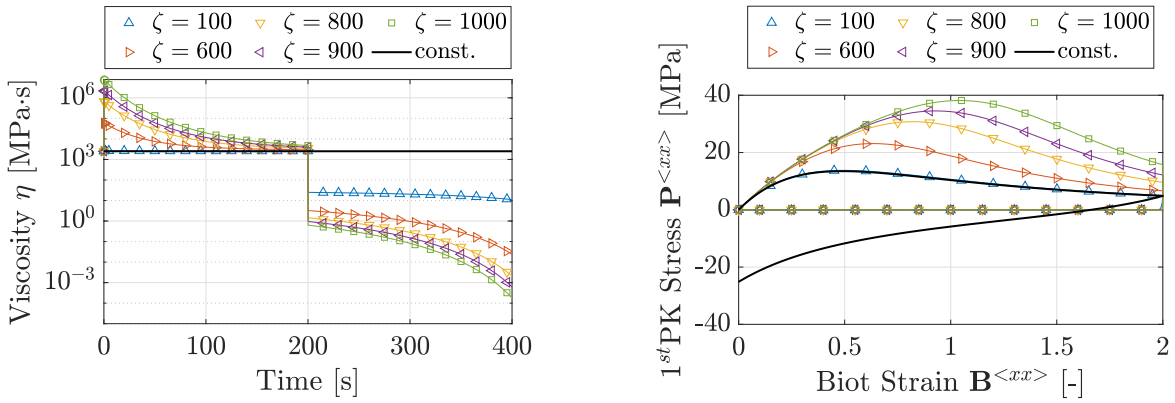

Figure 4.22.: Exemplary Calculation for the Network A, with varying ζ; Viscosity (left), 1^{st}PK Stress (right)

Conversely, ξ undergoes multiplication with the exponential function and influences its magnitude significantly. Fig. 4.23 vividly illustrates the discernible opening or closure of the hysteresis, contingent upon the value of ξ.

Table 4.7.: Exemplary Parameters for Network B, with varying ξ

τ	μ	η_0	χ	ζ	$\boldsymbol{\xi}$
100	25	1	0	0.001	**var.**

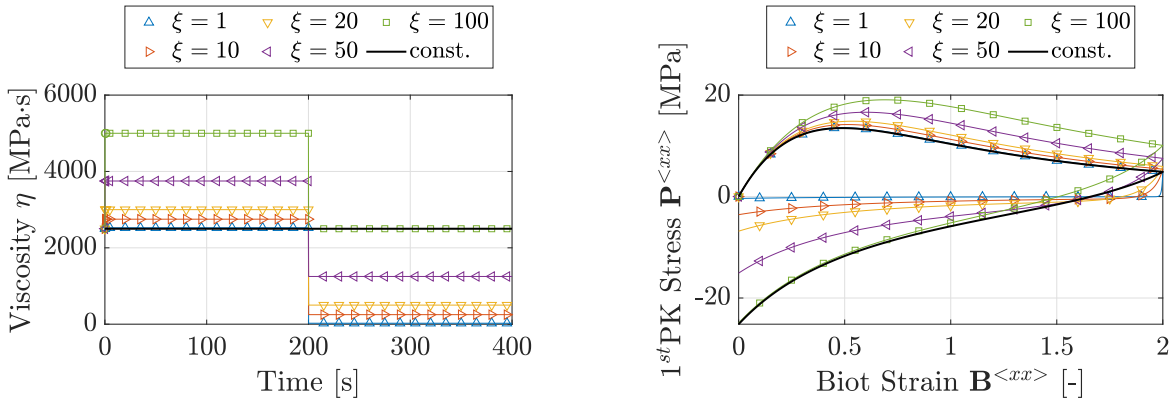

Figure 4.23.: Exemplary Calculation for the Network A, with varying ξ; Viscosity (left), 1^{st}PK Stress (right)

4.4.3. Considerations regarding the relaxation behavior

Concerning the relaxation behavior, categorizing the networks into two groups is reasonable. Group 1, consisting of networks A and B, is distinguished by the nearly uniform distribution of individual relaxation times, τ, spanning multiple decades to ensure a gradual evolution across the time spectrum. Group 2, comprising network C, conversely, is characterized by a pronounced increase in stiffness under load, followed by a rapid decrease in stiffness upon initiating the relaxation process, implemented through the term $(1-\gamma exp(\mathbf{D}_M))$, which significantly diminishes the viscosity during relaxation processes, contingent upon the parameter γ.

$$\eta_D = 2\eta_0 C_{30}\left(\frac{||\mathbf{C}||}{\sqrt{3}}\right)^{\chi}\left[\frac{1}{2}\tau\cdot\Big(1+sign(\mathbf{D}:\mathbf{C})\Big)\cdot\Big|1-\gamma exp(||\mathbf{D}||)\Big| + exp\Big(\zeta||\mathbf{D}||\Big)\xi\right]$$

The influence of the parameter gamma on the viscosity within network C and the stress is depicted in Fig. 4.24. However, when calibrating γ, one must be very careful that the value of the viscosity function does not get negative.

Table 4.8.: Exemplary Parameters for Network C, with varying γ

τ	C_{30}	η_0	χ	ζ	ξ	γ
100000	0.01	1	7	20	0.01	**var.**

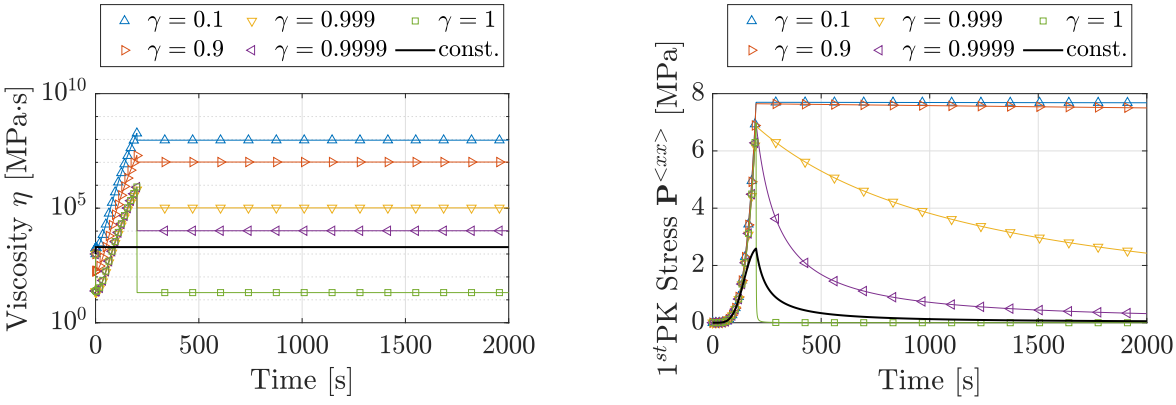

Figure 4.24.: Exemplary Calculation for the Network C, with varying γ; Viscosity (left), 1^{st}PK Stress (right)

4.5. Parameter Identification

By utilizing the results of the material characterization experiments and the presented material model, capable of qualitatively reproducing the phenomena observed during the experiments, these two elementary components are now to be brought together by adjusting the model parameters so that the experiments can be reproduced as accurately as possible.

The process of isolating the material parameters that best represent the behavior observed in the test is called parameter identification. The principle of parameter identification is minimizing the error that results from the difference between the model calculation, depending on the corresponding material parameters and the experimental measurements. The minimization of this error follows the basic rules of optimization (cf. Sec. 2.4), and depending on the kind of problem, there are several possible procedures. Global optimization methods are advantageous for problems dependent on many parameters and can have various local minima. One possibility for global optimization is the global search algorithm from Matlab, described in more detail below.

4.5.1. Matlab - Globalsearch

Run Start Point The user defines a starting value $x_{0,ini}$. This initial value has an objective function value $f(x_{0,ini})$ and represents a point in the n-dimensional parameter space, where n equals the number of parameters to be optimized. The local solver *fmincon* is started from this initial value. If it converges, the location of the solution point $x_{0,sol}$ and its function value $f(x_{0,sol})$ is determined, and a critical distance and a critical function value are initialized as limits. The critical distance is calculated from a distance between the start point $x_{0,ini}$ and endpoint $x_{0,sol}$ of this optimization. It forms a basin of attraction around the solution point, subject to the heuristic assumption that it is spherical with a radius of

$$r_{0,sol} = |x_{0,sol} - x_{0,ini}| \tag{4.41}$$

The second limit value, called *score* of the function, is calculated from the objective function value at the end of the optimization $f(x_{0,sol})$ and a weighted portion that takes into account the sum of possible boundary condition $g_i(x)$ violations.

$$s_{0,sol} = f(x_{0,sol}) + w \cdot \sum_{i=1}^{m} viol(g_i(x_{0,sol})) \tag{4.42}$$

Considering the possible violation of boundary conditions ensures that the solution points are feasible and results in a *score* equal the objective function value.

Create Trial Points In a second step, the *scattersearch* algorithm creates trial points *NumTrialPoints* that lie within the limits specified by the user and represent potential starting values. A subset of these trial points *NumStageOnePoints* is selected and their score evaluated. The point with the best score serves as the starting value for a further local optimization and the remaining points of the subset are removed from the list of trial points. If the starting point $x_{1,ini}$ with $f(x_{1,ini})$ converges and thus results in another solution point $x_{1,sol}$ with a corresponding function value $f(x_{1,sol})$, score $s_{1,sol}$ and distance $r_{1,sol}$ are determined. If both starting points $x_{0,ini}$ and $x_{1,ini}$ have converged, a first limit for a possible function value, called *LocalSolverThreshold*, results in $min(f(x_{0,sol}); f(x_{1,sol}))$. If neither of the two values exists or they are infeasible, the *LocalSolverThreshold* corresponds the penalty function value of the Stage 1 start point $s_{1,ini}$.

In addition, two categories of counters are created to ensure the threshold values are flexible. One counter lists how often the local optimizer was not started because the score of a trial point is greater than the threshold value (*localSolverThreshold*). In the other category, each basin has a separate counter, which is incremented if a trial point is within a corresponding basin.

Main Loop The individual trial points are analyzed point by point. The population size and, therefore, the number of trial points can be adjusted in each iteration (see scatter search [116]). In order to decide whether the local optimization is executed for the corresponding point, it is first checked whether the score of the point exceeds the current threshold value (*localSolverThreshold*) and whether the point lies within an existing basin. If the score of the point does not exceed the threshold nor is within a basin of attraction, the local optimization is executed.

If the local optimization runs, all counters are set to zero. If the solver converges, the algorithm checks whether the solution point differs from the existing ones. On the one hand, it checks whether the distance between the solution point and the other solution points does not fall below a limit value *XTolerance* and, on the other hand, whether the objective function value of the solution point ($f(x_{k,sol})$) differs sufficiently from the function values of the other solution points. The user can determine the two corresponding limit values with *XTolerance* and *FunctionTolerance*. If neither falls below the limit values, a new element is created in the solution vector. If specific points fall below both limits simultaneously, the solution points are considered identical, and no new element is created.

If a new element is created, the threshold is simultaneously replaced by the score of the trial point $x_{k,ini}$ of the current iteration step, and the basin radius for $x_{k,sol}$ is defined as the maximum distance of the current starting point $x_{k,ini}$ to the solution point $x_{k,sol}$ and the maximum radius of the other points.

If the local solver is not executed, the corresponding counters are incremented, and all others are set to zero, ensuring that the limit values are only adjusted if a corresponding threshold has been violated several times in direct succession. If a certain number of consecutive iterations *MaxWaitCycle* have taken place without starting the optimization, the limit values are adjusted to prevent the algorithm from running empty. Two cases are distinguished. If a violation of the *localthreshold* is the reason for not running the optimizer, the threshold is adjusted with a *PenaltyThresholdFactor*. If a violation of the basin is the reason, the corresponding radius is adjusted with a *BasinRadiusFactor*.

This algorithm runs until either the maximum number of iteration steps has been reached, all start values have been checked or the maximum time has been exceeded.

4.5.2. Matlab - Globalsearch adapted

The material model depends on 46 parameters, each with its unique role. Among these, the parameter gamma holds particular significance. It must be chosen carefully to ensure that the term $(1-\gamma exp(\mathbf{D}_M))$ is larger than zero and the viscosity is greater than one. While the other parameters can be chosen arbitrarily, limiting them to certain intervals of possible values is reasonable. The selection of these boundaries is a delicate balance between minimizing the run time of the optimization algorithm and obtaining the best possible values. If the limits are too large, the algorithm may run for an uneconomically long time. On the other hand, if the limits are too narrow, relevant values may be overlooked. Within the optimization, the greatest challenge is overcoming local minima, which are numerous in an n-dimensional parameter space.

Matlab's *globalsearch* algorithm, utilizing the local optimization solver *fmincon*, was selected

to overcome these local minima. As described above, this algorithm performs numerous optimizations by cleverly varying the parameters and saves the one with the best approximation. The start values and limits of the individual parameters are shown in the following tables. It is crucial to mention that the parameters are varied on a logarithmic scale. This ensures that even parameters that differ by several orders of magnitude can be varied uniformly.

Tab. 4.9 shows the boundary conditions of the global optimization algorithm used for the parameter identification. These boundaries, in particular, explained in Sec. 4.5.1, were extended by *DistanceThresholdFactor*, adjusting the criteria for every basin, *PenaltyThresholdFactor*, controlling the respective *localSolverThreshold*, *MaxTime*, specifying the maximum time in [s] the algorithm runs, and *StartPointsToRun*, deciding whether the start values lie within user-defined boundaries or not.

Table 4.9.: Boundary Conditions for global optimization

NumTrialPoints	3e4	[-]
BasinRadiusFactor	0.5	[-]
DistanceThresholdFactor	0.5	[-]
MaxWaitCycle	50	[-]
NumStageOnePoints	1000	[-]
PenaltyThresholdFactor	0.4	[-]
FunctionTolerance	1e-4	[-]
MaxTime	432000	[s]
StartPointsToRun	bounds	[-]
XTolerance	2e-4	[-]

The error between the model calculation and the measurement results, which the parameter identification aims to minimize, is calculated by the *evalError* function and passed to the optimization algorithm, comparing the error to a user-defined threshold. This function depends on the test procedure (strain, time), the current parameter vector, and the test results (stress). The *evalError* function calculates an error by calculating the model response using strain, time, and parameter vector and comparing the result to the respective measurement. This error, directly connected to the parameter vector $\mathbf{p}$, is calculated according to the Euclidean norm:

$$err(\mathbf{p}) = \sqrt{\sum_{i=1}^{N} \left(\frac{\mathbf{P}_{M,Experiment}^{<xx>,(i)} - \mathbf{P}_{M,Model}^{<xx>,(i)}(\mathbf{p})}{\mathbf{P}_{M,Experiment}^{<xx>,(i)}} \right)^2} \tag{4.43}$$

The following diagram (Fig. 4.25) illustrates the essential components of the optimization process, starting with the measurement data and the initial set of parameters. The measurement input remains constant, and the parameter vector constantly changes in each iteration step, aiming to minimize the difference between test data and model calculation. The iteration continues until the error between the model calculation and the measured data is lower than a user-defined threshold, indicating the final parameter set.

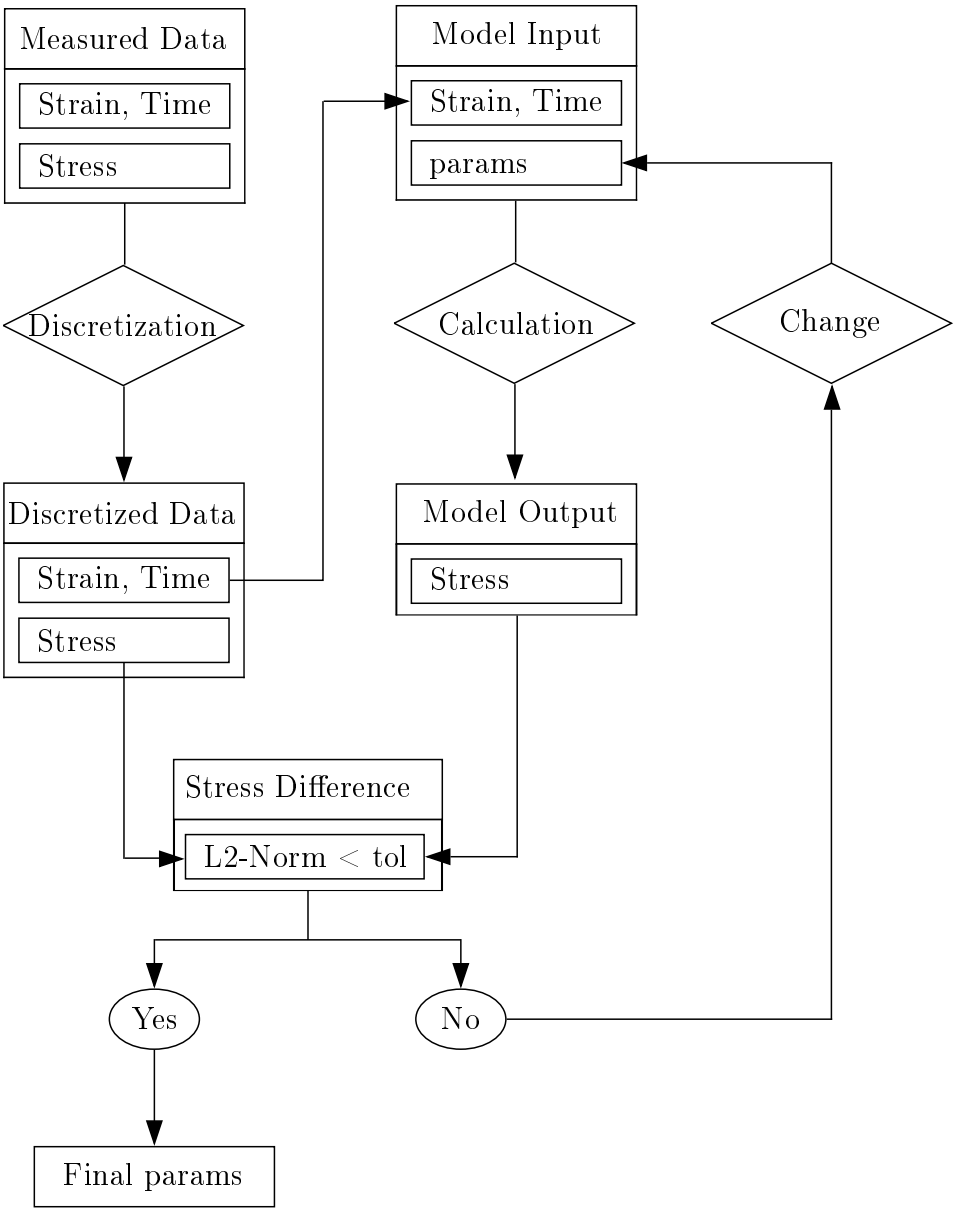

Figure 4.25.: Essential components of the optimization algorithm

The optimization procedure unfolds in three steps, sequentially releasing the final parameter set. For each step, the respective test data, which serves as input for the error calculation, and the particular formulation of the viscosity functions along with the corresponding parameter set are adjusted. Each step is described individually in more detail below. However, a decisive step in the optimization procedure is the choice of start values for the particular parameters of the set. As the set contains physical quantities such as shear modulus, relaxation times, and the phenomenological derived parameters, the values inside the parameter set differ by several orders of magnitude. This large discrepancy between the single values would complicate the optimization process. Therefore, the parameters are transformed to a logarithmic scale to overcome this problem. So, inside the optimization algorithm, the parameters appear as the logarithm (log10) of the individual parameter. However, when calculating the error by utilizing the error function, the values are passed in logarithmic scale and inside the error function transformed to standard scale for calculation of the model response.

Optimization - Step 1 The first part of the parameter set $\mathbf{p}_1 = [\tau; \mu; C30; s_0; \chi]^T$ is identified by utilizing the viscosity functions

$$\eta_{D,A} = \eta_0 \mu \Big(\frac{||\mathbf{C}||}{\sqrt{3}} \Big)^{\chi} \Big[\tau \cdot exp\Big(- \frac{||\mathbf{T}||}{s_0} \Big) \Big]$$

$$\eta_{D,B} = \eta_0 \mu \Big(\frac{||\mathbf{C}||}{\sqrt{3}} \Big)^{\chi} \Big[\tau \Big]$$

$$\eta_{D,C} = 2\eta_0 C_{30} \Big(\frac{||\mathbf{C}||}{\sqrt{3}} \Big)^{\chi} \Big[\tau \cdot \Big| 1 - exp(||\mathbf{D}||) \Big| + 1 \Big]$$

for the model calculation, the results of the failure, and the relaxation tests as input data. At this point, it is crucial to note that only the 3-hour relaxation tests were considered for the optimization, as the 12-hour tests will serve validation purposes. Tab. 4.10 shows the respective parameters, categorized in start values (ini), lower (lb), and upper boundaries (up). According to the *bounds* option of the *StartPointsToRun* boundary, the algorithm only varies the parameters within these limits, speeding up the optimization process.

Table 4.10.: Parameters for Maxwell elements Network A (k = 1 to 5)

τ	lb	-2	-1	0	1	2	3	4	5	6	4
	ini	-1	0	1	2	3	4	5	6	7	6
	ub	0	1	2	3	4	5	6	7	8	8
μ	lb	-1	-1	-1	-1	-2	-2	-2	-2	-2	
	ini	1	1	1	0.5	-1	-1	-1	-1	-1	
	ub	2	1.5	1	1	0.5	0.5	0.5	0.5	0.5	
C_{30}	lb	-3									
	ini	-1									
	ub	0									
s_0	lb	-1	-1	-1	-1	-1					
	ini	0	0	0	0	0					
	ub	1	1	1	1	1					
χ	lb	0	0								
	ini	0.5	0.5								
	ub	1	1								

Optimization - Step 2 In the second step, the set of input test data is extended by the results of the cyclic tests. Expanding the considered test data comes with an extension of the viscosity function, taken into account for optimization. As the signum function was introduced to cover the material behavior during unloading processes, the viscosity is enriched by a signum function. Furthermore, a new vector $\mathbf{p}_2$, containing the material parameters ξ aligned to the

signum functions, is introduced.

$$\eta_{D,A} = \eta_0 \mu \Big(\frac{||\mathbf{C}||}{\sqrt{3}} \Big)^{\chi} \Big[\frac{1}{2} \tau \cdot exp\Big(-\frac{||\mathbf{T}||}{s_0} \Big) \Big(1 + sign(\mathbf{D} : \mathbf{C}) \Big) + exp\Big(||\mathbf{D}|| \Big) \xi \Big]$$

$$\eta_{D,B} = \eta_0 \mu \Big(\frac{||\mathbf{C}||}{\sqrt{3}} \Big)^{\chi} \Big[\frac{1}{2} \tau \Big(1 + sign(\mathbf{D} : \mathbf{C}) \Big) + exp\Big(||\mathbf{D}|| \Big) \xi \Big]$$

$$\eta_{D,C} = 2\eta_0 C_{30} \Big(\frac{||\mathbf{C}||}{\sqrt{3}} \Big)^{\chi} \Big[\frac{1}{2} \tau \Big(1 + sign(\mathbf{D} : \mathbf{C}) \Big) \Big| 1 - exp(||\mathbf{D}||) \Big| + exp\Big(||\mathbf{D}|| \Big) \xi \Big]$$

The parameters $\mathbf{p}_1 = [\tau; \mu; C30; s_0; \chi]^T$, determined in the first step of the optimization, also serve to calculate the model response within the optimization process. However, they are kept as identified in the first step. The start values and the lower and upper limits of the parameters to be varied in the second optimization step are plotted in Tab. 4.11.

Table 4.11.: Parameters for Maxwell elements Network A (k = 1 to 5)

ξ	lb	-3	-3	-3	-3	-3	-3	-3	-3	-3	-3
	ini	-1	-1	-1	-1	-1	-1	-1	-1	-1	-1
	ub	1	1	1	1	1	1	1	1	1	1

Optimization - Step 3 In the third and final step of the parameter identification, the same input test data as used in the second step is utilized. However, the viscosity function is enriched by two additional parameters, stored in the parameter vector $\mathbf{p}_3 = [\zeta; \gamma]^T$.

$$\eta_{D,A} = \eta_0 \mu \Big(\frac{||\mathbf{C}||}{\sqrt{3}} \Big)^{\chi} \Big[\frac{1}{2} \tau \cdot exp\Big(-\frac{||\mathbf{T}||}{s_0} \Big) \Big(1 + sign(\mathbf{D} : \mathbf{C}) \Big) + exp\Big(\zeta ||\mathbf{D}|| \Big) \xi \Big]$$

$$\eta_{D,B} = \eta_0 \mu \Big(\frac{||\mathbf{C}||}{\sqrt{3}} \Big)^{\chi} \Big[\frac{1}{2} \tau \Big(1 + sign(\mathbf{D} : \mathbf{C}) \Big) + exp\Big(\zeta ||\mathbf{D}|| \Big) \xi \Big]$$

$$\eta_{D,C} = 2\eta_0 C_{30} \Big(\frac{||\mathbf{C}||}{\sqrt{3}} \Big)^{\chi} \Big[\frac{1}{2} \tau \Big(1 + sign(\mathbf{D} : \mathbf{C}) \Big) \Big| 1 - \gamma exp(||\mathbf{D}||) \Big| + exp\Big(\zeta ||\mathbf{D}|| \Big) \xi \Big]$$

As in the second step, the already identified parameter vectors $\mathbf{p}_1$ and $\mathbf{p}_2$ are used to calculate the model response but are not varied.

Table 4.12.: Parameters for Maxwell elements Network A (k = 1 to 5)

ζ	lb	-3	-3	-3	-3	-3	-3	-3	-3	-3	-3
	ini	0	0	0	0	0	0	0	0	0	0
	ub	3	3	3	3	3	3	3	3	3	3
γ	lb	-3									
	ini	0									
	ub	3									

After the third optimization step, all parameters are stored in the parameter-vector $\mathbf{p} = [\mathbf{p}_1; \mathbf{p}_2; \mathbf{p}_3]$. Tab. 4.13 and 4.14 contain all identified material parameters, categorized according to the individual networks.

Table 4.13.: Parameters for Maxwell elements Network A (k = 1 to 5)

k	1	2	3	4	5
$\tau^{(k)}$ [s]	12.11e-2	53.12e-2	51.94e-1	63.16e0	43.93e2
$\mu^{(k)}$ [MPa]	25.90e0	73.25e-1	19.17e-1	52.06e-2	22.48e-2
$\chi^{(k)}$ [-]	62.26e-1	62.26e-1	62.26e-1	62.26e-1	62.26e-1
$s_0^{(k)}$ [MPa]	24.20e-1	57.81e-1	21.83e-1	42.75e-1	15.65e-2
$\zeta^{(k)}$ [-]	14.03e-2	30.84e0	42.14e-1	10.00e2	12.41e-3
$\xi^{(k)}$ [-]	11.34e-4	16.97e-4	30.24e-3	16.93e-4	95.07e-1

Table 4.14.: Parameters for Maxwell elements Network B (l = 1 to 4) and Network C (m = 1)

l	1	2	3	4
$\tau^{(l)}$ [s]	17.49e3	11.92e4	10.24e5	10.01e6
$\mu^{(l)}$ [MPa]	48.11e-3	72.13e-3	94.30e-3	63.65e-3
$\chi^{(l)}$ [-]	62.26e-1	62.26e-1	62.26e-1	62.26e-1
$\zeta^{(l)}$ [-]	74.37e-2	91.98e1	15.08e-1	36.04e-1
$\xi^{(l)}$ [-]	19.23e-2	10.00e-4	10.00e0	49.40e-2

m	1
$\tau^{(m)}$ [s]	80.17e4
$C_{30}^{(m)}$ [MPa]	10.52e-3
$\chi^{(m)}$ [-]	69.27e-1
$\gamma^{(m)}$ [-]	10.00e-1
$\zeta^{(m)}$ [-]	21.04e0
$\xi^{(m)}$ [-]	38.74e-4

4.6. Model Calculation

After calibrating the parameters of the material model using the experimental data from Ch. 3, the agreement of the calculation and the actual measurement are now checked in terms of recalculation and validation. For this purpose, the tests considered for the parameter identification are used for the recalculation, and further tests not considered for the parameter identification are used for the validation. In both cases, each input for the model calculation follows the respective experimental test specifications. A comparison graph plotting the calculation and experiment and an error graph plotting the measured and the calculated stresses against the measured ones illustrate the quality of each calculation. In the best case, if the experiment and calculation match precisely, the result is a line with a 45° angle.

4.6.1. Recalculation

The recalculation checks how well the parameter identification worked using the same tests used for model calibration as the basis for the calculation. If the results match precisely, the model is validated for these tests. However, this does not necessarily mean that the model works for test specifications or loads other than those of the calibration tests.

Tension-Tests until failure The comparison between the experimental data and the model calculations for the tests until failure demonstrates an excellent agreement up to a strain of

150 [%] and a stress level of 20 MPa, as shown in Fig. 4.26. Notably, the model's response generally tends to be stiffer than the measured data. Especially for the highest strain rate of 0.1 [1/s], at higher strains, the calculation overestimated the stress of the experiment up to 20 [%].

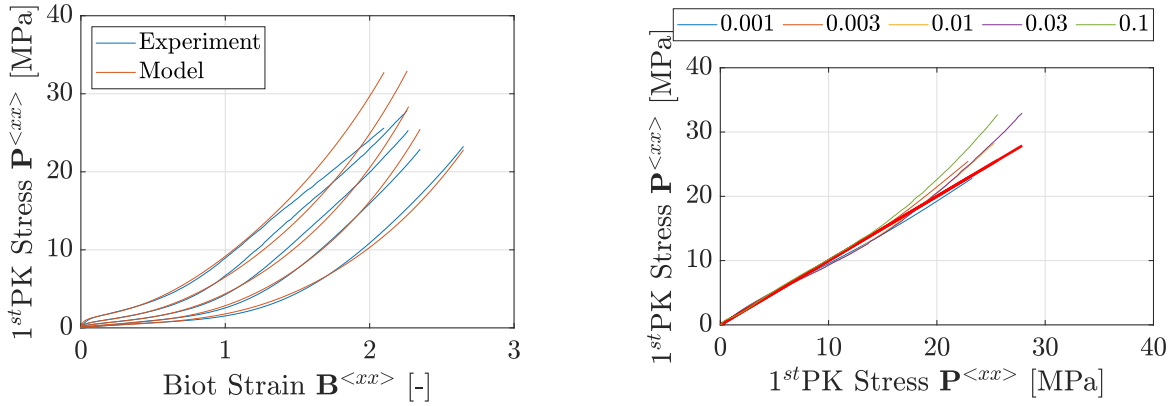

Figure 4.26.: Tension until Failure - Comparison (left); Error (right)

Cyclic Tests The cyclic tests have been classified into two pairs, characterized by the applied strain rate and the turning point, where a "turning point" signifies the specific strain level reversing the loading direction.

In the first group, these tests share a consistent applied strain rate but exhibit variations in their turning points. Remarkably, the agreement between the test data and the model calculations is decisive for the turning points corresponding to high strains. However, it is essential to acknowledge that the relative error tends to increase for turning points associated with more minor strains, as demonstrated in Fig. 4.27. Despite these variations, the model offers a qualitatively accurate representation of the overall behavior. Notably, the model captures the intricate shape of the hysteresis, illustrating the distinctive behavior during the transition from loading to unloading, even for scenarios involving significantly different strain levels.

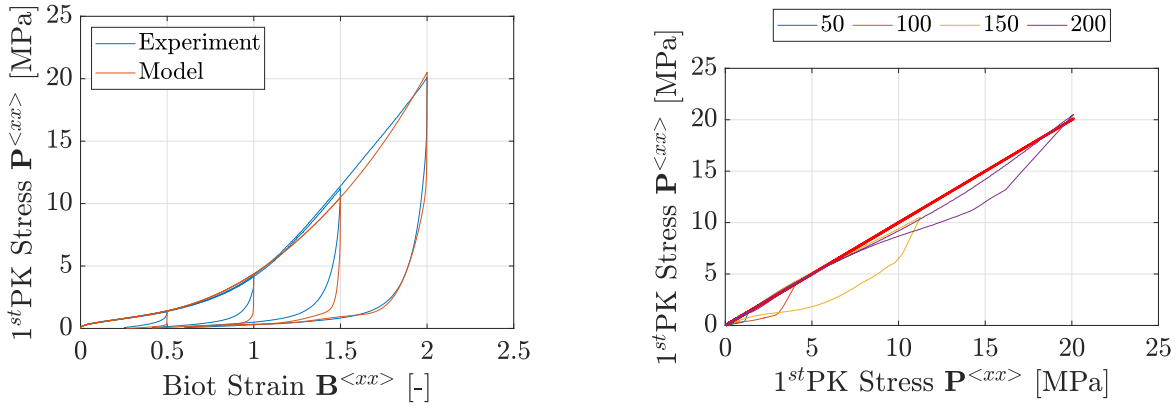

Figure 4.27.: Cyclic Tests at the same Strain Rate, loaded to different Strain Levels - Comparison (left); Error (right)

The second group of tests comprises those with a turning point at the same strain level (150 [%]) but all undergoing varying strain rates. The model calculations exhibit a high agreement with the experimental data in these tests, particularly for the cases with the highest strain rate. However, as the strain level decreases, the agreement becomes less accurate. Nevertheless, it is

essential to note that the qualitative behavior is well-replicated within this second group, just as within the first group of tests (cf. Fig. 4.28).

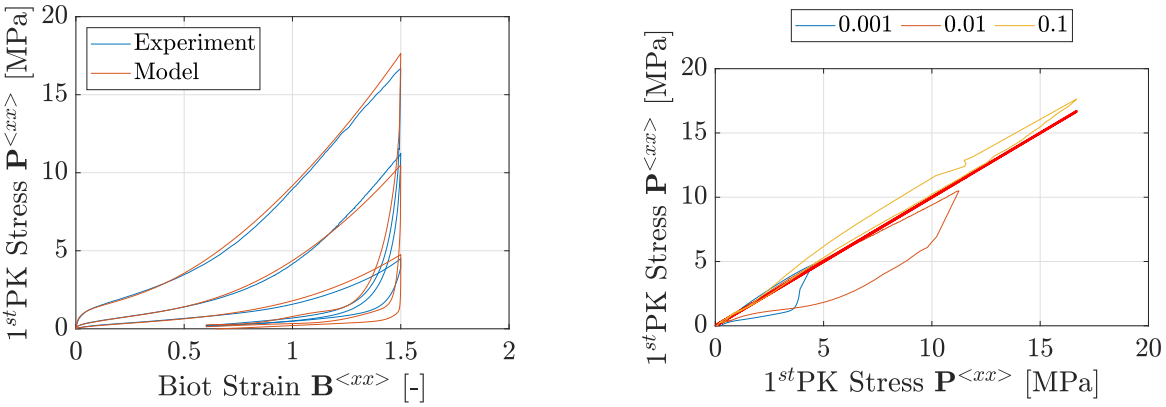

Figure 4.28.: Cyclic Tests at different Strain-Rates, loaded to the same Strain Level - Comparison (left); Error (right)

Tab. 4.15 displays the respective areas of the hystereses of the cyclic tests for the test results and the model calculation. The size of the area indicates the amount of energy dissipated by the material. The lower the strain rate and level of the turning point, the bigger the deviation between calculation and experiment, a conclusion also drawn from the above graphs. A detailed overview of the respective areas is depicted in the Appendix.

Table 4.15.: Areas of the single hystereses indicating the dissipated energy

Specification	$A_{Experiment}$	A_{Model}	$\frac{A_{Model}}{A_{Experiment}} - 1$
0.01, 50	0.2931	0.3698	0.2617
0.01, 100	1.2691	1.5682	0.2358
0.01, 150	4.2404	4.7169	0.1124
0.01, 200	11.2302	10.9004	-0.029
0.001, 150	1.4022	2.0208	0.4412
0.1, 150	7.5791	7.7073	0.0169

Relaxation Tests Several relaxation tests were carried out and categorized into two groups. These groups differ in the strain rate and the corresponding holding level, which is the point at which the strain is kept constant. It should be noted that the tests used for the recalculation, as with the parameter identification, correspond to the tests with a holding time of three hours.

The first group comprises four tests, each corresponding to different strain levels (50, 100, 150, 200 [%]) but approached with a consistent strain rate of 0.01 [1/s]. Notably, these particular tests are synchronized with the cyclic tests performed at the same rate, and their turning points align precisely with the strain levels encountered in the cyclic tests. The results exhibit excellent agreement, as depicted in Figure 4.29.

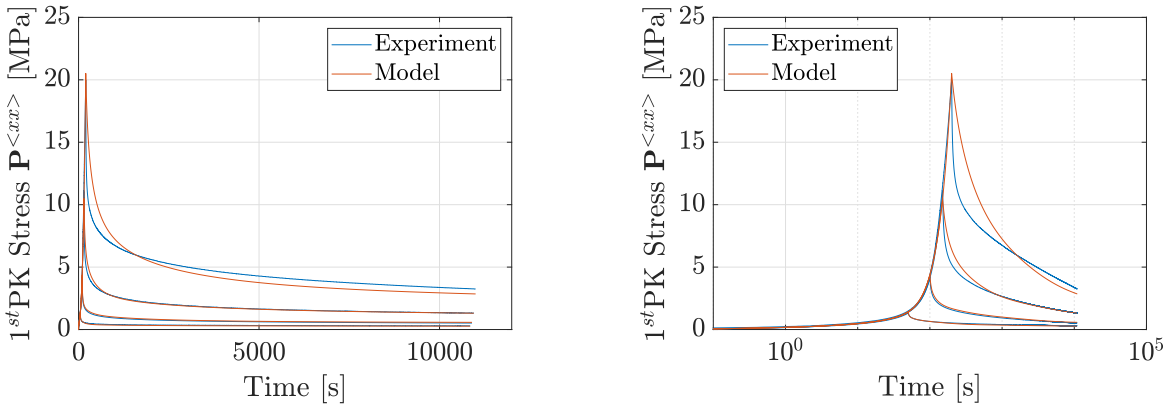

Figure 4.29.: Relaxation Tests loaded with the same Strain Rate up to different Strain Levels - Comparison: Normal Scale (left), Logarithmic Scale (right)

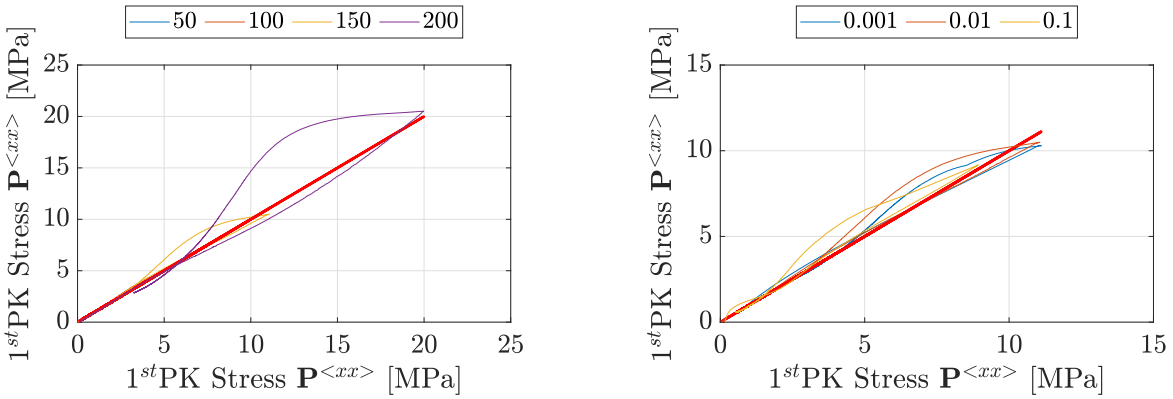

Figure 4.30.: Relaxation tests loaded with the same (left) and different strain rate (right) up to different strain levels - Error

The second group comprises three relaxation tests, each conducted at varying strain rates: 0.1, 0.01, and 0.001, and each loaded to different strain levels, specifically 100, 150, and 200. Notably, the selection of these strain levels was designed to pair the highest strain level with the lowest strain rate, and so on. This approach was adopted to investigate the distinct response of the material for similar strain levels but under varying time histories. The relaxation tests, conducted at various strain rates and levels, as shown in Figure 4.31, also demonstrate excellent agreement.

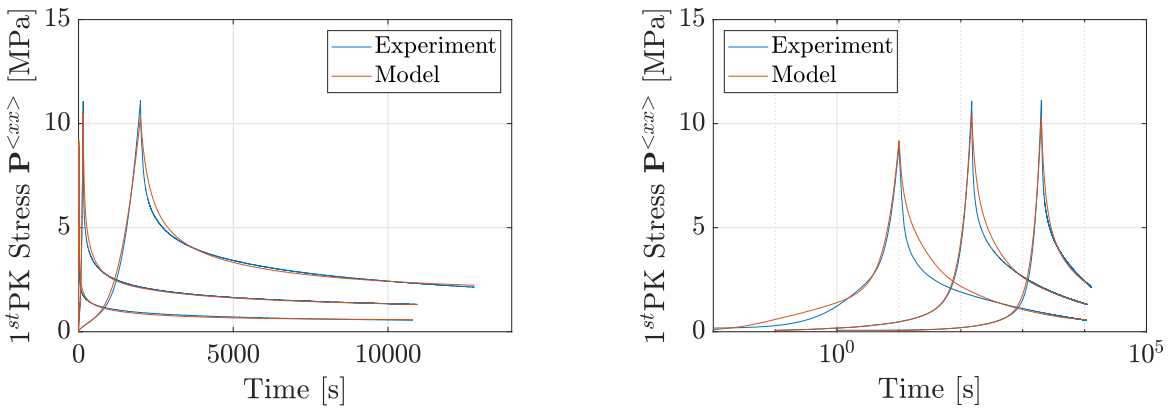

Figure 4.31.: Relaxation Tests loaded with different Strain Rates up to different Strain Levels - Comparison: Normal Scale (left), Logarithmic Scale (right)

4.6.2. Validation

After successfully demonstrating the quality of the model concerning the recalculation of the tests included in the parameter identification process, this section aims to check the model's transferability to loading configurations not taken into account in the parameter identification. Two test cases are analyzed for this purpose: The extension of the relaxation tests to 12 hours from series one and several test specifications with an applied constant displacement rate presented in [193], which is currently under revision, and referred to as test series three. The tests of test series three followed the same conditioning, using the same testing device under the same climate as described in Sec. 3.1.1. However, these tests were carried out with displacement control instead of strain rate control, utilizing an optical measuring device to track the deformations.

Relaxation Tests - Test Series One The relaxation tests were carried out the same way as in the previous section, whereby the holding time was increased from 3 to 12 hours. The results are shown in Fig. 4.32 and Fig. 4.34 as comparison plots in standard and logarithmic scale, the quality is demonstrated with the help of error plots (cf. 4.33 and 4.35).

The tests with the same strain rate (0.01 [1/s]) show excellent agreement for the holding levels of 50 to 150 [%]. The curve agrees qualitatively for elongation of 200 [%] but deviates significantly more overall than the other tests, especially in the area of the first stiffness drop. In general, the deviation in the area of the first striking drop in stiffness deviates more strongly with increasing strain levels.

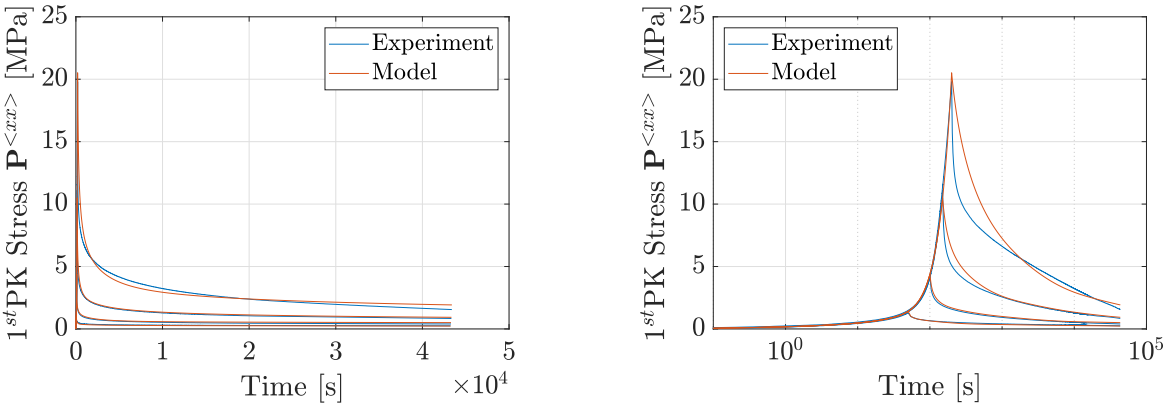

Figure 4.32.: Relaxation Tests loaded with the same Strain Rate up to different Strain Levels - Comparison: Normal Scale (left), Logarithmic Scale (right)

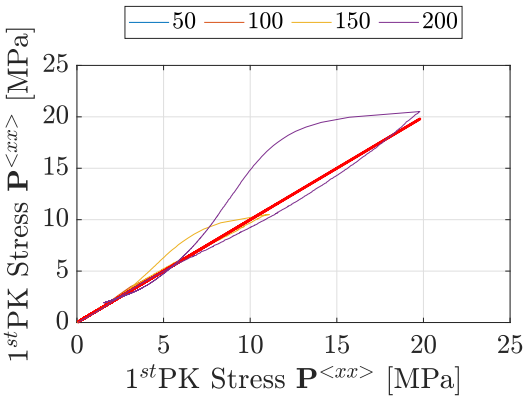

Figure 4.33.: Relaxation Tests loaded with the same Strain Rate up to different Strain Levels - Error

The tests with different strain rates and levels show a varying quality. The tests with the highest strain rate (0.1 [1/s]) deviate more strongly at the beginning, in the area of the first drop in stiffness, and then adapt to the experimentally determined curve as the holding time increases. The test with the lowest strain rate matches the material behavior from the experiments excellently at the beginning but deviates more strongly as the holding time increases. However, looking at the test curve in the logarithmic scale reveals a strong kink with a decreased stiffness, which may indicate an inconsistency during this test. As described in the previous section, the test with the mean strain rate shows good agreement over the entire range, with slightly overestimating the stiffness in the initial range.

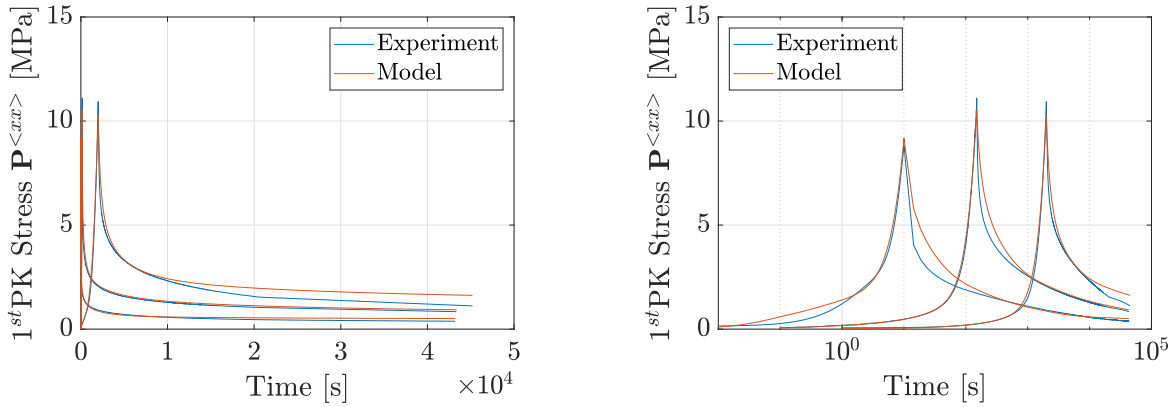

Figure 4.34.: Relaxation Tests loaded with different Strain Rates up to different Strain Levels - Comparison: Normal Scale (left), Logarithmic Scale (right)

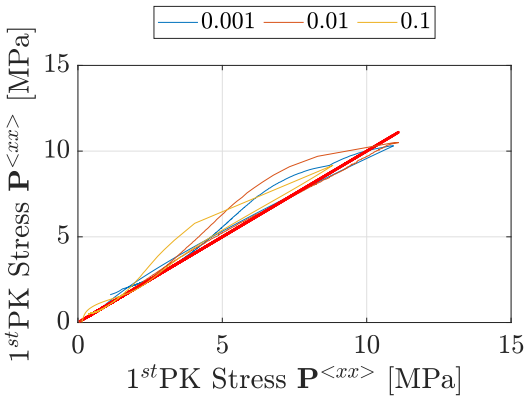

Figure 4.35.: Relaxation Tests loaded with different Strain Rates up to different Strain Levels - Error

Tension Tests - Test Series Three The tension tests used for validation were carried out at two constant displacement rates of 5 and 50 [mm/min]. Fig. 4.36 illustrates the resulting strain applied over time corresponding to the two displacement rates. It is pretty evident that the strain over time courses, representing the strain rate, is no longer constant and, therefore, differs from the specifications used for the parameter identification.

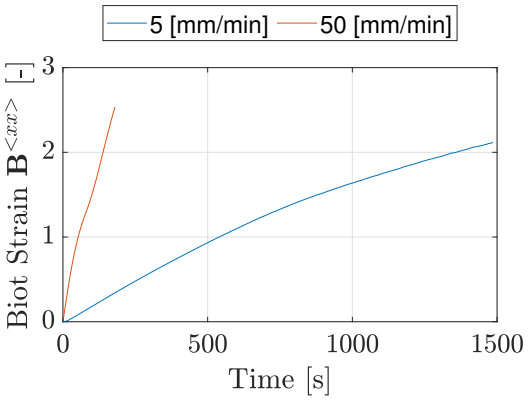

Figure 4.36.: Test procedure for the tension tests at two different different displacement rates

Fig. 4.37 presents the experimental results, the model calculation, and the deviation between experiment and modeling. There is an almost perfect match for the lower displacement rate and an ideal coincidence for the high displacement rate up to a strain 200 [%]. However, For higher strains, the deviation between model and experiment increases to 50 [%].

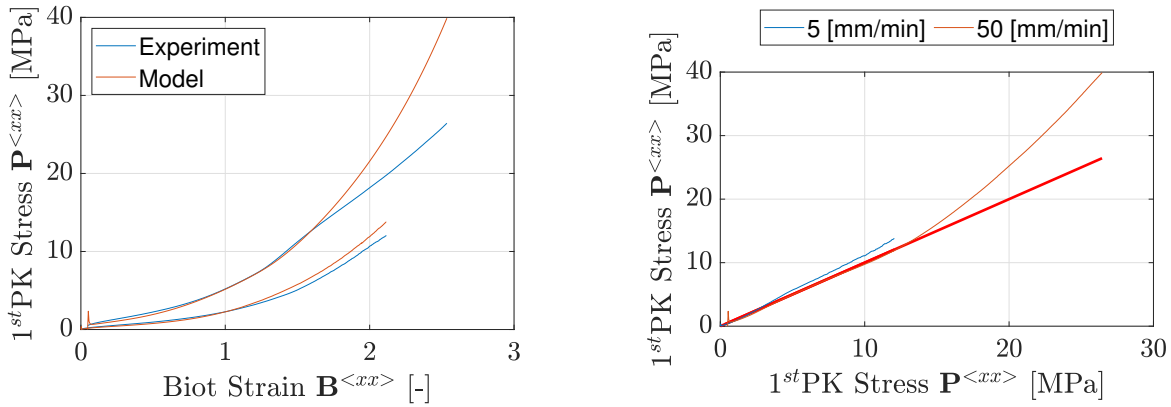

Figure 4.37.: Tension tests with different constant displacement rates - comparison (left); error (right)

Cyclic Tests - Test Series Three The cyclic tests of series three show two decisive characteristics: First, they were carried out with a constant displacement rate, which resulted in a variable strain rate. Second, they have two loading and unloading cycles. Both conditions have not been considered for parameter identification, so these tests are ideal for validation. Two distinct displacement rates were considered (Offereins). Fig. 4.38 displays the test procedures for a velocity of 5 and 50 [mm/min].

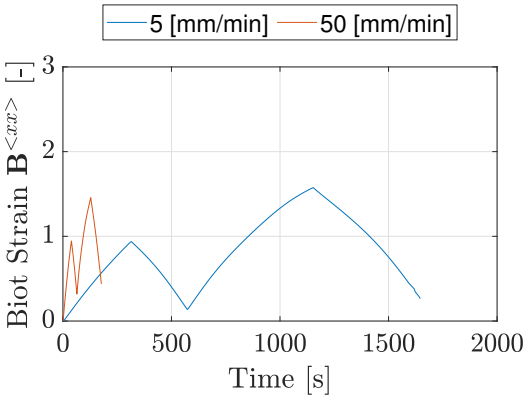

Figure 4.38.: Test procedure for the cyclic tests at two different displacement rates

Fig. 4.39 shows the experimental and modeling results concerning the low displacement rate. The model results excellently reproduce the test results on the loading paths, but there is a more significant deviation in the unloading paths. However, the qualitative behavior coincides quite well.

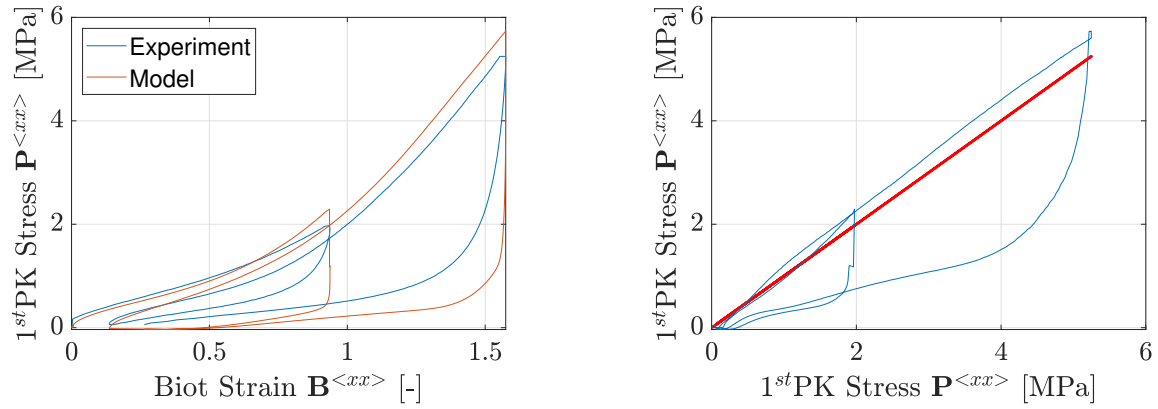

Figure 4.39.: Cyclic test at 5 [mm/min] displacement rate - comparison (left); error (right)

Fig. 4.40 presents the results for the higher strain rate, showing a perfect coincidence for the first loading path but with a more significant deviation for the second path, especially in the beginning. However, the representation of the test results on the unloading path is better concerning the higher displacement rate than the lower one. Again, the qualitative behavior is presented excellently.

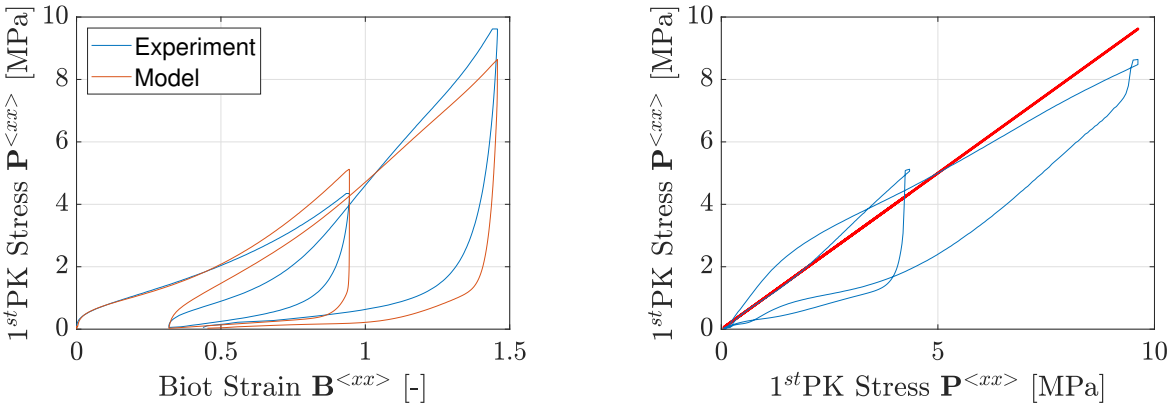

Figure 4.40.: Cyclic test at 50 [mm/min] displacement rate - comparison (left); error (right)

Relaxation - Test Series Three The relaxation test approached with a displacement rate of 50 [mm/min] follows the test specification illustrated in Fig. 4.41, concerning standard and logarithmic representation.

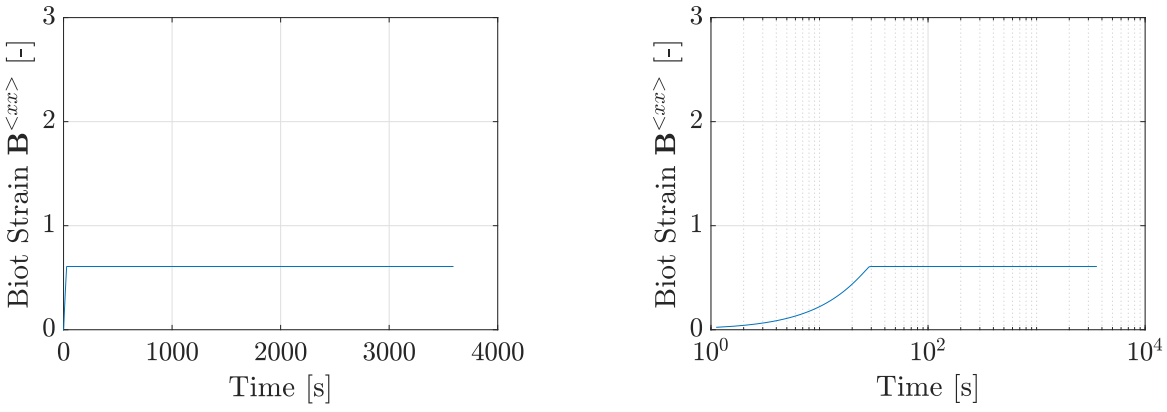

Figure 4.41.: Test procedure for the relaxation test achieved at a displacement rate - standard scale (left); logarithmic scale (right)

The results show pretty similar courses, which excellently represent qualitative behavior.

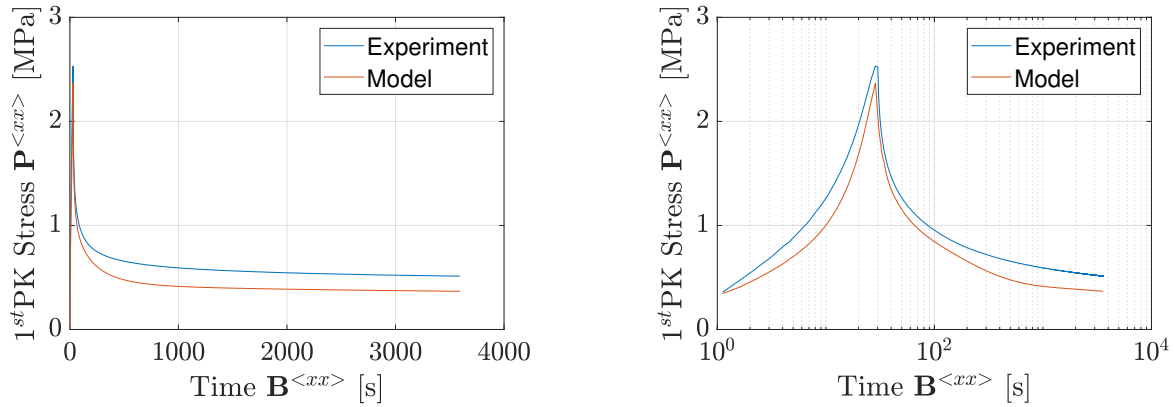

Figure 4.42.: Relaxation test - comparison in standard scale (left); in logarithmic scale (right)

However, glancing at Fig. 4.43, the modeling results show lower stresses over the whole course.

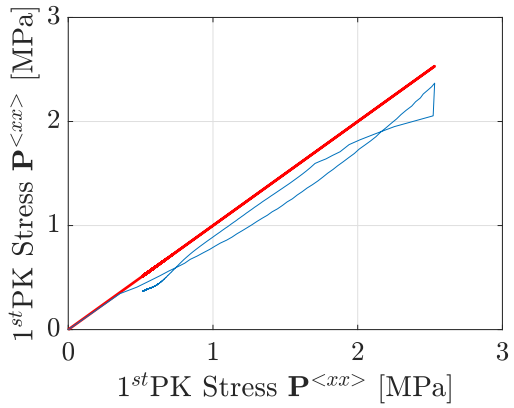

Figure 4.43.: Relaxation test - Error

4.6.3. Precalculation

Relaxation tests are now simulated over 24 hours to visualize the material at the end of a residual load-bearing capacity test. The strain levels are approached at a strain rate of 0.01 [1/s] and kept constant at the corresponding level. Figs. 4.44 and 4.45 illustrate the simulation results in standard and logarithmic representation, with the respective strain levels shown in the legends of the figures.

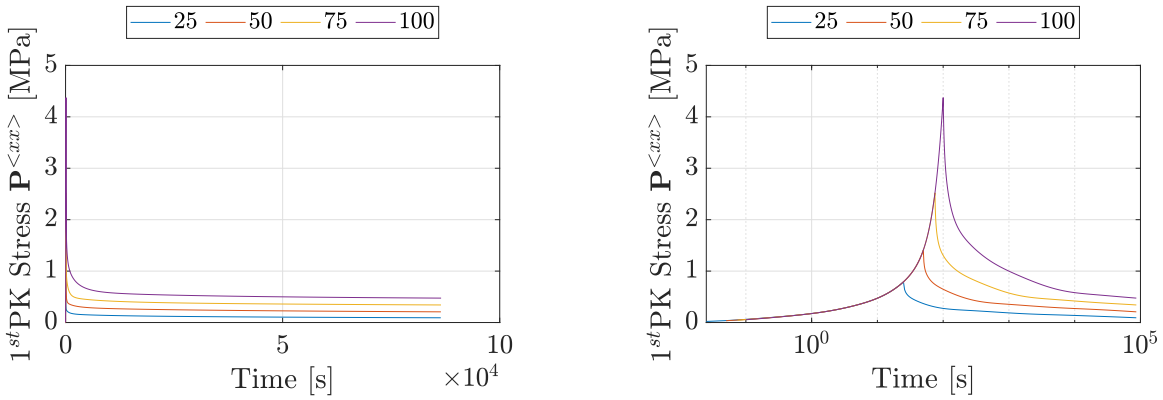

Figure 4.44.: Stress over Time: normal scale (left); logarithmic scale (right)

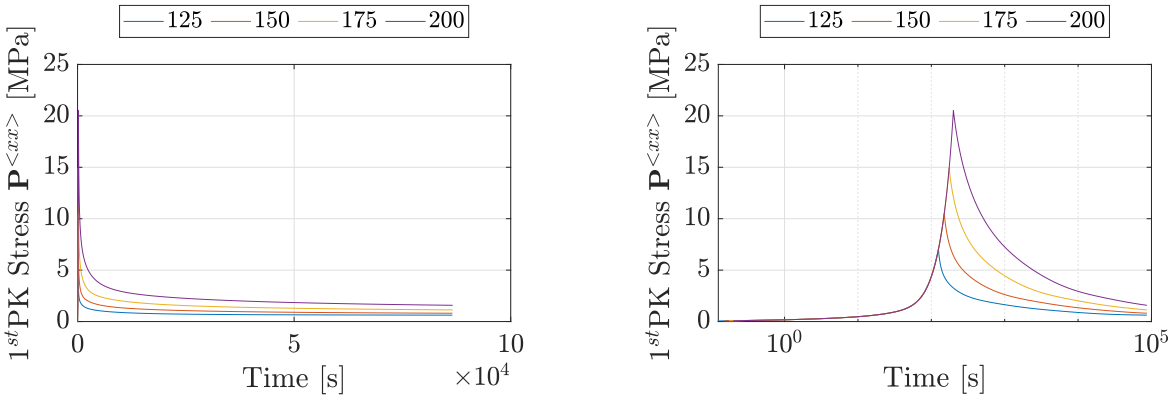

Figure 4.45.: Stress over Time: normal scale (left); logarithmic scale (right)

Taking each stress-strain pair at the end of a relaxation test, i.e., after a simulated time of 24 h, and plotting them in a stress-strain diagram, the result is similar to that shown in Fig. 3.29.

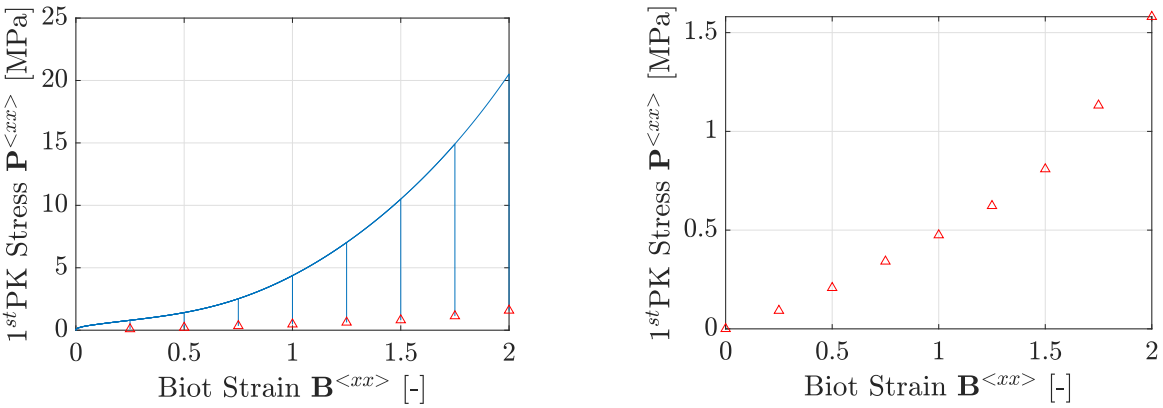

Figure 4.46.: Stress over Strain (left); strain/stress pairs at 24 h (right)

5. Engineering Approaches

After introducing the complex material model describing PVB at finite strains, three simplified approaches are presented to assess the problem of residual load-bearing capacity. The first approach utilizes a hyperelastic model based on the evaluation of the staircase test (cf. Sec. 3.3.5.1) and has already been published in Pauli and Siebert [199]. The second approach presents a model describing the residual load-bearing capacity of coarse-breaking laminates and is based on a simplified version of the general model presented in Ch. 4. Within the third part a simplified approach concerning a one-dimensional failure criterion is presented.

5.1. Hyperelastic Approach

The hyperelastic approach, originally published in [199], follows the assumption that a polymeric material subjected to prolonged processes can be described by the laws of elasticity. The evaluation of the staircase test provided a procedure to evaluate the response of PVB for such slow processes (cf. Sec. 3.3.5). Within the presented approach, a hyperelastic Yeoh model is calibrated on the curve evaluated from the staircase test (cf. 3.29 (right)). Tab. 5.1 presents the respective material parameters. The commercial FEM program Ansys (version 2023 R1)

Table 5.1.: Material Parameters for Hyperelastic Approach

C_{10}	C_{20}	C_{30}	κ
0.0823	0.0205	0.0012	100
0.0823	0.0205	0.0012	0.02

[8] served for the following simulations.

A FEM simulation, based on the calibrated material parameters, is carried out using the geometry of specimen Typ B. Only a quarter of the plane (without considering the clamped area) and half the thickness of the specimen is modeled to save computation time. Fig. 5.1 shows the respective boundary conditions that ensure the requirements concerning symmetry and that all planes considered only move in the desired direction.

A comparison of the resulting strain-stress curve and the evaluated points from Fig. 3.29 illustrates the goodness of the simulation. Tab. 5.2 presents the setup of the numerical model:

Table 5.2.: Properties of the FEM model

Elementype	Solid185, fully integrated with $\bar{B}$ method, mixed u-P formulation
Elementsize	1 [mm]
Elementshape	rectangle
Solver	EQSLV Sparse, LNSRCH On

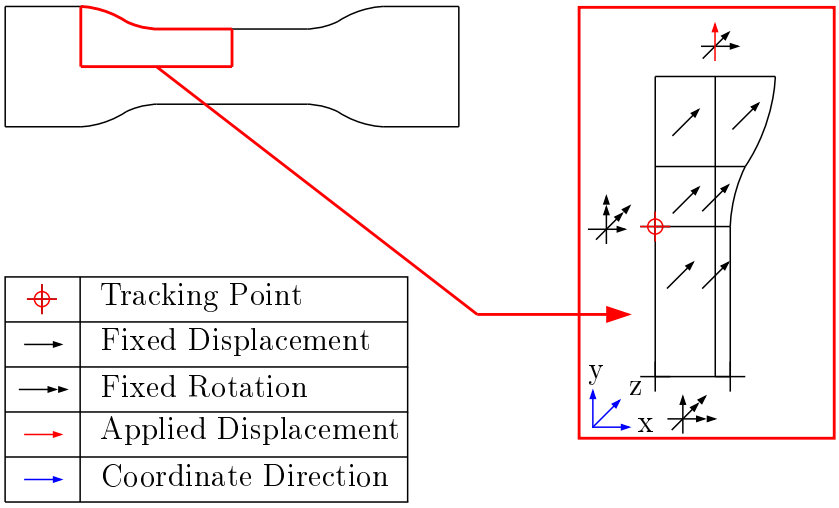

Figure 5.1.: Boundary conditions of FEM model (cf. [199])

Fig. 5.2 shows the intersection points evaluated from the experiments along with the linear extrapolation (cf. 3.3.5.1) and the result of the numerical simulation. The comparison of simulation and evaluated points leads to a decent coincidence.

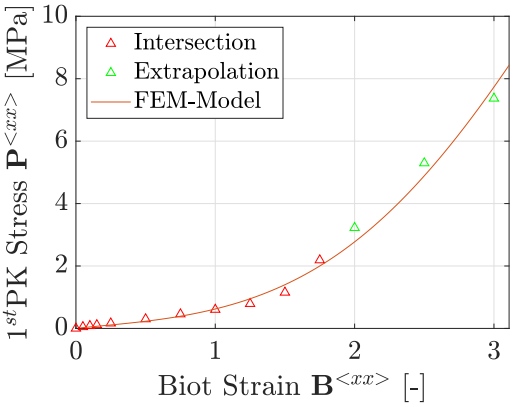

Figure 5.2.: Modeling Result

5.2. Simplified Residual Load Bearing Model

To directly use the derived material model for engineering practice without a FEM implementation, in the following a simplified approach, similar to that proposed by Kott [157], Belis et al. [19], Botz et al. [31], is presented. In contrast to the approach presented by Belis et al. [19], this model does not account for delamination.

The overall assumption is that coarse-breaking glass commonly forms only a few critical cracks that cause the collapse of the whole structure. The fracture pattern is predominantly influenced by the loading situation and the support conditions. For two-sided supported glass panes, the most critical breakage pattern is a single crack in the middle of the supports. This pattern was observed by Kott [157] and denoted as line mechanism L1. Similar considerations were carried out by Franz [107], who utilized the TCB test to investigate this condition experimentally. Botz [30] built up on these investigations. By assuming a perfectly coincident crack, a flow joint is formed along the crack. This joint consists of a pair of forces consisting of the broken edge of the glass and the interlayer. As the glass is stiffer by magnitude compared to the interlayer, the tensile forces taken by the interlayer are critical and accurate material modeling is compulsory.

Belis et al. [19] and Kott [157] assumed constant yield stress within the interlayer and assumed plastic material laws. Belis et al. [19] extended the approach of [157] by taking into account delamination. However, as plasticity does not cover time-dependent behavior, decisive effects are left out by these approaches.

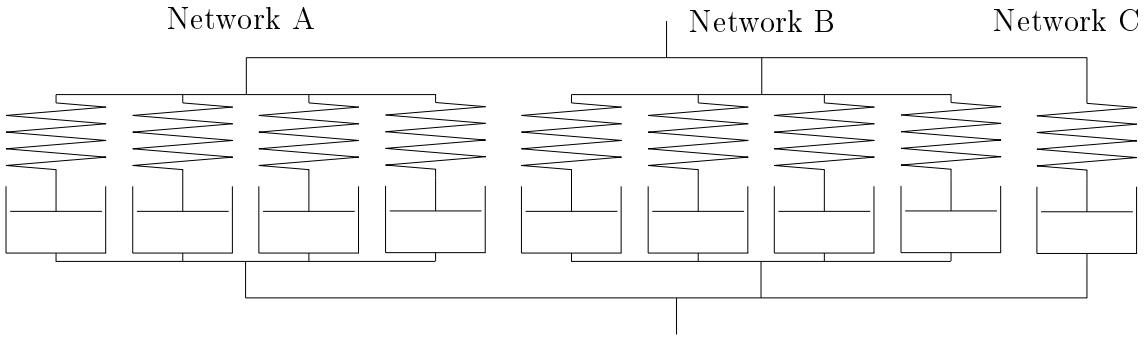

Figure 5.3.: Reduced Network model based on Maxwell elements

The model presented in the following is a simplified version of the model derived in Ch. 4 and accounts for time-dependent effects. For this simplified approach, the last Maxwell element of Network A is removed and the viscosity functions aligned to the networks are reduced to the following description:

$$\eta_{D,A} = \eta_0 \mu \Big(\frac{||\mathbf{C}||}{\sqrt{3}} \Big)^{\chi} \Big[\tau \cdot exp\Big(- \frac{||\mathbf{T}||}{s_0} \Big) \Big]$$

$$\eta_{D,B} = \eta_0 \mu \Big(\frac{||\mathbf{C}||}{\sqrt{3}} \Big)^{\chi} \Big[\tau \Big]$$

$$\eta_{D,C} = 2\eta_0 C_{30} \Big(\frac{||\mathbf{C}||}{\sqrt{3}} \Big)^{\chi} \Big[\tau \cdot \Big| 1 - exp(||\mathbf{D}||) \Big| + 1 \Big],$$

These descriptions coincide with the representation of the viscosity functions utilized for the first step of the parameter identification (compare Sec. 4.5). As the first step of the parameter identification revealed a good result regarding the description of the relaxation behavior, it seems promising for the following considerations. Tab.s 5.3 and 5.4 summarize the material parameters identified in the first step of the optimization procedure. As η_0 is set to be equal to one, it is not listed in the subsequent tables. Fig. 5.4 illustrates the modeling of the relaxation tests utilizing these material parameters compared to the experimental results.

Table 5.3.: Parameters for Kelvin Voigt elements Network A (k = 1 to 5)

k	1	2	3	4
$\tau^{(k)}$ [s]	12.11e-2	53.12e-2	51.94e-1	63.16e0
$\mu^{(k)}$ [MPa]	25.90e0	73.25e-1	19.17e-1	52.06e-2
$\chi^{(k)}$ [-]	62.26e-1	62.26e-1	62.26e-1	62.26e-1
$s_0^{(k)}$ [MPa]	24.20e-1	57.81e-1	21.83e-1	42.75e-1

Fig. 5.4 emphasizes the accuracy of the simplified material model in describing the relaxation behavior of PVB.

Table 5.4.: Parameters for Kelvin Voigt elements Network B (l = 1 to 4) and Network C (m = 1)

l	1	2	3	4	m	1
$\tau^{(l)}$ [s]	17.49e3	11.92e4	10.24e5	10.01e6	$\tau^{(m)}$ [s]	80.17e4
$\mu^{(l)}$ [MPa]	48.11e-3	72.13e-3	94.30e-3	63.65e-3	$C_{30}^{(m)}$ [MPa]	10.52e-3
$\chi^{(l)}$ [-]	62.26e-1	62.26e-1	62.26e-1	62.26e-1	$\chi^{(m)}$ [-]	69.27e-1

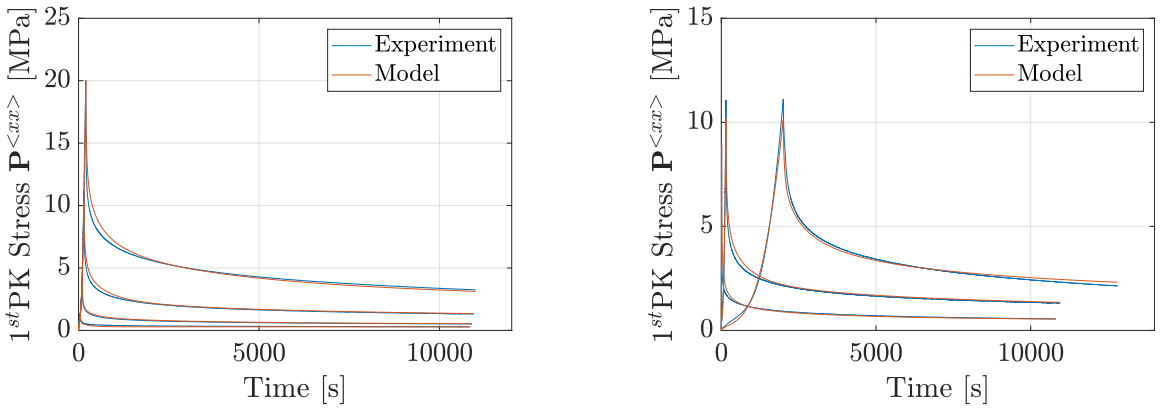

Figure 5.4.: Comparison between simplified model and relaxation experiment

It is common practice to formulate viscoelastic material models concerning strains as driving quantities [236, 226]. However, the load-bearing capacity of laminated safety glass is governed by creep loads, which makes a direct application of the model, formulated with respect to strains utilizing the rheological assumptions of the Maxwell model, complicated. However, the Kelvin Voigt model utilizes stresses as driving forces and, therefore, seems promising for the following approach. From a rheological point of view, the spring and damper elements connected in series are replaced by spring and damper elements connected in parallel (compare Fig. 5.5).

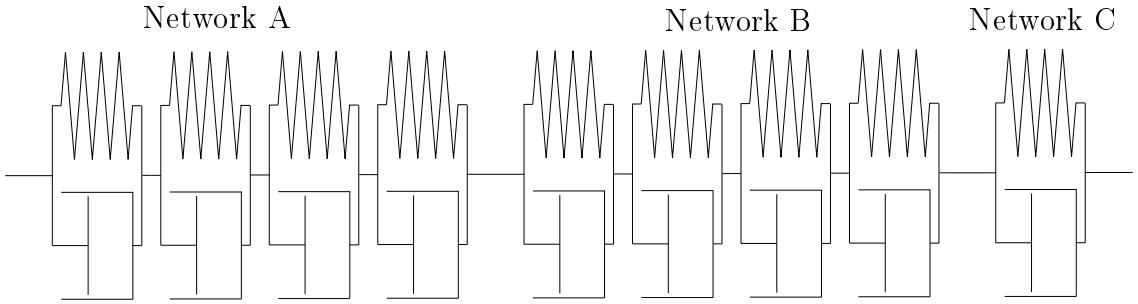

Figure 5.5.: Reduced Network model based on Maxwell elements

In the following, incompressible material behavior is assumed, and only the uniaxial stress state is considered. Due to the incompressibility constraint, it is further assumed that the evolution equations representing the time-dependent stretch of the model follow a deviatoric formulation. This assumption is directly connected to the evolution equations based on the Maxwell model. Furthermore, the evolution equation is formulated on the reference configuration. Due to the different structure of the model, resulting in equal deformations for spring and damper, a multiplicative split of the deformation gradient is no longer necessary. The governing equation for a single Kelvin Voigt element considering only the deviatoric parts of the second

Piola Kirchhoff stress tensor, results in:

$$dev(\mathbf{T}^{<xx>}) = dev(\mathbf{T}_{el}^{<xx>}) + dev(\mathbf{T}_{in}^{<xx>}) \tag{5.1}$$

The general description of the deviatoric stress tensor considering only uniaxial loading yields:

$$dev(\mathbf{T}) = \begin{bmatrix} \frac{2}{3}\mathbf{T}^{<xx>} & 0 & 0 \\ 0 & -\frac{1}{3}\mathbf{T}^{<xx>} & 0 \\ 0 & 0 & -\frac{1}{3}\mathbf{T}^{<xx>} \end{bmatrix} \tag{5.2}$$

$$\tag{5.3}$$

Following Eq. 5.2, the driving stress, results in:

$$dev(\mathbf{T}^{<xx>}) = \frac{2}{3}\mathbf{T}^{<xx>} \tag{5.4}$$

The deviator of the elastic part of the stress, represented by the spring, with respect to an uniaxial stress state, leads to

$$dev(\mathbf{T}_{el}^{<xx>}) = 2\frac{\partial \Psi_{iso}(\mathbf{C})}{\partial \mathrm{I}_{\mathbf{C}}}\Big[\mathbf{1} - \frac{1}{3}(\mathbf{C} : \mathbf{1})\mathbf{C}^{-1}\Big] = 2\frac{\partial \Psi_{iso}(\mathbf{C})}{\partial \mathrm{I}_{\mathbf{C}}}\Big[1 - \frac{1}{3}(1 + \frac{2}{\lambda^3})\Big] = \frac{4}{3}\frac{\partial \Psi_{iso}(\mathbf{C})}{\partial \mathrm{I}_{\mathbf{C}}}\Big[1 - \frac{1}{\lambda^3}\Big] \tag{5.5}$$

where $\lambda = \lambda_{el} = \lambda_{in}$. The deviator of the inelastic part of the stress, represented by the dashpot, equals the product of the viscosity function and the time derivative of the first entry of the Green Lagrange strain tensor.

$$dev(\mathbf{T}_{in}^{<xx>}) = \frac{2}{3}\eta\dot{\mathbf{E}}^{<xx>} = \frac{2}{3}\eta\frac{1}{2}\dot{\mathbf{C}}^{<xx>} = \frac{2}{3}\eta\frac{1}{2}(\dot{\lambda}\lambda + \lambda\dot{\lambda}) = \frac{2}{3}\eta\dot{\lambda}\lambda, \tag{5.6}$$

Merging Eq.'s 5.4 to 5.6, yields

$$\frac{2}{3}\mathbf{T}^{<xx>} = \frac{4}{3}\frac{\partial \Psi_{iso}(\mathbf{C})}{\partial \mathrm{I}_{\mathbf{C}}}\Big[1 - \frac{1}{\lambda^3}\Big] + \frac{2}{3}\eta\dot{\lambda}\lambda \tag{5.7}$$

Rearranging Eq. 5.7 results in the formulation of the evolution equation of the stretch:

$$\dot{\lambda} = \frac{1}{\eta}\Big[\frac{\mathbf{T}^{<xx>}}{\lambda} - 2\frac{\partial \Psi_{iso}(\mathbf{C})}{\partial \mathrm{I}_{\mathbf{C}}}\Big(\frac{1}{\lambda} - \frac{1}{\lambda^4}\Big)\Big] \tag{5.8}$$

The total model, considering all networks and utilizing the Biot strain as output, leads to the following:

$$\mathbf{B}^{<xx>} = \sum_{k=1}^{4}\Big[\lambda^{(k)} - 1\Big] + \sum_{l=1}^{4}\Big[\lambda^{(l)} - 1\Big] + \sum_{m=1}^{1}\Big[\lambda^{(m)} - 1\Big] \tag{5.9}$$

$$\dot{\lambda}^{(k)} = \frac{\frac{\mathbf{T}^{<xx>}}{\lambda^{(k)}} - \mu^{(k)}\Big(\frac{1}{\lambda^{(k)}} - \frac{1}{\lambda^{4,(k)}}\Big)}{\eta_0^{(k)}\mu^{(k)}\Big(\frac{||\mathbf{C}||}{\sqrt{3}}\Big)^{\chi^{(k)}}\Big[\tau^{(k)} \cdot exp\Big(-\frac{||\mathbf{T}||}{s_0^{(k)}}\Big)\Big]} \tag{5.10}$$

$$\dot{\lambda}^{(l)} = \frac{\frac{\mathbf{T}^{<xx>}}{\lambda^{(l)}} - \mu^{(l)}\Big(\frac{1}{\lambda^{(l)}} - \frac{1}{\lambda^{4,(l)}}\Big)}{\eta_0^{(l)}\mu^{(l)}\Big(\frac{||\mathbf{C}||}{\sqrt{3}}\Big)^{\chi^{(l)}}\Big[\tau^{(l)}\Big]} \tag{5.11}$$

$$\dot{\lambda}^{(m)} = \frac{\frac{\mathbf{T}^{<xx>}}{\lambda^{(m)}} - 6C_{30}^{(m)}(\mathrm{I}_{\mathbf{C}} - 3)^2\Big(\frac{1}{\lambda^{(m)}} - \frac{1}{\lambda^{4,(m)}}\Big)}{2\eta_0^{(m)}C_{30}^{(m)}\Big(\frac{||\mathbf{C}||}{\sqrt{3}}\Big)^{\chi^{(m)}}\Big[\tau^{(m)} \cdot \Big|1 - exp(||\mathbf{D}||)\Big| + 1\Big]} \tag{5.12}$$

The single differential equations, Eq. 5.9 is depending on, are solved with the same Euler backward integration scheme as utilized for the model based on Maxwell elements (cf. Sec. 4.3). For evaluation of the model, a creep process presented by [193], which is currently under revision, is predicted by the model. Fig. 5.6 and 5.7 show the results. The qualitative course is matched in a satisfying way. However, there are deviations between the curves.

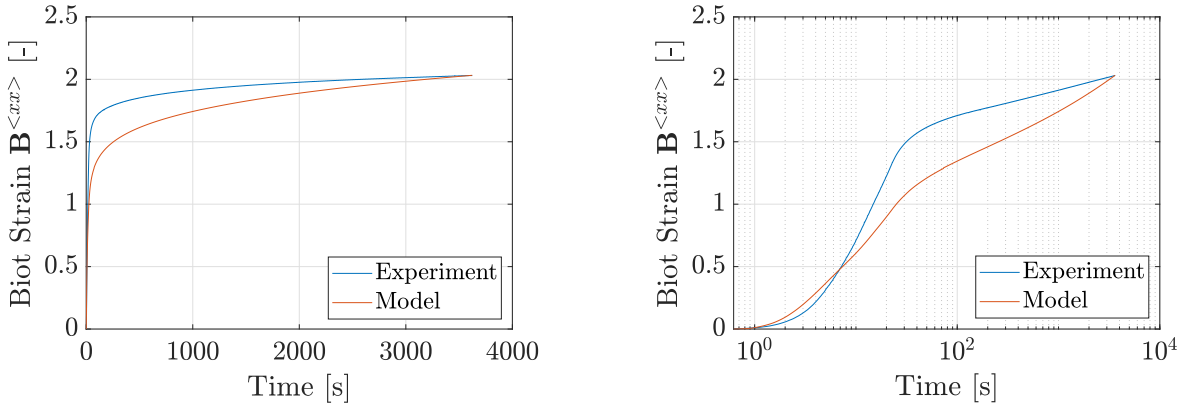

Figure 5.6.: Comparison of Creep Test and Experiment in standard and log scale

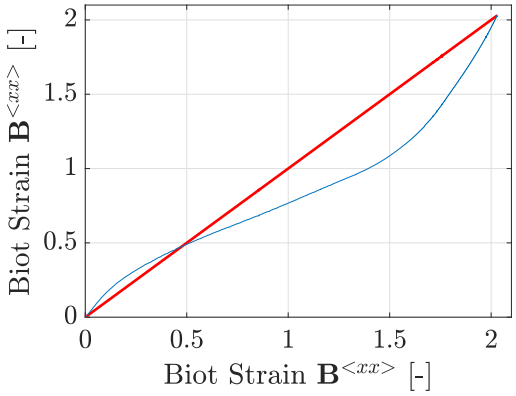

Figure 5.7.: Modeling Result

In addition to the validation calculation, different load cases were calculated. Each of the loads was approached with a force rate of 1 [N/s]. Fig. 5.8 shows the results of the numerical example, considernig creep loads of 25, 50, 100, 200, and 300 [N] for a duration of 24 [h].

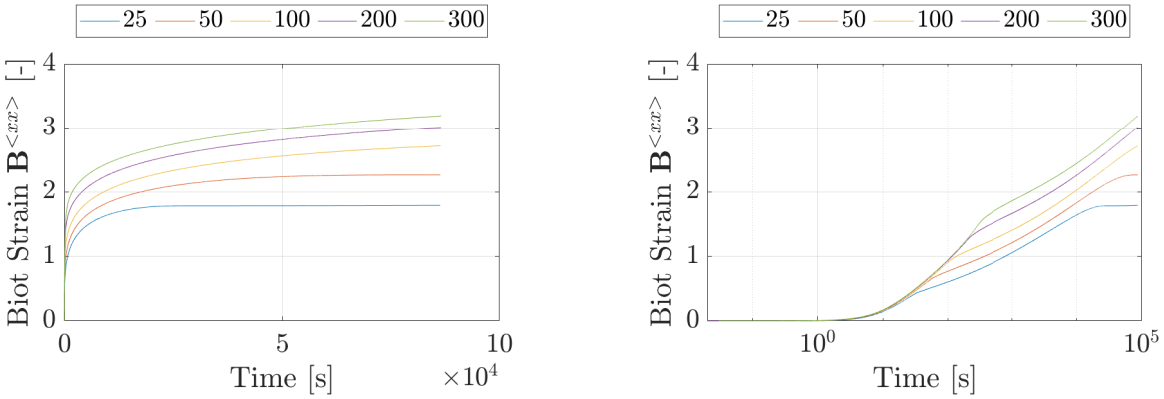

Figure 5.8.: Precalculation of Creep Test for five different loads in [N]

As the approach was validated for the uniaxial stress state, it is transformed to the planar tension state to match the requirement of the considered application more precisely. The total model, considering planar tension, results in:

$$\mathbf{B}^{<xx>} = \sum_{k=1}^{4}\Big[\lambda^{(k)} - 1\Big] + \sum_{l=1}^{4}\Big[\lambda^{(l)} - 1\Big] + \sum_{m=1}^{1}\Big[\lambda^{(m)} - 1\Big] \tag{5.13}$$

$$\dot{\lambda}^{(k)} = \frac{\frac{\mathbf{T}^{<xx>}}{\lambda^{(k)}} - \frac{\mu^{(k)}}{2}\Big(2 - \frac{\lambda^{2,(k)}+1}{\lambda^{4,(k)}}\Big)}{\eta_0^{(k)}\mu^{(k)}\Big(\frac{||\mathbf{C}||}{\sqrt{3}}\Big)^{\chi^{(k)}}\Big[\tau^{(k)} \cdot exp\Big(-\frac{||\mathbf{T}||}{s_0^{(k)}}\Big)\Big]} \tag{5.14}$$

$$\dot{\lambda}^{(l)} = \frac{\frac{\mathbf{T}^{<xx>}}{\lambda^{(l)}} - \frac{\mu^{(l)}}{2}\Big(2 - \frac{\lambda^{2,(l)}+1}{\lambda^{4,(l)}}\Big)}{\eta_0^{(l)}\mu^{(l)}\Big(\frac{||\mathbf{C}||}{\sqrt{3}}\Big)^{\chi^{(l)}}\Big[\tau^{(l)}\Big]} \tag{5.15}$$

$$\dot{\lambda}^{(m)} = \frac{\frac{\mathbf{T}^{<xx>}}{\lambda^{(m)}} - 3C_{30}^{(m)}(\mathrm{I}_\mathbf{C} - 3)^2\Big(2 - \frac{\lambda^{2,(m)}+1}{\lambda^{4,(m)}}\Big)}{2\eta_0^{(m)}C_{30}^{(m)}\Big(\frac{||\mathbf{C}||}{\sqrt{3}}\Big)^{\chi^{(m)}}\Big[\tau^{(m)} \cdot \Big|1 - exp(||\mathbf{D}||)\Big| + 1\Big]} \tag{5.16}$$

This simplified material can now be used for the residual load-bearing model to describe the deformation within the interlayer caused by force-driven loading situations. Fig. 5.9 shows the underlying kinematic considerations. The overall system is idealized as a combination of two simple truss structures. On top of Fig. 5.9, the overall system is depicted. It consists of two trusses, assumed to be completely rigid, connected by a joint. Furthermore, it is assumed that the trusses can slide off the bearings if the deflection in the middle surpasses a particular limit. The joint is represented by a force pair consisting of a pressure share represented by the glass edges and a tensile component represented by the interlayer. The kinematic of the joint is idealized by another truss model consisting of a completely rigid component in the vertical direction and a deformable component in the horizontal direction. The deformable truss element is governed by the material model represented in Eq.'s 5.13 to 5.16. The overall structure (in the following referred to as the global model) and the representation of the joint (in the following referred to as the local system) share the same kinematics. Therefore, the angle α calculated in the local system leads to the displacement in the overall system.

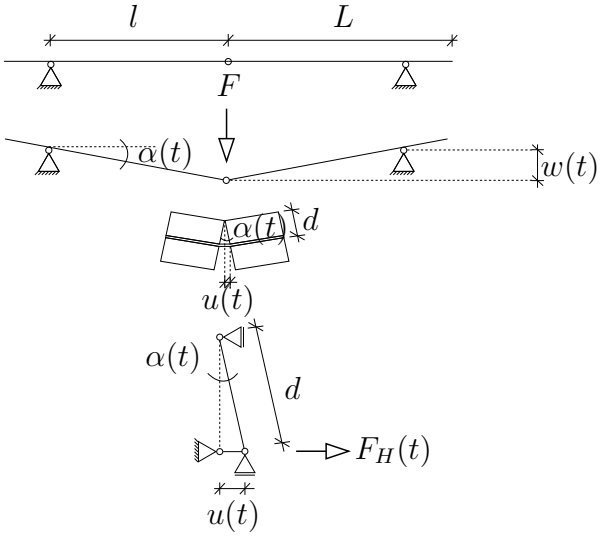

Figure 5.9.: Kinematic of the simplified residual load-bearing model

The equations describing the kinematic are summarized in the following:

$$sin(\alpha(t)) = \frac{u(t)}{d} \tag{5.17}$$

$$cos(\alpha(t)) = \frac{\sqrt{d^2 - u(t)^2}}{d} \tag{5.18}$$

$$F_H(t) = F\cos(\alpha(t))\sin(\alpha(t)) = F\frac{u(t)\sqrt{d^2 - u(t)^2}}{d^2} \tag{5.19}$$

$$w(t) = tan(\alpha(t))l \tag{5.20}$$

$$\tag{5.21}$$

To start the kinematic, an initial deformation $u(t = 0) = u_0$ must be assumed, which is considered the interlayer's initial length. By placing a load on the system, the deformation $u(t)$ increases over time according to the material model, represented in Eq.'s 5.13 to 5.16. Botz [30] proposed similar kinematic considerations but did not utilize a time-dependent material model to describe the interlayer. With Eq.'s 5.17 to 5.20, utilizing the kinematic within the lokal system, all deflections in the global system can be calculated. Two cases for the collapse of the system can be defined:

- the stress within the interlayer reaches the yield stress (cf. Sec. 5.3)
- the deflection increases so much that the trusses slip of the supports (if $\sqrt{w(t)^2 + l^2} \geq L$)

5.3. Failure

A material model describing the time-dependent behavior of PVB at finite strains within the intact state has been successfully developed, verified, and validated. However, for the actual design of the material, the intact state and the failure must be considered. The 46 tensile tests at seven different strain rates conducted until failure serve as a promising database. All stresses and strains at failure were already evaluated in Sec. 3.3.2. However, in the following sections, a more precise evaluation will be carried out considering the overall distribution of the data and suggestions for a failure criterion on the design level according to DIN EN 1990:2021-10 [81].

The test results revealed that the stresses at failure are distributed almost horizontally while the strains at failure increase with decreasing strain rate. Noteworthy, 1^{st}PK stresses, and Biot strains were considered at this time. At first glance, utilizing the stress at failure seems most promising, as it is constantly distributed over the strain rates. However, a failure criterion on the 1^{st}PK stress is not suitable for covering the material's behavior exposed to creep loads, as it does not consider the actual deformation of the specimens. Utilizing the failure Biot strain would account for creep loads, but it would also mean including the strain rate in the failure criterion, a requirement that would complicate the approach. The Cauchy stress, on the other hand, combines the advantages of both as it accounts for creep loads and can be summarized into one value.

For the following considerations, the Cauchy stresses at failure are assumed to follow a lognormal distribution with the $m_{y,F} = 4.5179$ and $s_{y,F} = 0.0974$. This assumption is based on the statistical evaluation within Sec. 3.3.2.1. Although the Burr distribution approximated the data the best, the lognormal was preferred as it is a common approach in structural engineering practice.

Based on the semi-probabilistic design concept (DIN EN 1990:2021-10 [81], level I), a characteristic strength value and a partial safety factor are calibrated for PVB. DIN EN 1990:2021-10

[81], Eq. D.1, under the assumption of a lognormal distribution reads:

$$X_d = \eta_d \frac{X_k}{\gamma_m} = \frac{\eta_d}{\gamma_m} exp(m_y - k_n s_y) \tag{5.22}$$

where X_k is the characteristic strength value represented by the 5 [%] quantile, η_d is a conversion factor accounting for the kind of experiment and the type of material. Solving Eq. 5.22 for the characteristic quantity X_k under the consideration of lognormal distribution leads to the characteristic failure strength of the material. With k_n according to DIN EN 1990:2021-10 [81], Tab. D.1, for an unknown coefficient of variation V_x and a database with more than 30 values, the characteristic Cauchy stress of PVB at failure leads to:

$$X_k = exp(m_{y,Fal.} - k_n s_{y,Fal.}) = exp(4.5179 - 1.645 \cdot 0.0974) = 78.08[MPa] \tag{5.23}$$

According to DIN EN 1990:2021-10 [81], Eq. C.12, for an actual design, the structural resistance, derived by utilizing the factor γ_{Rd} covering modeling imprecisions, in addition to the factor γ_m covering material uncertainties, must be considered.

$$R_d = R\frac{1}{\gamma_{Rd}}(\frac{\eta_d}{\gamma_m} X_k) \tag{5.24}$$

The equation for the partial safety factor results in [98]:

$$\gamma_M = \frac{\gamma_{Rd}\gamma_m}{\eta_d} = \frac{1}{\eta_d} exp(\alpha_R \beta V_R - k_n V_F) \tag{5.25}$$

According to DIN EN 1990:2021-10 [81], Eq. C.7, under fullfilling

$$0.16 < \frac{\sigma_E}{\sigma_R} < 7.6 \tag{5.26}$$

the resistance weighting factor results in $\alpha_R = 0.8$ and $\beta = 4.7$ under the assumption of a Resistance Class RC2 considering a target value of the reliability index for one year (DIN EN 1990:2021-10 [81], Tab. C.2). To evaluate the variance of the model Var_M, the experimentally explored failure stresses were compared to the one calculated by the model. The design value of the failure strength served as the basis for the comparison. However, as the variance of the model directly influenced the calculation of the partial safety factor, which again influenced the design strength, the evaluation of Var_M was carried out iteratively. The variance of the geometry Var_G was evaluated according to the parameters presented by [159] who investigated a mean value of $m_{x,G} = 0.767$ [mm] with a standard deviation of $s_{x,G} = 0.009$ [mm] for geometric measurements of PVB samples. The material variance follows from the failure stresses. In total, the following variances arise [97]:

$$Var_F = \sqrt{exp(s_{y,F}^2) - 1} = 0.0976$$

$$Var_G = \frac{s_{x,G}}{m_{x,G}} = \frac{0.009}{0.767} = 0.0117$$

$$Var_M = \frac{\sqrt{\frac{1}{n-1}(x_{i,M} - m_{x,M})^2}}{m_{x,M}} = 0.0660$$

$$Var_R = \sqrt{Var_F^2 + Var_G^2 + Var_M^2} = 0.1184$$

Considering all these values, the partial safety factor results in the following value [97]:

$$\gamma_M = e^{\alpha\beta Var_R - k_n Var_F} = e^{0.8 \cdot 4.7 \cdot 0.1184 - 1.645 \cdot 0.0976} = 1.3294 \tag{5.27}$$

The value η_d is a scaling factor [97] which is assumed to be equal to one as the evaluated tests are close to the real application considered to be configuration described in Sec. 5.2. The design value of the resistance results in:

$$X_d = \frac{X_k}{\gamma_M} = \frac{78.0770}{1.3294} = 58.7294[MPa] \tag{5.28}$$

Fig. 5.10 shows the design value utilizing the 5 [%] quantile of the Cauchy stress as failure criterion as the limit of the curves of the experimental results and the modeling results. On the left, Cauchy stresses are depicted; on the right, 1^{st}PK stresses. It is obvious that only utilizing the Cauchy stress accounts for the variation in failure strains with respect to the applied strain rate.

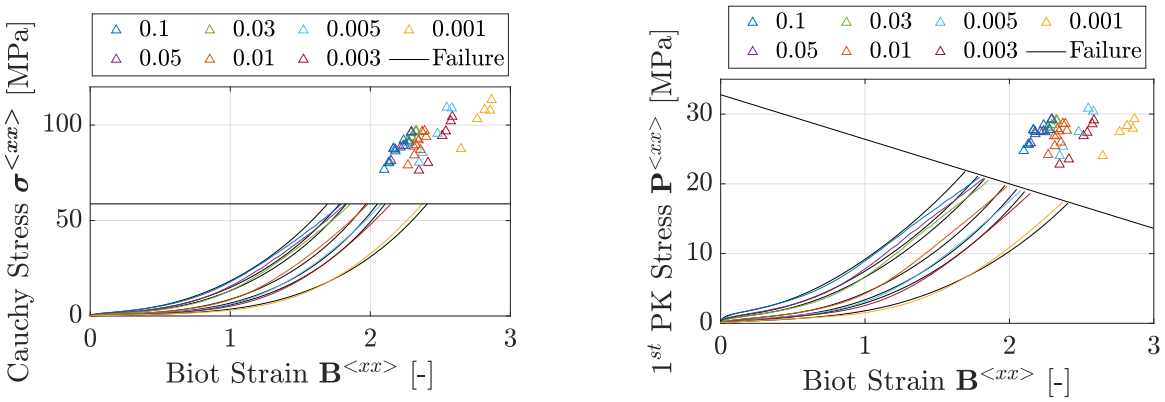

Figure 5.10.: Statistical evaluation of failure stress

6. Discussion

The residual load-bearing capacity of laminated glass is a topic that is receiving more and more attention with the increased use of glass as a load-bearing element. An experimental investigation of it is currently common practice but is very time and cost-consuming. A theoretical examination of the residual load-bearing capacity of laminated glass would be a more sustainable approach. However, although it would be allowed by CEN/TS 19100-2:2024-01 [45], a reliable modeling approach still needs to be addressed. Due to the interaction between the polymeric interlayer and the brittle breaking glass, various complex mechanisms must be considered, and it is a very complicated task to theoretically describe the residual load-bearing behavior of laminated glass. Depending on the degree of glass toughening, different patterns arise during breakage [158, 207], that lead to different characterization approaches. Most approaches to describe the residual load-bearing behavior are analytical [157, 19, 110, 111, 112]. However, there also exist some numerical approaches [15, 265]. Regarding the analytical approaches, the residual load-bearing behavior of laminates made from coarse breaking glasses is described explicitly [157, 19] while laminates made from fine breaking glass are described with an equivalent stiffness [110, 111, 112]. The numerical approaches use a description via DEM or FEM/DEM. Either way, the interlayer plays a crucial role, being the ligament between the broken glass shards [67].

Therefore, it is essential to characterize and describe the interlayer under the circumstances of a broken laminate. The experimental investigation of the residual load-bearing behavior according to the DIN 18008-1:2020-05 [68] reveals two main characteristics: the large deformation of the interlayer and its dependency on time. There are some investigations of the relaxation [231] and creep behavior [30] as well as investigations on the unloading behavior [103]. However, several aspects, such as considering the rate dependency for relaxation or creep or different load levels for the unloading behavior, still need to be included. Furthermore, the previously mentioned modeling approaches, which use linear elastic [110, 111, 112] or elastoplastic [157, 19, 15, 265] models for the interlayer do not describe its complex behavior sufficiently. Even approaches commonly used to describe the interlayer alone such as hyperelasticity [165, 159], linear viscoelasticity [30], and finite linear viscoelasticity [203, 2] are not sufficient to describe PVB [103]. On the other hand, several modeling approaches for different materials can qualitatively describe some individual characteristics of PVB [33, 34, 236, 226, 279, 228]. However, to the author's knowledge, no material model is precisely tailored to the complex material behavior of PVB so far. Therefore, this work aimed to first characterize the PVB with respect to large deformations and time dependency and, afterward, to design a model to describe the observed material behavior.

Following DIN EN 1990:2021-10 [81], there are two fundamental components for a design concept of the residual load-bearing capacity of laminated safety glass: The impacts on the laminate and its respective response in the fully fractured state and the corresponding resistance. Therefore, two required explorations arise: The investigation and modeling of the material behavior in its intact state and the investigation and modeling of failure. In this context, it is important to note that *intact* means the undamaged state of the fully fractured laminate, and *failure* means its collapse. More precisely, the intact state and failure of the PVB were investigated in this study. However, the following part is organized into experiments, modeling, and engineer-

ing approaches. The experiments and the modeling are only discussed for the intact state, as the failure is discussed within the section concerning the engineering approaches.

6.1. Experiments

The experimental investigations of the intact state aimed to explore the behavior of PVB up to finite strains under the consideration of time dependency. This examination should provide a sound basis for a mechanical description of PVB in the context of the impact on the load-bearing capacity of LSG in the fully broken state. In line with DIN 18008-1:2020-05 [68], the testing conditions were limited to a temperature of 20 $[°C]$ and 50 $[\%]$. However, it must be mentioned that each specimen was conditioned to this climate, but the humidity within the test container could not be controlled and took values of 65±5 $[\%rH]$. As the focus was on the time dependency of the material, the exploration was limited to the uniaxial stress state. This assumption goes along with previous investigations on PVB [165, 103, 30, 231]. For coarse-breaking glass, the only configuration showing residual load-bearing capacity with PVB interlayer [157], the predominantly deformation state is uniaxial or planar tension. For several polymers, planar tension and uniaxial cause similar stresses, with planar tension achieving slightly higher stresses [251]. More precisely, the investigations were carried out on specimens punched out from sheets of Trosifol®UltraClear - B200NR PVB in the geometry proposed by Becker [18].

The experimental study was categorized into three parts, each governed by a phenomenon directly aligned to the Frobenius scalar product of the deformation rate tensor and the right Cauchy Green tensor ($\mathbf{D} : \mathbf{C}$). Thereby, values greater than zero indicated loading (group 1), values smaller than zero unloading (group 2), and values equal to zero constant loading (group 3). The tests of group 1 were carried out until failure at seven different strain rates, equally distributed from 0.001 to 0.1 [1/s]. The tests of groups 2 and 3 were conducted at the strain rates 0.1, 0.01, and 0.001 [1/s], loaded to different strain levels. All tests were carried out with the universal testing machine Z2.5 manufactured by ZwickRoell GmbH & Co. KG, and the deformation of each specimen during the test was measured by a mechanical extensometer directly attached to the specimen at the respective measuring distance (cf. Sec. 2.6.2.5). A special feature of that extensometer was the utilization by the testing machine to measure and control the size and rate of displacement applied to the specimen. The rate was constantly related to the initial measuring length. This way of controlling the velocity of the test has a big advantage over control via the crosshead bar of the machine, that observed effects can be directly related to a constant strain rate, which is the driving quantity in rheological considerations (cf. Sec. 2.2.4). To further categorize and evaluate the experimental results gained by the study that was presented in Ch. 3, they are compared to results that were obtained from other research groups currently and over the last years. The considered investigations are summarized in detail in Ch. 3. Nevertheless, the main findings are presented in the following. However, the behavior of PVB depends on several effects, such as precise chemical composition, temperature, humidity, loading time, and strain rate, which make a comparison of different studies a challenging task.

Although the general chemical composition of standard PVB is equal for any manufacturer, individual products vary slightly from one manufacturer to another. These minor differences in the composition, however, can influence the material behavior. Within the studies under consideration, several materials, such as Butacide®[22], S-LEX™[140], Solutia®RB-41 [134], Trosifol®BG [165, 30, 43], and Saflex®RB-41 [64, 152, 231], were investigated.

Besides the chemical formulation of the respective materials, the geometry of the specimens varied among the studies considered. When considering the strain rate as a comparative feature, the displacement rate of the testing machine and the reference length utilized to derive the strain

inside the specimen must be taken into account to calculate the strain rate. However, different samples have different reference lengths, and therefore, different strain rates are found when considering the same displacement rate. In other words, the specimen's geometry directly affects the applied strain rate for displacement-controlled tests. Nevertheless, Kuntsche [165], Botz [30], Schuster [231] utilized the shape proposed by Becker [18], Iwasaki and Sato [140], Liu et al. [172] chose the specimen *JIS 2* according to JIS K 7113:1995 [145], Hooper et al. [134], Del Linz et al. [64] chose the *Typ 2* according to [36], [270] employed specimens according to DIN 53504:2017-03 [71], and Centelles et al. [43], Knight et al. [152] used specimens according to ASTM D638-10:2010 [13].

A further decisive parameter is the device measuring the deformation during the test. The most common approach is a digital recording of the deformation using optical extensometers [22, 140, 134, 172, 165, 270, 64, 103, 152, 231]. Therefore, common practice is to apply the displacement rate via the control of the crosshead of the testing machine and to track the corresponding strains. However, this procedure makes a comparison between the individual test results quite challenging, as some authors name displacement rates [165, 140, 172, 152] and others name strain rates [22, 134, 64, 270] although it is not clear how the strain rate is evaluated. The control of the displacement during the test is directly aligned with measuring the deformation. However, with the common procedure in optical measuring, it is impossible to apply a constant strain rate with respect to the reference measuring length, and, as a consequence, the strain rates of the specimens with different reference lengths differ.

The last and most crucial influence parameter is the testing climate. Of the considered researches from literature, Hooper et al. [134] conducted their tests at 25±3 [$°C$] without specifying the humidity, Kuntsche [165] at 22.5±0.5 [$°C$] and humidities of 40±10 [%rH], Xu et al. [270] at 23 [$°C$] and humidities 25±5 [%rH], Del Linz et al. [64], Elzière [103] at 20 [$°C$] without specifying humidity, Centelles et al. [43] at 24 [$°C$], Knight et al. [152] room climate, and Schuster [231] at 20 [$°C$] and 50 [%rH]. These slight variations have a crucial influence on the material behavior, as the respective temperatures are within the glass transition region, which shows a very steep gradient in stiffness. Furthermore, as discovered by Botz [30], changes in humidity can also influence material behavior decisively.

All these factors influence the results and make the comparison between different research groups a very challenging task. However, concerning the tensile tests [22, 140, 172, 134, 165, 270, 64, 43, 152], it is noticeable that all curves show the same characteristics. They show a strongly rate-dependent initial stiffness, followed by a decisive stiffness reduction and an almost horizontal region for intermediate strains, and a substantial increase of stiffness for large strains until failure. Furthermore, the tests all lie in the same range of values. The cyclic tests, consisting of one loading curve followed by an unloading curve, follow the same behavior as the tensile tests until the turning point is reached. The behavior on the unloading is characterized by a steep stiffness drop, followed by an asymptotic approach to zero. The test results of Elzière [103] and the results of this thesis are in good agreement. They are comparable as both test series were carried out at 20 [$°C$] and the same strain rates. However, [103] used an optical extensometer and did not specify the used material nor the humidity during testing, all likely causing the slight variation between the test results. The relaxation tests follow the same behavior as the tensile tests until the constant strain level is reached and the stress drops immediately, followed by a slow increase of stress. The tests of Elzière [103], Schuster [231], and the ones carried out in this work were approached with different rates, a fact which makes a comparison difficult as the relaxation behavior strongly depends on the initial strain rate (cf. Sec. 3.3.4). However, the curves show good agreement, especially with the ones of Schuster [231].

Overall, the experiments revealed excellent results with slight variations between the single

samples of one procedure (cf. App. A). The test results serve as a sound basis for characterizing PVB interlayer considering time-dependent behavior at large deformations under different loading conditions, such as tension until failure, cyclic, and relaxation, all conditions concerning different strain rates and, relating to the cyclic and residual tests, to different strain levels. Furthermore, this experimental study reveals decisive insights into laminated safety glass's overall residual load-bearing behavior as the interlayer plays the most crucial role. Following Kott [157], laminated with PVB interlayer only shows residual load-bearing capacity when made of coarse-breaking glasses. As the fracture follows a stochastic pattern, with only a few critical cracks, depending on the support conditions, uniaxial stress is the predominant state observed within the interlayer. This stress state aligns with uniaxial or planar tensile deformation depending on the geometric boundary conditions.

However, there are also situations where the interlayer is exposed to stress states other than uniaxial, which are not covered by this experimental campaign. Furthermore, only one particular temperature and humidity were investigated, limiting the experimental findings to this specific condition. As it is commonly done in investigating material behavior and modeling it, the strain was the driving quantity, limiting the tests over a long duration to relaxation without considering Creep tests.

6.2. Modeling

In line with the experimental investigations and according to [81], also the modeling is categorized into the response of the fully fractured laminate to external impacts and its corresponding resistance. The effect on the laminate is directly connected to the impact on the interlayer and is referred to as the intact behavior in the following. The resistance is described by a failure criterion based on the experimental investigations. However, considerations regarding failure are presented in Sec. 6.3.3.

The presented model for describing PVB with respect to finite strains and time-dependent effects is based on the general structures proposed by Reese and Govindjee [214], Middendorf [180]. From a rheological point of view, it consists of 10 Maxwell elements in parallel. These elements follow the same fundamental concepts as described by the theory of linear viscoelasticity; however, they are transformed to finite deformation utilizing a multiplicative split of the deformation gradient into an elastic and inelastic part, and the concept of *Dual Variables* established by Haupt and Tsakmakis [126]. Furthermore, the elements consist of hyperelastic springs and nonlinear dampers. Following the network concept proposed by Bergström and Boyce [25], Boyce et al. [34], the Maxwell elements are categorized into three networks, A, B, and C, each represented by an individual energy potential and viscosity function. The individual viscosity functions are designed based on phenomenological considerations drawn from the experimental results. Particular components of the viscosity functions represent respective effects and are described as scalar-tensor functions. The right Cachy Green tensor $\mathbf{C}$, the deformation rate tensor $\mathbf{D}$, and the 2^{nd} Piola Kirchhoff stress tensor $\mathbf{T}$ are utilized. Some of these components were specifically designed for this model; others were adapted from literature. These criteria are all based on scalar tensor-functions: A function depending on $\mathbf{C}$ utilized to represent the stiffness increase for large deformations was adapted from Sedlan and Haupt [236], a function based on $\mathbf{T}$ to model the stiffness drop directly following the initial material response from Lion [169], and function containing $\mathbf{D}$ from Scheffer et al. [226]. In addition, each viscosity function is multiplied by a scalar value, designed to consider temperature influences but not utilized in this work.

Furthermore, two components utilizing the strain rate tensor were particularly designed for this model. Overall, the deformation rate tensor is used as an indicator for different loading

situations, directly aligned to the three groups of experiments. The energy function of networks A and B is based on the Neo Hookean potential, and the energy function of network C is based on a modified Yeoh potential [226]. This model covers rate dependency, loading, unloading, and relaxation. While many of these parameters lack physical significance, they influence the shape of the viscosity function. The model incorporates 10 Maxwell elements and 45 material parameters, a considerable number attributable to the diverse phenomena being described and the time-dependent behavior over an extended period. Ensuring a smooth progression of the material response necessitates modeling roughly one Maxwell element per time decade. The number of Maxwell elements follows the consideration of the generalized Maxwell model, which describes time-dependent material behavior ranging over several decades. It is aligned to the representation of the interlayer for small deformations using a Prony series [165, 161, 231]. As the model is based on phenomenological considerations, predicting material behavior beyond the limits considered for model calibration should be done with caution.

This model differs from established models in the field of polymer mechanics. In contrast to models describing elastomers [169, 25, 236, 226, 149], it does not utilize an infinity stiffness. Infinity stiffness is not confused with infinite stiffness and represents the material process at infinite slow processes or infinite long loadings. This coincides with the general behavior of thermoplastics as non-crosslinked polymers. Compared to the presented model, the models designed for thermoplastics [33, 34, 184, 279] are based on viscoplastic formulation. This aspect contradicts the observations of Kuntsche [165], Schuster [231], who discovered that PVB is purely viscoelastic. In addition, the presented model follows readily designed viscosity functions that are particularly tailored to describe the behavior of PVB. Furthermore, the presented model comprises a considerably higher number of Maxwell elements.

In structural glass design, the predominant modeling approaches for PVB under large deformations considering quasistatic loads have traditionally centered around hyperelasticity. Noteworthy contributions in this field encompass the utilization of hyperelastic models by Kuntsche [165], Wang et al. [264], Kraus [159], Pauli and Siebert [199]. However, recently, Schuster [231] employed the model proposed by Schapery [223, 224] to capture finite nonlinear viscoelastic phenomena. On the other hand, several approaches for dynamic loads exist, such as slow velocity impact [2, 222] and blast [203, 66, 197]. These approaches utilize models of finite linear viscoelasticity [203, 2, 222, 66], finite viscoelasticity [64], and finite viscoplasticity [197]. However, as these approaches are concerned with dynamic loads, the loading conditions considerably differ from quasistatic considerations.

The recalculation of the test results for calibrating the material parameters yields excellent results. However, the material response is slightly overestimated at large deformations, especially for higher strain rates. Furthermore, the representation of the unloading behavior is less accurate, especially for minor strains and slow strain rates. However, the qualitative shape of the hystereses is replicated in an acceptable way. Even the prediction of test results that were not considered for calibration led to reasonable results. More precisely, displacement-controlled tensile, relaxation and cyclic tests containing two loading and unloading paths were calculated and compared to test data. Furthermore, the relaxation tests with a duration of 12 [h] were recalculated and compared to the test results, although only data with a 3 [h] duration was considered for the parameter identification. Subsequently, these calculations were expanded to 24 [h] to serve as a basis for comparing with the engineering approach discussed in Sec. 6.3.1. With the separation of the deformation gradient into a thermal $\mathbf{F}_\theta$ and a mechanical part $\mathbf{F}_M$ and the introduction of the scalar factor η_0 premultiplied to the viscosity function, the model has the basic structure to be expanded to describe effects related to temperature.

For the overall topic of the investigation of the laminated safety glass in the fully fractured state, the model is a big step in the direction of the theoretical description of the residual

load-bearing capacity. On the one hand, it can be used to describe the interlayer within overall modeling approaches numerical [15, 265] and analytical [157, 19, 110]. On the other hand, the model can be used to characterize interface parameters to describe delamination. Within this context, the model parameters are calibrated on the results of TCT [165, 107, 103, 53] or Peel tests [203]. It is crucial to employ a material model that accurately describes the interlayer behavior in this procedure to avoid evaluating incorrect interface parameters.

However, besides the significant advantages the presented model brings to modeling the residual load-bearing behavior of laminated glass, some limitations should also be noted. The model is designed for one specific temperature and humidity that align with the experimental investigations. This fact limits the model to these particular conditions, which is an explicit limitation considering the material's sensitivity to temperature [165, 159, 231] and humidity [31]. A second aspect in line with the experimental investigation based on uniaxial tension is the choice of the energy functions for the hyperelastic potentials depending on the first invariant of the Cauchy Green Deformation tensor. This reduction to the first invariant can lead to inaccurate results when considering biaxial stress states. Furthermore, the implementation of the model into commercial FEM software, crucial for complex investigations, such as the detailed evaluation of the interface behavior or setting up a complex three-dimensional model, is yet to come.

6.3. Engineering Approach

Three engineering approaches were presented to provide a straightforward description of the PVB in the context of residual load-bearing capacity. These approaches comprise a method utilizing a special test procedure to describe the interlayer behavior at long durations, a simplified model for the description of the residual loadbearing capacity of a two-side supported laminate with coincident crack, and a failure criterion based on the uniaxial test data.

6.3.1. Hyperelasticity

This modeling approach has been originally published in Pauli and Siebert [199].

There are several approaches to model the material behavior of Standard PVB in the regime of large deformations. One of the approaches, as presented by Du Bois et al. [100], Kuntsche [165], Kraus [159], Wang et al. [264], is the description with a hyperelastic material model. To evaluate this approach, a distinction between short-term dynamic loads with high loading rates and long-term static loads with low loading rates.

For modeling short-term, dynamic loads (e.g., explosions, impacts) characterized by very high strain rates and extremely short load durations, it can be reasonable to employ a hyperelastic material model directly calibrated on test data [100, 264]. This approach is justifiable because relaxation processes have minimal impact on viscoelastic materials at extremely short load durations. An appropriate strategy building up on this consideration would be to fit a hyperelastic material model to data from tests conducted at very high strain rates. Applying the same approach to residual load-bearing capacity under quasi-static loads, it seems reasonable to calibrate a hyperelastic material model using data from tests conducted at low strain rates or velocities [165, 159]. However, it is crucial to acknowledge that this approach tends to overestimate the stiffness of the interlayer as it does not consider the relaxation processes that take predominatly govern the material behavior at long loading durations.

This work introduces a straightforward procedure to characterize and model the long-term response of Polyvinyl Butyral (PVB) within large deformations. The methodology involves conducting and evaluating a stepwise relaxation test, termed *staircase test* (cf. Sec. 3.3.5.1

for the evaluation procedure). Within this approach, the time-independent response of the material is isolated, and the viscoelastic hysteresis reduces to an elastic curve. This curve can serves as the basis for the calibration of hyperelastic material models.

Fig. 6.1 illustrates the approach of this work in comparison to modeling approaches found in the literature [100, 165, 162, 264]. While each of these works introduces several hyperelastic material models, for comparison in this study, only one model from each literature source is selected. Additionally, the curves representing results from the literature were calculated analytically for the uniaxial stress state using the provided parameters (refer to Table 6.1) and considering the incompressibility constraint.

Tab. 6.1 shows the material parameters of hyperelastic material models for PVB under quasistatic conditions found in literature.

Table 6.1.: Parameters, given from literature

Du Bois et al. [100]	α_1	α_2	μ_1	μ_2
Ogden	2	-2	3.2	-0.12
Kuntsche [165]	C_{10}	C_{20}	C_{30}	
Yeoh	1.101	0.03638	0.01482	
Wang et al. [264]	μ_1	μ_2		
Mooney Rivlin	5.212	-3.264		
Kraus [159]	G_e	G_c	d	b
Extended Tube	-0.270	1.641	0.2	9.059

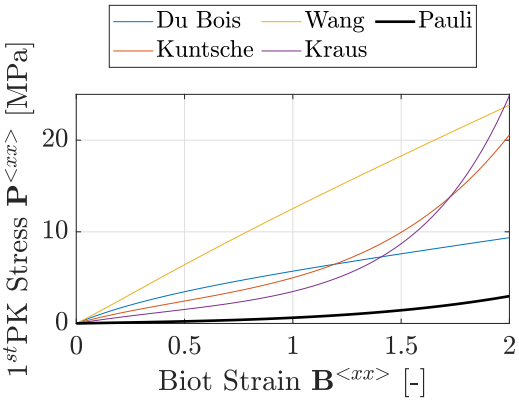

Figure 6.1.: Comparison of Modeling Results

Tt is noteworthy that the modeling approaches presented by [165, 159] consider quasistatic loads, and the approaches presented by [100, 264] consider dynamic approaches. As the approach adopted in this work endeavors to minimize time influences on the material response by a special test procedure, it predicts a considerably lower material response than the other approaches. However, for further discussion of the comparison between the individual groups, the reader is referred to the original work [199].

Nevertheless, some restrictions of this approach are be pointed out in the following. Considering thermoplastic material behavior in general, it is obvious that there is no stiffness left when time tends toward infinity. However, two decisive simplifications can be considered within

the context of residual load-bearing capacity. First, only quasi-static loading behavior must be considered (no cyclic loading); second, according to actual practice, the material behavior must be predicted for 24 [h] [68]. To evaluate this engineering approach, the Yeoh model derived from the staircase test is compared with calculations carried out by the finite viscoelastic material model derived within this work. Therefore, several relaxation tests were calculated (cf. Sec. 4.6.3) and the stress strain pair for each test was plotted within a strain stress diagram together with the result of curve evaluated by the staircase test (cf. Fig. 6.2).

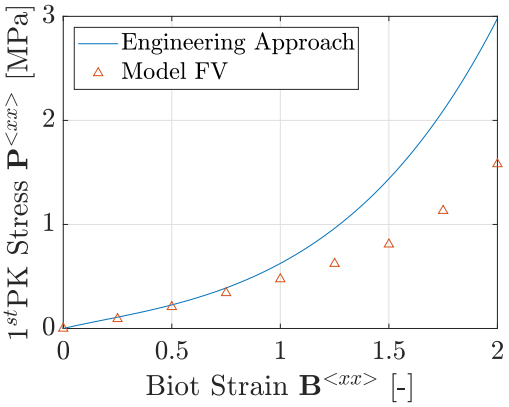

Figure 6.2.: Comparison between Model and Enginnering Approach

Comparing the engineering approach to the calculations of the finite viscoelastic model shows a very good agreement up to a stress of 100 [%], for larger strains, the engineering approach overestimates the stress response compared to the FV model. However, for further evaluation, the curves would have be compared to the values at the end of relaxation tests with a duration of 24 [h]. Nevertheless, the presented approach seems to be a reasonable method of evaluting the material behavior of interlayers, not only PVB, by utilizing a single test.

6.3.2. Residual Load-Bearing Model

A straightforward residual load-bearing model for describing laminated glass with fracture pattern according to the line mechanism L1, defined by Kott [157], was presented in Sec. 5.2. Franz [107], Botz [30] extensively investigated and discussed the same behavior using TCB test studies. Furthermore, Kott [157], Belis et al. [19] proposed modeling approaches for this state. The presented approach is built upon these considerations; however, the plastic material formulation of the interlayer proposed by Kott [157], Belis et al. [19] is replaced by a model of finite viscoelasticity to cover time-dependent effects, as they predominantly affected the residual load-bearing behavior [30]. However, the presented approach does not cover effects caused by delamination, which is a significant limitation as Franz [107], Botz [30] discovered, delamination is one decisive for the residual load-bearing capacity and increases with time. Nevertheless, it could be added to the displacement u, for example, utilizing a similar approach to that proposed by Belis et al. [19]. Incorporating the delamination, the model could serve as an easy handling tool to asses the residual load-bearing capacity of two side-supported laminates with PVB interlayer and coarse-breaking glass.

6.3.3. Failure

The couterpart of the investigations regarding the intact state, which represent the impact side of the design equation [81], is the the description of the resistance. In the context of

residual load-bearing capacity, it is concerned with the investigation and characterization of the collapse of fully fractured laminated glass. As the collapse of the laminate within the ultimate limit state can be directly related to it, the further considerations are based on the interlayer. Within this section the experimental part of the investigation as well as the modeling part are described together as they are closely linked with each other. Uniaxial tension tests were carried out until failure, considering seven different strain rates. The statistical evaluation of the failure revealed that the distribution of the data could be described as a lognormal distribution. Furthermore, a direct relation between strain rate and strain at failure could be observed. Taking this effect into account, the Cauchy stress in the uniaxial direction was chosen as the failure criterion. The transfer from the measured 1^{st}PK stresses was carried out using the consideration of incompressible material behavior. A one-dimensional criterion is the most simple case of defining a failure criterion. However, in the case of residual load-bearing capacity, the intermediate layer acts as a bridging element between single glass shards [67] and carries only tensile loads. For coarse-breaking glass, which is the only configuration showing residual load-bearing capacity with PVB interlayer [157], the predominantly deformation state is uniaxial or planar tension. Therefore, a failure criterion on uniaxial tensile data seems reasonable. Furthermore, a characteristic failure strength was evaluated, and a partial safety factor was calibrated based on the assumption of a lognormal distribution. Using the failure criterion and the partial safety factor in combination with the simplified model presented in the last section appears to be a promising combination.

However, this topic must be treated cautiously, as the design criterion only holds for the exact state considered for calibration, so, in this case, the uniaxial stress state. The proposed criterion can not simply be transferred to other cases where different stress states might occur. A broader database of test results is required to derive a more general failure criterion applicable to various stress and deformation states. The stress or strain states to be considered must be chosen concerning the application. For example, the predominant stress state in a two-side supported laminated glass is in a uniaxial direction, which is why the suggested failure criterion could be applied. However, in this case, particular caution regarding the effects caused by transversal contraction is required. Furthermore, for complex considerations utilizing FEM to simulate a broken laminated, explicitly taking into detail load-bearing mechanisms such as friction of the glass shards and delamination of the interlayer several stress and deformation states must be taken into account. A common approach to describe the failure of an isotropic material is the description within principal stress, strain, or stretch space employing a deviatoric and hydrostatic split, resulting in a deviatoric plane perpendicular to a hydrostatic axis [155]. Nearly incompressible elastomers, for example, possess a dilatational failure linked to the hydrostatic components and a distortional failure related to the deviatoric components as illustrated by Rosendahl et al. [220]. Different failure stresses or strains are located at different and mark the edges of the deviatoric plane, representing material failure. The shape of this edge can be represented by different geometric shapes, which can depend on several parameters. The shape usually changes along the hydrostatic axis. Various tests must be carried out to approach the respective geometric failure surface as well as possible. These experiments range from uni- and biaxial tension over shear to hydrostatic compression. Drass et al. [99] presented a promising criterion for silicone adhesives based on uniaxial, biaxial, and so-called pancake tests. In conclusion, additional tests are required for a more general failure criterion and partial safety factor for PVB accounting for multiaxial loadings.

7. Conclusion and Outlook

The aim of this work was a contribution to the theoretical description of the residual load-bearing capacity of laminated glass with PVB interlayer. Besides several load-bearing mechanisms within the fractured state of the laminate, the interlayer was identified as the most crucial part. Therefore, acurately describing the material behavior of PVB is considered the essential part. With regard to the experimental evaluation according to DIN 18008-1:2020-05 [68], the material behavior at 20 $[°C]$ considering large deformations and time-dependency, was assumed to be the decisive configuration.

Therefore, a comprehensive finite nonlinear viscoelastic model has been developed to effectively capture the time-dependent behavior of Polyvinyl Butyral (PVB) concerning this decisive temperature. This model comprises a network of 10 Maxwell elements connected in parallel, with each component incorporating both a nonlinear damper and a hyperelastic spring. By utilizing viscosity functions with internal process variables, the dampers provide a robust and phenomenological description of the behavior of PVB in the regime of finite strains. The model was implemented numerically and calibrated on uniaxial test data under the assumption of incompressibility. The model's calculations have demonstrated a commendable alignment between the experimental findings and the model's predictions, even for processes not considered for parameter parameter identification.

Furthermore, an approach was presented to utilize a simplified version of the model within an engineering approach describing the residual load-bearing capacity of a two-side supported coincidentally broken laminated glass with PVB interlayer. In addition, a simple failure criterion based on the Cauchy stresses at failure, examined during the experimental investigations, was proposed for this application. Besides the actual description of time effects, an engineering approach describing the material behavior at long durations by utilizing a hyperelastic formulation was presented. This approach comprised a particular test procedure and evaluation process.

However, to increase the general applicability of the model, the test data must be expanded by further experiments considering different temperatures and humidities as well as different stress states. Based on this database, the potential and viscosity function would have to be adopted; however, it would have to use the same structure as presented. Furthermore, the results at different stress states would serve as the basis for a more general failure criterion. In addition, to utilize the presented model within commercial FEM software, such as Ansys and Abaqus, the formulation of a particular user subroutine is required. These software tools offer the option of implementing specially defined material models via a user subroutine based on the tangent operators of the material model.

In conclusion, a very promising material model for PVB at finite strains considering time dependence was derived and successfully calibrated. Furthermore, two different simplified engineering approaches were presented to describe the interlayer within the residual load-bearing capacity of laminated glass. However, there is still a need for future research, especially concerning the consideration of different climates and multiaxial loading from an experimental point of view and considering these effects within the material model and failure criterion, as well as implementing these models in FEM.

Bibliography

[1] H. Altenbach. *Kontinuumsmechanik: Einführung in die materialunabhängigen und materialabhängigen Gleichungen*. Springer Vieweg, Berlin Heidelberg, 2012. ISBN 978-3-662-57503-1.

[2] C. Alter, S. Kolling, and J. Schneider. An enhanced non–local failure criterion for laminated glass under low velocity impact. *International Journal of Impact Engineering*, 109: 342–353, 2017. ISSN 0734-743X. doi: 10.1016/j.ijimpeng.2017.07.014.

[3] L. Anand. On H. Hencky's approximate strain-energy function for moderate deformations. *Journal of Applied Mechanics*, 46:78–82, 1979. ISSN 0021-8936. doi: 10.1115/1.3424532.

[4] L. Anand. A constitutive model for compressible elastomeric solids. *Computational Mechanics*, 18:339–355, 1996. ISSN 0178-7675. doi: 10.1007/BF00376130.

[5] S. C. Angelides, J. P. Talbot, and M. Overend. The effects of high strain-rate and in-plane restraint on quasi-statically loaded laminated glass: a theoretical study with applications to blast enhancement. *Glass Structures & Engineering*, 4:403–420, 2019. ISSN 2363-5142. doi: 10.1007/s40940-019-00107-4.

[6] S. C. Angelides, J. P. Talbot, and M. Overend. High strain-rate effects from blast loads on laminated glass: An experimental investigation of the post-fracture bending moment capacity based on time - temperature mapping of interlayer yield stress. page 121658, 2021.

[7] S. C. Angelides, J. P. Talbot, and M. Overend. The influence of fracture pattern on the residual resistance of laminated glass at high strain-rates: an experimental investigation of the post-fracture bending moment capacity based on time-temperature mapping of interlayer yield stress. *Glass Structures & Engineering*, 7:549–568, 2022. ISSN 2363-5150. doi: 10.1007/s40940-022-00168-y.

[8] Ansys, Inc. Ansys Mechanical, 2021.

[9] T. Arens, F. Hettlich, C. Karpfinger, U. Kockelkorn, K. Lichtenegger, and H. Stachel. *Mathematik*. Springer Spektrum, Berlin, 2018. ISBN 978-3-662-56740-1.

[10] A. S. Argon, J. Megusar, and N. J. Grant. Shear band induced dilations in metallic glasses. 19(5):591–596, 1985. ISSN 0036-9748.

[11] E. M. Arruda and M. C. Boyce. A three-dimensional constitutive model for the large stretch behavior of rubber elastic materials. *Journal of the Mechanics and Physics of Solids*, 41(2):389–412, 1993. ISSN 0022-5096. doi: 10.1016/0022-5096(93)90013-6.

[12] ASTM D1349-99:2005. Standard Practice for Rubber-Standard Temperatures for Testing.

[13] ASTM D638-10:2010. Standard Test Method for Tensile Properties of Plastics.

[14] A. G. Atkins and Y. W. Mai. Residual strain energy in elastoplastic adhesive and cohesive fracture. *International Journal of Fracture*, 30:203–221, 1986. ISSN 0376-9429. doi: 10.1007/BF00019777.

[15] D. Baraldi, A. Cecchi, and P. Foraboschi. Broken tempered laminated glass: non-linear discrete element modeling. *Composite Structures*, 140:278–295, 2016. ISSN 0263-8223.

[16] G. I. Barenblatt. The Mathematical Theory of Equilibrium Cracks in Brittle Fracture. *Advances in Applied Mechanics*, 7:55–129, 1962. ISSN 0065-2156. doi: 10.1016/S0065-2156(08)70121-2.

[17] K.-J. Bathe. *Finite element procedures*. Prentice Hall, Englewood Cliffs, New Jersey, 1995. ISBN 978-0-9790049-0-2.

[18] F. Becker. *Entwicklung einer Beschreibungsmethodik für das mechanische Verhalten unverstärkter Thermoplaste bei hohen Deformationsgeschwindigkeiten*. Dissertation, Martin-Luther-Universität Halle-Wittenberg, Halle-Wittenberg, 2009.

[19] J. Belis, D. Delince, D. Callewaert, R. van Impe, and J. Depauw. Plastic deformation of polymer interlayers during post-breakage behavior of laminated glass - partim 1: analytical approach. *International Journal of Modern Physics B*, 22(31n32):5509–5514, 2008. ISSN 0217-9792. doi: 10.1142/S0217979208050735.

[20] S. J. Bennison and I. Stelzer. Structural properties of laminated glass. *Proceedings of the Glass Performance Days, Tampere*, 2009.

[21] S. J. Bennison, A. Jagota, and C. A. Smith. Fracture of Glass/Poly(vinyl butyral) (Butacite®) Laminates in Biaxial Flexure. *Journal of the American Ceramic Society*, 82(7):1761–1770, 1999. ISSN 0002-7820. doi: 10.1111/j.1151-2916.1999.tb01997.x.

[22] S. J. Bennison, J. Sloan, D. Kistunas, P. Buehler, T. Amos, and C. Smith. Laminated glass for blast mitigation: role of interlayer properties. *Proceedings of the Glass Processing Days, Tampere*, pages 17–20, 2005.

[23] J. S. Bergström. *Large strain time-Dependent behavior of elastomeric materials*. Dissertation, Massachusetts Institute of Technology, Massachusetts, 1999.

[24] J. S. Bergström. *Mechanics of solid polymers: theory and computational modeling*. Elsevier, Amsterdam, 2015. ISBN 9780323311502.

[25] J. S. Bergström and M. C. Boyce. Constitutive modeling of the large strain time-dependent behavior of elastomers. *Journal of the Mechanics and Physics of Solids*, 46(5):931–954, 1998. ISSN 0022-5096. doi: 10.1016/S0022-5096(97)00075-6.

[26] L. Biolzi and M. Simoncelli. Overall response of 2-ply laminated glass plates under out-of-plane loading. *Engineering Structures 256*, 256:113967, 2022. ISSN 0141-0296. doi: 10.1016/j.engstruct.2022.113967.

[27] J. E. Bischoff, E. M. Arruda, and K. Grosh. A new constitutive model for the compressibility of elastomers at finite deformations. *Rubber Chemistry and Technology*, 74(4):541–559, 2001. ISSN 0035-9475. doi: 10.5254/1.3544956.

[28] P. J. Blatz and W. L. Ko. Application of Finite Elastic Theory to the Deformation of Rubbery Materials. *Transactions of the Society of Rheology*, 6:223–251, 1962. ISSN 0038-0032. doi: 10.1122/1.548937.

[29] J. Bonet and R. D. Wood. *Nonlinear continuum mechanics for finite element analysis*. Camebridge University Press, 1997. ISBN 9780521572729.

[30] M. Botz. *Beitrag zur versuchstechnischen und numerischen Beschreibung von Verbundglas mit PVB-Zwischenschicht im intakten und gebrochenen Zustand*. Dissertation, Universität der Bundeswehr München, Neubiberg, 2020.

[31] M. Botz, K. Wilhelm, and G. Siebert. Experimental investigations on the creep behaviour of PVB under different temperatures and humidity conditions. *Glass Structures & Engineering*, 4:389–402, 2019. ISSN 2363-5142. doi: 10.1007/s40940-019-00098-2.

[32] M. C. Boyce and E. M. Arruda. Constitutive Models of Rubber Elasticity: A Review. *Rubber Chemistry and Technology*, 73(3):504–523, 2000. ISSN 0035-9475. doi: 10.5254/1.3547602.

[33] M. C. Boyce, D. M. Parks, and A. S. Argon. Large inelastic deformation of glassy polymers. part I: rate dependent constitutive model. *Mechanics of Materials*, 7(1):15–33, 1988. ISSN 0167-6636. doi: 10.1016/0167-6636(88)90003-8.

[34] M. C. Boyce, S. Socrate, and P. G. Llana. Constitutive model for the finite deformation stress–strain behavior of poly(ethylene terephthalate) above the glass transition. *Polymer*, 41(6):2183–2201, 2000. ISSN 0032-3861. doi: 10.1016/S0032-3861(99)00406-1.

[35] H. F. Brinson and L. C. Brinson. *Polymer Engineering Science and Viscoelasticity: An Introduction*. Springer, New York, 2015. ISBN 978-1-4899-7484-6.

[36] BS ISO 37:2005. Rubber, vulcanized or thermoplastic- determination of tensile stress-strain properties.

[37] J. C. Butcher. *Numerical methods for ordinary differential equations*. Wiley & Sons, Inc., Hoboken, New Jersey, 2016. ISBN 978-1-119-12150-3.

[38] R. H. Byrd, M. E. Hribar, and J. Nocedal. An Interior Point Algorithm for Large-Scale Nonlinear Programming. *SIAM Journal on Optimization*, 9(4):877–900, 1999. ISSN 1052-6234. doi: 10.1137/S1052623497325107.

[39] R. H. Byrd, J. C. Gilbert, and J. Nocedal. A trust region method based on interior point techniques for nonlinear programming. *Mathematical Programming*, 89:149–185, 2000. ISSN 1436-4646. doi: 10.1007/PL00011391.

[40] G. T. Camacho and M. Ortiz. Computational modelling of impact damage in brittle materials. *International Journal of Solids and Structures*, 33(20-22):2899–2938, 1996. ISSN 0020-7683. doi: 10.1016/0020-7683(95)00255-3.

[41] L. Caprioli. Su un criterio per l'esistenza dell'energia di deformazione. *Bollettino dell'Unione Matematica Italiana*, 10(4):481–483, 1955. ISSN 0392-4041.

[42] G. Castori and E. Speranzini. Structural analysis of failure behavior of laminated glass. *Composites Part B: Engineering*, 125:89–99, 2017. ISSN 1359-8368. doi: 10.1016/j.compositesb.2017.05.062.

[43] X. Centelles, M. Martín, A. Solé, J. R. Castro, and L. F. Cabeza. Tensile test on interlayer materials for laminated glass under diverse ageing conditions and strain rates. *Construction and Building Materials*, 243:118230, 2020. ISSN 0950-0618. doi: 10.1016/j.conbuildmat.2020.118230.

[44] CEN/TS 19100-1:2024-01. Design of glass structures - Part 1: Basis of design and materials; German version CEN/TS 19100-1:2021.

[45] CEN/TS 19100-2:2024-01. Design of glass structures - Part 2: Design of out-of-plane loaded glass components; German version CEN/TS 19100-2:2021.

[46] CEN/TS 19100-3:2024-06. Design of glass structures - Part 3: Design of in-plane loaded glass components and their mechanical joints; German version CEN/TS 19100-3:2021.

[47] M. Cervera, G. B. Barbat, M. Chiumenti, and J.-Y. Wu. A Comparative Review of XFEM, Mixed FEM and Phase-Field Models for Quasi-brittle Cracking. *Archives of Computational Methods in Engineering*, 29:1009–1083, 2022. ISSN 1886-1784. doi: 10.1007/s11831-021-09604-8.

[48] P. Chadwick. *Continuum Mechanics: Concise Theory and Problems*. Dover Publications, 1999. ISBN 978-0-486-40180-5.

[49] S. Chen, M. Zang, and W. Xu. A three-dimensional computational framework for impact fracture analysis of automotive laminated glass. *Computer Methods in Applied Mechanics and Engineering*, 294:72–99, 2015. ISSN 0045-7825. doi: 10.1016/j.cma.2015.06.005.

[50] S. Chen, M. Zang, D. Wang, Z. Zheng, and C. Zhao. Finite element modelling of impact damage in polyvinyl butyral laminated glass. *Composite Structures*, 138:1–11, 2016. ISSN 0263-8223. doi: 10.1016/j.compstruct.2015.11.042.

[51] S. Chen, M. Zang, D. Wang, S. Yoshimura, and T. Yamada. Numerical analysis of impact failure of automotive laminated glass: A review. *Composites Part B: Engineering*, 122:47–60, 2017. ISSN 1359-8368. doi: 10.1016/j.compositesb.2017.04.007.

[52] S. Chen, Z. Chen, X. Chen, and J. Schneider. Evaluation of the delamination performance of polyvinyl-butyral laminated glass by through-cracked tensile tests. *Construction and Building Materials*, 341:127914, 2022. ISSN 0950-0618. doi: 10.1016/j.conbuildmat.2022.127914.

[53] X. Chen, P. L. Rosendahl, S. Chen, and J. Schneider. On the delamination of polyvinyl butyral laminated glass: Identification of fracture properties from numerical modelling. *Construction and Building Materials*, 306:124827, 2021. ISSN 0950-0618. doi: 10.1016/j.conbuildmat.2021.124827.

[54] X. Chen, M. Schuster, and J. Schneider. On the pummel test and pummel-value evaluation of polyvinyl butyral laminated safety glass. *Composite Structures*, 280:114878, 2022. ISSN 0263-8223. doi: 10.1016/j.compstruct.2021.114878.

[55] B. D. Coleman. Mechanical and thermodynamical admissibility of stress-strain functions. *Archive for Rational Mechanics and Analysis*, 9:172–186, 1962. ISSN 1432-0673. doi: 10.1007/BF00253343.

[56] B. D. Coleman. Thermodynamics of materials with memory. *Archive for Rational Mechanics and Analysis*, 17:1–46, 1964. ISSN 0003-9527.

[57] B. D. Coleman. On thermodynamics, strain impulses, and viscoelasticity. *Archive for Rational Mechanics and Analysis*, 17:230–254, 1964. ISSN 0003-9527. doi: 10.1007/BF00282439.

[58] B. D. Coleman and M. E. Gurtin. Thermodynamics with Internal State Variables. *The Journal of Chemical Physics*, 47(2):597–613, 1967. ISSN 0021-9606. doi: 10.1063/1.1711937.

[59] B. D. Coleman and W. Noll. Foundations of Linear Viscoelasticity. *Reviews of Modern Physics*, 33:239–249, 1961. ISSN 0034-6861. doi: 10.1103/RevModPhys.33.239.

[60] P. A. Cundall and O. D. L. Strack. A discrete numerical model for granular assemblies. *Géotechnique*, 29(1):47–65, 1979. ISSN 0016-8505. doi: 10.1680/geot.1979.29.1.47.

[61] G. D'Ambrosio, L. Galuppi, and G. Royer-Carfagni. A simple model for the post-breakage response of laminated glass under in-plane loading. *Composite Structures*, 230:111426, 2019. ISSN 0263-8223. doi: 10.1016/j.compstruct.2019.111426.

[62] G. D'Ambrosio, L. Galuppi, and G. Royer-Carfagni. Post-breakage in-plane stiffness of laminated glass: an engineering approach. *Glass Structures & Engineering*, 4:421–432, 2019. ISSN 2363-5142. doi: 10.1007/s40940-019-00099-1.

[63] R. de Borst, M. A. Crisfield, J. J. C. Remmers, and C. V. Verhoosel. *Nonlinear finite element analysis of solids and structures*. Wiley & Sons, Inc., Hoboken, New Jersey, 2012. ISBN 978-1-118-37601-0.

[64] P. Del Linz, Y. Wang, P. A. Hooper, H. Arora, D. Smith, L. Pascoe, D. Cormie, B. R. K. Blackman, and J. P. Dear. Determining Material Response for Polyvinyl Butyral (PVB) in Blast Loading Situations. *Experimental Mechanics*, 56:1501–1517, 2016. ISSN 0014-4851. doi: 10.1007/s11340-016-0179-5.

[65] P. Del Linz, P. A. Hooper, H. Arora, Y. Wang, D. Smith, B. R. K. Blackman, and J. P. Dear. Delamination properties of laminated glass windows subject to blast loading. *International Journal of Impact Engineering*, 105:39–53, 2017. ISSN 0734-743X. doi: 10.1016/j.ijimpeng.2016.05.015.

[66] P. Del Linz, X. Liang, P. A. Hooper, H. Arora, L. Pascoe, D. Smith, D. Cormie, and J. P. Dear. A numerical method for predicting the deformation of crazed laminated windows under blast loading. *Engineering Structures*, 172:29–40, 2018. ISSN 0141-0296. doi: 10.1016/j.engstruct.2018.05.030.

[67] D. Delincé. *Experimental approaches for assessing time and temperature dependent performances of fractured laminated safety glass*. Dissertation, Ghent University, Ghent, 2014.

[68] DIN 18008-1:2020-05. Glas im Bauwesen - Bemessungs- und Konstruktionsregeln - Teil 1: Begriffe und allgemeine Grundlagen.

[69] DIN 18008-5:2013-07. Glas im Bauwesen - Bemessungs- und Konstruktionsregeln - Teil 5: Zusatzanforderungen an begehbare Verglasungen.

[70] DIN 18008-6:2018-02. Glas im Bauwesen - Bemessungs- und Konstruktionsregeln - Teil 6: Zusatzanforderungen an zu Instandhaltungsmaßnahmen betretbare Verglasungen und an durchsturzsichere Verglasungen.

[71] DIN 53504:2017-03. Prüfung von Kautschuk und Elastomeren - Bestimmung von Reißfestigkeit, Zugfestigkeit, Reißdehnung und Spannungswerten im Zugversuch.

[72] DIN EN 12150-1:2020-07. Glass in building - Thermally toughened soda lime silicate safety glass - Part 1: Definition and description; German version EN 12150-1:2015+A1:2019.

[73] DIN EN 12150-2:2005-01. Glass in building - Thermally toughened soda lime silicate safety glass - Part 2: Evaluation of conformity/Product standard; German version EN 12150-2:2004.

[74] DIN EN 12337-1:2000-11. Glass in building - Chemically strengthened soda lime silicate glass - Part 1: Definition and description; German version EN 12337-1:2000.

[75] DIN EN 12337-2:2005-01. Glass in building - Chemically strengthened soda lime silicate glass - Part 2: Evaluation of conformity/Product standard; German version EN 12337-2:2004.

[76] DIN EN 12600:2003-04. Glass in building - Pendulum tests - Impact test method and classification for flat glass; German version EN 12600:2002.

[77] DIN EN 16613:2020-01. Glass in building - Laminated glass and laminated safety glass - Determination of interlayer viscoelastic properties; German version EN 16613:2019.

[78] DIN EN 1863-1:2012-02. Glass in building - Heat strengthened soda lime silicate glass - Part 1: Definition and description; German version 1863-1:2011.

[79] DIN EN 1863-2:2005-01. Glass in building - Heat strengthened soda lime silicate glass - Part 2: Evaluation of conformity/Product standard; German version EN 1863-2:2004.

[80] DIN EN 1895:2002-02. Adhesives for paper and board, packaging and disposable sanitary products - 180° "T" peel test for a flexible-to-flexible assembly; German version EN 1895:2001.

[81] DIN EN 1990:2021-10. Eurocode: Basis of structural design; German version EN 1990:2002 + A1:2005 + A1:2005/AC:2010.

[82] DIN EN 572-1:2016-06. Glass in building - Basic soda-lime silicate glass products - Part 1: Definitions and general physical and mechanical properties; German version EN 572-1:2012+A1:2016.

[83] DIN EN 572-2:2012-11. Glass in building - Basic soda lime silicate glass products - Part 2: Float glass; German version EN 572-2:2012.

[84] DIN EN 899-1:2018-03. Plastics - Determination of creep behaviour - Part 1: Tensile creep (ISO 899-1:2017); German version EN ISO 899-1:2017.

[85] DIN EN ISO 12543-1:2022-03. Glass in building - Laminated glass and laminated safety glass - Part 1: Vocabulary and description of component parts (ISO 12543-1:2021); German version EN ISO 12543-1:2021.

[86] DIN EN ISO 12543-2:2022-03. Glass in building - Laminated glass and laminated safety glass - Part 2: Laminated safety glass (ISO 12543-2:2021); German version EN ISO 12543-2:2021.

[87] DIN EN ISO 12543-3:2022-03. Glass in building - Laminated glass and laminated safety glass - Part 3: Laminated glass (ISO 12543-3:2021); German version EN ISO 12543-3:2021.

[88] DIN EN ISO 17892-10:2019-04. Geotechnical investigation and testing - Laboratory testing of soil - Part 10: Direct shear tests (ISO 17892-10:2018); German version EN ISO 17892-10:2018.

[89] DIN EN ISO 291:2008-08. Plastics - Standard atmospheres for conditioning and testing (ISO 291:2008); German version EN ISO 291:2008.

[90] DIN EN ISO 527-1:2019-12. Plastics - Determination of tensile properties - Part 1: General principles (ISO 527-1:2019); German version EN ISO 527-1:2019.

[91] DIN EN ISO 527-2:2012-06. Plastics - Determination of tensile properties - Part 2: Test conditions for moulding and extrusion plastics (ISO 527-2:2012); German version EN ISO 527-2:2012.

[92] DIN EN ISO 527-3:2019-02. Plastics - Determination of tensile properties - Part 3: Test conditions for films and sheets (ISO 527-3:2018); German version EN ISO 527-3:2018.

[93] DIN EN ISO 6721-1:2019-09. Plastics - Determination of dynamic mechanical properties - Part 1: General principles (ISO 6721-1:2019); German version EN ISO 6721-1:2019.

[94] DIN EN ISO 7500-1:2018-06. Metallic materials - Calibration and verification of static uniaxial testing machines - Part 1: Tension/compression testing machines - Calibration and verification of the force-measuring system (ISO 7500-1:2018); German version EN ISO 7500-1:2018.

[95] L. C. W. Dixon and G. P. Szego. *Towards Global Optimisation 2*. North-Holland Publishing Company, Amsterdam, 1978. ISBN 978-0444851710.

[96] H. Domininghaus. *Kunststoffe*. Springer, Berlin Heidelberg, 2008. ISBN 978-3-540-21410-6.

[97] M. Drass and M. A. Kraus. Dimensioning of silicone adhesive joints: Eurocode-compliant, mesh-independent approach using the FEM. *Glass Structures & Engineering*, 5:349–369, 2020. ISSN 2363-5142. doi: 10.1007/s40940-020-00128-4.

[98] M. Drass and M. A. Kraus. Semi-Probabilistic Calibration of a Partial Material Safety Factor for Structural Silicone Adhesives - Part I: Derivation. *International Journal of Structural Glass and Advanced Materials Research*, 4(1):56–68, 2020. ISSN 2616-4507. doi: 10.3844/sgamrsp.2020.56.68.

[99] M. Drass, P. L. Rosendahl, and M. A. Kraus. Coupled distortional-dilatational failure mode concept for silicone adhesives. *Mechanics of Materials*, 148:103511, 2020. ISSN 0167-6636. doi: 10.1016/j.mechmat.2020.103511.

[100] P. A. Du Bois, S. Kolling, and W. Fassnacht. Modelling of safety glass for crash simulation. *Computational Materials Science*, 28(3-4):675–683, 2003. ISSN 0927-0256. doi: 10.1016/j.commatsci.2003.08.023.

[101] D. S. Dugdale. Yielding of steel sheets containing slits. *Journal of the Mechanics and Physics of Solids*, 8(2):100–104, 1960. ISSN 0022-5096. doi: 10.1016/0022-5096(60)90013-2.

[102] R. B. Dupaix and M. C. Boyce. Constitutive modeling of the finite strain behavior of amorphous polymers in and above the glass transition. *Mechanics of Materials*, 39(1):39–52, 2007. ISSN 0167-6636. doi: 10.1016/j.mechmat.2006.02.006.

[103] P. Elzière. *Laminated glass: dynamic rupture of adhesion*. dissertation, Université Pierre & Marie Curie - Paris 6, Paris, 2016.

[104] F. Ensslen. *Zum Tragverhalten von Verbund-Sicherheitsglas unter Berücksichtigung der Alterung der Polyvinylbutyral-Folie*. Dissertation, Ruhr-Universität Bochum, Bochum, 2005.

[105] S. Feirabend and W. Sobek. Bewehrtes verbundsicherheitsglas. *Stahlbau*, 77(S1):16–22, 2008. ISSN 0038-9145. doi: 10.1002/stab.200810027.

[106] P. J. Flory. Thermodynamic relations for high elastic materials. *Transactions of the Faraday Society*, 57:829–838, 1961. ISSN 0014-7672. doi: 10.1039/tf9615700829.

[107] J. Franz. *Untersuchungen zur Resttragfähigkeit von gebrochenen Verglasungen: Investigation of the residual load-bearing behaviour of fractured glazing*. Springer Vieweg, Berlin Heidelberg, 2015. ISBN 978-3-662-48555-2.

[108] J. Franz and J. Schneider. Through-cracked-tensile tests with polyvinylbutyral (PVB) and different adhesion grades. *Proceedings of the Engineering transparency, Düsseldorf*, pages 135–142, 2014.

[109] Y.-C. Fung. *A first course in continuum mechanics*. Prentice-Hall, Englewood Cliffs, New Jersey, 1977. ISBN 9780133183115.

[110] L. Galuppi and G. Royer-Carfagni. A homogenized model for the post-breakage tensile behavior of laminated glass. *Composite Structures*, 154:600–615, 2016. ISSN 0263-8223. doi: 10.1016/j.compstruct.2016.07.052.

[111] L. Galuppi and G. Royer-Carfagni. A homogenized analysis à la Hashin for cracked laminates under equi-biaxial stress. Applications to laminated glass. *Composites Part B: Engineering*, 111:332–347, 2017. ISSN 1359-8368. doi: 10.1016/j.compositesb.2016.11.027.

[112] L. Galuppi and G. Royer-Carfagni. The post-breakage response of laminated heat-treated glass under in plane and out of plane loading. *Composites Part B: Engineering*, 147:227–239, 2018. ISSN 1359-8368. doi: 10.1016/j.compositesb.2018.04.005.

[113] W. Gao and M. Zang. The simulation of laminated glass beam impact problem by developing fracture model of spherical DEM. *Engineering Analysis with Boundary Elements*, 42:2–7, 2014. ISSN 0955-7997. doi: 10.1016/j.enganabound.2013.11.011.

[114] D. Garcia-Gonzalez, R. Zaera, and A. Arias. A hyperelastic-thermoviscoplastic constitutive model for semi-crystalline polymers: Application to PEEK under dynamic loading conditions. *International Journal of Plasticity*, 88:27–52, 2017. ISSN 0749-6419. doi: 10.1016/j.ijplas.2016.09.011.

[115] A. N. Gent and G. R. Hamed. Peel mechanics for an elastic-plastic adherend. *Journal of Applied Polymer Science*, 21(10):2817–2831, 1977. ISSN 0021-8995. doi: 10.1002/app.1977.070211018.

[116] F. Glover. A template for scatter search and path relinking. In *Artificial Evolution*, pages 13–51. Springer, 1998. doi: 10.1007/BFb0026589.

[117] A. E. Green and J. E. Adkins. *Large elastic deformations and non-linear continuum mechanics*. Oxford University Press, 1970. ISBN 978-0198533344.

[118] G. Green. On the Propagation of Light in Crystallized Media. *Transactions of the Cambridge Philosophical Society*, 7:121–140, 1839.

[119] M. S. Green and A. V. Tobolsky. A New Approach to the Theory of Relaxing Polymeric Media. *The Journal of Chemical Physics*, 14(2):80–92, 1946. ISSN 0021-9606. doi: 10.1063/1.1724109.

[120] M. E. Gurtin. *An introduction to continuum mechanics*. Academic press, New York, 1982. ISBN 978-0123097507.

[121] P. Hála, A. Zemanová, J. Zeman, and M. Šejnoha. Numerical study on failure of laminated glass subjected to low-velocity impact. *Glass Structures & Engineering*, 8:99–117, 2022. ISSN 2363-5142. doi: 10.1007/s40940-022-00210-z.

[122] Z. Hashin. Analysis of cracked laminates: a variational approach. *Mechanics of Materials*, 4(2):121–136, 1985. ISSN 0167-6636. doi: 10.1016/0167-6636(85)90011-0.

[123] P. Haupt. On the mathematical modelling of material behavior in continuum mechanics. *Acta Mechanica*, 100:129–154, 1993. ISSN 0001-5970. doi: 10.1007/BF01174786.

[124] P. Haupt. Thermodynamics of Solids. In W. Muschik, editor, *Non-Equilibrium Thermodynamics with Application to Solids*, pages 65–138. Springer, 1993. doi: 10.1007/978-3-7091-4321-6_2.

[125] P. Haupt. *Continuum Mechanics and Theory of Materials*. Springer, Berlin Heidelberg, 2000. ISBN 978-3-662-04109-3.

[126] P. Haupt and C. Tsakmakis. On the application of dual variables in continuum mechanics. *Continuum Mechanics and Thermodynamics*, 1:165–196, 1989. ISSN 0935-1175. doi: 10.1007/BF01171378.

[127] T. Heimes. *Finite Thermoviskoelastizität*. Forschungs- und Seminarbericht 1/04, Universität der Bundeswehr München, Neubiberg, 2004.

[128] H. D. Hidallana-Gamage, D. P. Thambiratnam, and N. J. Perera. Numerical modelling and analysis of the blast performance of laminated glass panels and the influence of material parameters. *Engineering Failure Analysis*, 45:65–84, 2014. ISSN 1350-6307. doi: 10.1016/j.engfailanal.2014.06.013.

[129] A. Hillerborg, M. Modéer, and P.-E. Petersson. Analysis of crack formation and crack growth in concrete by means of fracture mechanics and finite elements. *Cement and Concrete Research*, 6(6):773–781, 1976. ISSN 0008-8846. doi: 10.1016/0008-8846(76)90007-7.

[130] G. A. Holzapfel. On large strain viscoelasticity: continuum formulation and finite element applications to elastomeric structures. *International Journal for Numerical Methods in Engineering*, 39(22):3903–3926, 1996. ISSN 0029-5981. doi: 10.1002/(SICI)1097-0207(19961130)39:22<3903::AID-NME34>3.0.CO;2-C.

[131] G. A. Holzapfel. *Nonlinear solid mechanics: a continuum approach for engineering science*. Wiley & Sons, Ltd., Chichester, United Kingdon, 2000. ISBN 978-0-471-82319-3.

[132] G. A. Holzapfel and J. C. Simo. A new viscoelastic constitutive model for continuous media at finite thermomechanical changes. *International Journal of Solids and Structures*, 33(20-22):3019–3034, 1996. ISSN 0020-7683. doi: 10.1016/0020-7683(95)00263-4.

[133] M. S. Hoo Fatt and X. Ouyang. Three-dimensional constitutive equations for Styrene Butadiene Rubber at high strain rates. *Mechanics of Materials*, 40(1-2):1–16, 2008. ISSN 0167-6636. doi: 10.1016/j.mechmat.2007.06.002.

[134] P. A. Hooper, B. R. K. Blackman, and J. P. Dear. The mechanical behaviour of poly(vinyl butyral) at different strain magnitudes and strain rates. *Journal of Materials Science*, 47:3564–3576, 2012. ISSN 0022-2461. doi: 10.1007/s10853-011-6202-4.

[135] P. A. Hooper, R. A. M. Sukhram, B. R. K. Blackman, and J. P. Dear. On the blast resistance of laminated glass. *International Journal of Solids and Structures*, 49(6):899–918, 2012. ISSN 0020-7683. doi: 10.1016/j.ijsolstr.2011.12.008.

[136] ISO 6721-11:2019-06. Plastics - Determination of dynamic mechanical properties - Part 11: Glass transition temperature.

[137] ISO 6721-4:2019-05. Plastics - Determination of dynamic mechanical properties - Part 4: Tensile vibration - Non-resonance method.

[138] ISO 7500-1:2018-02. Metallic materials - Calibration and verification of static uniaxial testing machines - Part 1: Tension/compression testing machines - Calibration and verification of the force-measuring system.

[139] ISO 9513:2012-12. Metallic materials - Calibration of extensometer systems used in uniaxial testing.

[140] R. Iwasaki and C. Sato. The influence of strain rate on the interfacial fracture toughness between PVB and laminated glass. *Journal de Physique IV (Proceedings)*, 134:1153–1158, 2006. ISSN 1764-7177. doi: 10.1051/jp4:2006134176.

[141] A. Jagota, S. J. Bennison, and C. A. Smith. Analysis of a compressive shear test for adhesion between elastomeric polymers and rigid substrates. *International Journal of Fracture*, 104:105–130, 2000. ISSN 0376-9429. doi: 10.1023/A:1007617102311.

[142] F. Jarre and J. Stoer. *Optimierung*. Springer, Berlin Heidelberg, 2004. ISBN 978-3-642-18785-8.

[143] G. Jaumann. Elektromagnetische Vorgänge in bewegten Medien. *Annalen der Physik*, 324(5):881–917, 1906. ISSN 0003-3804. doi: 10.1002/andp.19063240502.

[144] S. Ji and J. Karlovšek. Calibration and uniqueness analysis of microparameters for DEM cohesive granular material. *International Journal of Mining Science and Technology*, 32 (1):121–136, 2022. ISSN 2095-2686. doi: 10.1016/j.ijmst.2021.11.003.

[145] JIS K 7113:1995. Testing method for tensile properties of plastics.

[146] K. W. Johansen. *Yield-line theory*. Cement and Concrete Association, London, 1962.

[147] J. Johnsen, A. H. Clausen, F. Grytten, A. Benallal, and O. S. Hopperstad. A thermo-elasto-viscoplastic constitutive model for polymers. *Journal of the Mechanics and Physics of Solids*, 124:681–701, 2019. ISSN 0022-5096. doi: 10.1016/j.jmps.2018.11.018.

[148] G. R. Johnson and W. H. Cook. Fracture characteristics of three metals subjected to various strains, strain rates, temperatures and pressures. *Engineering Fracture Mechanics*, 21(1):31–48, 1985. ISSN 0013-7944. doi: 10.1016/0013-7944(85)90052-9.

[149] C. Justine. *Zum Materialverhalten von Mineralvlies: Experimente, Modellbildung und Berechnung*. Berichte des Instituts für Mechanik. Kassel University Press, Kassel, 2008. ISBN 978-3-89958-435-6.

[150] L. M. Kachanov. *Introduction to continuum damage mechanics*. Springer Science+Business Media, Dordrecht, 1986. ISBN 978-90-247-3319-4.

[151] M. Kaliske and G. Heinrich. An Extended Tube-Model for Rubber Elasticity: Statistical-Mechanical Theory and Finite Element Implementation. *Rubber Chemistry and Technology*, 72(4):602–632, 1999. ISSN 0035-9475. doi: 10.5254/1.3538822.

[152] J. T. Knight, A. A. El-Sisi, A. H. Elbelbisi, M. Newberry, and H. A. Salim. Mechanical Behavior of Laminated Glass Polymer Interlayer Subjected to Environmental Effects. *Polymers*, 14(23):5113, 2022. ISSN 2073-4360. doi: 10.3390/polym14235113.

[153] S. L. Koh and A. C. Eringen. On the foundations of non-linear thermo-viscoelasticity. *International Journal of Engineering Science*, 1(2):199–229, 1963. ISSN 0020-7225. doi: 10.1016/0020-7225(63)90034-x.

[154] S. Kolling, P. A. Du Bois, D. J. Benson, and W. W. Feng. A tabulated formulation of hyperelasticity with rate effects and damage. *Computational Mechanics*, 40:885–899, 2007. ISSN 0178-7675. doi: 10.1007/s00466-006-0150-x.

[155] V. A. Kolupaev. *Equivalent stress concept for limit state analysis*. Springer International Publishing, Basel, 2018. ISBN 978-3-319-73048-6.

[156] N. Koprowski-Theiß, M. Johlitz, and S. Diebels. Modelling of a Cellular Rubber with Nonlinear Viscosity Functions. *Experimental Mechanics*, 51:749–765, 2011. ISSN 0014-4851. doi: 10.1007/s11340-010-9376-9.

[157] A. Kott. *Zum Trag- und Resttragverhalten von Verbundsicherheitsglas*. IBK-Bericht. vdf Hochschulverlag, Zürich, 2007. ISBN 978-3-7281-3131-7.

[158] A. Kott and T. Vogel. *Versuche zum Trag- und Resttragverhalten von Verbundsicherheitsglas*. IBK-Bericht. vdf Hochschulverlag, Zürich, 2006. ISBN 978-3-7281-3073-0.

[159] M. A. Kraus. *Machine Learning Techniques for the Material Parameter Identification of Laminated Glass in the Intact and Post-Fracture State*. Dissertation, Universität der Bundeswehr München, Neubiberg, 2019.

[160] M. A. Kraus and M. Drass. Artificial intelligence for structural glass engineering applications — overview, case studies and future potentials. *Glass Structures & Engineering*, 5:247–285, 2020. ISSN 2363-5142. doi: 10.1007/s40940-020-00132-8.

[161] M. A. Kraus and M. Niederwald. Generalized Collocation Method using Stiffness Matrices in the Context of the Theory of Linear Viscoelasticity (GUSTL): Technische Mechanik; 37; 1; 82-106; ISSN 2199-9244 / Technische Mechanik; 37; 1; 82-106; ISSN 2199-9244. *Technische Mechanik - European Journal of Engineering Mechanics*, 37(1):82–106, 2017. ISSN 0232-3869. doi: 10.24352/UB.OVGU-2017-084.

[162] M. A. Kraus, M. Schuster, J. K. Kuntsche, G. Siebert, and J. Schneider. Parameter identification methods for visco-and hyperelastic material models. *Glass Structures & Engineering*, 2:147–167, 2017. ISSN 2363-5142. doi: 10.1007/s40940-017-0042-9.

[163] M. A. Kraus, M. Schuster, M. Botz, J. Schneider, and G. Siebert. Thermorheologische Untersuchungen der Verbundglaszwischenschichten PVB und EVA. *ce/papers*, 2(1):159–172, 2018. ISSN 2509-7075. doi: 10.1002/cepa.639.

[164] D. V. Kubair and P. H. Geubelle. Comparative analysis of extrinsic and intrinsic cohesive models of dynamic fracture. *International Journal of Solids and Structures*, 40(15):3853–3868, 2003. ISSN 0020-7683. doi: 10.1016/s0020-7683(03)00171-9.

[165] J. K. Kuntsche. *Mechanisches Verhalten von Verbundglas unter zeitabhängiger Belastung und Explosionsbeanspruchung: Mechanical behaviour of laminated glass under time-dependent and explosion loading.* Mechanik, Werkstoffe und Konstruktion im Bauwesen. Springer Vieweg, Berlin Heidelberg, 2015. ISBN 978-3-662-48830-0.

[166] M. Larcher, G. Solomos, F. Casadei, and N. Gebbeken. Experimental and numerical investigations of laminated glass subjected to blast loading. *International Journal of Impact Engineering*, 39(1):42–50, 2012. ISSN 0734-743X. doi: 10.1016/j.ijimpeng.2011.09.006.

[167] E. H. Lee. Elastic-Plastic Deformation at Finite Strains. *Journal of Applied Mechanics*, 36(1):1–6, 1969. ISSN 0021-8936. doi: 10.1115/1.3564580.

[168] Z. Lei and M. Zang. An approach to combining 3D discrete and finite element methods based on penalty function method. *Computational Mechanics*, 46:609–619, 2010. ISSN 0178-7675. doi: 10.1007/s00466-010-0502-4.

[169] A. Lion. A constitutive model for carbon black filled rubber: Experimental investigations and mathematical representation. *Continuum Mechanics and Thermodynamics*, 8:153–169, 1996. ISSN 0935-1175. doi: 10.1007/BF01181853.

[170] A. Lion. A physically based method to represent the thermo-mechanical behaviour of elastomers. *Acta Mechanica*, 123:1–25, 1997. ISSN 0001-5970. doi: 10.1007/BF01178397.

[171] A. Lion. Constitutive modelling in finite thermoviscoplasticity: a physical approach based on nonlinear rheological models. *International Journal of Plasticity*, 16(5):469–494, 2000. ISSN 0749-6419. doi: 10.1016/S0749-6419(99)00038-8.

[172] B. Liu, Y. Sun, Y. Li, Y. Wang, D. Ge, and J. Xu. Systematic experimental study on mechanical behavior of PVB (polyvinyl butyral) material under various loading conditions. *Polymer Engineering & Science*, 52(5):1137–1147, 2012. ISSN 0032-3888. doi: 10.1002/pen.22175.

[173] B. Liu, T. Xu, X. Xu, Y. Wang, Y. Sun, and Y. Li. Energy absorption mechanism of polyvinyl butyral laminated windshield subjected to head impact: Experiment and numerical simulations. *International Journal of Impact Engineering*, 90:26–36, 2016. ISSN 0734-743X. doi: 10.1016/j.ijimpeng.2015.11.010.

[174] F. J. Lockett. *Nonlinear viscoelastic solids.* Academic Press, London New York, 1972. ISBN 978-0124543508.

[175] J. Lubliner. On the structure of the rate equations of materials with internal variables. *Acta Mechanica*, 17:109–119, 1973. ISSN 0001-5970. doi: 10.1007/BF01260883.

[176] J. Lubliner. A model of rubber viscoelasticity. *Mechanics Research Communications*, 12 (2):93–99, 1985. ISSN 0093-6413. doi: 10.1016/0093-6413(85)90075-8.

[177] J E. Mark. *Physical properties of polymers handbook*. Springer, New York London, 2007. ISBN 978-0387312354.

[178] M. Martín, X. Centelles, A. Solé, C. Barreneche, A. I. Fernández, and L. F. Cabeza. Polymeric interlayer materials for laminated glass: A review. *Construction and Building Materials*, 230:116897, 2020. ISSN 0950-0618. doi: 10.1016/j.conbuildmat.2019.116897.

[179] G. A. Maugin and W. Muschik. Thermodynamics with Internal Variables. Part I. General Concepts. *Journal of non-equilibrium thermodynamics*, 19:217–249, 1994. ISSN 1437-4358. doi: 10.1515/jnet.1994.19.3.217.

[180] P. Middendorf. *Geometrisch nichtlineare Viskoelastizität*. Forschungs- und Seminarbericht 2/01, Universität der Bundeswehr München, Neubiberg, 2001.

[181] C. Miehe. Aspects of the formulation and finite element implementation of large strain isotropic elasticity. *International Journal for Numerical Methods in Engineering*, 37(12): 1981–2004, 1994. ISSN 0029-5981. doi: 10.1002/nme.1620371202.

[182] N. Moës, J. Dolbow, and T. Belytschko. A finite element method for crack growth without remeshing. *International Journal for Numerical Methods in Engineering*, 46 (1):131–150, 1999. ISSN 0029-5981. doi: 10.1002/(SICI)1097-0207(19990910)46:1<131::AID-NME726>3.0.CO;2-J.

[183] M. Mooney. A Theory of Large Elastic Deformation. *Journal of Applied Physics*, 11(9): 582–592, 1940. ISSN 0021-8979. doi: 10.1063/1.1712836.

[184] A. D. Mulliken and M. C. Boyce. Mechanics of the rate-dependent elastic–plastic deformation of glassy polymers from low to high strain rates. *International Journal of Solids and Structures*, 43(5):1331–1356, 2006. ISSN 0020-7683. doi: 10.1016/j.ijsolstr.2005.04.016.

[185] S. Muralidhar, A. Jagota, S. J. Bennison, and S. Saigal. Mechanical behaviour in tension of cracked glass bridged by an elastomeric ligament. *Acta Materialia*, 48(18-19):4577–4588, 2000. ISSN 1359-6454. doi: 10.1016/S1359-6454(00)00244-5.

[186] A. Needleman. A Continuum Model for Void Nucleation by Inclusion Debonding. *Journal of Applied Mechanics*, 54(3):525–531, 1987. ISSN 0021-8936. doi: 10.1115/1.3173064.

[187] J. H. Nielsen. Remaining stress-state and strain-energy in tempered glass fragments. *Glass Structures & Engineering*, 2:45–56, 2017. ISSN 2363-5142. doi: 10.1007/s40940-016-0036-z.

[188] J. H. Nielsen and M. Bjarrum. Deformations and strain energy in fragments of tempered glass: experimental and numerical investigation. *Glass Structures & Engineering*, 2:133–146, 2017. ISSN 2363-5142. doi: 10.1007/s40940-017-0043-8.

[189] J. H. Nielsen, J. F. Olesen, and H. Stang. The Fracture Process of Tempered Soda-Lime-Silica Glass. *Experimental Mechanics*, 49:855–870, 2009. ISSN 0014-4851. doi: 10.1007/s11340-008-9200-y.

[190] J. H. Nielsen, J. Schneider, and M. A. Kraus. *The In-plane Expansion of Fractured Thermally Pre-stressed Glass Panes: -An equivalent temperature difference model for engineering glass design*, volume 327. 2022. doi: 10.1016/j.conbuildmat.2022.126849.

[191] W. Noll. *On the foundation of the mechanics of continuous media.* Technical report no. 17, Carnegie Institute of Technology, Pittsburgh, 1957.

[192] W. Noll. A mathematical theory of the mechanical behavior of continuous media. *Archive for Rational Mechanics and Analysis*, 2:197–226, 1958. ISSN 0003-9527. doi: 10.1007/BF00277929.

[193] D. Offereins, A. Pauli, and G. Siebert. Mechanical Performance Of Liquid Cold-Poured Interlayer Adhesives In Comparison To PVB, EVA, And Ionomers. *Glass Structures & Engineering*, 9:569–586, 2024. ISSN 2363-5142. doi: 10.1007/s40940-024-00274-z.

[194] R. W. Ogden. Large deformation isotropic elasticity – on the correlation of theory and experiment for incompressible rubberlike solids. *Proceedings of the Royal Society of London. A, Mathematical and Physical Sciences*, 326(1567):565–584, 1972. ISSN 0080-4630. doi: 10.1098/rspa.1972.0026.

[195] R. W. Ogden. Volume changes associated with the deformation of rubber-like solids. *Journal of the Mechanics and Physics of Solids*, 24(6):323–338, 1976. ISSN 0022-5096. doi: 10.1016/0022-5096(76)90007-7.

[196] J. G. Oldroyd. On the formulation of rheological equations of state. *Proceedings of the Royal Society of London. A, Mathematical and Physical Sciences*, 200(1063):523–541, 1950. ISSN 0080-4630. doi: 10.1098/rspa.1950.0035.

[197] K. Osnes, J. K. Holmen, O. S. Hopperstad, and T. Børvik. Fracture and fragmentation of blast-loaded laminated glass: An experimental and numerical study. *International Journal of Impact Engineering*, 132:103334, 2019. ISSN 0734-743X. doi: 10.1016/j.ijimpeng.2019.103334.

[198] H. Parisch. *Festkörper-Kontinuumsmechanik: Von den Grundgleichungen zur Lösung mit finiten Elementen.* Vieweg+Teubner, Wiesbaden, 2003. ISBN 978-3-519-00434-9.

[199] A. Pauli and G. Siebert. Simplified approach for modeling standard PVB at large deformations and long-term loading. *Glass Structures & Engineering*, 9:59–73, 2024. ISSN 2363-5142. doi: 10.1007/s40940-023-00236-x.

[200] A. Pauli and G. Siebert. Investigations on the finite strain behavior of standard PVB: experiment and modeling. *Glass Structures & Engineering*, 9:587–606, 2024. ISSN 2363-5142. doi: 10.1007/s40940-024-00247-2.

[201] A. Pauli, M. A. Kraus, and G. Siebert. Experimental and numerical investigations on glass fragments: shear-frame testing and calibration of Mohr–Coulomb plasticity model. *Glass Structures & Engineering*, 6:65–87, 2021. ISSN 2363-5142. doi: 10.1007/s40940-020-00143-5.

[202] J. Pelfrene, S. van Dam, and W. van Paepegem. Numerical analysis of the peel test for characterisation of interfacial debonding in laminated glass. *International Journal of Adhesion and Adhesives*, 62:146–153, 2015. ISSN 0143-7496. doi: 10.1016/j.ijadhadh.2015.07.010.

[203] J. Pelfrene, J. K. Kuntsche, S. van Dam, W. van Paepegem, and J. Schneider. Critical assessment of the post-breakage performance of blast loaded laminated glazing: Experiments and simulations. *International Journal of Impact Engineering*, 88:61–71, 2016. ISSN 0734-743X. doi: 10.1016/j.ijimpeng.2015.09.008.

[204] J. Pelfrene, S. van Dam, R. Sevenois, F. Gilabert, and W. van Paepegem. Fracture Simulation of Structural Glass by Element Deletion in Explicit FEM. *Challenging Glass Conference Proceedings*, 5:439–454, 2016. ISSN 2589-8019. doi: 10.7480/cgc.5.2270.

[205] Y. Peng, J. Yang, C. Deck, and R. Willinger. Finite element modeling of crash test behavior for windshield laminated glass. *International Journal of Impact Engineering*, 57:27–35, 2013. ISSN 0734-743X. doi: 10.1016/j.ijimpeng.2013.01.010.

[206] M. Polanco-Loria, A. H. Clausen, T. Berstad, and O. S. Hopperstad. Constitutive model for thermoplastics with structural applications. *International Journal of Impact Engineering*, 37(12):1207–1219, 2010. ISSN 0734-743X. doi: 10.1016/j.ijimpeng.2010.06.006.

[207] N. Pourmoghaddam and J. Schneider. Experimental investigation into the fragment size of tempered glass. *Glass Structures & Engineering*, 3:167–181, 2018. ISSN 2363-5142. doi: 10.1007/s40940-018-0062-0.

[208] N. Pourmoghaddam, M. A. Kraus, J. Schneider, and G. Siebert. Relationship between strain energy and fracture pattern morphology of thermally tempered glass for the prediction of the 2D macro-scale fragmentation of glass. *Glass Structures & Engineering*, 4: 257–275, 2019. ISSN 2363-5142. doi: 10.1007/s40940-018-00091-1.

[209] T. Pyttel, H. Liebertz, and J. Cai. Failure criterion for laminated glass under impact loading and its application in finite element simulation. *International Journal of Impact Engineering*, 38(4):252–263, 2011. ISSN 0734-743X. doi: 10.1016/j.ijimpeng.2010.10.035.

[210] R. Raghava, R. M. Caddell, and G. S. Y. Yeh. The macroscopic yield behaviour of polymers. *Journal of Materials Science*, 8:225–232, 1973. ISSN 0022-2461. doi: 10.1007/BF00550671.

[211] P. Rahul-Kumar, A. Jagota, S. J. Bennison, and S. Saigal. Cohesive element modeling of viscoelastic fracture: application to peel testing of polymers. *International Journal of Solids and Structures*, 37(13):1873–1897, 2000. ISSN 0020-7683. doi: 10.1016/S0020-7683(98)00339-4.

[212] P. Rahul-Kumar, A. Jagota, S. J. Bennison, and S. Saigal. Interfacial failures in a compressive shear strength test of glass/polymer laminates. *International Journal of Solids and Structures*, 37(48-50):7281–7305, 2000. ISSN 0020-7683. doi: 10.1016/S0020-7683(00)00199-2.

[213] T. Ree and H. Eyring. Theory of Non-Newtonian Flow. I. Solid Plastic System. *Journal of Applied Physics*, 26(7):793–800, 1955. ISSN 0021-8979. doi: 10.1063/1.1722098.

[214] S. Reese and S. Govindjee. A theory of finite viscoelasticity and numerical aspects. *International Journal of Solids and Structures*, 35(26-27):3455–3482, 1998. ISSN 0020-7683. doi: 10.1016/S0020-7683(97)00217-5.

[215] E. Riande, R. Diaz-Calleja, M. Prolongo, R. Masegosa, and C. Salom. *Polymer viscoelasticity: Stress and strain in practice*. CRC Press, Boca Raton, 1999. ISBN 978-0824779047.

[216] R. S. Rivlin. Large elastic deformations of isotropic materials. I. Fundamental concepts. *Philosophical Transactions of the Royal Society of London. A, Mathematical and Physical Sciences*, 240(822):459–490, 1948. ISSN 0080-4614. doi: 10.1098/rsta.1948.0002.

[217] R. S. Rivlin. Large elastic deformations of isotropic materials. II. Some uniqueness theorems for pure, homogeneous deformation. *Philosophical Transactions of the Royal Society of London. A, Mathematical and Physical Sciences*, 240(822):491–508, 1948. ISSN 0080-4614. doi: 10.1098/rsta.1948.0003.

[218] R. S. Rivlin. Large elastic deformations of isotropic materials. III. Some simple problems in cyclindrical polar co-ordinates. *Philosophical Transactions of the Royal Society of London. A, Mathematical and Physical Sciences*, 240(823):509–525, 1948. ISSN 0080-4614. doi: 10.1098/rsta.1948.0004.

[219] R. S. Rivlin. Large elastic deformations of isotropic materials IV. further developments of the general theory. *Philosophical Transactions of the Royal Society of London. A, Mathematical and Physical Sciences*, 241(835):379–397, 1949. ISSN 0080-4614. doi: 10.1098/rsta.1948.0024.

[220] P. L. Rosendahl, M. Drass, J. Felger, J. Schneider, and W. Becker. Equivalent strain failure criterion for multiaxially loaded incompressible hyperelastic elastomers. *International Journal of Solids and Structures*, 166:32–46, 2019. ISSN 0020-7683. doi: 10.1016/j.ijsolstr.2019.01.030.

[221] J. Rösler, H. Harders, and M. Bäker. *Mechanisches Verhalten der Werkstoffe, address = Wiesbaden, publisher = Springer Vieweg, isbn = 978-3-8348-2241-3.* 2012.

[222] A. Rühl, S. Kolling, and J. Schneider. Characterization and modeling of poly(methyl methacrylate) and thermoplastic polyurethane for the application in laminated setups. *Mechanics of Materials*, 113:102–111, 2017. ISSN 0167-6636. doi: 10.1016/j.mechmat.2017.07.018.

[223] R. A. Schapery. A Theory of Nonlinear Thermoviscoelasticity Based on Irreversible Thermodynamics. *Proceedings of the 5th U.S. National Congress of Applied Mechanics*, pages 511–530, 1966.

[224] R. A. Schapery. On the characterization of nonlinear viscoelastic materials. *Polymer Engineering & Science*, 9(4):295–310, 1969. ISSN 0032-3888. doi: 10.1002/pen.760090410.

[225] T. Scheffer. *Charakterisierung des nichtlinear-viskoelastischen Materialverhaltens gefüllter Elastomere.* Dissertation, Universität des Saarlandes, Homburg, 2016.

[226] T. Scheffer, F. Goldschmidt, and S. Diebels. Implementation of the strongly pronounced non-linear viscoelasticity of an incompressible filled rubber. *Technische Mechanik*, 35(2):119–132, 2015. ISSN 0232-3869. doi: 10.24352/UB.OVGU-2017-074.

[227] J. Schneider, J. K. Kuntsche, S. Schula, F. Schneider, and J.-D. Wörner. *Glasbau: Grundlagen, Berechnung, Konstruktion.* Springer Vieweg, Berlin Heidelberg, 2016. ISBN 978-3-540-68927-0.

[228] J. Schröder, A. Lion, and M. Johlitz. Numerical studies on the self-heating phenomenon of elastomers based on finite thermoviscoelasticity. *Journal of Rubber Research*, 24:237–248, 2021. ISSN 1511-1768. doi: 10.1007/s42464-021-00089-5.

[229] S. Schula. *Charakterisierung der Kratzanfälligkeit von Gläsern im Bauwesen*. Mechanik, Werkstoffe und Konstruktion im Bauwesen. Springer Vieweg, Berlin, Heidelberg, 2015. ISBN 978-3-662-47781-6.

[230] C. Schuler. *Einfluss des Materialverhaltens von Polyvinylbutyral auf das Tragverhalten von Verbundsicherheitsglas in Abhängigkeit von Temperatur und Belastung*. Dissertation, Technische Universität München, München, 2003.

[231] M. Schuster. *Characterization of Laminated Safety Glass Interlayers: Thermorheology, Crystallinity and Viscoelasticity*. Mechanik, Werkstoffe und Konstruktion im Bauwesen. Springer Vieweg, Wiesbaden, 2023. ISBN 978-3-658-39820-0.

[232] M. Schuster, J. Schneider, and T. an Nguyen. Investigations on the execution and evaluation of the Pummel test for polyvinyl butyral based interlayers. *Glass Structures & Engineering*, 5:371–396, 2020. ISSN 2363-5142. doi: 10.1007/s40940-020-00120-y.

[233] M. Schuster, K. Thiele, and J. Schneider. Investigations on the viscoelastic material behaviour and linearity limits of PVB. *ce/papers*, 4(6):207–223, 2021. ISSN 2509-7075. doi: 10.1002/cepa.1633.

[234] F. R. Schwarzl. *Polymermechanik: Struktur und mechanisches Verhalten von Polymeren*. Springer, Berlin Heidelberg, 1990. ISBN 978-3-540-51965-2.

[235] K. Sedlan. *Viskoelastisches materialverhalten von elastomerwerkstoffen: Experimentelle untersuchung und modellbildung*. Dissertation, Universität Gesamthochschule Kassel, Kassel, 2001.

[236] K. Sedlan and P. Haupt. Nichtlineare Viskoelastizität von gummiartigen Werkstoffen: Experimentelle Untersuchung, Modellierung und Identifikation. *Technische Mechanik - European Journal of Engineering Mechanics*, 19(4):269–278, 1999. ISSN 0232-3869.

[237] M. Seshadri, S. J. Bennison, A. Jagota, and S. Saigal. Mechanical response of cracked laminated plates. *Acta Materialia*, 50(18):4477–4490, 2002. ISSN 1359-6454. doi: 10.1016/S1359-6454(02)00255-0.

[238] Y. Sha, C. Y. Hui, E. J. Kramer, P. D. Garrett, and J. W. Knapczyk. Analysis of adhesion and interface debonding in laminated safety glass. *Journal of Adhesion Science and Technology*, 11(1):49–63, 1997. ISSN 0169-4243. doi: 10.1163/156856197X01010.

[239] G. Siebert and I. Maniatis. *Tragende Bauteile aus Glas - Grundlagen, Konstruktion, Bemessung, Beispiele*. Ernst & Sohn, Berlin, 2012. ISBN 978-3-433-02914-5.

[240] J. C. Simo. On a fully three-dimensional finite-strain viscoelastic damage model: Formulation and computational aspects. *Computer Methods in Applied Mechanics and Engineering*, 60(2):153–173, 1987. ISSN 0045-7825. doi: 10.1016/0045-7825(87)90107-1.

[241] J. C. Simo and T. J. R. Hughes. *Computational inelasticity*. Springer, New York, 1998. ISBN 978-0-387-97520-7.

[242] G. F. Smith and R. S. Rivlin. The Strain-Energy Function for Anisotropic Elastic Materials. *Transactions of the American Mathematical Society*, 88:175–193, 1958. ISSN 0002-9947. doi: 10.1090/S0002-9947-1958-0095618-2.

[243] J.-H. Song, H. Wang, and T. Belytschko. A comparative study on finite element methods for dynamic fracture. *Computational Mechanics*, 42:239–250, 2008. ISSN 0178-7675. doi: 10.1007/s00466-007-0210-x.

[244] A. J. M. Spencer. *Continuum mechanics*. Dover Publications, Inc., 2004. ISBN 978-0486139470.

[245] G. Tamman. *Der Glaszustand*. Leopold Voß, Leipzig, 1933.

[246] M. Teotia and R. K. Soni. Applications of finite element modelling in failure analysis of laminated glass composites: A review. *Engineering Failure Analysis*, 94:412–437, 2018. ISSN 1350-6307. doi: 10.1016/j.engfailanal.2018.08.016.

[247] M. Timmel, S. Kolling, Peter Osterrieder, and P. A. Du Bois. A finite element model for impact simulation with laminated glass. *International Journal of Impact Engineering*, 34 (8):1465–1478, 2007. ISSN 0734-743X. doi: 10.1016/j.ijimpeng.2006.07.008.

[248] L. R. G. Treloar. *The physics of rubber elasticity*. Oxford University Press Inc., 1975. ISBN 978-0-19-857027-1.

[249] L. R.G. Treloar. The elasticity of a network of long-chain molecules - I. *Transactions of the Faraday Society*, 39:36–41, 1942.

[250] L. R.G. Treloar. The elasticity of a network of long-chain molecules - II. *Transactions of the Faraday Society*, 39:241–246, 1943.

[251] L. R.G. Treloar. Stress-strain data for vulcanized rubber under various types of deformation. *Rubber Chemistry and Technology*, 17(4):813–825, 1944. ISSN 1943-4804. doi: 10.5254/1.3546701.

[252] L. R.G. Treloar. The elasticity of a network of long-chain molecules - III. *Transactions of the Faraday Society*, 42:83–94, 1946.

[253] C. Truesdell. The Mechanical Foundations of Elasticity and Fluid Dynamics. *Journal of Rational Mechanics and Analysis*, 1:125–300, 1952. ISSN 0022-2518. doi: 10.1512/iumj.1952.1.51005.

[254] C. Truesdell. A theorem on the isotropy groups of a hyperelastic material. *Proceedings of the National Academy of Sciences of the United States of America*, 52(4):1081–1083, 1964. ISSN 0027-8424. doi: 10.1073/pnas.52.4.1081.

[255] C. Truesdell and W. Noll. The Non-Linear Field Theories of Mechanics. In S. Flügge, editor, *Encyclopedia of Physics*, Principles of Classical Mechanics and Field Theory, pages 1–579. Springer, 1965. doi: 10.1007/978-3-662-10388-3_1.

[256] C. Truesdell and R. Toupin. The Classical Field Theories. In S. Flügge, editor, *Encyclopedia of Physics*, Principles of Classical Mechanics and Field Theory, pages 226–858. Springer, 1960. doi: 10.1007/978-3-642-45943-6_2.

[257] N. W. Tschoegl. *The Phenomenological Theory of Linear Viscoelastic Behavior: An Introduction*. Springer, Berlin Heidelberg, 1989. ISBN 978-3-642-73604-9.

[258] Z. Ugray, L. Lasdon, J. Plummer, F. Glover, J. Kelly, and R. Martí. Scatter Search and Local NLP Solvers: A Multistart Framework for Global Optimization. *INFORMS Journal on Computing*, 19(3):328–340, 2007. doi: 10.1287/ijoc.1060.0175.

[259] K. C. Valanis. Thermodynamics of Large Viscoelastic Deformations. *Journal of Mathematics and Physics*, 45(1-4):197–212, 1966. doi: 10.1002/sapm1966451197.

[260] M. J. van den Bosch, P.J.G. Schreurs, and M.G.D. Geers. An improved description of the exponential Xu and Needleman cohesive zone law for mixed-mode decohesion. *Engineering Fracture Mechanics*, 73(9):1220–1234, 2006. ISSN 0013-7944. doi: 10.1016/j.engfracmech.2005.12.006.

[261] F. T. Wall. Statistical Thermodynamics of Rubber. *The Journal of Chemical Physics*, 10(2):132–134, 1942. ISSN 0021-9606. doi: 10.5254/1.3543134.

[262] R. A. Waltz, J. L. Morales, J. Nocedal, and D. Orban. An interior algorithm for nonlinear optimization that combines line search and trust region steps. *Mathematical Programming*, 107:391–408, 2006. ISSN 0025-5610. doi: 10.1007/s10107-004-0560-5.

[263] M. C. Wang and E. Guth. Statistical Theory of Networks of Non-Gaussian Flexible Chains. *The Journal of Chemical Physics*, 20(7):1144–1157, 1952. ISSN 0021-9606. doi: 10.1063/1.1700682.

[264] X. Wang, J. Yang, F. Wang, Q. Liu, and H. Xu. Simulating the impact damage of laminated glass considering mixed mode delamination using FEM/DEM. *Composite Structures*, 202:1239–1252, 2018. ISSN 0263-8223. doi: 10.1016/j.compstruct.2018.05.127.

[265] X. Wang, J. Yang, Z. Pan, F. Wang, Y. Meng, and Y. Zhu. Exploratory investigation into the post-fracture model of laminated tempered glass using combined Voronoi-FDEM approach. *International Journal of Mechanical Sciences*, 190:105989, 2021. ISSN 0020-7403. doi: 10.1016/j.ijmecsci.2020.105989.

[266] F. Wellershoff, M. Illguth, and T. van der Horst. Tragverhalten von gebrochenem Verbundsicherheitsglas aus Einscheibensicherheitsglas im biaxialen Spannungszustand. *ce/papers*, 4(5):329–344, 2021. ISSN 2509-7075. doi: 10.1002/cepa.1616.

[267] M. L. Williams, R. F. Landel, and J. D. Ferry. The Temperature Dependence of Relaxation Mechanisms in Amorphous Polymers and Other Glass-forming Liquids. *Journal of the American Chemical Society*, 77(14):3701–3707, 1955. ISSN 0002-7863. doi: 10.1021/ja01619a008.

[268] J. Xu, Y. Li, X. Chen, Y. Yan, D. Ge, M. Zhu, and B. Liu. Characteristics of windshield cracking upon low-speed impact: Numerical simulation based on the extended finite element method. *Computational Materials Science*, 48(3):582–588, 2010. ISSN 0927-0256. doi: 10.1016/j.commatsci.2010.02.026.

[269] W. Xu, M. Zang, and W. Gao. Adaptive combined DE/FE algorithm for brittle fracture of plane stress problems. *Computational Mechanics*, 54:535–546, 2014. ISSN 0178-7675. doi: 10.1007/s00466-014-1004-6.

[270] X. Xu, B. Liu, Y. Wang, and Y. Li. Research on Temperature and Strain Rate Dependent Viscoelastic Response of Polyvinyl Butaral Film. *SAE International Journal of Materials and Manufacturing*, 9(3):788–793, 2016. ISSN 1946-3979. doi: 10.4271/2016-01-0519.

[271] X. Xu, J. Xu, J. Chen, P. Li, B. Liu, and Y. Li. Investigation of dynamic multi-cracking behavior in PVB laminated glass plates. *International Journal of Impact Engineering*, 100:62–74, 2017. ISSN 0734-743X. doi: 10.1016/j.ijimpeng.2016.10.013.

[272] X. Xu, Di W., M. Zang, and S. Chen. Development of an intrinsic solid-shell cohesive zone model for impact fracture of windshield laminated glass. *International Journal of Impact Engineering*, 163:104187, 2022. ISSN 0734-743X. doi: 10.1016/j.ijimpeng.2022.104187.

[273] K. Yano. *Theory of lie derivatives and its applications*. Dover Publications, Inc., Mineola, New York, 2020. ISBN 978-0486842097.

[274] O. H. Yeoh. Characterization of Elastic Properties of Carbon-Black-Filled Rubber Vulcanizates. *Rubber Chemistry and Technology*, 63(5):792–805, 1990. ISSN 0035-9475. doi: 10.5254/1.3538289.

[275] M. Y. Zang, Z. Lei, and S. F. Wang. Investigation of impact fracture behavior of automobile laminated glass by 3D discrete element method. *Computational Mechanics*, 41: 73–83, 2007. ISSN 0178-7675. doi: 10.1007/s00466-007-0170-1.

[276] S. Zaremba. Le principe des mouvements relatifs et les equations de la mecanique physique. *Bulletin International Académie Science Cracovie*, pages 614–621, 1903.

[277] X. Zhang, H. Hao, and G. Ma. Parametric study of laminated glass window response to blast loads. *Engineering Structures*, 56:1707–1717, 2013. ISSN 0141-0296. doi: 10.1016/j.engstruct.2013.08.007.

[278] S. Zhao, L. R. Dharani, L. Chai, and S. D. Barbat. Analysis of damage in laminated automotive glazing subjected to simulated head impact. *Engineering Failure Analysis*, 13 (4):582–597, 2006. ISSN 1350-6307. doi: 10.1016/j.engfailanal.2004.12.038.

[279] H. Zhu, H. Ou, and A. Popov. A new phenomenological constitutive model for thermoplastics. *Mechanics of Materials*, 157:103817, 2021. ISSN 0167-6636. doi: 10.1016/j.mechmat.2021.103817.

[280] O. C. Zienkiewicz and Y. K. Cheung. *The finite element in structural and continuum mechanics*. McGraw-Hill Publishing Company Limited, London, 1967.

A. Experimental Results

A.1. Control Tests

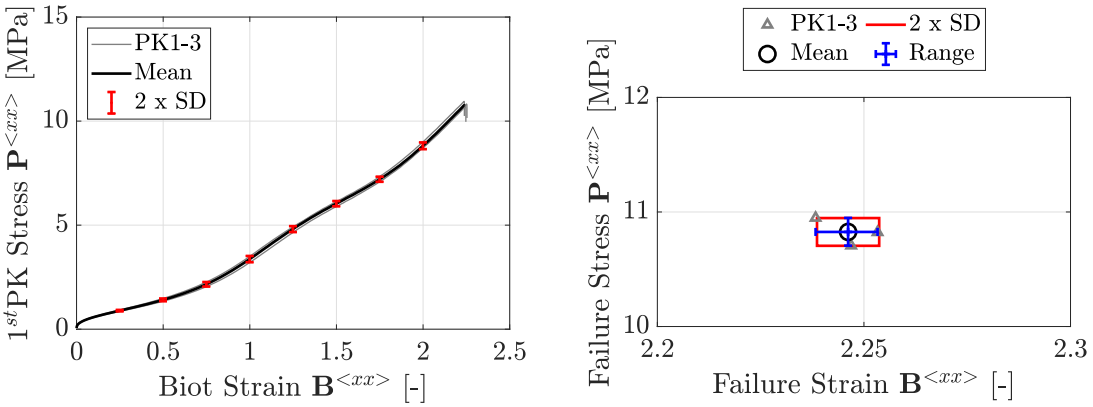

Figure A.1.: Tension until breakage - $\dot{\mathbf{B}}^{<xx>} = 0.01$ [1/s]; with attached clamp

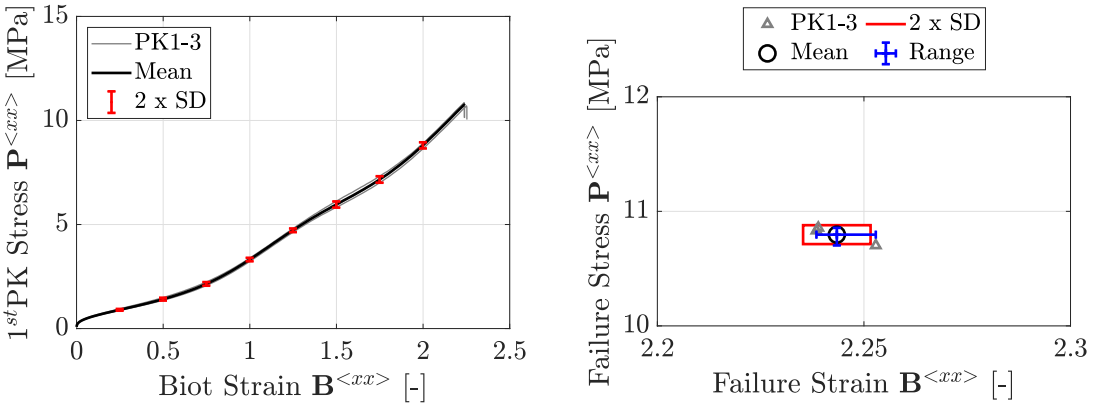

Figure A.2.: Tension until breakage - $\dot{\mathbf{B}}^{<xx>} = 0.01$ [1/s]; without attached clamp

A.2. Tension until Failure

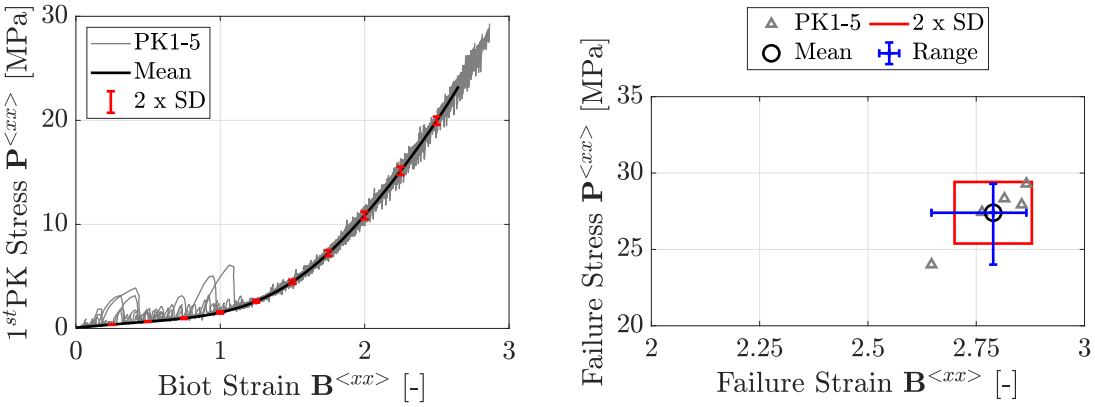

Figure A.3.: Tension until failure - $\dot{\mathbf{B}}^{<xx>} = 0.001$ [1/s]

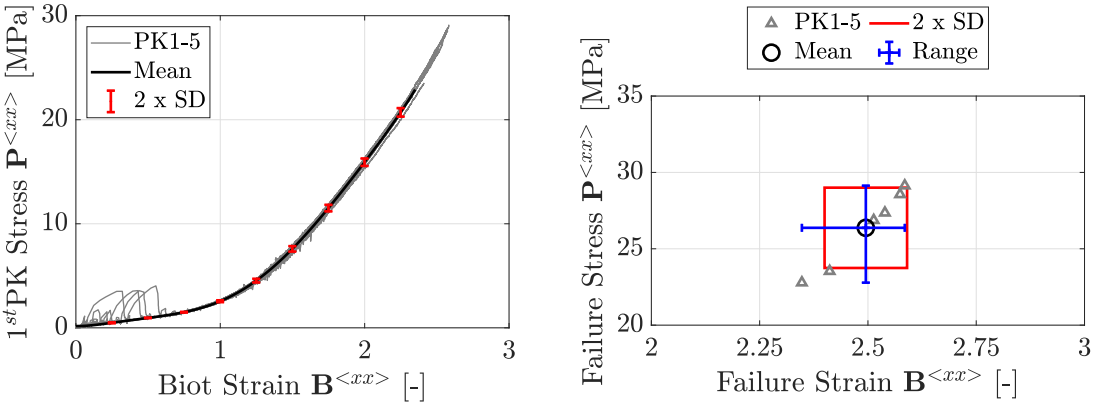

Figure A.4.: Tension until failure - $\dot{\mathbf{B}}^{<xx>} = 0.003$ [1/s]

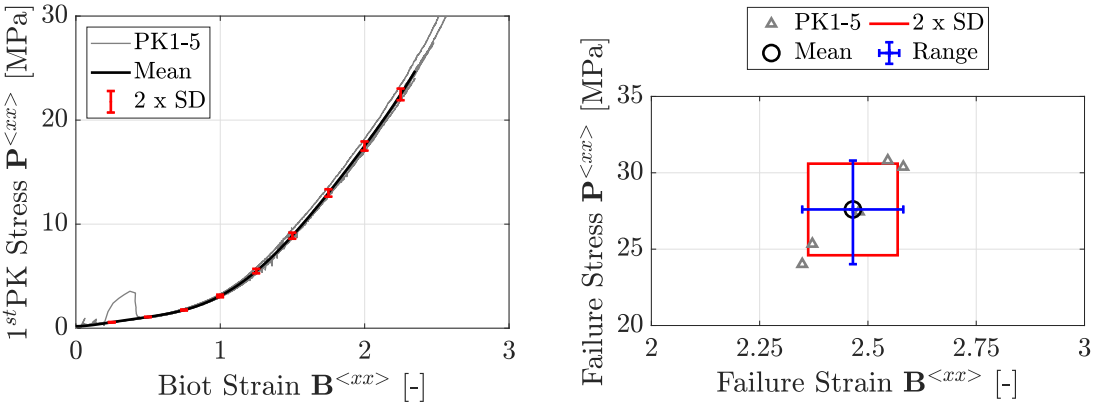

Figure A.5.: Tension until failure - $\dot{\mathbf{B}}^{<xx>} = 0.005$ [1/s]

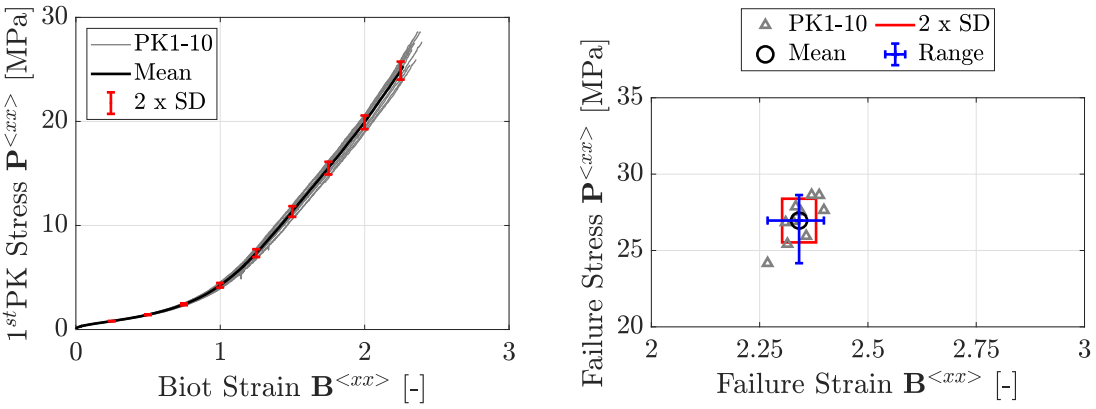

Figure A.6.: Tension until failure - $\dot{\mathbf{B}}^{<xx>} = 0.01$ [1/s]

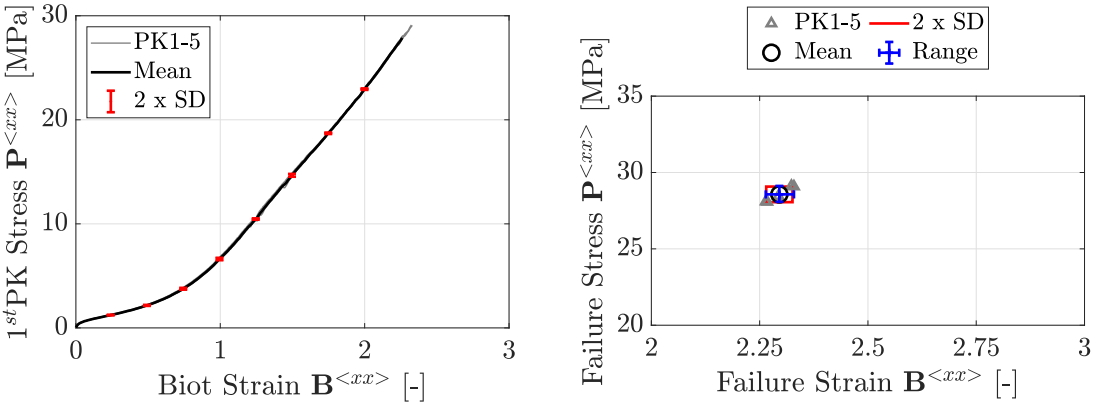

Figure A.7.: Tension until failure - $\dot{\mathbf{B}}^{<xx>} = 0.03$ [1/s]

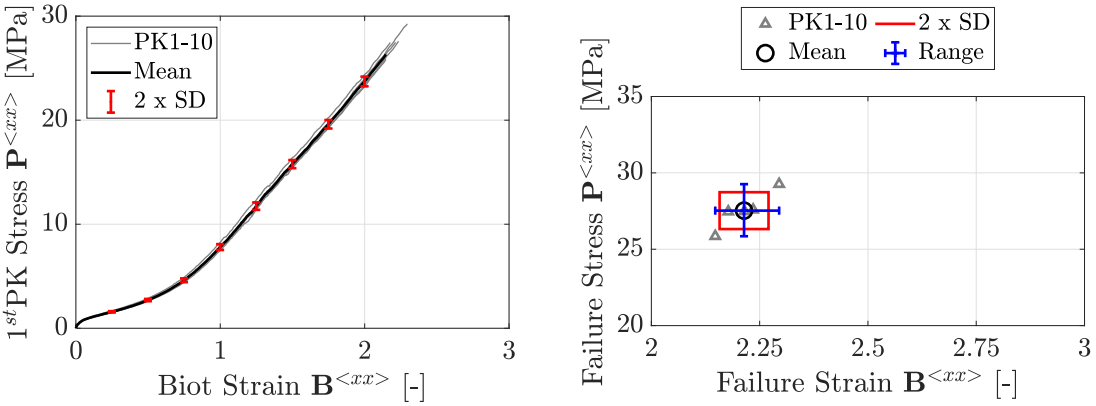

Figure A.8.: Tension until failure - $\dot{\mathbf{B}}^{<xx>} = 0.05$ [1/s]

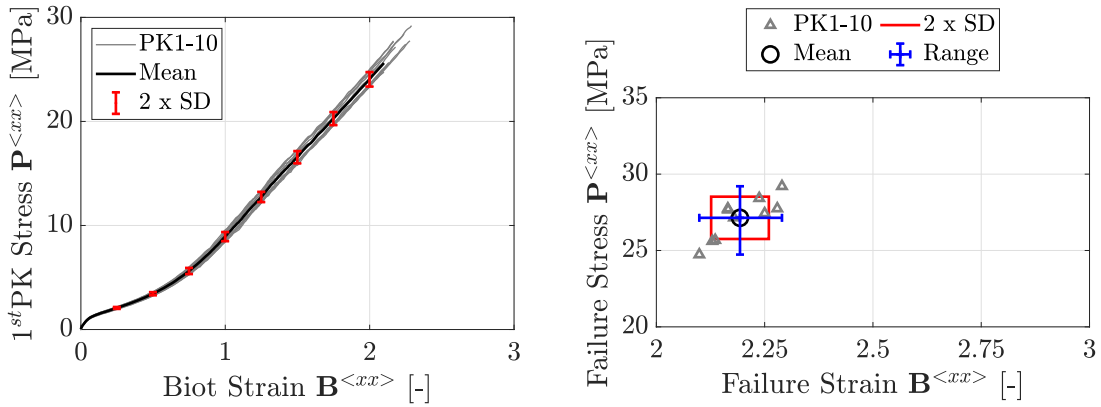

Figure A.9.: Tension until failure - $\dot{\mathbf{B}}^{<xx>} = 0.1$ [1/s]

A.3. Cyclic Tests

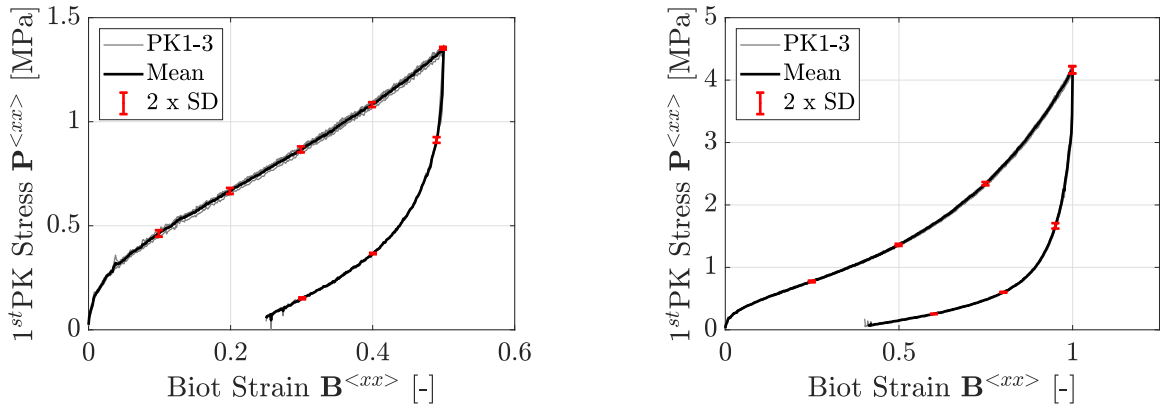

Figure A.10.: Cyclic tests - $\dot{\mathbf{B}}^{<xx>} = 0.01$ [1/s] (left); Cyclic $\dot{\mathbf{B}}^{<xx>} = 0.01$ [1/s] (right)

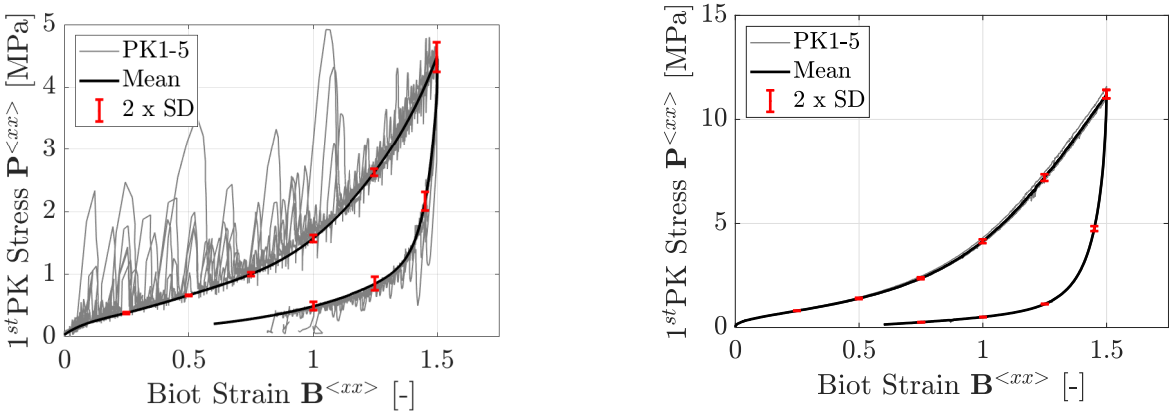

Figure A.11.: Cyclic tests - $\dot{\mathbf{B}}^{<xx>} = 0.001$ [1/s] (left); Cyclic $\dot{\mathbf{B}}^{<xx>} = 0.01$ [1/s] (right)

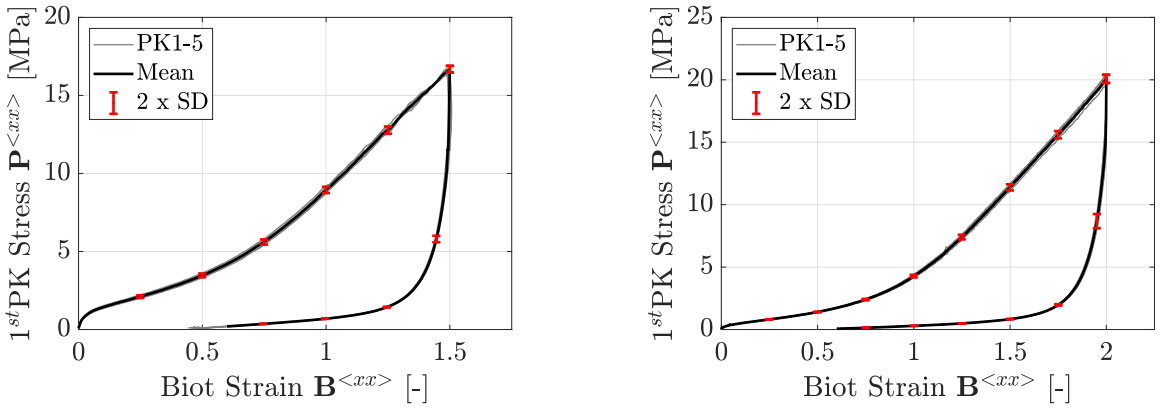

Figure A.12.: Cyclic tests - $\dot{\mathbf{B}}^{<xx>} = 0.1$ [1/s], Cyclic $\dot{\mathbf{B}}^{<xx>} = 0.01$ [1/s]

A.4. Relaxation Tests

A.4.1. Strain Rate 0.001

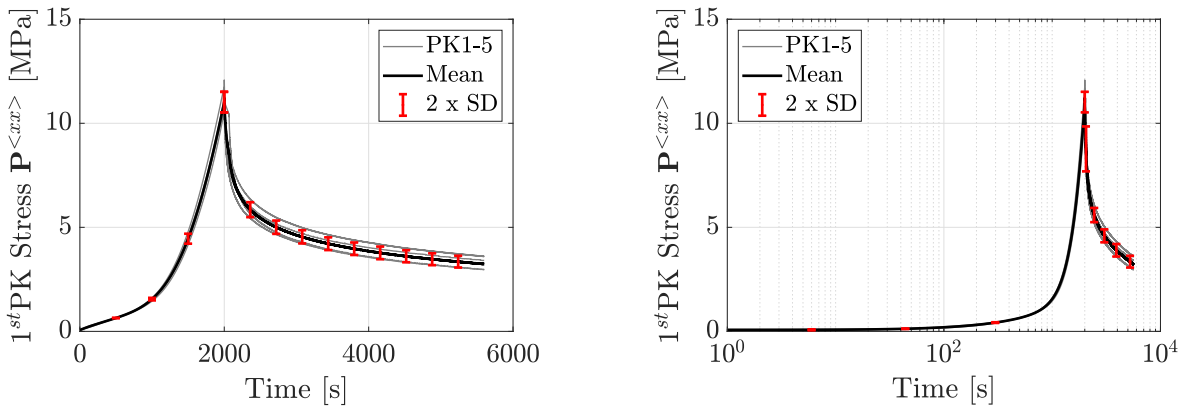

Figure A.13.: Relaxation test - $\dot{\mathbf{B}}^{<xx>} = 0.001$ [1/s], $\mathbf{B}^{<xx>} = 200$ [%] (Duration **1h**)

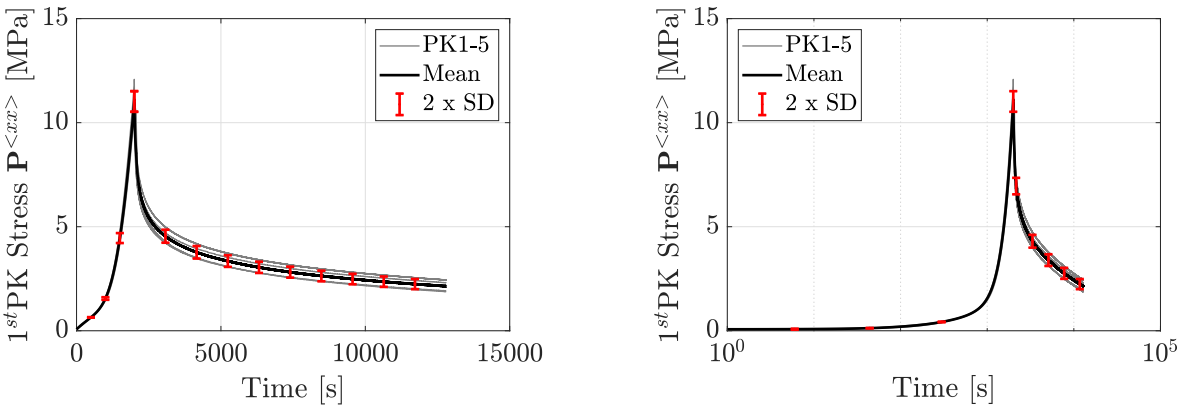

Figure A.14.: Relaxation test - $\dot{\mathbf{B}}^{<xx>} = 0.001$ [1/s], $\mathbf{B}^{<xx>} = 200$ [%] (Duration **3h**)

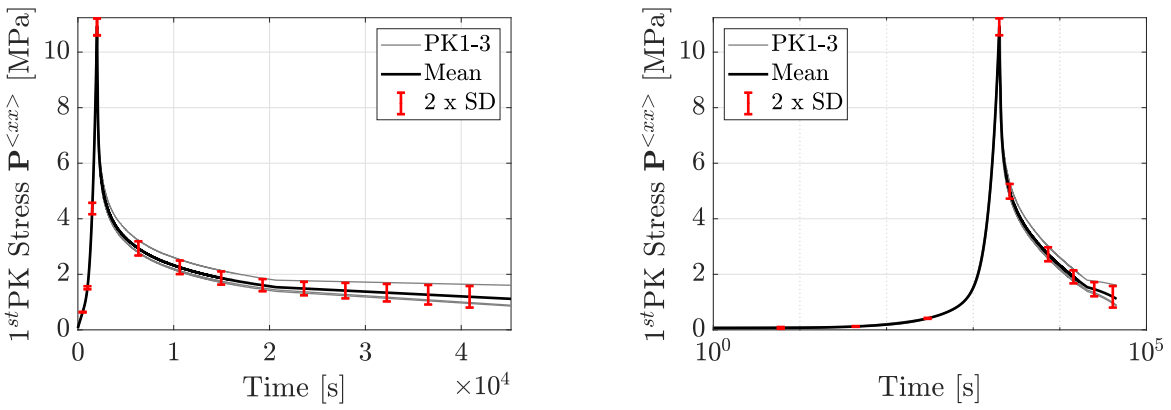

Figure A.15.: Relaxation test - $\dot{\mathbf{B}}^{<xx>} = 0.001$ [1/s], $\mathbf{B}^{<xx>} = 200$ [%] (Duration **12h**)

A.4.2. Strain Rate 0.01

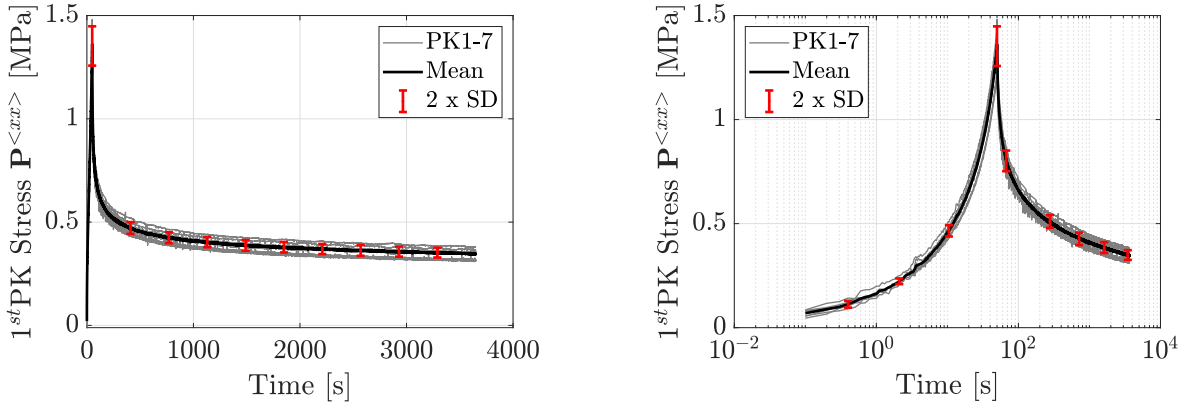

Figure A.16.: Relaxation test - $\dot{\mathbf{B}}^{<xx>} = 0.01$ [1/s], $\mathbf{B}^{<xx>} = 50$ [%] (Duration **1h**)

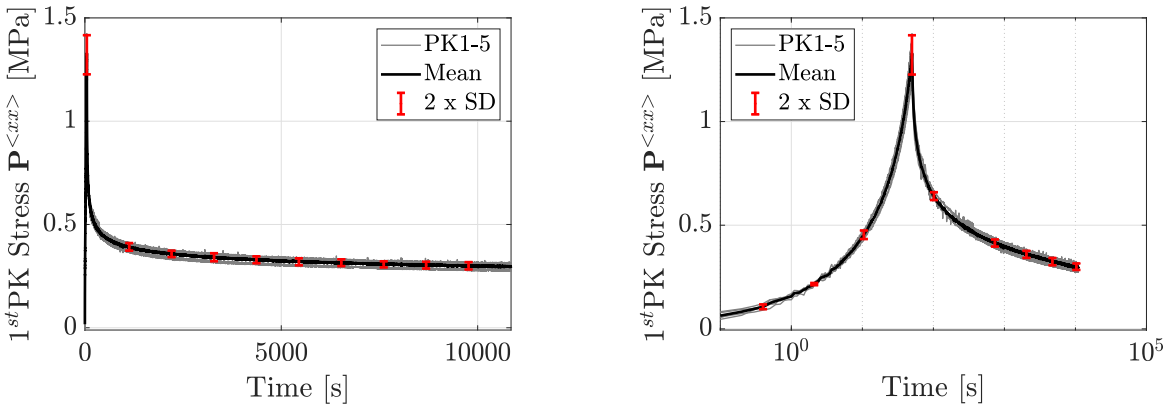

Figure A.17.: Relaxation test - $\dot{\mathbf{B}}^{<xx>} = 0.01$ [1/s], $\mathbf{B}^{<xx>} = 50$ [%] (Duration **3h**)

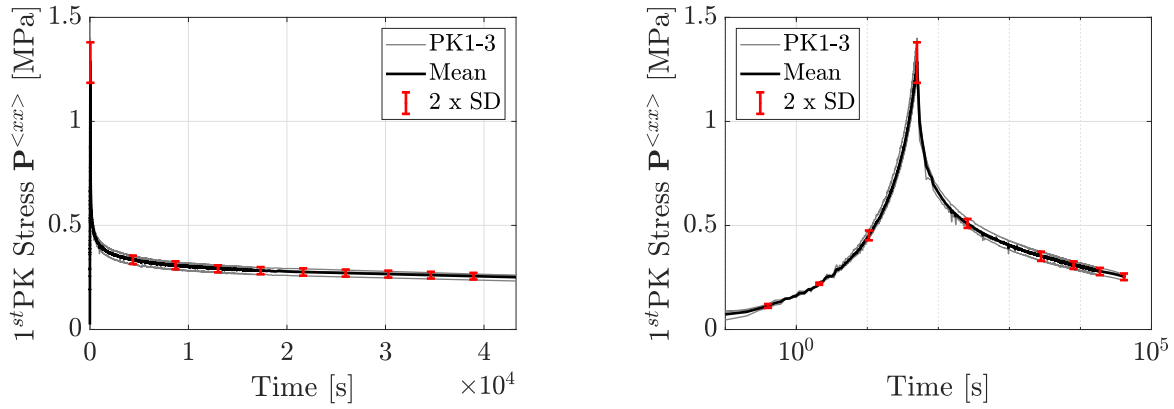

Figure A.18.: Relaxation test - $\dot{\mathbf{B}}^{<xx>} = 0.01$ [1/s], $\mathbf{B}^{<xx>} = 50$ [%] (Duration **12h**)

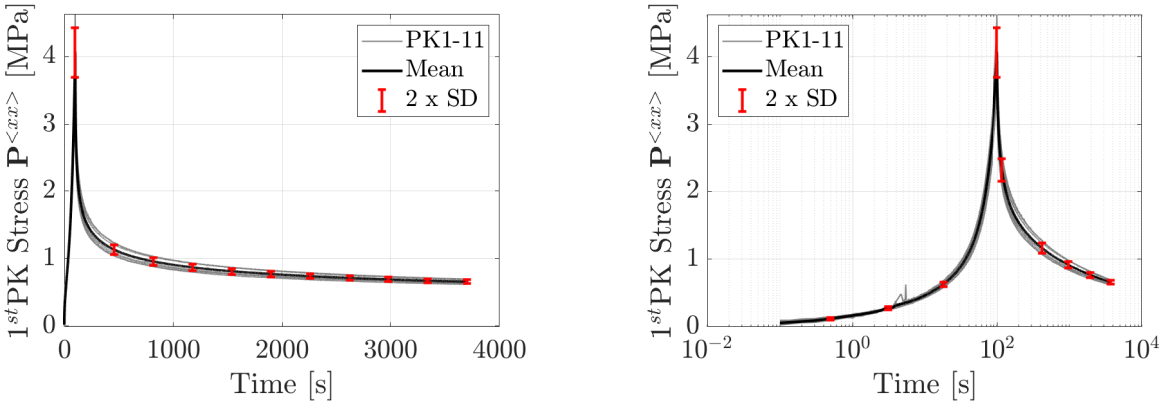

Figure A.19.: Relaxation test - $\dot{\mathbf{B}}^{<xx>} = 0.01$ [1/s], $\mathbf{B}^{<xx>} = 100$ [%] (Duration **1h**)

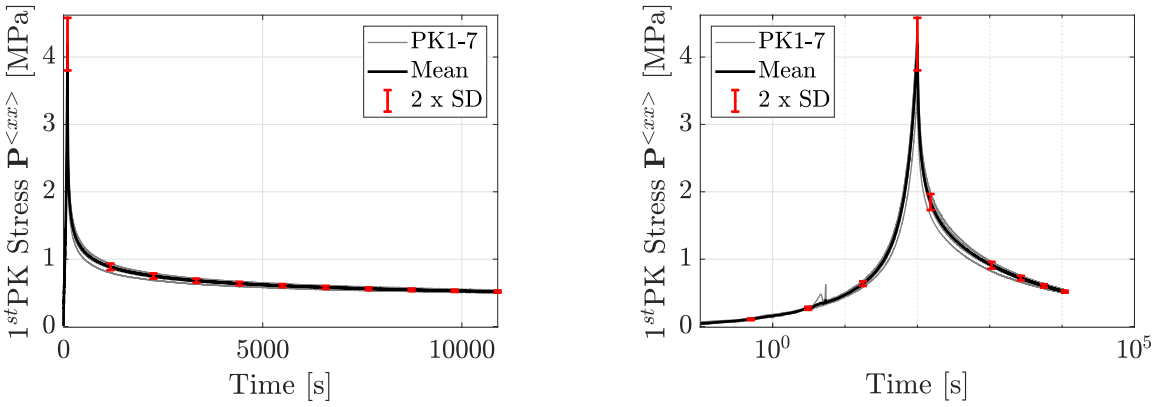

Figure A.20.: Relaxation test - $\dot{\mathbf{B}}^{<xx>} = 0.01$ [1/s], $\mathbf{B}^{<xx>} = 100$ [%] (Duration **3h**)

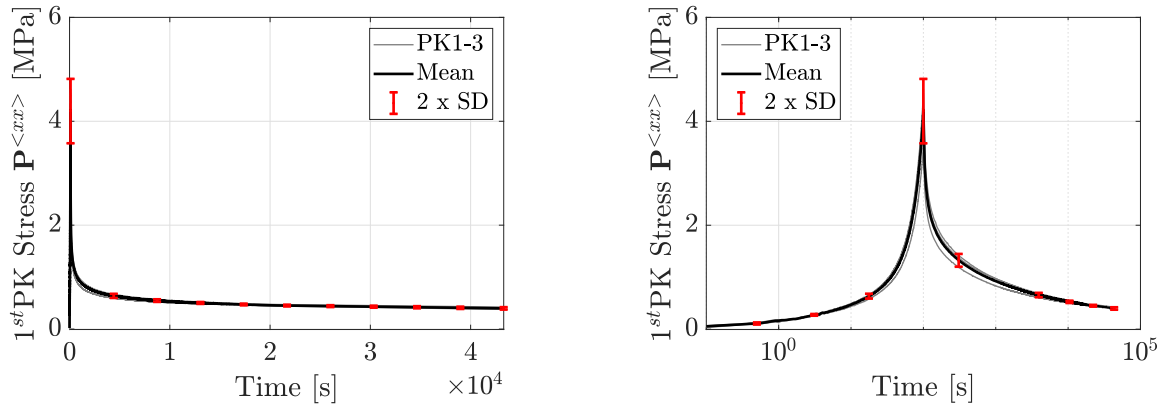

Figure A.21.: Relaxation test - $\dot{\mathbf{B}}^{<xx>} = 0.01$ [1/s], $\mathbf{B}^{<xx>} = 100$ [%] (Duration **12h**)

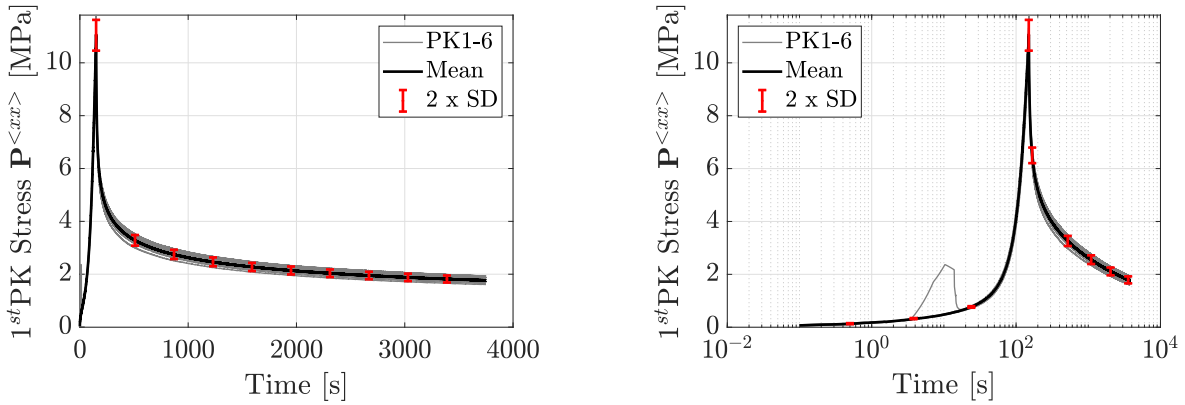

Figure A.22.: Relaxation test - $\dot{\mathbf{B}}^{<xx>} = 0.01$ [1/s], $\mathbf{B}^{<xx>} = 150$ [%] (Duration **1h**)

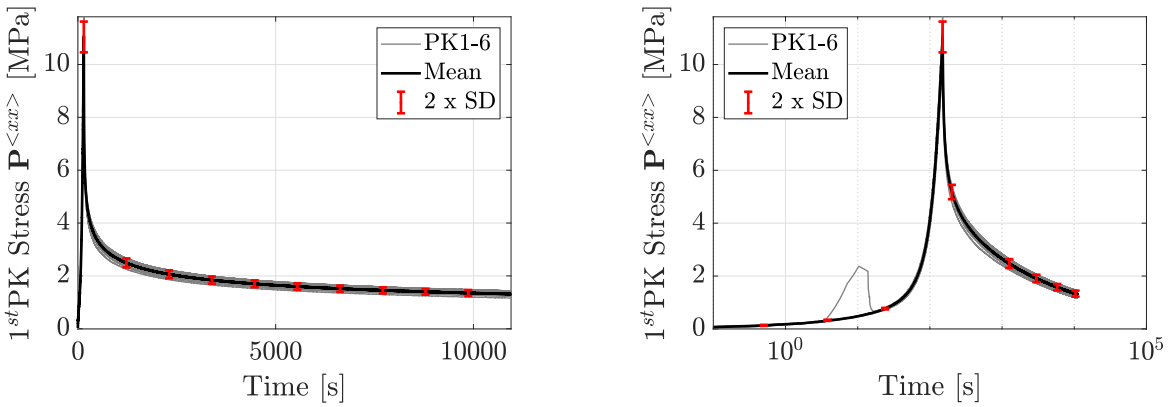

Figure A.23.: Relaxation test - $\dot{\mathbf{B}}^{<xx>} = 0.01$ [1/s], $\mathbf{B}^{<xx>} = 150$ [%] (Duration **3h**)

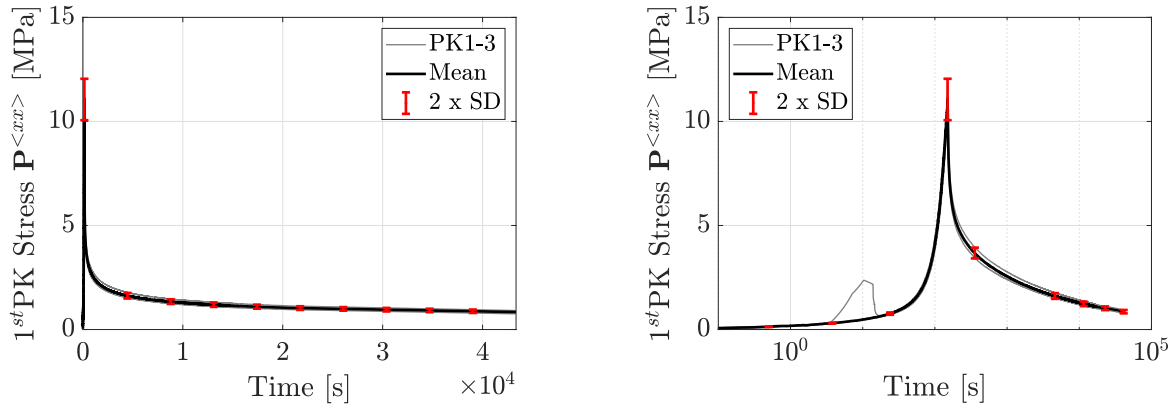

Figure A.24.: Relaxation test - $\dot{\mathbf{B}}^{<xx>} = 0.01$ [1/s], $\mathbf{B}^{<xx>} = 150$ [%] (Duration **12h**)

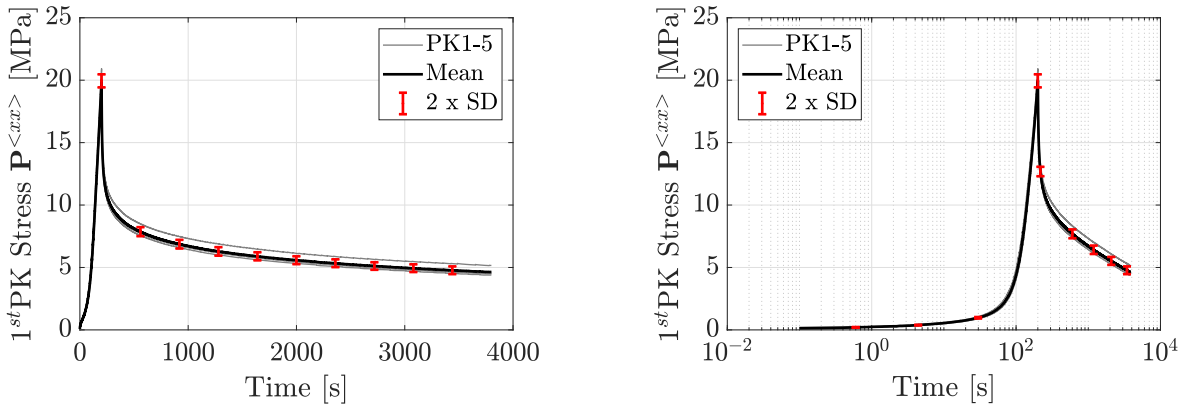

Figure A.25.: Relaxation test - $\dot{\mathbf{B}}^{<xx>} = 0.01$ [1/s], $\mathbf{B}^{<xx>} = 200$ [%] (Duration **1h**)

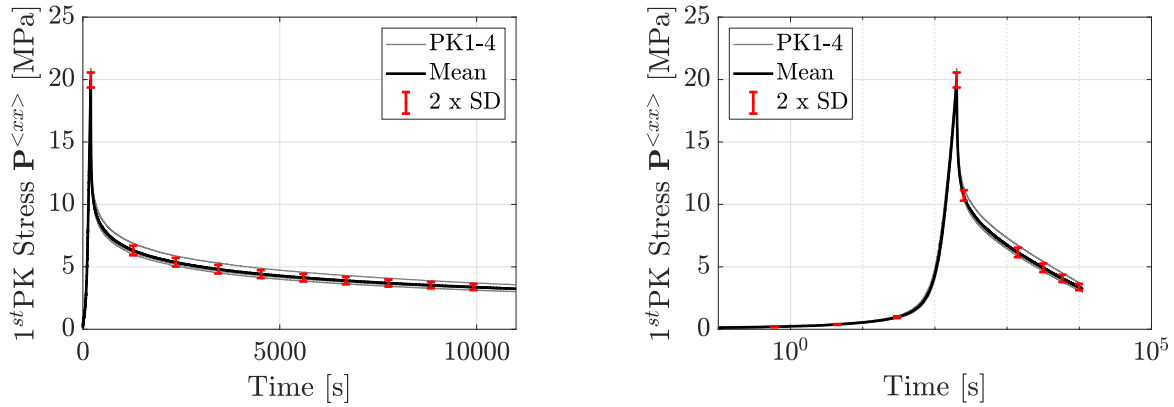

Figure A.26.: Relaxation test - $\dot{\mathbf{B}}^{<xx>} = 0.01$ [1/s], $\mathbf{B}^{<xx>} = 200$ [%] (Duration **3h**)

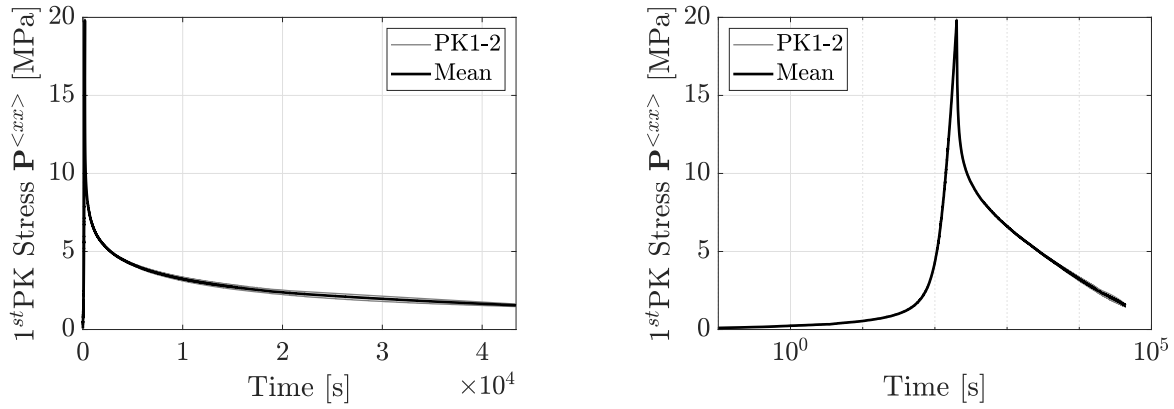

Figure A.27.: Relaxation test - $\dot{\mathbf{B}}^{<xx>} = 0.01$ [1/s], $\mathbf{B}^{<xx>} = 200$ [%] (Duration **12h**)

A.4.3. Strain Rate 0.1

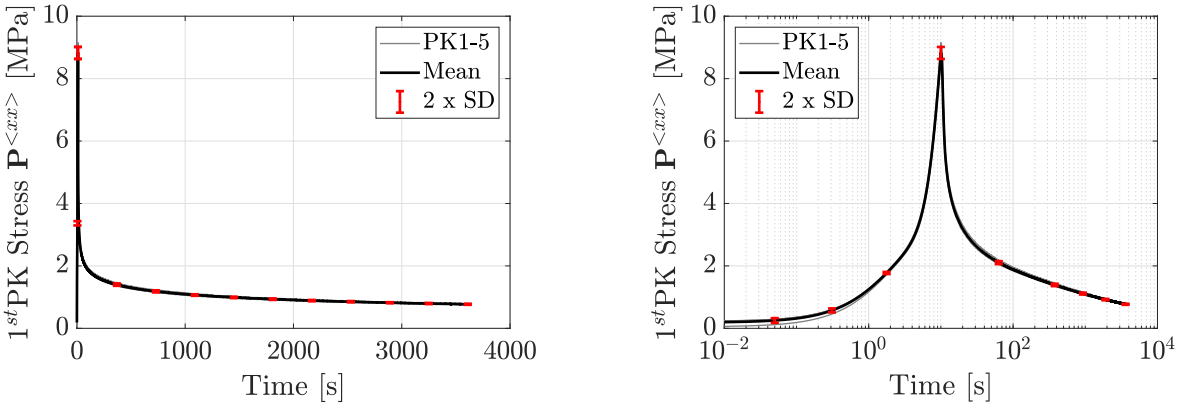

Figure A.28.: Relaxation test - $\dot{\mathbf{B}}^{<xx>} = 0.1$ [1/s], $\mathbf{B}^{<xx>} = 100$ [%] (Duration **1h**)

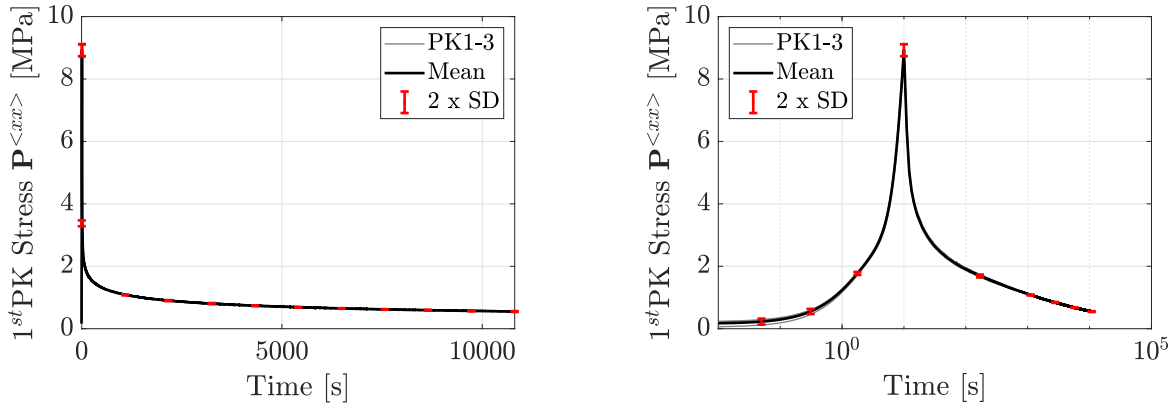

Figure A.29.: Relaxation test - $\dot{\mathbf{B}}^{<xx>} = 0.1$ [1/s], $\mathbf{B}^{<xx>} = 100$ [%] (Duration **3h**)

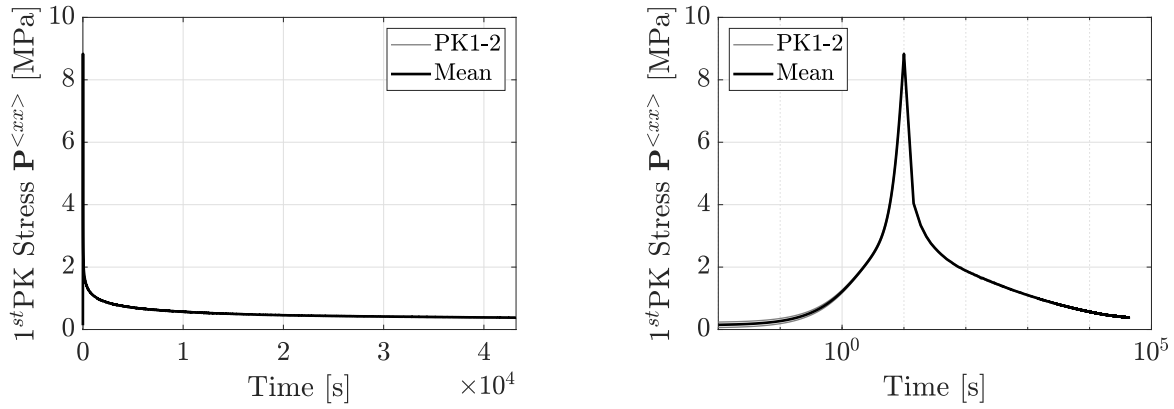

Figure A.30.: Relaxation test - $\dot{\mathbf{B}}^{<xx>} = 0.1$ [1/s], $\mathbf{B}^{<xx>} = 100$ [%] (Duration **12h**)

A.5. Evaluation of Hystereses

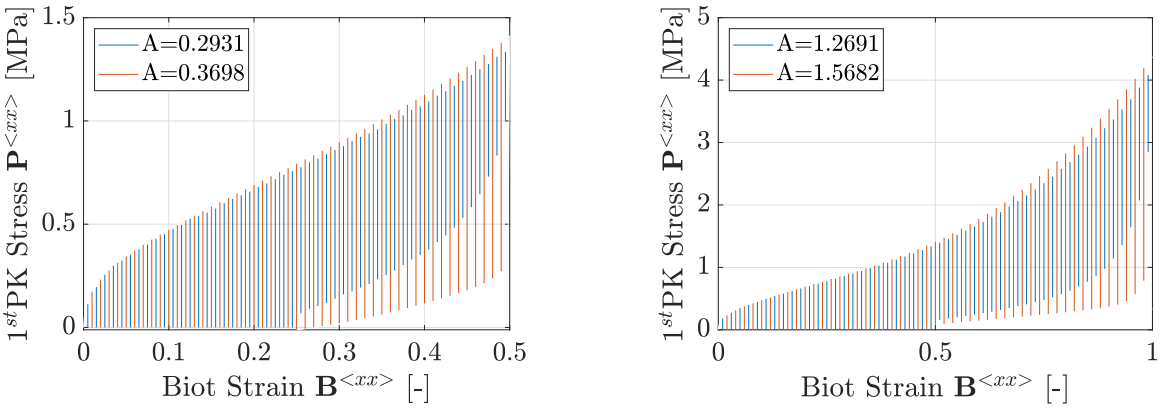

Figure A.31.: Cyclic Tests at different Strain-Rates, loaded to the same Strain Level - Comparison (left); Error (right)

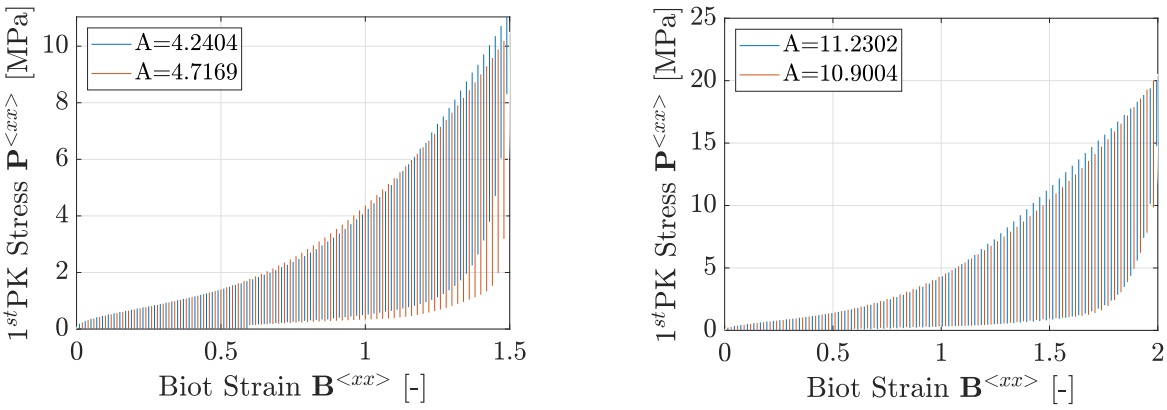

Figure A.32.: Cyclic Tests at different Strain-Rates, loaded to the same Strain Level - Comparison (left); Error (right)

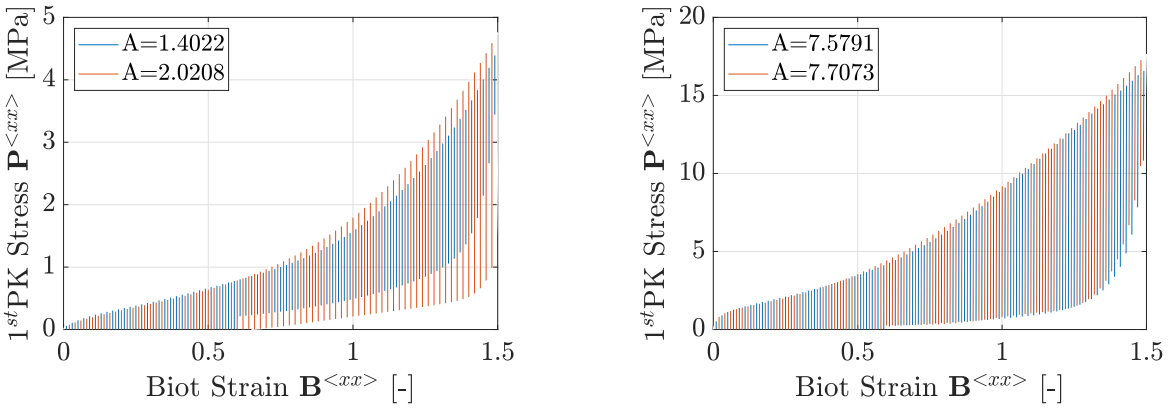

Figure A.33.: Cyclic Tests at different Strain-Rates, loaded to the same Strain Level - Comparison (left); Error (right)

A.6. Staircase Tests

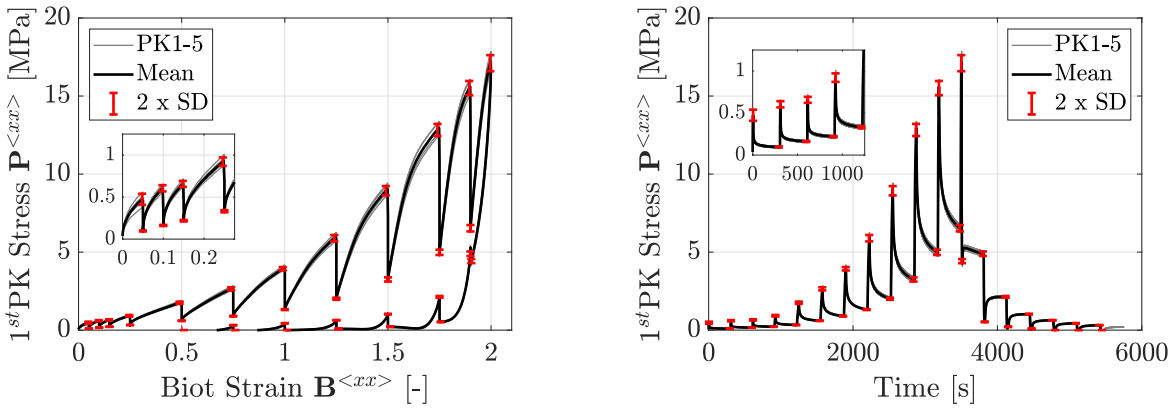

Figure A.34.: Staircase test - $\dot{\mathbf{B}}^{<xx>} = 0.01$

A.7. Temperature

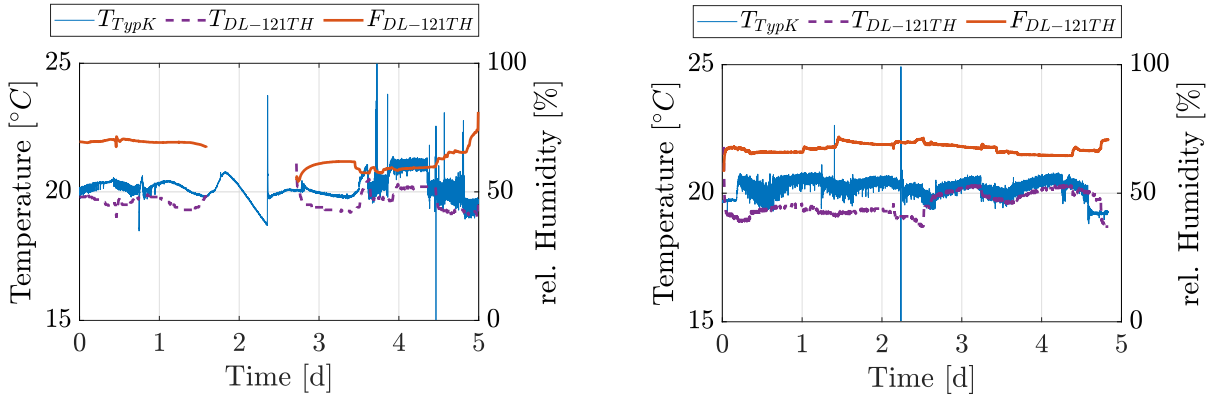

Figure A.35.: Measurement of temperature and humidity, year 2023, KW 30 (left) and KW31 (right)

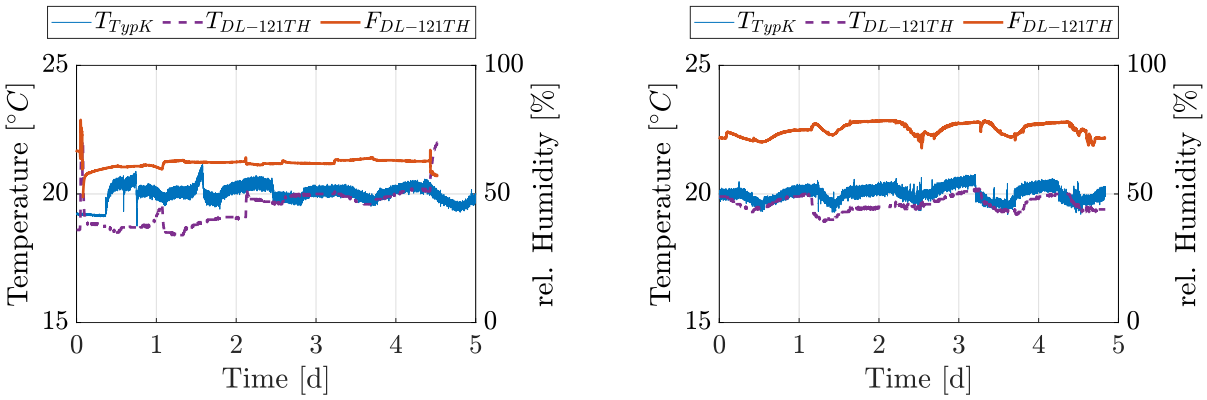

Figure A.36.: Measurement of temperature and humidity, year 2023, KW 32 (left) and KW33 (right)

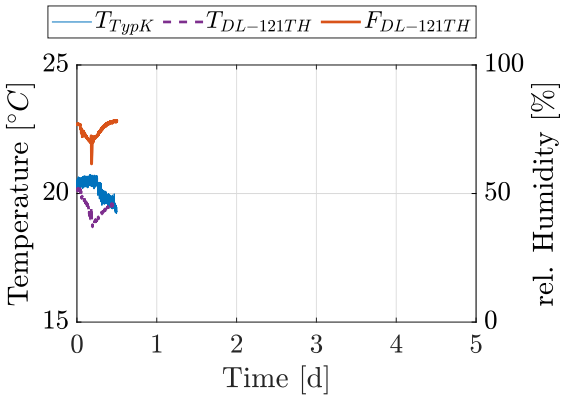

Figure A.37.: Measurement of temperature and humidity, year 2023, KW 34

B. Analytical Calculations

B.1. Analytical Solution of differential equation of linear viscoelasticity

Boundary conditions of the three-parameter Maxwell model:

$$\sigma = \sigma^{eq} + \sigma^{ov} \tag{B.1}$$
$$\sigma^{eq} = E \cdot \varepsilon \tag{B.2}$$
$$\sigma^{ov} = E_{el} \cdot \varepsilon_{el} = \eta \cdot \dot{\varepsilon}_{in} \tag{B.3}$$
$$\varepsilon = \varepsilon_{el} + \varepsilon_{in} \tag{B.4}$$

Manipulating that system of equations such, that it is only dependent on the stress $\sigma(t)$ and the strain $\varepsilon(t)$ as well as their derivatives with respect to time, leads results in:

$$\dot{\sigma} = E \cdot \dot{\varepsilon} + E_{el} \cdot \dot{\varepsilon}_{el} \tag{B.5}$$
$$\dot{\varepsilon}_{el} = \dot{\varepsilon} - \dot{\varepsilon}_{in} \tag{B.6}$$
$$\dot{\varepsilon}_{in} = \frac{\sigma^{ov}}{\eta} \tag{B.7}$$
$$\sigma^{ov} = \sigma - E \cdot \varepsilon \tag{B.8}$$

$$\begin{aligned} \dot{\sigma} &= E \cdot \dot{\varepsilon} + E_{el} \cdot (\dot{\varepsilon} - \dot{\varepsilon}_{in}) \\ &= E \cdot \dot{\varepsilon} + E_{el} \cdot (\dot{\varepsilon} - \frac{\sigma^{ov}}{\eta}) \\ &= E \cdot \dot{\varepsilon} + E_{el} \cdot (\dot{\varepsilon} - \frac{\sigma - E \cdot \varepsilon}{\eta}) \end{aligned} \tag{B.9}$$

sorting Eq. B.9 leads to the differential equation of linear viscoelasticity:

$$\sigma + \frac{\eta}{E_{el}}\dot{\sigma} = E \cdot \varepsilon + \eta\frac{E + E_{el}}{E_{el}}\dot{\varepsilon} \tag{B.10}$$

Solving the inhomogeneous differential equation of the type $a(x) \cdot y\prime(x) + b(x) \cdot y(x) = c(x)$ yields:

$$\sigma_h(t) = C \cdot e^{-\int \frac{b(x)}{a(x)} dx} = C \cdot e^{-\frac{E_{el}}{\eta} t} \tag{B.11}$$

$$\dot{\sigma}_h(t) = -\frac{E_{el}}{\eta} \cdot C \cdot e^{-\frac{E_{el}}{\eta} t} \tag{B.12}$$

$$\sigma_p(t) = c(t) \cdot e^{-\frac{E_{el}}{\eta} t} \tag{B.13}$$

$$\dot{\sigma}_p(t) = \dot{c}(t) \cdot e^{-\frac{E_{el}}{\eta} t} - \frac{E_{el}}{\eta} \cdot c(t) \cdot e^{-\frac{E_{el}}{\eta} t} \tag{B.14}$$

Using $\sigma(t) = \sigma_h + \sigma_p$ leads to:

$$C \cdot e^{-\frac{E_{el}}{\eta} t} + c(t) \cdot e^{-\frac{E_{el}}{\eta} t} - \frac{\eta}{E_{el}} \cdot \frac{E_{el}}{\eta} \cdot C \cdot e^{-\frac{E_{el}}{\eta} t} + \frac{\eta}{E_{el}} \cdot \dot{c}(t) \cdot e^{-\frac{E_{el}}{\eta} t} - \frac{\eta}{E_{el}} \cdot \frac{E_{el}}{\eta} \cdot c(t) \cdot e^{-\frac{E_{el}}{\eta} t} = E \cdot \varepsilon(t) + \eta \frac{E + E_{el}}{E_{el}} \dot{\varepsilon}(t) \tag{B.15}$$

Sorting and shortening Eq. (B.15) yields:

$$\frac{\eta}{E_{el}} \cdot \dot{c}(t) \cdot e^{-\frac{E_{el}}{\eta} t} = E \cdot \varepsilon(t) + \eta \frac{E + E_{el}}{E_{el}} \dot{\varepsilon}(t) \tag{B.16}$$

$$\dot{c}(t) = \frac{E E_{el}}{\eta} \cdot \varepsilon(t) \cdot e^{\frac{E_{el}}{\eta} t} + (E + E_{el}) \cdot \dot{\varepsilon}(t) \cdot e^{\frac{E_{el}}{\eta} t} \tag{B.17}$$

using

$$\left(\varepsilon(t) \cdot e^{\frac{E_{el}}{\eta} t}\right)^{\cdot} = \dot{\varepsilon}(t) \cdot e^{\frac{E_{el}}{\eta} t} + \varepsilon(t) \cdot \frac{E_{el}}{\eta} \cdot e^{\frac{E_{el}}{\eta} t} \rightarrow \varepsilon(t) \cdot \frac{E_{el}}{\eta} \cdot e^{\frac{E_{el}}{\eta} t} = \left(\varepsilon(t) \cdot e^{\frac{E_{el}}{\eta} t}\right)^{\cdot} - \dot{\varepsilon}(t) \cdot e^{\frac{E_{el}}{\eta} t}$$

results in

$$\begin{aligned} \dot{c}(t) &= E \cdot \left(\varepsilon(t) \cdot e^{\frac{E_{el}}{\eta} t}\right)^{\cdot} - E \cdot \dot{\varepsilon}(t) \cdot e^{\frac{E_{el}}{\eta} t} + (E + E_{el}) \cdot \dot{\varepsilon}(t) \cdot e^{\frac{E_{el}}{\eta} t} \\ \dot{c}(t) &= E \cdot \left(\varepsilon(t) \cdot e^{\frac{E_{el}}{\eta} t}\right)^{\cdot} + E_{el} \cdot \dot{\varepsilon}(t) \cdot e^{\frac{E_{el}}{\eta} t} \end{aligned} \tag{B.18}$$

Integrating Eq. B.18 and solving for σ_p results in:

$$\begin{aligned} \sigma_p(t) = c(t) \cdot e^{-\frac{E_{el}}{\eta} t} &= E \cdot \varepsilon(t) \cdot e^{\frac{E_{el}}{\eta} t} \cdot e^{-\frac{E_{el}}{\eta} t} + \int_0^t E_{el} \cdot \dot{\varepsilon}(s) \cdot e^{\frac{E_{el}}{\eta} s} \cdot e^{-\frac{E_{el}}{\eta} t} ds = \\ &= E \cdot \varepsilon(t) \cdot + \int_0^t E_{el} \cdot \dot{\varepsilon}(s) \cdot e^{-\frac{E_{el}}{\eta} (t-s)} ds \end{aligned} \tag{B.19}$$

Eq. B.20

$$\sigma(t) = \sigma_h(t) + \sigma_p(t) = C \cdot e^{-\frac{E_{el}}{\eta}t} + E \cdot \varepsilon(t) \cdot + \int_{s=0}^{s=t} E_{el} \cdot \dot{\varepsilon}(s) \cdot e^{-\frac{E_{el}}{\eta}(t-s)} ds \tag{B.20}$$

together with the requirement $\sigma(t=0) = 0$ and $\varepsilon(t=0) = 0$ leads to the linear functional of the linear viscoelasticity:

$$\sigma(t) = E \cdot \varepsilon(t) + \int_{s=0}^{s=t} E_{el} \cdot e^{-\frac{E_{el}}{\eta}(t-s)} \frac{d\varepsilon(s)}{ds} ds = \int_{s=0}^{s=t} \left\{ E + E_{el} \cdot e^{-\frac{E_{el}}{\eta}(t-s)} \right\} \frac{d\varepsilon(s)}{ds} ds \tag{B.21}$$

Solving the differential equation in an integral sense, yields:

$$\sigma(t) = E \cdot \varepsilon(t) + \int_{s=0}^{s=t} E_{el} \cdot e^{-\frac{E_{el}}{\eta}(t-s)} \frac{d\varepsilon(s)}{ds} ds = \int_{s=0}^{s=t} \left[E + E_{el} \cdot e^{-\frac{E_{el}}{\eta}(t-s)} \right] \frac{d\varepsilon(s)}{ds} ds \tag{B.22}$$

Solving the integral for the stationary case ($\dot{\varepsilon} = \dot{\varepsilon}_0$) yields:

$$\sigma(t) = E \cdot \varepsilon(t) + E_{el} e^{-\frac{E_{el}}{\eta}t} \int_{s=0}^{s=t} e^{\frac{E_{el}}{\eta}s} \dot{\varepsilon}_0 ds = E \cdot \varepsilon(t) \cdot + E_{el} e^{-\frac{E_{el}}{\eta}t} \left[\frac{\eta}{E_{el}} e^{\frac{E_{el}}{\eta}s} \dot{\varepsilon}_0 \right]_0^t = \tag{B.23}$$

$$= E \cdot \varepsilon(t) + E_{el} e^{-\frac{E_{el}}{\eta}t} \left[\frac{\eta}{E_{el}} e^{\frac{E_{el}}{\eta}t} \dot{\varepsilon}_0 - \frac{\eta}{E_{el}} \dot{\varepsilon}_0 \right] = E \cdot \varepsilon(t) + \dot{\varepsilon}_0 \eta \left[1 - e^{-\frac{E_{el}}{\eta}t} \right] \tag{B.24}$$

For the unloading path of a single, symmetric cycle, under the consideration $\dot{\varepsilon}_{0,1} = -\dot{\varepsilon}_{0,2}$ and $\tau = \frac{\eta}{E_{el}}$:

$$\sigma = \int_{s=0}^{s=\frac{T}{2}} E_{el} \dot{\varepsilon}_{0,1} e^{-\frac{t-s}{\tau}} ds + \int_{s=\frac{T}{2}}^{s=T} E_{el} \dot{\varepsilon}_{0,2} e^{-\frac{t-s}{\tau}} ds = E_{el} \dot{\varepsilon}_0 e^{\frac{-t}{\tau}} \left[\int_{s=0}^{s=\frac{T}{2}} e^{\frac{s}{\tau}} ds - \int_{s=\frac{T}{2}}^{s=t} e^{\frac{s}{\tau}} ds \right] = \tag{B.25}$$

$$= E_{el} \tau \dot{\varepsilon}_0 e^{\frac{-t}{\tau}} \left[\left(e^{\frac{T/2}{\tau}} - 1 \right) - \left(e^{\frac{t}{\tau}} - e^{\frac{T/2}{\tau}} \right) \right] = \eta \dot{\varepsilon}_0 \left[2e^{\frac{T/2}{\tau}} - e^{\frac{-t}{\tau}} - 1 \right] \tag{B.26}$$

Taking only the time-dependent stiffness $E_R(t) = E + E_{el} \cdot e^{-\frac{E_{el}}{\eta}t}$ and normalize it by the use of the function $E_0 = E + E_{el}$ and with respect to that $\frac{E}{E_0} + \frac{E_{el}}{E_0} = 1$ yields the so called Prony series:

$$\frac{E_R(t)}{E_0} = \frac{E}{E_0} + \frac{E_{el}}{E_0} \cdot e^{-\frac{E_{el}}{\eta}t} = 1 - \frac{E_{el}}{E_0} + \frac{E_{el}}{E_0} \cdot e^{-\frac{E_{el}}{\eta}t} = 1 - \frac{E_{el}}{E_0}(1 - e^{-\frac{E_{el}}{\eta}t}) \tag{B.27}$$

B.2. Analytical Solution of the functional of finite linear viscoelasticity

For the following consideration also consider Bergström [24]. Considering again the Prony-Series, Eq. B.27 and introducing $g_R(t) = \frac{E_R(t)}{E_0}$ yields:

$$\sigma(t) = \int_{s=0}^{s=t} \left[\frac{E}{E_0} + \frac{E_{el}}{E_0} e^{-\frac{t-s}{\tau}} \right] E_0 \frac{d\varepsilon(s)}{ds} ds = \int_{s=0}^{s=t} g_R(t-s) E_0 \frac{d\varepsilon(s)}{ds} ds \tag{B.28}$$

Integration Eq. B.28 by parts leads to:

$$\sigma(t) = E_0\varepsilon(t) - \int_{s=0}^{s=t} \dot{g}_R(t-s)E_0\varepsilon(s)ds \tag{B.29}$$

Using the hyperelastic stress function σ_{hyp} for $E_0\varepsilon(t)$ results in:

$$\sigma(t) = \sigma_{hyp}(\varepsilon(t)) - \int_{s=0}^{s=t} \dot{g}_R(t-s)\sigma_{hyp}(\varepsilon(s))ds \tag{B.30}$$

Introducing $g = \frac{E_{el}}{E_0}$ and taking only the right side of Eq. B.30 leads to:

$$\int_{s=0}^{s=t} \frac{d}{ds}\Big[(1-g) + ge^{-\frac{t-s}{\tau}}\Big]\sigma_{hyp}(\varepsilon(s))ds \tag{B.31}$$

Choosing the limits of the integral from $s = 0$ to $s = t + \Delta t$ yields:

$$\int_{s=0}^{s=t+\Delta t} \frac{d}{ds}\Big[(1-g) + ge^{-\frac{t+\Delta t-s}{\tau}}\Big]\sigma_{hyp}(\varepsilon(s))ds \tag{B.32}$$

Splitting it up, Eq. B.32 leads to:

$$\begin{aligned}
&\int_{s=0}^{s=t} \frac{d}{ds}\Big[(1-g) + ge^{-\frac{t+\Delta t-s}{\tau}}\Big]\sigma_{hyp}(\varepsilon(s))ds + \int_{s=t}^{s=t+\Delta t} \frac{d}{ds}\Big[(1-g) + ge^{-\frac{t+\Delta t-s}{\tau}}\Big]\sigma_{hyp}(\varepsilon(s))ds = \\
&= \int_{s=0}^{s=t} \frac{g}{\tau}\Big[e^{-\frac{t+\Delta t-s}{\tau}}\Big]\sigma_{hyp}(\varepsilon(s))ds + \int_{s=t}^{s=t+\Delta t} \frac{g}{\tau}\Big[e^{-\frac{t+\Delta t-s}{\tau}}\Big]\sigma_{hyp}(\varepsilon(s))ds
\end{aligned} \tag{B.33}$$

Integrating Eq. B.33 separately, yields for the first part:

$$\int_{s=0}^{s=t} \frac{g}{\tau}\Big[e^{-\frac{t+\Delta t-s}{\tau}}\Big]\sigma_{hyp}(\varepsilon(s))ds = e^{-\frac{\Delta t}{\tau}} \int_{s=0}^{s=t} \frac{g}{\tau}\Big[e^{-\frac{t-s}{\tau}}\Big]\sigma_{hyp}(\varepsilon(s))ds \tag{B.34}$$

The second part needs to be integrated by parts. First of all the hyperelastic stress is partly linearised, as follows:

$$\sigma_{hyp}(s) = \sigma_{hyp}(t) + \Delta\sigma_{hyp}\frac{s-t}{\Delta t} \tag{B.35}$$

and

$$\Delta\sigma_{hyp} = \sigma_{hyp}(\varepsilon(t+\Delta t)) - \sigma_{hyp}(\varepsilon(t)) \tag{B.36}$$

$$\begin{aligned}\int_{s=t}^{s=t+\Delta t} \frac{g}{\tau}\left[e^{-\frac{t+\Delta t-s}{\tau}}\right]\left[\sigma_{hyp}(t) + \Delta\sigma_{hyp}\frac{s-t}{\Delta t}\right]ds = \int_{s=t}^{s=t+\Delta t} \frac{g}{\tau}\left[e^{-\frac{t+\Delta t-s}{\tau}}\right]\sigma_{hyp}(t)ds + \\ + \int_{s=t}^{s=t+\Delta t} \frac{g}{\tau}\left[e^{-\frac{t+\Delta t-s}{\tau}}\right]\Delta\sigma_{hyp}\frac{s}{\Delta t}ds - \int_{s=t}^{s=t+\Delta t} \frac{g}{\tau}\left[e^{-\frac{t+\Delta t-s}{\tau}}\right]\Delta\sigma_{hyp}\frac{t}{\Delta t}ds\end{aligned} \tag{B.37}$$

The first part results in:

$$\int_{s=t}^{s=t+\Delta t} \frac{g}{\tau}\left[e^{-\frac{t+\Delta t-s}{\tau}}\right]\sigma_{hyp}(t)ds = \left[\tau\frac{g}{\tau}e^{-\frac{t+\Delta t-s}{\tau}}\sigma_{hyp}(t)\right]_{s=t}^{s=t+\Delta t} = g\sigma_{hyp}(t)\left[1-e^{-\frac{\Delta t}{\tau}}\right] \tag{B.38}$$

Integrating the second part of Eq. B.37 by parts, results in:

$$\begin{aligned}&\int_{s=t}^{s=t+\Delta t} \frac{g}{\tau}\left[e^{-\frac{t+\Delta t-s}{\tau}}\right]\Delta\sigma_{hyp}\frac{s}{\Delta t}ds = \left[\tau\frac{g}{\tau}e^{-\frac{t+\Delta t-s}{\tau}}\Delta\sigma_{hyp}\frac{s}{\Delta t}\right]_{s=t}^{s=t+\Delta t} - \\ &- \int_{s=t}^{s=t+\Delta t} \tau\frac{g}{\tau}\left[e^{-\frac{t+\Delta t-s}{\tau}}\right]\Delta\sigma_{hyp}\frac{1}{\Delta t}ds = \left[g\Delta\sigma_{hyp}\frac{t+\Delta t}{\Delta t}\right] - \\ &\left[ge^{-\frac{\Delta t}{\tau}}\Delta\sigma_{hyp}\frac{t}{\Delta t}\right] - \left[\tau ge^{-\frac{t+\Delta t-s}{\tau}}\Delta\sigma_{hyp}\frac{1}{\Delta t}\right]_{s=t}^{s=t+\Delta t} = \\ &= g\frac{\Delta\sigma_{hyp}}{\Delta t}\left[t+\Delta t - te^{-\frac{\Delta t}{\tau}} - \tau + \tau e^{-\frac{\Delta t}{\tau}}\right]\end{aligned} \tag{B.39}$$

The third part yields:

$$\begin{aligned}&\int_{s=t}^{s=t+\Delta t} \frac{g}{\tau}\left[e^{-\frac{t+\Delta t-s}{\tau}}\right]\Delta\sigma_{hyp}\frac{t}{\Delta t}ds = \left[\tau\frac{g}{\tau}e^{-\frac{t+\Delta t-s}{\tau}}\Delta\sigma_{hyp}\frac{s}{\Delta t}\right]_{s=t}^{s=t+\Delta t}\Delta\sigma_{hyp}\frac{t}{\Delta t} = \\ &= g\Delta\sigma_{hyp}\frac{t}{\Delta t}\left[1-e^{-\frac{\Delta t}{\tau}}\right]\end{aligned} \tag{B.40}$$

Putting the parts together, results in:

$$\begin{aligned}&g\frac{\Delta\sigma_{hyp}}{\Delta t}\left[t+\Delta t - te^{-\frac{\Delta t}{\tau}} - \tau + \tau e^{-\frac{\Delta t}{\tau}}\right] - g\frac{\Delta\sigma_{hyp}}{\Delta t}\left[t - te^{-\frac{\Delta t}{\tau}}\right] = \\ &g\frac{\Delta\sigma_{hyp}}{\Delta t}\left[\Delta t - \tau + \tau e^{-\frac{\Delta t}{\tau}}\right]\end{aligned} \tag{B.41}$$

In total the result is:

$$\begin{aligned}\sigma(t) = \sigma_{hyp}(\varepsilon(t)) - e^{-\frac{\Delta t}{\tau}}\int_{s=0}^{s=t} \frac{g}{\tau}\left[e^{-\frac{t-s}{\tau}}\right]\sigma_{hyp}(\varepsilon(s))ds - g\sigma_{hyp}(t)\left[1-e^{-\frac{\Delta t}{\tau}}\right] - \\ - g\frac{\Delta\sigma_{hyp}}{\Delta t}\left[\Delta t - \tau + \tau e^{-\frac{\Delta t}{\tau}}\right]\end{aligned} \tag{B.42}$$

C. Publications and Presentations

C.1. Journal Articles

A. Pauli, M. A. Kraus, and G. Siebert. Experimental and numerical investigations on glass fragments: shear-frame testing and calibration of Mohr-Coulomb plasticity model. *Glass Structures & Engineering*, 6:65-87, 2021. ISSN 2363-5142. doi: 10.1007/s40940-020-00143-5.

A. Pauli and G. Siebert. Simplfied approach for modeling standard PVB at large deformations and long-term loading. *Glass Structures & Engineering*, 9:59-73, 2024. ISSN 2363-5142. doi: 10.1007/s40940-023-00236-x.

A. Pauli and G. Siebert. Investigations on the finite strain behavior of standard PVB: experiment and modeling. textitGlass Structures & Engineering, 9:587-606, 2024. ISSN 2363-5142. doi: 10.1007/s40940-024-00247-2.

D. Offereins, A. Pauli, and G. Siebert. Mechanical Performance Of Liquid Cold-Poured Interlayer Adhesives In Comparison To PVB, EVA, And Ionomers. *Glass Structures & Engineering*, 9:569-586, 2024. ISSN 2363-5142. doi: 10.1007/s40940-024-00274-z.

C.2. Contribution to Year Books

A. Pauli, M. A. Kraus, M. Drass and G. Siebert. (2020). Simulation von Verbundsicherheitsglas aus Einscheibensicherheitsglas im gebrochenen Zustand. *ce/papers*, 4(1):119-129, 2021.

M. A. Kraus and A. Pauli. Konstitutive Modellierung der Bruchfragmente thermisch vorgespannter Gläser innerhalb der Plastizitätstheorie – Experiment und Numerik. *ce/papers*, 4(5):271-282, 2021.

C.3. Conference Papers & Presentations

A. Pauli, M. A. Kraus and G. Siebert. Experimental and Methodical Investigations on the Hyperelasticity of Standard PVB. Glass Performance Days, Tampere, Finland 26.06 - 28.06.2019

A. Pauli, M. Illguth, F. Wellershoff, G. Siebert and M. A. Kraus. Experimental and Numerical Investigations on the finite strain viscoelasticity of Standard PVB. Challenging Glass Conference - Volume 8, Ghent, Belgium, 23.06 - 24.06.2022

M. Baric, A. Pauli and G. Siebert. Experimental investigations on EVA interlayers in the regime of large deformations in the context of the examination of the residual load bearing capacity of LSG. The 9th International Conference On Structural Engineering, Mechanics And Computation, Cape Town, South Africa, 05.09 - 07.09.2022

A. Pauli, D. Offereins and G. Siebert. Numerical Modelling of UV-curing acrylate adhesives. Glass Performance Days, Tampere, Finland, 14.06. – 16.06.2023

A. Pauli and G. Siebert. Structural Design of Glass-Elements in Bridge-Constructions. 13th - Japanese-German Bridge Symposium, Osaka, Japan, 08.09. - 09.01.2023
A. Pauli and G. Siebert. Investigations on the finite strain behavior of standard PVB: experiment and modeling. Challenging Glass Conference - Volume 9, Delft, Netherlands, 19.06 - 20.06.2024